Roy C.P. Kerckhoffs *Editor*

Patient-Specific Modeling of the Cardiovascular System

Technology-Driven Personalized Medicine

Springer

Patient Specific Modeling of the Cardiovascular System

Technology-Driven Personalized Medicine

Roy C.P. Kerckhoffs
Editor

Patient Specific Modeling of the Cardiovascular System

Technology-Driven Personalized Medicine

Springer

Editor
Roy C.P. Kerckhoffs
University of California San Diego
Department of Bioengineering
9500 Gillman Drive
La Jolla, CA 92093-0412
USA
roy@bioeng.ucsd.edu

ISBN 978-1-4419-6690-2 e-ISBN 978-1-4419-6691-9
DOI 10.1007/978-1-4419-6691-9
Springer New York Dordrecht Heidelberg London

Library of Congress Control Number: 2010933851

Foreword

Peter Hunter

Computational physiology for the cardiovascular system is entering a new and exciting phase of clinical application. Biophysically based models of the human heart and circulation, based on patient-specific anatomy but also informed by population atlases and incorporating a great deal of mechanistic understanding at the cell, tissue, and organ levels, offer the prospect of evidence-based diagnosis and treatment of cardiovascular disease.

The clinical value of patient-specific modeling is well illustrated in application areas where model-based interpretation of clinical images allows a more precise analysis of disease processes than can otherwise be achieved. For example, Chap. 6 in this volume, by Speelman et al., deals with the very difficult problem of trying to predict whether and when an abdominal aortic aneurysm might burst. This requires automated segmentation of the vascular geometry from magnetic resonance images and finite element analysis of wall stress using large deformation elasticity theory applied to the geometric model created from the segmentation. The time-varying normal and shear stress acting on the arterial wall is estimated from the arterial pressure and flow distributions. Thrombus formation is identified as a potentially important contributor to changed material properties of the arterial wall. Understanding how the wall adapts and remodels its material properties in the face of changes in both the stress loading and blood constituents associated with inflammatory processes (IL6, CRP, MMPs, etc.) is a major challenge for this field and one that calls on a robust framework for multiscale modeling (see below) as well as the detection of blood biomarkers that provide further patient-specific data. Note that an increasing trend in biomechanics research, where there is a need to model tissue adaptation to a changing environment, is to underpin constitutive models with microstructural tissue models that deal with structure/function relations and to link these models through mixture theory to the cellular signaling pathways that alter gene expression and hence tissue composition.

Another example of patient-specific modeling using image data is described in Chap. 10 by Sermesant and Razavi on "Personalized computational models of the heart for cardiac resynchronization therapy (CRT)," which addresses the question of why one third of heart failure patients who receive CRT apparently gain no benefit. The premise is that patient outcomes can be improved by optimizing lead placement using predictive subject-specific anatomically and biophysically based

modeling of a patient's heart (in this case using eikonal equations). The data sources from the XMR suite at King's College London (which includes an MR scanner and an X-ray C-arm) are anatomical MRI, endocardial mapping, cine MRI, and left ventricular pressure via a catheter.

Chapter 1 provides an overview of imaging modalities with which the image data are obtained that serve as the basis for 3D patient-specific modeling. The chapter specifically focuses on patients with heart rhythm disorders, such as atrial fibrillation. Therapeutic strategies for dealing with atrial fibrillation based on a biophysical model of the human atria are discussed by Virag et al. in Chap. 4. Patient-specific image segmentation for heart modeling is illustrated by Vadakkumpadan et al. in Chap. 9. Here the challenges are achieving image segmentation for both the ventricular geometry and the fibrous structure of myocardium. Chapter 8 by Wenk et al. examines myocardial material properties and stress distributions in normal and failing human hearts. An application of patient-specific modeling to the hypoxic response and microvasculature dynamics is given by Nathan and Qutub in Chap. 11. Sachse in Chap. 3 provides a discussion on imaging modalities at the (sub-)cellular level of cardiac physiology and the promise of patient-specific modeling at the cellular level. In comparison to these biophysically detailed models, the simpler heart and circulation models of Arts et al. in Chap. 2 offer the prospect of rapid parameter estimation in a clinical setting. The future in my view lies in combining both types of models such that the parameters of the simpler models can be linked to the more biophysically detailed models that provide a more mechanistic understanding of disease processes.

A recent trend in clinical application modeling is to combine patient-specific information (especially from clinical imaging) with population data stored in an atlas. For example, Chap. 7 by Backhaus et al. describes the Cardiac Atlas Project (CAP), which is establishing a web-accessible structural and functional atlas of the normal and pathological heart for clinical, research and educational purposes. This database or atlas, which is based on open source PACS system (Dm4chee) coupled with open source graphical display software (cmgui) and web2.0 metadata technologies, contains anatomical and functional heart data from 10,000 patients. An initial goal of the atlas, based on fitting finite element geometric models to each individual heart, is to facilitate statistical analysis across population groups of regional heart shape and wall motion characteristics, and to facilitate data fusion between different imaging protocols and modalities. In order to link this subject-specific kinematic information to the physical mechanisms behind cardiac function, the CAP database is also designed to include annotated clinical data from, for example, coronary angiography, ECG, histology, blood proteins, peptides, and other serological data. In combination with whole heart multiscale finite element modeling tools this will offer an immensely valuable resource for studying the clinically important mechanisms behind cardiac diseases. In the longer term it may also include genetic information as this becomes available.

The use of patient-specific modeling to assist with decision-making in critical care is another important topic – addressed in Chap. 5 by Neal. The need for almost real-time solution in this situation means that the models are typically based on

ordinary differential equations (ODEs), rather than partial differential equations (PDEs). A number of examples are given including hemodynamic models for cardiac output estimation and simulating the response to traumatic brain injury, and models of glucose and insulin dynamics for controlling blood glucose levels. The major challenges with these models are (i) the need for rapid parameter estimation, and (ii) the need to link the parameters of these ODE models to more biophysically based PDE models.

In Chap. 12, an overview is given of a software structure to create patient-specific models. It focuses on the modular nature of models for multi-scale systems, the interactions between different scales and the importance of databases to generate the predictions required by physicians.

An essential prerequisite for the inclusion of models in clinical workflows is the establishment of modeling standards and web-accessible model and data repositories that demonstrate model reproducibility. These issues are touched on in a number of chapters of the book. For a model to be worth including as part of a clinical workflow, as when used within a diagnostic process, the model outputs, for given inputs, must be demonstrably reproducible to within machine precision. To this end, the modeling community has invested much effort over the last few years in establishing XML-based standards for biological modeling, in particular the SBML (http://www.sbml.org), CellML (http://www.cellml.org) and FieldML (http://www.fieldml.org) standards. Minimum information standards, such as MIRIAM (http://www.ebi.ac.uk/miriam) for model annotation and MIASE (http://www.biomodels.net/miase) for annotation of a simulation experiment, have been developed. Model repositories based on these standards are also well developed, for example, biomodels.org and models.cellml.org. Furthermore, open source software packages that use these standards and include the Application Programming Interfaces (APIs) that enable the models in the web databases to be imported into the simulation environments, are also now well developed – and are used by many of the authors in this volume. Another key challenge to embedding models in clinical workflows is the development of metadata standards that link the components of the models to the biological and clinical terms used in the standard ontologies such as the Gene Ontology (GO – http://www.geneontology.org) for molecular and cellular processes, the Foundation Model of Anatomy (FMA – sig.biostr.washington.edu/projects/fm/AboutFM.html) for anatomical nomenclature and relationships and SNOMED CT (http://www.ihtsdo.org) for clinical terms, including the terminology associated with disease. Another role for the metadata associated with CellML and FieldML models is to connect models used in clinical workflows to the electronic health records (EHRs) used in healthcare systems for storing patient data.

This book is very timely and the editor is to be congratulated for bringing together a very interesting and relevant set of chapters from some of the world's leading cardiovascular modelers.

Preface

Advances in medical technologies such as noninvasive imaging have had a proven impact on diagnosis, surgical planning, and clinical management with resultant improvements in clinical outcomes. In research, new and improved imaging modalities, combined with novel genetically engineered animal models and recent advances in genomic and proteomic profiling, are increasing our integrative knowledge of pathophysiology from the level of molecular networks to organ systems scales. This has led many workers to suggest that these advancements may accelerate progress to personalized and predictive medicine [2].

In traditional medicine, findings from large clinical trials determine clinical treatments. Based on a trial, a particular therapy may benefit a majority of patients, but differences between individuals can dramatically impact the outcome and efficacy of a specific therapy [5]. The characteristics of an individual undergoing therapy likely differ from the mean of the clinical trial population, thus the therapy may not benefit every patient, or worse, may even complicate the disease process. Physicians therefore take into account differences like gender, weight, height, and age in their clinical decisions, but numerous other patient characteristics – not necessarily of pathological nature – may still lead to adverse effects. Personalized and predictive medicine tries to fill that gap by using information from that patient's gene or protein profile.

In a parallel development, ongoing improvements in computation power have facilitated the solving of computational models of physiology of increasing complexity (for example, the high-performance Graphical Processor Unit (GPU) Radeon R800 of ATI from 2009 is about 50 billion times faster than the IBM 1620 from 1961). For many models in physiology, it is impossible to find an analytical solution and computers are used to obtain numerical solutions. Many computational models of physiology are written in terms of coupled ordinary and/or partial differential equations (ODEs and/or PDEs). An example of a set of coupled ODEs is the description of sodium and potassium ion kinetics through nerve membrane (with time as the independent variable), proposed by Hodgkin and Huxley [4]. A partial differential equation is an equation where a function depends on more independent variables. An example of a PDE is the monodomain equation that describes the propagation of cellular transmembrane voltage as a function of three spatial dimensions and time. One of the most used computational tools for solving

PDEs on a complex domain, such as the heart, is the finite element method. In the finite element method, the entire geometric reconstruction of the anatomy (obtained, for example, by MRI) is subdivided into smaller elements, with bordering pointwise nodes to construct a mesh [3]. The solution is approximated on the mesh by linear or higher-order functions, which are defined in the elements. The finite element method is used for models throughout this book to solve, for example, for atrial electrophysiology (Chap. 4), ventricular mechanics (Chap. 8), ventricular electrophysiology (Chap. 9), ventricular electromechanics (Chaps. 9–12), and blood–wall interactions in abdominal aortic aneurysms (Chap. 6).

Computational models of physiology are based on physico-chemical principles and are testable, reproducible, and allow easy manipulation of parameters without affecting others [1, 6]. Such models have already proven to be useful in elucidating biological mechanisms in health and disease [11] from gene to whole-organ level [10]. For example, a sensitivity analysis with a computational model of dyssynchronous heart failure showed that ventricular dilation and electrical dyssynchrony combined, synergistically decreased regional cardiac function [7]. Clinical indices of regional cardiac function that are based on strain magnitudes are sensitive to this combination, whereas indices that are based on strain timing are insensitive to this combination. The study also showed that strain magnitude-based indices reflect better the relative nonuniform distribution of regional work in the myocardium. These findings might explain why strain magnitude-based indices of cardiac regional function are better predictors of reverse remodeling in cardiac resynchronization therapy [8].

Because of these advancements in technology and increased knowledge of physiological mechanisms, it has been proposed that computational models of physiology tailored to individual patient characteristics will eventually prove to be a valuable and versatile technology that improves medical care in a myriad of disciplines [9] and especially in cardiology could serve as an enabler of personalized medicine [11]. This book therefore focuses on the potential of patient-specific computational models of cardiovascular physiology to predict or optimize outcomes of clinical treatments. Two main reasons underlie this choice: first, cardiovascular disease is still the leading cause of death in most industrialized countries; second, cardiac models represent one of the most advanced areas of computational biology, bridging from the subcellular to the circulatory level [12], making them an excellent candidate for mechanistic patient-specific modeling.

Chapter 1 provides an overview of imaging modalities, which can be used to create patient-specific models. It also discusses anatomical models already being used in the clinic, which are used to visualize impulse conduction in the atria measured by electroanatomic mapping. Finally, electrophysiology research is discussed that may be translated to the bedside.

It is important that for the creation of a patient-specific model, patient burden – i.e., due to measurements of a patient's state – is kept to a minimum. Chapter 2 focuses on obtaining patient-specific cardiovascular models in which adaptation rules are used. This approach leads to a reduction in the number of measurements that are needed to adjust for patient-specific fitting and conventional

measurements can be used much more efficiently, enabling to obtain hidden diagnostic information that normally would depend completely on invasive techniques. In addition, the model proposed in this chapter may also be used to assess different treatment protocols by simulation of the prognosis after intended treatments.

Chapter 3 provides an overview of techniques related to modeling of normal and diseased cardiac cells focusing on approaches that have a high potential for clinical translation. The chapter discusses how cellular structure and function are altered in cardiac disease, methods for measuring these alterations, and briefly discusses mathematical approaches for functional modeling of (altered) cellular electrophysiology.

An example of a future application of a mechanistic model of atrial fibrillation – and how it may be used in the clinic – is given in Chap. 4. Different types of sustained atrial fibrillation dynamics were simulated and the results agreed with those observed in the clinic.

Whereas the majority of recent patient-specific models include 3D representations of organs [9], Chap. 5 discusses the application of simpler models in critical care. This chapter illustrates several hemodynamic and glucose/insulin models that have been developed and already applied in critical care settings to manage patient homeostasis. Although many of these simpler models have existed for decades, their use in critical care patient-specific modeling has become available only recently.

The risk of abdominal aortic aneurysm (AAA) rupture is nowadays mainly estimated based on the maximum diameter of the dilated aorta. Chapter 6 describes the current status of AAA wall stress analyses – obtained from patient-specific models – including the discussion of relevant factors like initial wall stress, nonlinear material behavior, and thrombus. The chapter also discusses the clinical perspectives of AAA wall stress analysis with respect to AAA rupture risk and growth.

Not all model parameters can be obtained patient-specifically. Therefore, a need exists for a publicly accessible database that offers supplemental data. Chapter 7 describes the Cardiac Atlas Project (CAP), which is a web-accessible structural and functional atlas of the normal and pathological heart for clinical, research, and educational purposes. This atlas' purpose extends beyond the "normal" database: an initial goal of the atlas is to facilitate statistical analysis across population groups of regional heart shape and wall motion characteristics, via the application of mathematical modeling tools.

A noninvasive method for estimating myocardial material properties in vivo would be of great value in the design and evaluation of new surgical and medical strategies to treat and/or prevent heart failure. In Chap. 8, finite element models of a normal human subject and a patient with diastolic heart failure were created using tagged magnetic resonance (MR) images and noninvasive left ventricular (LV) pressure measurements. Diastolic and systolic myocardial material parameters were estimated by matching LV volumes and stresses were evaluated.

One of the parameters that cannot be obtained directly and patient-specifically is myocardial fiber architecture in the ventricles. Chapter 9 describes a method for constructing models of whole-heart electrophysiology and electromechanics from

structural and diffusion tensor magnetic resonance images acquired ex vivo, and presents a processing pipeline for estimating patient-specific myocardial fiber orientations from images scanned in vivo. These modeling techniques in combination with the proposed methodology for estimating patient-specific myocardial fiber orientations constitute a step toward patient-specific simulations of cardiac electrophysiology and mechanics.

Of all heart failure patients, those with the additional complication of dyssynchronous contraction (often due to a conduction defect such as bundle branch block) have the worst prognosis. Cardiac resynchronization therapy (CRT) involves placing a pacemaker to improve the synchronicity of cardiac contraction. It has recently been shown that CRT is an effective method of treating patients with dyssynchronous heart failure, inducing significant reductions in morbidity and mortality in large clinical trials. However, clinical trials have also demonstrated that up to 30% of patients may be classified as non-responders. The development of patient-specific models may maximize response to CRT. In Chap. 10, a computational model of cardiac electromechanics based on a clinical case was successfully used to predict the acute effects of ventricular pacing on cardiac function with four different pacing conditions.

The three leading causes of death in most industrialized countries (cardiovascular disease, cancer, and stroke) involve an hypoxic response. Individual patients can vary tremendously in their response to hypoxic exposure, and to therapies targeting hypoxic pathways. In Chap. 11, the sources of patient variability related to oxygen sensing and response are discussed and computational modeling approaches are addressed. These models capture essential processes involved in hypoxia and microvascular dynamics, and offer promise as tools to advance patient-specific therapeutic design.

Building a patient-specific model of the heart involves many steps from data acquisition to model result. Chapter 12 discusses a multiscale framework for modeling of cardiac electromechanics that includes a model database, image segmentation, and several mechanistic models from cell to system.

References

1. Bassingthwaighte, J. B., Chizeck, H. J. and Atlas, L. E. (2006) Strategies and tactics in multiscale modeling of cell-to-organ systems. *Proceedings of the IEEE* **94,** 819–831.
2. Ginsburg, G. S. and McCarthy, J. J. (2001) Personalized medicine: revolutionizing drug discovery and patient care. *Trends in Biotechnology* **19,** 491–496.
3. Hashim, S. and Richens, D. (2006) Finite element method in cardiac surgery. *Interact CardioVasc Thorac Surg* **5,** 5–8.
4. Hodgkin, A. L. and Huxley, A. F. (1952) A quantitative description of membrane current and its application to conduction and excitation in nerve. *Journal of Physiology* **117,** 500–544.
5. Kent, D. M. and Hayward, R. A. (2007) Limitations of Applying Summary Results of Clinical Trials to Individual Patients: The Need for Risk Stratification. *JAMA* **298,** 1209–1212.
6. Kerckhoffs, R. C. P., Narayan, S. M., Omens, J. H., Mulligan, L. J. and McCulloch, A. D. (2008) Computational modeling for bedside application. *Heart Failure Clinics* **4,** 371–378.

7. Kerckhoffs, R. C. P., Omens, J. H., McCulloch, A. D. and Mulligan, L. J. (2010) Ventricular dilation and electrical dyssynchrony synergistically increase regional mechanical non-uniformity but not mechanical dyssynchrony: A computational model. *Circulation: Heart Failure* **3,** 528–536.
8. Kirn, B., Jansen, A., Bracke, F., van Gelder, B., Arts, T. and Prinzen, F. W. (2008) Mechanical discoordination rather than dyssynchrony predicts reverse remodeling upon cardiac resynchronization. *Am J Physiol Heart Circ Physiol* **295,** H640–H646.
9. Neal, M. L. and Kerckhoffs, R. (2010) Current progress in patient-specific modeling. *Brief Bioinform* **11,** 111–126.
10. Noble, D. (2006) Systems biology and the heart. *Biosystems* **83,** 75–80.
11. Reumann, M., Gurev, V. and Rice, J. J. (2009) Computational modeling of cardiac disease: potential for personalized medicine. *Personalized Medicine* **6,** 45–66.
12. Southern, J., Pitt-Francis, J., Whiteley, J., Stokeley, D., Kobashi, H., Nobes, R., Kadooka, Y. and Gavaghan, D. (2008) Multi-scale computational modelling in biology and physiology. *Prog Biophys Mol Biol* **96,** 60–89.

Contents

Contributors

Jazmin Aguado-Sierra
Department of Bioengineering, University of California,
9500 Gilman Drive La Jolla, Mailcode #0412, San Diego, CA 92093-0412, USA

Hermenegild Arevalo
Johns Hopkins University, CSEB Room 218, 3400 N Charles St.,
Baltimore, MD 21218, USA

Theo Arts
Department of Biomedical Engineering, Maastricht University,
Maastricht, The Netherlands

Michael Backhaus
Department of Anatomy with Radiology, University of Auckland,
85 Park Road, Auckland 1142, New Zealand

Mariëlle Bosboom
Departmant of Biomedical Engineering, Maastricht University Medical Center,
6202 AZ, PO Box 5800, Maastricht, The Netherlands

Stuart G. Campbell
Department of Bioengineering, University of California at San Diego,
9500 Gilman Dr, La Jolla, CA 92093-0412, USA

Guangming Cheng
Department of Surgery, University of California at San Francisco,
4150 Clement Street, San Francisco, CA 94121, USA

Jae Do Chung
University of Auckland, Department of Anatomy with Radiology,
85 Park Road, Auckland1142, New Zealand

Jason Constantino
Johns Hopkins University, CSEB Room 218, 3400 N Charles St.,
Baltimore, MD 21218, USA

Brett R. Cowan
Department of Anatomy with Radiology, University of Auckland,
85 Park Road, Auckland 1142, New Zealand

Tammo Delhaas
Department of Physiology, Maastricht University, UNS 50, 6200MD Maastricht,
The Netherlands

Dirk Donker
Department of Cardiology, Maastricht University Medical Center,
UNS 50, 6200MD Maastricht, The Netherlands

Carissa G. Fonseca
Department of Anatomy with Radiology, University of Auckland,
85 Park Road, Auckland 1142, New Zealand

Julius M. Guccione
Division of Surgical Services (112D), Department of Veterans Affairs Medical Center, University of California at San Francisco, Building 2, Room 101, 4150 Clement Street,
San Francisco, CA 94121, USA

Viatcheslav Gurev
Johns Hopkins University, CSEB Room 218, 3400 N Charles St., Baltimore,
MD 21218, USA

Darlene Hunt
Department of Bioengineering, University of California at San Diego,
9500 Gilman Dr, La Jolla, CA 92093-0412, USA

Peter Hunter
Bioengineering Institute, University of Auckland, Level 6, 70 Symonds St.,
Auckland, New Zealand

Lukas Kappenberger
University of Lausanne, Chemin de la Rosiere 46, 1012 Lausanne, Switzerland

Roy C. P. Kerckhoffs
Department of Bioengineering, University of California at San Diego,
9500 Gilman Dr, La Jolla, CA 92093-0412, USA

Wilco Kroon
Depratment of Biomedical Engineering, Maastricht University Medical Center,
6202 AZ Maastricht, The Netherlands

David E. Krummen
University of California San Diego and VA San Diego Healthcare System,
3350 La Jolla Village Drive, Cardiology Section 111A, San Diego,
CA 92161, USA

Fred Lionetti
Department of Bioengineering, University of California at San Diego,
9500 Gilman Dr, La Jolla, CA 92093-0412, USA

Joost Lumens
Department of Biomedical Engineering, Maastricht University, UNS 50,
6200 MD Maastricht, The Netherlands

Andrew D. McCulloch
Department of Bioengineering, University of California at San Diego,
9500 Gilman Dr, La Jolla, CA 92093-0412, USA

Sanjiv M. Narayan
Division of Cardiology 111A, UCSD and VA San Diego Healthcare System,
3350 La Jolla Village Drive, San Diego, CA 92161, USA

Joanna Nathan
Department of Bioengineering, Rice University, Houston, TX 77005, USA

Maxwell L. Neal
Department of Medical Education and Biomedical Informatics,
University of Washington, 1959 NE Pacific Street, Box 357240,
Seattle, WA 98195-7240, USA

Gainyu Oshodi
UCSD and VA San Diego Healthcare System, 3350 La Jolla Village Drive,
Cardiology Section 111A, San Diego, CA 92161, USA

Frits W. Prinzen
Department of Physiology, Maastricht University, UNS 50, 6200 MD Maastricht,
The Netherlands

Amina A. Qutub
Department of Bioengineering, BioSciences Research Collaborative,
Rice University, 6500 Main St., Rm 613, Houston, TX 77030, USA

Mark B. Ratcliffe
San Francisco VA Medical Center, University of California at San Francisco,
4150 Clement Street, San Francisco, CA 94121, USA

Reza Razavi
Division of Imaging Sciences, St Thomas' Hospital, The Rayne Institute,
King's College London, London SE1 7EH, UK

Frank B. Sachse
Nora Eccles Harrison Cardiovascular Research and Training Institute,
and Bioengineering Department, University of Utah, 95 South 2000 East,
Salt Lake City, UT, USA

David A. Saloner
University of California at San Francisco, 4150 Clement Street,
San Francisco, CA 94121, USA

Geert W. H. Schurink
Department of Surgery, Maastricht University Medical Center, 6202 AZ,
Maastricht, The Netherlands

Maxime Sermesant
Asclepios Team INRIA, 2004 route des Lucioles, 06 902, Sophia Antipolis,
France

Lambert Speelman
Biomechanics Laboratory, Department of Biomedical Engineering,
Erasmus Medical Center Rotterdam, PO Box 2040, Ee2322,
3000 CA Rotterdam, The Netherlands

Kay Sun
University of California at San Francisco, 4150 Clement Street,
San Francisco, CA 94121, USA

Wenchao Tao
Department of Anatomy with Radiology, University of Auckland,
85 Park Road, Auckland 1142, New Zealand

Natalia Trayanova
Johns Hopkins University, CSEB Room 216, 3400 N Charles St.,
Baltimore, MD 21218, USA

Laurent Uldry
Swiss Federal Institute of Technology, EPFL-STI-IEL-LTS1, Station 11,
1015 Lausanne, Switzerland

Fijoy Vadakkumpadan
Institute for Computational Medicine and Department of Biomedical Engineering,
Johns Hopkins University, CSEB room 218, 3400 N Charles St,
Baltimore, MD 21218, USA

Frans N.v.d. Vosse
Department of Biomedical Engineering, Eindhoven University of Technology,
WH 4.131, 5600 PO Box 513, MB Eindhoven, The Netherlands

Jean-Marc Vesin
Swiss Federal Institute of Technology, EPFL-STI-IEL-LTS1, Station 11,
1015 Lausanne, Switzerland

Nathalie Virag
Medtronic Europe Sàrl, Route du Molliau, Tolochenaz, CH-1131, Switzerland

Joseph C. Walker
University of California at San Francisco, 4150 Clement Street,
San Francisco, CA 94121, USA

Jonathan F. Wenk
Department of Veterans Affairs, Medical Center,
Building 2, Room 106, 4150 Clement Street, San Francisco, CA 94121, USA

Alistair A. Young
Department of Anatomy with Radiology, University of Auckland,
85 Park Road, Auckland 1142, New Zealand

Zhihong Zhang
University of California at San Francisco, 4150 Clement Street,
San Francisco, CA 94121, USA

Chapter 1
Integrating State-of-the-Art Computational Modeling with Clinical Practice: The Promise of Numerical Methods

David E. Krummen, Gainyu Oshodi, and Sanjiv M. Narayan

1.1 Introduction

The use of numerical methods in clinical medicine has grown exponentially over the past decade. This is particularly true in clinical cardiac electrophysiology (EP), which is focused on the diagnosis, prevention and treatment of heart rhythm abnormalities. Part of the reason for this is the suitability of cardiac rhythm pathology to numerical modeling. At the tissue level, the mechanisms of electrical propagation within the heart are relatively deterministic both in health and during arrhythmias [31]. As a result, for many applications, there is remarkable correlation between prediction and measurement [30]. Another reason is the availability of detailed anatomical and physiologic imaging data in cardiology, including: echocardiography (transthoracic, transesophageal, and intracardiac), computed tomography (CT), magnetic resonance imaging (MRI), nuclear medicine, and positron emission tomography.

Significant progress has also been made towards understanding more basic pathophysiologic mechanisms of arrhythmias. Genetic studies have revealed the specific channel defects responsible for the Long QT [80] and Brugada Syndromes [22], for example. Similarly, patch-clamp techniques have shed light upon the chronic effects of atrial fibrillation on cellular ion currents [85]. However, extending the cellular pathophysiologic mechanism to tissue and whole-organ level treatment is difficult. For instance, although the ionic mechanisms for Brugada syndrome have been known for nearly 15 years, only recently was it found that electrical sequelae were due to localized mechanisms that could be treated by ablation [49]. Similarly, there remains a substantial gap between our understanding of disease mechanism and effective therapy for many arrhythmia disorders. For many of these diseases, advances in computational modeling may play an integral role in advancing our

D.E. Krummen (✉)
University of California San Diego and VA San Diego Healthcare System,
3350 La Jolla Village Drive, Cardiology Section 111A, San Diego, CA 92161, USA
e-mail: dkrummen@ucsd.edu

R.C.P. Kerckhoffs (ed.), *Patient-Specific Modeling of the Cardiovascular System: Technology-Driven Personalized Medicine*, DOI 10.1007/978-1-4419-6691-9_1,

understanding and management. For instance, modeling may be able to more accurately predict the location of the sustaining sites of atrial fibrillation, allowing curative ablation, or may be able to predict the optimal site of left ventricular lead position in patients undergoing biventricular implantable defibrillator implantation.

This chapter will review the current use of computer modeling in the treatment of cardiovascular disease in the area of cardiac electrophysiology. We will then discuss potential future directions in the field. We believe that the implementation of modeling in clinical medicine holds great potential for diagnosing and treating complex heart rhythm disorders.

1.2 Imaging Methods Used in Patient-Specific Modeling

Diagnostic imaging plays a central role in patient-specific modeling, combining anatomic and physiologic measurements to evaluate, characterize and display cardiovascular structure and function.

1.2.1 Echocardiography

Echocardiography studies the interaction between ultrasound and cardiac tissues or blood. This information includes both position (echo) and speed (Doppler) information which are then used to create 2D and 3D displays of cardiac structure and function. Transthoracic [9] and intracardiac [65] ultrasound are currently used to provide information about ventricular dyssynchrony that can assist with cardiac resynchronization therapy (CRT). In some cases, echocardiography is used in real-time to guide catheter position during ablation [19]. Additionally, anatomic data from intracardiac echo may also be integrated into 3D electroanatomic models for mapping and ablation [72]. From a modeling perspective, echo data may also be used to estimate local tissue strain using speckle tracking [37], providing regional data for finite-element models, as described below.

1.2.2 Computed Tomography

X-ray energy passing through tissue is selectively absorbed, scattered, or transmitted based upon the tissue properties. Integrating this information from multiple angles as the X-ray source and detectors are rotated around the patient creates a detailed 2-dimensional image of a particular “slice” of a patient’s anatomy. Computational methods are used to combine data from adjoining “slices” to form 3D anatomic models of patient anatomy. These models can be integrated into real time mapping systems to create detailed cardiac models for ablation [3]. These models can be used for many purposes in electrophysiology, including understanding the anatomy of patients with congenital heart disease with arrhythmias undergoing ablation [79],

defining the location of scar in patients undergoing endocardial ventricular tachycardia (VT) ablation [3], and localizing the coronary arteries in patients having an epicardial VT ablation [86].

1.2.3 Nuclear Imaging

Nuclear tracers, which are selectively absorbed by cardiac tissue, can be detected and used to evaluate functional differences in blood flow and cardiac viability. Myocardial ischemia is a common, reversible cause of ventricular tachycardia [40], and can be detected using nuclear imaging prior to implantable cardioverter-defibrillator (ICD) implantation or VT ablation. Data from nuclear imaging is not frequently used to build computer models for arrhythmia analysis at this time, although recent work [17] suggests incorporation of positron emission tomography images may reduce or eliminate the need for detailed substrate mapping during ventricular tachycardia ablation procedures.

1.2.4 Magnetic Resonance Imaging

During an MRI, the magnetic moments of protons within the body align with the direction of a magnetic field. A radio frequency electromagnetic field is then briefly turned on, causing the protons to alter their alignment relative to the field. When this field is turned off the protons return to the original magnetization alignment, creating a signal that can be detected by the scanner. The position of protons in the body can be determined by applying additional magnetic fields during the scan, which allows an image of the body to be built up. As a result, MRI has greater contrast than CT in the visualization of soft tissue, with the additional benefit of not requiring ionizing radiation. Recent research has shown the utility of mapping ventricular scar using MRI during VT ablation [14]. Like CT data, MRI anatomical data is commonly used in EP procedures.

Delayed enhancement MRI techniques permit identification of scar location and extent. This information has shown to be useful for predicting risk [71] of sudden cardiac arrest, and showing lesion extent after ablation of atrial fibrillation [46]. Diffusion tensor MRI data provides information on myocardial fiber angles [27], which may be useful to predict wavefront conduction properties.

1.2.5 Use of Imaging Data

Alone or in combination, these imaging techniques can be used to diagnose conditions associated with clinical arrhythmias, such as arrhythmogenic right ventricular cardiomyopathy using MRI [73] or left atrial thrombus with intracardiac ultrasound [60]. They are also used to monitor disease progression (measuring left ventricular ejection fraction several months after myocardial infarction to assess need for a

ICD [16]), and track response to therapy (response to biventricular pacing using echocardiography [75]).

Imaging is also critically important in the creation of accurate, patient-specific clinical models. For many applications, the high-resolution, multi-slice CT or MRI data are important to capture anatomic details needed in the model, such as wall thickness and scar. For other applications, physiologic information, such as the cardiac output obtained from echocardiography, is important to understand the physiologic effects of different interventions, as required to evaluate the effects of different pacing regimens. Complex simulation, such as the study of the effects of resynchronization therapy on regional stress and strain, may require combining multiple imaging modalities into a model (see for example Chap. 10).

1.3 Current Use of Patient-Specific Models in Cardiac Electrophysiology

In the electrophysiology lab, computational modeling of both anatomy and electrical activation is routinely performed to define cardiac anatomy and guide intervention.

1.3.1 Overview of Modeling During Invasive Electrophysiology Study and Ablation

Current 3D electroanatomic mapping systems integrate catheter position to create a "shell" representing the internal volume of the chamber of interest. This shell may be used in isolation or "merged" with detailed 3D anatomic information from CT [3], MRI [7], and/or ultrasound imaging [57] data. As a result, clinically useful models of cardiac anatomy may be created, in which catheter movements are projected in real-time within the cardiac geometry. Using these anatomical maps, additional information can be added to gain further insight into an individual patient's condition, including electrogram voltage (substrate mapping) and temporal activation (activation mapping). Substrate mapping is currently used to define areas of scar in both the atria and ventricles [81], which is important since arrhythmias often critically depend upon the presence of scar and their associated conduction abnormalities. Substrate mapping has also been used to help diagnose arrhythmogenic right ventricular cardiomyopathy [12]. Activation mapping can illustrate the path by which wavefronts perpetuate arrhythmias, guiding ablation of critical pathways [2].

Another mapping technique involves evaluating the correlation between a paced beat and the native arrhythmia morphology, termed pace mapping, which can be used to localize an arrhythmia source [82]. Lastly, entrainment mapping localizes sites within an arrhythmia circuit. Recent studies entrainment mapping has improved our understanding of atrial flutter circuits [67].

These techniques have dramatically improved the accuracy and safety of radio-frequency ablation, but there remains significant room for improvement. Limitations of these techniques include respiratory changes in pulmonary venous anatomy between imaging and the EP study [50], and errors in the accuracy of map registration at baseline [26] and after the start of ablation [45]. Also, it is important to note that the majority of today's clinical models are anatomic; clinical functional modeling applications simulating action potential dynamics are not widely available.

1.3.2 Current Application of Computer Modeling in Atrial Arrhythmias

Atrial arrhythmias differ in their needs for modeling during invasive studies. An overview of the use of modeling for these arrhythmias, and of limitations of current technology, is discussed below.

1.3.2.1 Atrial Fibrillation

Currently, it is hypothesized that atrial fibrillation (AF) is maintained by focal ectopic beats predominantly from within the pulmonary vein [23] in paroxysmal AF and by multiple wavelet reentry in persistent AF [29]. Each type of AF requires a slightly different ablation strategy, necessitating different mapping techniques.

State of the art AF ablation often involves creation of a shell and integrating this shell with imaging data. Positional accuracy with current technology is approximately ±1.4 cm [4], and frequently better. The catheter can then be placed at either the ostium for paroxysmal AF, or in a wide circumferential pattern [1] around the pulmonary veins for persistent AF, rather than within the veins (which may cause stenosis), for ablation.

Once ablation begins, the model also serves to record the sites of ablation (Fig. 1.1). In this way, linear lesions can be created with sequential, adjoining ablation lesions to create lines of functional conduction block. This function is important to prevent multiple burns at the same site in the posterior left atrium, given the proximity to the esophagus [61] and the possibility of esophageal injury [62].

Other phenomena can be mapped in patients with atrial fibrillation. Locations of sites of autonomic innervation, called ganglionated plexi, can be localized using high-output pacing [42]. The locations of the plexi can then be noted within the atrial anatomic model for subsequent ablation, as these sites may be the source of focal triggers of AF [55].

Konings et al. [36] described the presence and distribution of fractionated electrograms during AF, and the complex fractionated atrial electrograms were later shown to be possible candidates for ablation [48]. Ideally, functional relationships could be compared simultaneous activation patterns of local tissue to identify sites which drive, or maintain AF. Recent work has enabled the simultaneous comparison

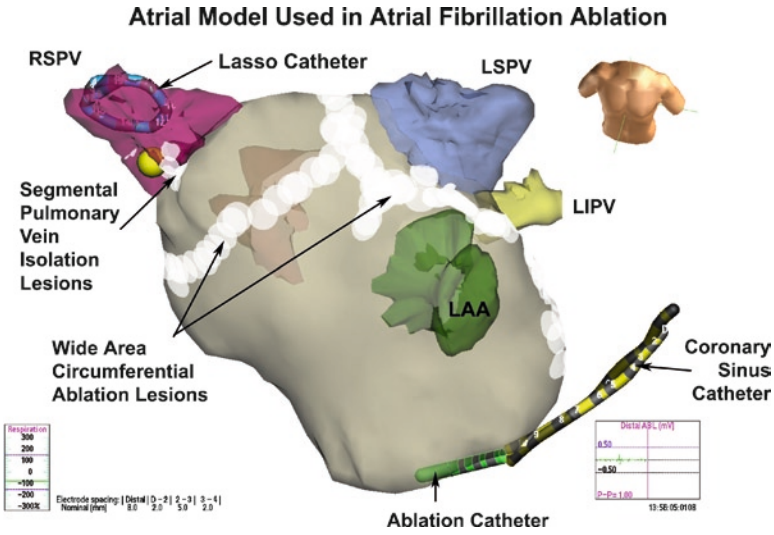

Fig. 1.1 3D electroanatomic model of *left* atrial anatomy (viewed from the *left* anterior oblique cranial angulation) created using the NavX system (St. Jude, CA) during a typical atrial fibrillation ablation. Real-time catheter positions are displayed (lasso catheter, coronary sinus catheter, and ablation catheter). Sites of ablation are noted by *white circles*. *RSPV* right superior pulmonary vein, *LSPV* left superior pulmonary vein, *LIPV* left inferior pulmonary vein, *LAA* left atrial appendage

of local rate and regularity, determined by Fast Fourier Transform, to identify drivers in near real time [39].

The use of current computational modeling in clinical practice has already had significant impact on clinical electrophysiology. The use of electroanatomical mapping systems has significantly reduced fluoroscopy exposure to patient and physician [76], and research suggests that incorporating CT data may improve outcome [33]. Improved methods of electroanatomic mapping may integrate ablation time and power to predict successful lesion creation, or identify potential sites of edema which may be resistant to ablation.

Detailed computational modeling has also provided significant insight into the mechanisms of AF initiation and maintenance (Chap. 4). Haissaguerre et al. found that AF cycle length is inversely proportional to the number of focal drivers sustaining fibrillation [25]. Gong et al. have shown the importance of dynamic repolarization heterogeneity in the initiation of AF with computer models. However, these applications are currently limited to the research laboratory due to time requirements.

Limitations and Future Directions. Currently, modeling in AF still suffers from notable shortcomings. For instance, with regard to AF ablation, CFAE are often mapped and targeted for ablation. However, the mechanisms of CFAE are not defined, and CFAE may not represent critical mechanisms for arrhythmias. Additionally, the mechanisms sustaining AF have not been fully elucidated, preventing

ablation of physiologic driver sites. Finally, mapping is typically performed on a point-by-point basis, although multisite mapping has been investigated [39].

1.3.2.2 Atypical Atrial Flutter and Focal Atrial Tachycardia

Atypical atrial flutter is a macro-reentrant atrial arrhythmia whose circuit does not involve the tissue between the inferior vena cava ostium and the tricuspid valve [68]. Similar to atrial fibrillation, atrial anatomic models of both the left and right atria are created. In contrast to AF, however, creating a map of atrial activation sequence (activation mapping) is central to localizing the atrial flutter. Once the reentrant pathway is known, an entrainment map is created. An entrainment map evaluates both the proximity to the circuit and the conduction properties of local tissue. The optimal site for ablation is a site both within the circuit and an area with relatively slow conduction velocity [6]. Ablation at this area is likely to cure the arrhythmia.

Focal atrial tachycardia is an arrhythmia caused by abnormal automaticity – a cluster of cells that have acquired the ability to depolarize spontaneously and rapidly, overdriving the normal pacemaker cells of the heart [68]. Like atypical atrial flutter, activation mapping is performed. Frequently, however, the arrhythmia is short-lived, and mapping needs to be performed rapidly. In many cases, a non-contact array is used to capture activation information, which is then projected onto a patient-specific model of atrial anatomy [53]. An example of an activation map of a focal atrial tachycardia created using a noncontact array is shown in Fig. 1.2.

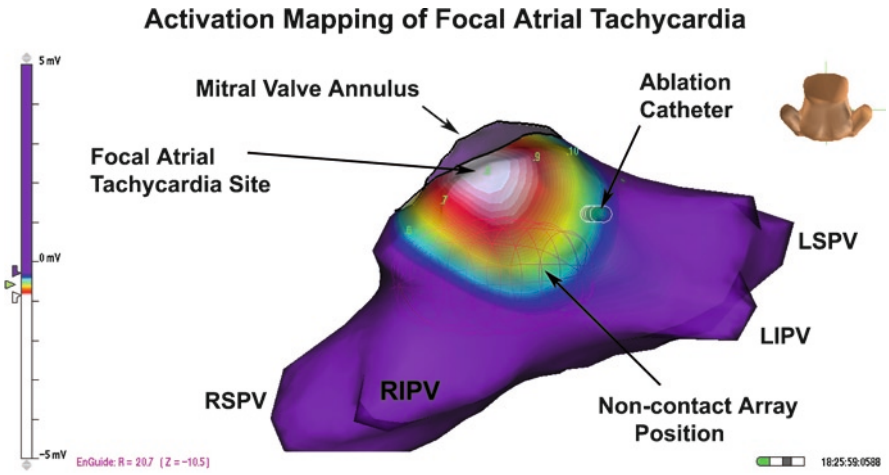

Fig. 1.2 Non-contact activation mapping of focal atrial tachycardia superimposed on a *left* atrial anatomic map combining anatomical and functional information to predict arrhythmia source. Ablation at the *white circle* terminated the arrhythmia, which could not subsequently be re-induced. *RSPV* right superior pulmonary vein, *LSPV* left superior pulmonary vein, *LIPV* left inferior pulmonary vein, *LAA* left atrial appendage, *RIPV* right inferior pulmonary vein

Limitations and Future Directions. Currently, both activation and entrainment mapping are time-intensive processes, requiring prolonged procedure times and X-ray exposure to the patient and physician during ablation of atypical atrial flutter or focal atrial tachycardia. Additionally, noncontact activation mapping may have limited accuracy at distances greater than 40 mm from the mapping catheter [78]. Future work may allow fully automated anatomical, activation, and entrainment mapping using robotic navigation systems, discussed below.

1.3.3 Current Application of Computer Modeling in Ventricular Arrhythmias

Ventricular arrhythmias also present specific challenges for both clinical and research-directed computational modeling.

1.3.3.1 Premature Ventricular Contractions and Ventricular Tachycardia

Recent research has shown that ablation of post-infarction premature ventricular contractions (PVCs) improves left ventricular function [69]. From a procedural standpoint, PVC ablation often involves creation of a left ventricular geometry and pace-mapping to find an identical paced morphology to the PVC.

VT ablation often involves creation of a left ventricular endocardial and sometimes epicardial anatomy, and a combination of scar, pace, and entrainment mapping (Fig. 1.3) to locate and ablate critical isthmuses [58].

Additionally, as VT procedures include more patients with nonischemic cardiomyopathy, epicardial ablation is more frequently attempted [10]. New techniques allow incorporation of cardiac CT scan data, showing the course of the major arteries [86] to avoid injury during ablation. Furthermore, mapping of the phrenic nerve [18] can be accomplished with high-output pacing and marking the electroanatomic map in order to prevent injury and ipsilateral diaphragmatic paralysis.

Limitations and Future Directions. VT ablation is typically guided to regions of scar [14]. However, alterations in ventricular action potential duration and conduction velocity cannot yet be integrated into clinical models. These may be useful in better defining critical areas for arrhythmia maintenance.

Additional challenges for current mapping techniques include the possibility of endocardial and epicardial wavefront dissociation [15], and cardiac movement during mapping [44]. Accurately modeling transmural wavefront heterogeneity may require modeling of anisotropy (the property of being directionally dependent) in wavefront velocity between longitudinal and transmural axes. The issue of cardiac movement is extremely complex for modelers, as movement has the potential to change electrophysiologic properties, such as conduction velocity, relative to their timing in the cardiac cycle.

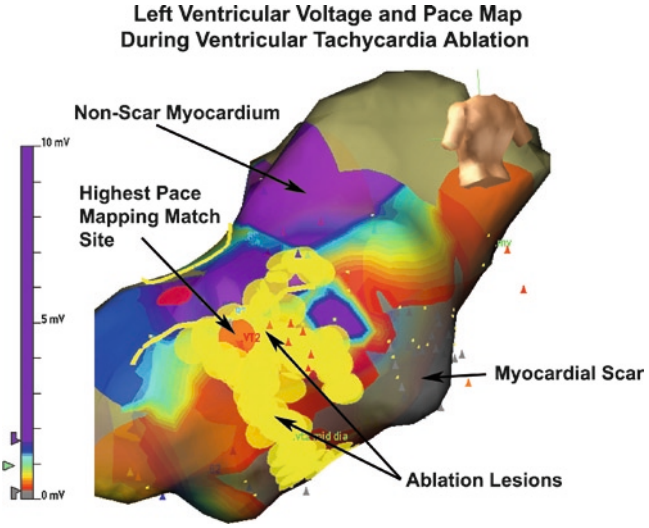

Fig. 1.3 *Left* ventricular voltage map projected on an endocardial LV model used for ablation of VT. *Red* denotes low voltage and *purple* as high. Ablation lesions are shown in *yellow* Ablation targeted VT sources in *scar* border (intermediate voltage, *yellow*). Patient has been free from VT for 6 months since ablation

1.3.3.2 Ventricular Fibrillation

Ventricular fibrillation (VF) is a life-threatening ventricular arrhythmia which accounts for approximately 120,000 deaths each year in the United States [11]. VF is characterized by rapid and irregular activation of the ventricular myocardium resulting in uncoordinated ventricular contraction. Survivors of VF typically undergo placement of an ICD [16], but until recently no specific therapies for VF existed.

In the last few years, however, both idiopathic [35] and post-infarction [54] ventricular fibrillation associated PVCs have been successfully ablated, reducing subsequent VF episodes. Additionally, Brugada and Long QT syndromes, associated with polymorphic VT (PMVT) and VF, have also reported successful ablation procedures [24]. These advances have been facilitated by the ability to map and ablate initiating beats. Although large-scale trials have not yet been performed in these populations, VF ablation has the potential to significantly reduce ICD shocks, which have a significant negative impact on patient quality of life [52] and may cause congestive heart failure and death [56].

Limitations and Future Directions. VF has only recently received attention for treatment with ablation [35]. Like AF, however, sustaining mechanisms are unable to be mapped and targeted in real-time. Similar to VT, altered tissue characteristics are unable to be incorporated into clinical models.

1.3.4 Application in Remote Catheter Manipulation

In the past, mapping and ablation were accomplished by the manual manipulation of catheters by physicians at the bedside. Presently, there are robotic systems which assume the task of physically moving catheters based upon input by physicians at computer stations [59]. This provides several advantages for patients and physicians: decreased fluoroscopy exposure for both the patient and physician, and highly repeatable catheter placement [66]. These systems are potentially important from a modeling perspective as well, since they could be used to systematically acquire data for anatomical and functional model creation [59]. Once arrhythmogenic sites have been identified, the ablation catheter may be directed to the specified site.

Limitations and Future Directions. Current robotic navigation systems are limited either by low force at the catheter-tissue interface (for magnetic systems [41]) or relative insensitivity of tip force for robotic systems [83]. Future work may be directed toward allowing both navigation methods to tailor ablation catheter tissue pressure to the size and depth of ablation lesion desired. Later versions of robotic navigation systems may allow the combination of automated data collection, patient-specific modeling, and semi-autonomous ablation: potentially an extremely useful tool in the management and treatment of arrhythmias.

1.3.5 Application in Cardiac Resynchronization Therapy

Currently, multiple imaging methods are used in cardiac resynchronization therapy. Echo modalities, including pulse Doppler [8], speckle tracking [74], and real-time 3D echocardiography [34] are used to evaluate for ventricular dyssynchrony. Preprocedure CT and delayed-enhancement MRI are used to define scar location and extent. Recent work has examined using magnetic navigation systems to guide LV lead placement [63].

Limitations and Future Directions. In a recent clinical trial, the presence of echocardiographic dyssynchrony in patients with a narrow QRS (duration <120 ms) did not predict response to CRT [5] in a large clinical trial. Future work may evaluate the utility of models to predict response to CRT, as discussed in Sect. 1.4.3 and Chap. 10.

1.3.6 Application in Sudden Cardiac Death

It is well established that patients with reduced left ventricular function are at increased risk of sudden cardiac death, and these patients routinely undergo ICD implantation [47]. Further attempts to identify at-risk individuals prior to device implantation have had mixed results. Numerical methods have included calculations

of microvolt T-wave alternans (TWA), heart rate variability (HRV), baroreflex sensitivity (BRS), and signal average ECG (SAECG). TWA measures subtle beat-to-beat alterations in the T-wave duration in patients at a heart rate of about 110 bpm. A recent trial has shown the negative predictive value of TWA to be approximately 95% [13]. This test is likely most useful in conjunction with invasive electrophysiology study [21], whose results provide additional information regarding SCD risk.

HRV measures low-frequency variations in heart rate, regulated by the autonomic nervous system [77]. Heart rate variability can be assessed by several metrics including frequency domain (Fast Fourier Transform (FFT) spectral analyses) and temporal domain (most commonly the standard deviation of the RR intervals, SDNN). Recent studies have shown predictive value for HRV indices [38], but large scale prospective trials are lacking.

Signal-averaged ECG techniques measure electrical potentials after the QRS (late-potentials). Savard et al. [70] found that SAECG help risk-stratify patients after myocardial infarction. Recent work supports the use of SAECG in the risk stratification of patients with Brugada syndrome [28].

Interesting work summarized by Ghanem et al. [20] has shown the utility of electrocardiographic imaging in potentially identifying pro-arrhythmic substrate, guiding therapy, and evaluating risk for sudden death. Additionally, several investigators [84] have shown the utility of multiscale modeling in predicting the effects of drug therapy on sudden cardiac death.

Limitations and Future Directions. Currently, noninvasive predictors of sudden death have suboptimal accuracy, requiring invasive electrophysiology study to improve identification of patients at risk [13] or the combination of multiple modalities to improve accuracy [21]. Additionally, multiscale modeling of the effects of medications on sudden death may show different effects within different models [84]. Despite these limitations, computer modeling may both help to identify mechanisms of VT/VF and improve the prediction of sudden death in patients by accurately simulating cardiac anatomy and pro-arrhythmic substrate.

1.4 Future Applications of Computer Modeling in Clinical Cardiac Electrophysiology

From the above discussion, it is clear that despite the great technological achievements in numerical techniques over the past few decades, the use of modeling has not yet reached its full potential. It can also be argued that future applications of computer modeling have even greater potential to significantly investigate, diagnose, and treat arrhythmia disorders. Future computer modeling may also allow a preview of the predicted effects of a particular therapy before that therapy is implemented. Below we discuss how techniques and disease-specific applications in computer modeling may impact clinical care in EP.

1.4.1 Atrial Arrhythmias

Patient-specific modeling has strong potential to improve the management and ablation of atrial arrhythmias. Currently, AF is treated in the EP lab in primarily an anatomical fashion, with a significant focus on pulmonary vein isolation [51] and the creation of linear lesions [1]. Future clinical modeling (Chap. 4) may permit lesions targeted precisely to the mechanisms which sustain AF, resulting in a much greater probability of AF cure with significantly less tissue destruction and atrial impairment [43]. This is important, as we do not fully understand the long-term implications of the extensive atrial ablation currently required for AF management.

Specifically, patient-specific computational modeling may be able to predict where the mechanisms that sustain human AF are most likely to lie. This would be accomplished by incorporating anatomical information from MRI scar imaging [64], fiber orientation either from MRI or anatomical studies to predict conduction, and activation maps either from multi-electrode catheters placed within the heart.

Even further in the future, surface electrogram data may be integrated into anatomical models to non-invasively localize driver sites. Once driver sites were identified, external beam radiation may be used to ablate these drivers, with minimal impact on normal tissue.

1.4.2 Ventricular Arrhythmias

Ventricular arrhythmias are also potential applications for patient-specific computational modeling. The mechanisms of VF, as described above, are poorly understood. Future computational modeling may include patient-specific anatomy from echo, CT, or MRI; ventricular fiber structure from diffusion tensor MRI [27]; and VF timing data from endocardial and epicardial catheters. These detailed models may begin to look for structure in the chaotic wavefronts to determine if particular locations are critically important to the maintenance of VF. Models could also explore the ionic disturbances within ventricular cells which support VF, and how drugs may be designed to block these effects [84].

1.4.3 Resynchronization Therapy and Congestive Heart Failure

Future applications of computational modeling may also include prediction of responders to CRT with biventricular defibrillators (see also Chap. 10). In our laboratory in collaboration with the Cardiac Mechanics Research Group at the Department of Bioengineering at the University of California San Diego (Chap. 12), we are working toward this end by the creation of patient-specific models of left and right heart structure, function, and electrical activation (Fig. 1.4).

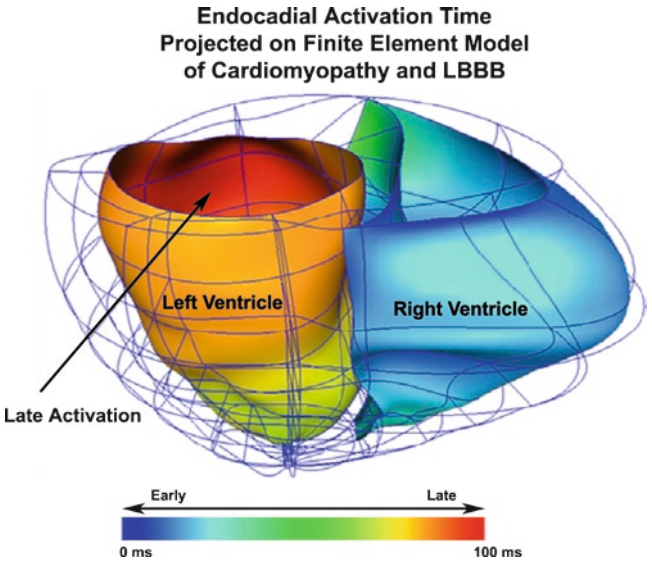

Fig. 1.4 Patient-specific finite element model of the *left* (*red*, late) and *right* ventricles (*blue*, early activation) in a patient with dilated cardiomyopathy and *left* bundle branch block. Model allows calculation of stress and strain throughout the myocardial walls for specific nodes, at which the equations governing activation and motion are solved. *LBBB* left bundle branch block. Shin, Jun. *Patient-specific Modeling of Cardiac Electromechanics in Dyssynchronous Heart Failure*. La Jolla, CA: UCSD, Master's thesis, 2009. With permission from Jun Shin

Presently, this is achieved with the use of patient-specific CT data, but may in the future include echo strain imaging, which has the potential to provide additional information about ventricular load characteristics. Applying known characteristics of normal, diseased, and scarred myocardium, responders to CRT may be predicted. For instance, it has been shown that strain heterogeneity, or mechanical discoordination [32], predicts CRT response more accurately than mechanical dyssynchrony.

As technology improves, it may also be possible to predict, in a patient-specific model, where the best location for LV lead placement, given a patient's venous anatomy. Thus, during left ventricular lead placement, once the coronary sinus venous anatomy is know, computer models could determine the optimum branch of the coronary sinus, and location within that branch, to place the left ventricular lead.

1.5 Conclusion

Complex numerical methods are currently used in electrophysiology to define patient anatomy, define arrhythmia pathways, and target ablation. However, patient specific modeling has significantly potential to advance future treatment of cardiac arrhythmias when functionally important myocardial sites or specific types of ion

channels can be predicted for individual patients. Achieving these goals will require advances in both the automation of time-intensive steps of modeling and merging of anatomical and functional data sets. Clearly, modeling is approaching the level of sophistication required to make the jump from laboratory to bedside for the benefit of patient care.

References

1. Arentz T, Weber R, Burkle G, Herrera C, Blum T, Stockinger J, Minners J, Neumann FJ, and Kalusche D. Small or large isolation areas around the pulmonary veins for the treatment of atrial fibrillation? Results from a prospective randomized study. *Circulation* 115: 3057–3063, 2007.
2. Badhwar N, Kalman JM, Sparks PB, Kistler PM, Attari M, Berger M, Lee RJ, Sra J, and Scheinman MM. Atrial tachycardia arising from the coronary sinus musculature: electrophysiological characteristics and long-term outcomes of radiofrequency ablation. *J Am Coll Cardiol* 46: 1921–1930, 2005.
3. Bello D, Kipper S, Valderrabano M, and Shivkumar K. Catheter ablation of ventricular tachycardia guided by contrast-enhanced cardiac computed tomography. *Heart Rhythm* 1: 490–492, 2004.
4. Bertaglia E, Brandolino G, Zoppo F, Zerbo F, and Pascotto P. Integration of 3-D left atrial magnetic resonance images into a real-time electroanatomic mapping system: validation of a registration method. *Pacing Clin Electrophysiol* 31: 273–282, 2008.
5. Beshai JF, Grimm RA, Nagueh SF, Baker JH, 2nd, Beau SL, Greenberg SM, Pires LA, and Tchou PJ. Cardiac-resynchronization therapy in heart failure with narrow QRS complexes. *N Engl J Med* 357: 2461–2471, 2007.
6. Bogun F, Bender B, Li YG, and Hohnloser SH. Ablation of atypical atrial flutter guided by the use of concealed entrainment in patients without prior cardiac surgery. *J Cardiovasc Electrophysiol* 11: 136–145, 2000.
7. Bogun FM, Desjardins B, Good E, Gupta S, Crawford T, Oral H, Ebinger M, Pelosi F, Chugh A, Jongnarangsin K, and Morady F. Delayed-enhanced magnetic resonance imaging in nonischemic cardiomyopathy: utility for identifying the ventricular arrhythmia substrate. *J Am Coll Cardiol* 53: 1138–1145, 2009.
8. Bonakdar HR, Jorat MV, Fazelifar AF, Alizadeh A, Givtaj N, Sameie N, Sadeghpour A, and Haghjoo M. Prediction of response to cardiac resynchronization therapy using simple electrocardiographic and echocardiographic tools. *Europace* 11: 1330–1337, 2009.
9. Brignole M, Oddone D, Maggi R, Lupi G, Bollini R, Corallo S, Robotti S, Solano A, Donateo P, and Croci F. Resynchronization of the left ventricular contraction by tailored programming of right and left ventricular pacing. *Europace* 10: 489–495, 2008.
10. Cano O, Hutchinson M, Lin D, Garcia F, Zado E, Bala R, Riley M, Cooper J, Dixit S, Gerstenfeld E, Callans D, and Marchlinski FE. Electroanatomic substrate and ablation outcome for suspected epicardial ventricular tachycardia in left ventricular nonischemic cardiomyopathy. *J Am Coll Cardiol* 54: 799–808, 2009.
11. Cobb LA, Fahrenbruch CE, Olsufka M, and Copass MK. Changing incidence of out-of-hospital ventricular fibrillation, 1980–2000. *Jama* 288: 3008–3013, 2002.
12. Corrado D, Basso C, Leoni L, Tokajuk B, Bauce B, Frigo G, Tarantini G, Napodano M, Turrini P, Ramondo A, Daliento L, Nava A, Buja G, Iliceto S, and Thiene G. 3-D electroanatomic voltage mapping increases accuracy of diagnosing arrhythmogenic right ventricular cardiomyopathy/dysplasia. *Circulation* 111: 3042–3050, 2005.
13. Costantini O, Hohnloser SH, Kirk MM, Lerman BB, Baker JH, 2nd, Sethuraman B, Dettmer MM, and Rosenbaum DS. The ABCD (Alternans Before Cardioverter Defibrillator) trial: strategies using T-wave alternans to improve efficiency of sudden cardiac death prevention. *J Am Coll Cardiol* 53: 471–479, 2009.

14. Desjardins B, Crawford T, Good E, Oral H, Chugh A, Pelosi F, Morady F, and Bogun F. Infarct architecture and characteristics on delayed enhanced magnetic resonance imaging and electroanatomic mapping in patients with postinfarction ventricular arrhythmia. *Heart Rhythm* 6: 644–651, 2009.
15. Eckstein J, Verheule S, de Groot NM, Allessie M, and Schotten U. Mechanisms of perpetuation of atrial fibrillation in chronically dilated atria. *Prog Biophys Mol Biol* 97: 435–451, 2008.
16. Epstein AE, Dimarco JP, Ellenbogen KA, Estes NA, 3rd, Freedman RA, Gettes LS, Gillinov AM, Gregoratos G, Hammill SC, Hayes DL, Hlatky MA, Newby LK, Page RL, Schoenfeld MH, Silka MJ, Stevenson LW, and Sweeney MO. ACC/AHA/HRS 2008 guidelines for device-based therapy of cardiac rhythm abnormalities: executive summary. *Heart Rhythm* 5: 934–955, 2008.
17. Fahmy TS, Wazni OM, Jaber WA, Walimbe V, Di Biase L, Elayi CS, DiFilippo FP, Young RB, Patel D, Riedlbauchova L, Corrado A, Burkhardt JD, Schweikert RA, Arruda M, and Natale A. Integration of positron emission tomography/computed tomography with electroanatomical mapping: a novel approach for ablation of scar-related ventricular tachycardia. *Heart Rhythm* 5: 1538–1545, 2008.
18. Fan R, Cano O, Ho SY, Bala R, Callans DJ, Dixit S, Garcia F, Gerstenfeld EP, Hutchinson M, Lin D, Riley M, and Marchlinski FE. Characterization of the phrenic nerve course within the epicardial substrate of patients with nonischemic cardiomyopathy and ventricular tachycardia. *Heart Rhythm* 6: 59–64, 2009.
19. Forleo GB, Pappalardo A, Avella A, Visigalli L, Dello Russo A, and Tondo C. Real-time integration of intracardiac echocardiography and 3D electroanatomical mapping to guide catheter ablation of isthmus-dependent atrial flutter in a patient with complete situs inversus and interruption of the inferior vena cava with azygos continuation. *J Interv Card Electrophysiol* 2009.
20. Ghanem RN. Noninvasive electrocardiographic imaging of arrhythmogenesis: insights from modeling and human studies. *J Electrocardiol* 40: S169–S173, 2007.
21. Gold MR, Bloomfield DM, Anderson KP, El-Sherif NE, Wilber DJ, Groh WJ, Estes NA, 3rd, Kaufman ES, Greenberg ML, and Rosenbaum DS. A comparison of T-wave alternans, signal averaged electrocardiography and programmed ventricular stimulation for arrhythmia risk stratification. *J Am Coll Cardiol* 36: 2247–2253, 2000.
22. Gussak I, Antzelevitch C, Bjerregaard P, Towbin JA, and Chaitman BR. The Brugada syndrome: clinical, electrophysiologic and genetic aspects. *J Am Coll Cardiol* 33: 5–15, 1999.
23. Haissaguerre M, Jais P, Shah DC, Takahashi A, Hocini M, Quiniou G, Garrigue S, Le Mouroux A, Le Metayer P, and Clementy J. Spontaneous initiation of atrial fibrillation by ectopic beats originating in the pulmonary veins. *N Engl J Med* 339: 659–666, 1998.
24. Haissaguerre M, Extramiana F, Hocini M, Cauchemez B, Jais P, Cabrera JA, Farre J, Leenhardt A, Sanders P, Scavee C, Hsu LF, Weerasooriya R, Shah DC, Frank R, Maury P, Delay M, Garrigue S, and Clementy J. Mapping and ablation of ventricular fibrillation associated with long-QT and Brugada syndromes. *Circulation* 108: 925–928, 2003.
25. Haissaguerre M, Lim KT, Jacquemet V, Rotter M, Dang L, Hocini M, Matsuo S, Knecht S, Jais P, and Virag N. Atrial fibrillatory cycle length: computer simulation and potential clinical importance. *Europace* 9 (Suppl 6): vi64–70, 2007.
26. Heist EK, Chevalier J, Holmvang G, Singh JP, Ellinor PT, Milan DJ, D'Avila A, Mela T, Ruskin JN, and Mansour M. Factors affecting error in integration of electroanatomic mapping with CT and MR imaging during catheter ablation of atrial fibrillation. *J Interv Card Electrophysiol* 17: 21–27, 2006.
27. Hsu EW and Henriquez CS. Myocardial fiber orientation mapping using reduced encoding diffusion tensor imaging. *J Cardiovasc Magn Reson* 3: 339–347, 2001.
28. Huang Z, Patel C, Li W, Xie Q, Wu R, Zhang L, Tang R, Wan X, Ma Y, Zhen W, Gao L, and Yan GX. Role of signal-averaged electrocardiograms in arrhythmic risk stratification of patients with Brugada syndrome: a prospective study. *Heart Rhythm* 6: 1156–1162, 2009.

29. Jalife J, Berenfeld O, and Mansour M. Mother rotors and fibrillatory conduction: a mechanism of atrial fibrillation. *Cardiovasc Res* 54: 204–216, 2002.
30. Kerckhoffs RC, Faris OP, Bovendeerd PH, Prinzen FW, Smits K, McVeigh ER, and Arts T. Electromechanics of paced left ventricle simulated by straightforward mathematical model: comparison with experiments. *Am J Physiol Heart Circ Physiol* 289: H1889–H1897, 2005.
31. Kerckhoffs RC, Narayan SM, Omens JH, Mulligan LJ, and McCulloch AD. Computational modeling for bedside application. *Heart Fail Clin* 4: 371–378, 2008.
32. Kirn B, Jansen A, Bracke F, van Gelder B, Arts T, and Prinzen FW. Mechanical discoordination rather than dyssynchrony predicts reverse remodeling upon cardiac resynchronization. *Am J Physiol Heart Circ Physiol* 295: H640–H646, 2008.
33. Kistler PM, Rajappan K, Jahngir M, Earley MJ, Harris S, Abrams D, Gupta D, Liew R, Ellis S, Sporton SC, and Schilling RJ. The impact of CT image integration into an electroanatomic mapping system on clinical outcomes of catheter ablation of atrial fibrillation. *J Cardiovasc Electrophysiol* 17: 1093–1101, 2006.
34. Kleijn SA, van Dijk J, de Cock CC, Allaart CP, van Rossum AC, and Kamp O. Assessment of intraventricular mechanical dyssynchrony and prediction of response to cardiac resynchronization therapy: comparison between tissue Doppler imaging and real-time 3-D echocardiography. *J Am Soc Echocardiogr* 22: 1047–1054, 2009.
35. Knecht S, Sacher F, Wright M, Hocini M, Nogami A, Arentz T, Petit B, Franck R, De Chillou C, Lamaison D, Farre J, Lavergne T, Verbeet T, Nault I, Matsuo S, Leroux L, Weerasooriya R, Cauchemez B, Lellouche N, Derval N, Narayan SM, Jais P, Clementy J, and Haissaguerre M. Long-term follow-up of idiopathic ventricular fibrillation ablation: a multicenter study. *J Am Coll Cardiol* 54: 522–528, 2009.
36. Konings KT, Smeets JL, Penn OC, Wellens HJ, and Allessie MA. Configuration of unipolar atrial electrograms during electrically induced atrial fibrillation in humans. *Circulation* 95: 1231–1241, 1997.
37. Korinek J, Kjaergaard J, Sengupta PP, Yoshifuku S, McMahon EM, Cha SS, Khandheria BK, and Belohlavek M. High spatial resolution speckle tracking improves accuracy of 2-dimensional strain measurements: an update on a new method in functional echocardiography. *J Am Soc Echocardiogr* 20: 165–170, 2007.
38. Koutelou M, Katsikis A, Flevari P, Theodorakis G, Livanis E, Georgiadis M, Voudris V, and Kremastinos D. Predictive value of cardiac autonomic indexes and MIBG washout in ICD recipients with mild to moderate heart failure. *Ann Nucl Med* 23: 677–684, 2009.
39. Krummen DE, Peng KA, Bullinga JR, and Narayan SM. Centrifugal gradients of rate and organization in human atrial fibrillation. *Pacing Clin Electrophysiol* 32: 1366–1378, 2009.
40. Lakireddy V, Bub G, Baweja P, Syed A, Boutjdir M, and El-Sherif N. The kinetics of spontaneous calcium oscillations and arrhythmogenesis in the in vivo heart during ischemia/reperfusion. *Heart Rhythm* 3: 58–66, 2006.
41. Latcu DG, Ricard P, Zarqane N, Yaici K, Rinaldi JP, Maluski A, and Saoudi N. Robotic magnetic navigation for ablation of human arrhythmias: initial experience. *Arch Cardiovasc Dis* 102: 419–425, 2009.
42. Lemery R, Birnie D, Tang AS, Green M, and Gollob M. Feasibility study of endocardial mapping of ganglionated plexuses during catheter ablation of atrial fibrillation. *Heart Rhythm* 3: 387–396, 2006.
43. Lemola K, Desjardins B, Sneider M, Case I, Chugh A, Good E, Han J, Tamirisa K, Tsemo A, Reich S, Tschopp D, Igic P, Elmouchi D, Bogun F, Pelosi F, Jr., Kazerooni E, Morady F, and Oral H. Effect of left atrial circumferential ablation for atrial fibrillation on left atrial transport function. *Heart Rhythm* 2: 923–928, 2005.
44. Lickfett L, Dickfeld T, Kato R, Tandri H, Vasamreddy CR, Berger R, Bluemke D, Luderitz B, Halperin H, and Calkins H. Changes of pulmonary vein orifice size and location throughout the cardiac cycle: dynamic analysis using magnetic resonance cine imaging. *J Cardiovasc Electrophysiol* 16: 582–588, 2005.
45. Martinek M, Nesser HJ, Aichinger J, Boehm G, and Purerfellner H. Accuracy of integration of multislice computed tomography imaging into 3-D electroanatomic mapping for real-time

guided radiofrequency ablation of left atrial fibrillation-influence of heart rhythm and radiofrequency lesions. *J Interv Card Electrophysiol* 17: 85–92, 2006.
46. McGann CJ, Kholmovski EG, Oakes RS, Blauer JJ, Daccarett M, Segerson N, Airey KJ, Akoum N, Fish E, Badger TJ, DiBella EV, Parker D, MacLeod RS, and Marrouche NF. New magnetic resonance imaging-based method for defining the extent of left atrial wall injury after the ablation of atrial fibrillation. *J Am Coll Cardiol* 52: 1263–1271, 2008.
47. Moss AJ, Zareba W, Hall WJ, Klein H, Wilber DJ, Cannom DS, Daubert JP, Higgins SL, Brown MW, and Andrews ML. Prophylactic implantation of a defibrillator in patients with myocardial infarction and reduced ejection fraction. *N Engl J Med* 346: 877–883, 2002.
48. Nademanee K, McKenzie J, Kosar E, Schwab M, Sunsaneewitayakul B, Vasavakul T, Khunnawat C, and Ngarmukos T. A new approach for catheter ablation of atrial fibrillation: mapping of the electrophysiologic substrate. *J Am Coll Cardiol* 43: 2044–2053, 2004.
49. Nakagawa E, Takagi M, Tatsumi H, and Yoshiyama M. Successful radiofrequency catheter ablation for electrical storm of ventricular fibrillation in a patient with Brugada syndrome. *Circ J* 72: 1025–1029, 2008.
50. Noseworthy PA, Malchano ZJ, Ahmed J, Holmvang G, Ruskin JN, and Reddy VY. The impact of respiration on left atrial and pulmonary venous anatomy: implications for image-guided intervention. *Heart Rhythm* 2: 1173–1178, 2005.
51. Oral H, Knight BP, Tada H, Ozaydin M, Chugh A, Hassan S, Scharf C, Lai SW, Greenstein R, Pelosi F, Jr., Strickberger SA, and Morady F. Pulmonary vein isolation for paroxysmal and persistent atrial fibrillation. *Circulation* 105: 1077–1081, 2002.
52. Passman R, Subacius H, Ruo B, Schaechter A, Howard A, Sears SF, and Kadish A. Implantable cardioverter defibrillators and quality of life: results from the defibrillators in nonischemic cardiomyopathy treatment evaluation study. *Arch Intern Med* 167: 2226–2232, 2007.
53. Patel AM, d'Avila A, Neuzil P, Kim SJ, Mela T, Singh JP, Ruskin JN, and Reddy VY. Atrial tachycardia after ablation of persistent atrial fibrillation: identification of the critical isthmus with a combination of multielectrode activation mapping and targeted entrainment mapping. *Circ Arrhythm Electrophysiol* 1: 14–22, 2008.
54. Peichl P, Cihak R, Kozeluhova M, Wichterle D, Vancura V, and Kautzner J. Catheter ablation of arrhythmic storm triggered by monomorphic ectopic beats in patients with coronary artery disease. *J Interv Card Electrophysiol* 27(1):51–59, 2010.
55. Po SS, Scherlag BJ, Yamanashi WS, Edwards J, Zhou J, Wu R, Geng N, Lazzara R, and Jackman WM. Experimental model for paroxysmal atrial fibrillation arising at the pulmonary vein-atrial junctions. *Heart Rhythm* 3: 201–208, 2006.
56. Poole JE, Johnson GW, Hellkamp AS, Anderson J, Callans DJ, Raitt MH, Reddy RK, Marchlinski FE, Yee R, Guarnieri T, Talajic M, Wilber DJ, Fishbein DP, Packer DL, Mark DB, Lee KL, and Bardy GH. Prognostic importance of defibrillator shocks in patients with heart failure. *N Engl J Med* 359: 1009–1017, 2008.
57. Rausch P, Manfai B, Varady E, and Simor T. Radiofrequency catheter ablation of left ventricular outflow tract tachycardia with the assistance of the CartoSound system. *Europace* 11: 1248–1249, 2009.
58. Reddy VY, Reynolds MR, Neuzil P, Richardson AW, Taborsky M, Jongnarangsin K, Kralovec S, Sediva L, Ruskin JN, and Josephson ME. Prophylactic catheter ablation for the prevention of defibrillator therapy. *N Engl J Med* 357: 2657–2665, 2007.
59. Reddy VY, Neuzil P, Malchano ZJ, Vijaykumar R, Cury R, Abbara S, Weichet J, McPherson CD, and Ruskin JN. View-synchronized robotic image-guided therapy for atrial fibrillation ablation: experimental validation and clinical feasibility. *Circulation* 115: 2705–2714, 2007.
60. Ren JF, Marchlinski FE, and Callans DJ. Left atrial thrombus associated with ablation for atrial fibrillation: identification with intracardiac echocardiography. *J Am Coll Cardiol* 43: 1861–1867, 2004.
61. Ren JF, Lin D, Marchlinski FE, Callans DJ, and Patel V. Esophageal imaging and strategies for avoiding injury during left atrial ablation for atrial fibrillation. *Heart Rhythm* 3: 1156–1161, 2006.

62. Ripley KL, Gage AA, Olsen DB, Van Vleet JF, Lau CP, and Tse HF. Time course of esophageal lesions after catheter ablation with cryothermal and radiofrequency ablation: implication for atrio-esophageal fistula formation after catheter ablation for atrial fibrillation. *J Cardiovasc Electrophysiol* 18: 642–646, 2007.
63. Rivero-Ayerza M, Jessurun E, Ramcharitar S, van Belle Y, Serruys PW, and Jordaens L. Magnetically guided left ventricular lead implantation based on a virtual 3-D reconstructed image of the coronary sinus. *Europace* 10: 1042–1047, 2008.
64. Rosendahl L, Ahlander BM, Bjorklund PG, Blomstrand P, Brudin L, and Engvall JE. Image quality and myocardial scar size determined with magnetic resonance imaging in patients with permanent atrial fibrillation: a comparison of two imaging protocols. *Clin Physiol Funct Imaging* 30(2):122–129, 2010.
65. Saksena S, Simon AM, Mathew P, and Nagarakanti R. Intracardiac echocardiography-guided cardiac resynchronization therapy: technique and clinical application. *Pacing Clin Electrophysiol* 32: 1030–1039, 2009.
66. Saliba W, Reddy VY, Wazni O, Cummings JE, Burkhardt JD, Haissaguerre M, Kautzner J, Peichl P, Neuzil P, Schibgilla V, Noelker G, Brachmann J, Di Biase L, Barrett C, Jais P, and Natale A. Atrial fibrillation ablation using a robotic catheter remote control system: initial human experience and long-term follow-up results. *J Am Coll Cardiol* 51: 2407–2411, 2008.
67. Santucci PA, Varma N, Cytron J, Akar JG, Wilber DJ, Al Chekakie MO, and Brysiewicz N. Electroanatomic mapping of postpacing intervals clarifies the complete active circuit and variants in atrial flutter. *Heart Rhythm* 6: 1586–1595, 2009.
68. Saoudi N, Cosio F, Waldo A, Chen SA, Iesaka Y, Lesh M, Saksena S, Salerno J, and Schoels W. Classification of atrial flutter and regular atrial tachycardia according to electrophysiologic mechanism and anatomic bases: a statement from a joint expert group from the Working Group of Arrhythmias of the European Society of Cardiology and the North American Society of Pacing and Electrophysiology. *J Cardiovasc Electrophysiol* 12: 852–866, 2001.
69. Sarrazin JF, Labounty T, Kuhne M, Crawford T, Armstrong WF, Desjardins B, Good E, Jongnarangsin K, Chugh A, Oral H, Pelosi F, Morady F, and Bogun F. Impact of radiofrequency ablation of frequent post-infarction premature ventricular complexes on left ventricular ejection fraction. *Heart Rhythm* 6: 1543–1549, 2009.
70. Savard P, Rouleau JL, Ferguson J, Poitras N, Morel P, Davies RF, Stewart DJ, Talajic M, Gardner M, Dupuis R, Lauzon C, Sussex B, Potvin L, and Warnica W. Risk stratification after myocardial infarction using signal-averaged electrocardiographic criteria adjusted for sex, age, and myocardial infarction location. *Circulation* 96: 202–213, 1997.
71. Schmidt A, Azevedo CF, Cheng A, Gupta SN, Bluemke DA, Foo TK, Gerstenblith G, Weiss RG, Marban E, Tomaselli GF, Lima JA, and Wu KC. Infarct tissue heterogeneity by magnetic resonance imaging identifies enhanced cardiac arrhythmia susceptibility in patients with left ventricular dysfunction. *Circulation* 115: 2006–2014, 2007.
72. Schwartzman D and Zhong H. On the Use of CartoSound for Left Atrial Navigation. *J Cardiovasc Electrophysiol* 2009.
73. Sen-Chowdhry S, Prasad SK, Syrris P, Wage R, Ward D, Merrifield R, Smith GC, Firmin DN, Pennell DJ, and McKenna WJ. Cardiovascular magnetic resonance in arrhythmogenic right ventricular cardiomyopathy revisited: comparison with task force criteria and genotype. *J Am Coll Cardiol* 48: 2132–2140, 2006.
74. Seo Y, Ishizu T, Sakamaki F, Yamamoto M, Machino T, Yamasaki H, Kawamura R, Yoshida K, Sekiguchi Y, Kawano S, Tada H, Watanabe S, and Aonuma K. Mechanical dyssynchrony assessed by speckle tracking imaging as a reliable predictor of acute and chronic response to cardiac resynchronization therapy. *J Am Soc Echocardiogr* 22: 839–846, 2009.
75. Shen X, Aronow WS, Nair CK, Holmberg MJ, Hee T, Maciejewski S, and Esterbrooks DJ. Are the extent, location, and score of segmental wall motion abnormalities related to cardiac resynchronization therapy response? *Echocardiography* 26: 1136–1145, 2009.
76. Sporton SC, Earley MJ, Nathan AW, and Schilling RJ. Electroanatomic versus fluoroscopic mapping for catheter ablation procedures: a prospective randomized study. *J Cardiovasc Electrophysiol* 15: 310–315, 2004.

77. Sztajzel J. Heart rate variability: a noninvasive electrocardiographic method to measure the autonomic nervous system. *Swiss Med Wkly* 134: 514–522, 2004.
78. Thiagalingam A, Wallace EM, Boyd AC, Eipper VE, Campbell CR, Byth K, Ross DL, and Kovoor P. Noncontact mapping of the left ventricle: insights from validation with transmural contact mapping. *Pacing Clin Electrophysiol* 27: 570–578, 2004.
79. Tops LF, de Groot NM, Bax JJ, and Schalij MJ. Fusion of electroanatomical activation maps and multislice computed tomography to guide ablation of a focal atrial tachycardia in a fontan patient. *J Cardiovasc Electrophysiol* 17: 431–434, 2006.
80. Towbin JA, Li H, Taggart RT, Lehmann MH, Schwartz PJ, Satler CA, Ayyagari R, Robinson JL, Moss A, and Hejtmancik JF. Evidence of genetic heterogeneity in Romano-Ward long QT syndrome. Analysis of 23 families. *Circulation* 90: 2635–2644, 1994.
81. Verma A, Marrouche NF, Schweikert RA, Saliba W, Wazni O, Cummings J, Abdul-Karim A, Bhargava M, Burkhardt JD, Kilicaslan F, Martin DO, and Natale A. Relationship between successful ablation sites and the scar border zone defined by substrate mapping for ventricular tachycardia post-myocardial infarction. *J Cardiovasc Electrophysiol* 16: 465–471, 2005.
82. Volkmer M, Ouyang F, Deger F, Ernst S, Goya M, Bansch D, Berodt K, Kuck KH, and Antz M. Substrate mapping vs. tachycardia mapping using CARTO in patients with coronary artery disease and ventricular tachycardia: impact on outcome of catheter ablation. *Europace* 8: 968–976, 2006.
83. Wazni OM, Barrett C, Martin DO, Shaheen M, Tarakji K, Baranowski B, Hussein A, Callahan T, Dresing T, Bhargava M, Kanj M, Tchou P, Natale A, and Saliba W. Experience with the Hansen robotic system for atrial fibrillation ablation-lessons learned and techniques modified: Hansen in the real world. *J Cardiovasc Electrophysiol* 20(11): 1193–1196, 2009.
84. Xia H, Zhao X, Bains J, and Wortham DC. Influence of channel blockers on cardiac alternans. *Conf Proc IEEE Eng Med Biol Soc* 1: 2823–2826, 2009.
85. Yagi T, Pu J, Chandra P, Hara M, Danilo P, Jr., Rosen MR, and Boyden PA. Density and function of inward currents in right atrial cells from chronically fibrillating canine atria. *Cardiovasc Res* 54: 405–415, 2002.
86. Zeppenfeld K, Tops LF, Bax JJ, and Schalij MJ. Images in cardiovascular medicine. Epicardial radiofrequency catheter ablation of ventricular tachycardia in the vicinity of coronary arteries is facilitated by fusion of 3-D electroanatomical mapping with multislice computed tomography. *Circulation* 114: e51–e52, 2006.

Chapter 2
Patient-Specific Modeling of Cardiovascular Dynamics with a Major Role for Adaptation

Theo Arts, Joost Lumens, Wilco Kroon, Dirk Donker, Frits Prinzen, and Tammo Delhaas

2.1 Introduction

Over the last few decades, technological developments have made diagnostic information of the cardiovascular system far more detailed. These improvements are prominently attributed to the general availability of many imaging techniques, such as ultrasonic echo imaging, computer tomography (CT), Magnetic Resonance Imaging (MRI), and Positron Emission Tomography (PET). After primary diagnosis, treatment starts by following a protocol that is considered best, given the available information. Following the standard route, such protocol is a result of empirical clinical studies, where effects of different treatments are compared statistically in large groups of patients with similar pathology. With increase of diagnostic detail, groups become less uniform, forcing us to make the subgroups smaller and more numerous. Due to the technological improvements, the choice and possible graduation of therapeutic interventions increase too. As a result, with the conventional epidemiological setup of such studies, it will ever be more difficult to reach the level of significance for obtaining better treatment protocols.

Instead of following the empirical route, we propose to pay extra attention to use physiological and physical principles in finding the most accurate diagnosis and best treatment for the patient. In contrast with the epidemiological approach, the physiological approach deals primarily with causes and effects. Many physiological relationships related to cell, tissue, organ, or whole system can be approached by a mathematical relation. Thus, patient characteristics may be simulated by a computer model, composed of a network of applied physiological relationships. By adjusting relevant parameters in the computer model, so that model simulation and measurements agree, we obtain a patient-specific simulation, which can be used for further improvement of diagnosis and better planning of treatment.

T. Arts (✉)
Department of Biomedical Engineering, Maastricht University,
Maastricht, The Netherlands
e-mail: t.arts@bf.unimaas.nl

R.C.P. Kerckhoffs (ed.), *Patient-Specific Modeling of the Cardiovascular System: Technology-Driven Personalized Medicine*, DOI 10.1007/978-1-4419-6691-9_2,

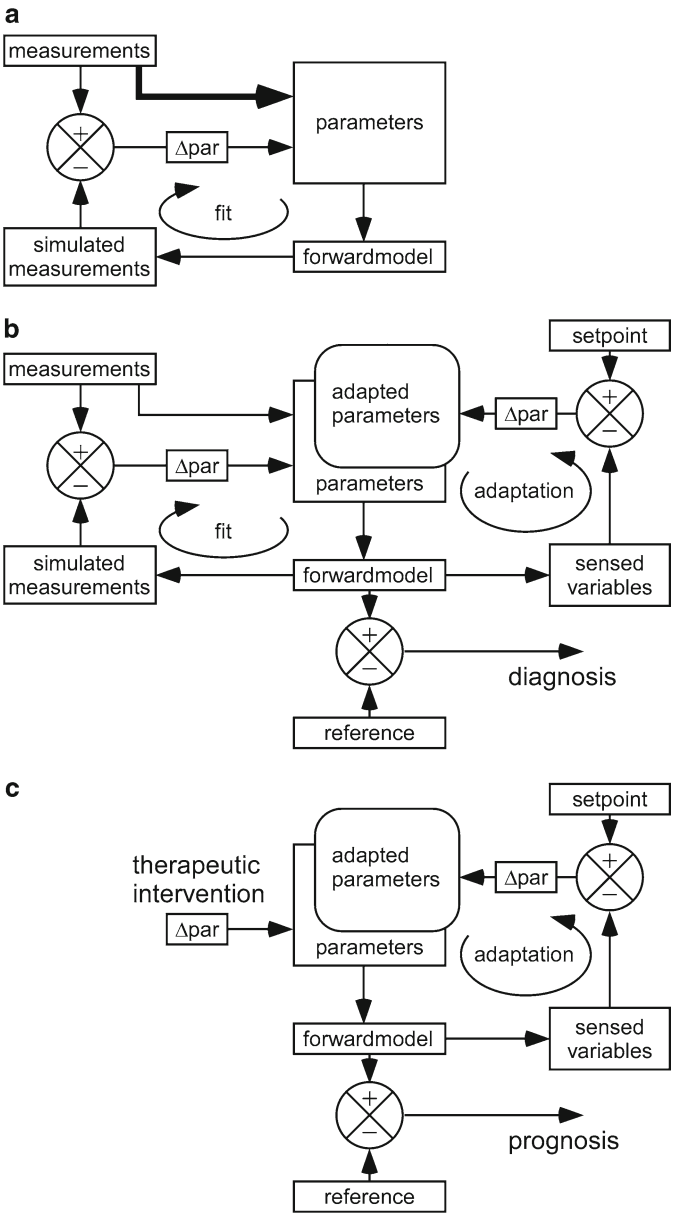

Fig. 2.1 Patient-specific modeling. (**a**) The forward model describes selected relevant physiologic processes. Many parameters of the model are obtained by direct measurement. A few parameters may be tuned to obtain a better fit with average physiological behavior. (**b**) With more comprehensive models, usually there are too many parameters for a reliable fit. Physiological knowledge of adaption of subsystems to load is used to simulate a most likely state of adaptation, thus narrowing down uncertainty in many parameters. A remaining relatively small set of parameters is fit to available measurements for assessment of the status of the patient. Investigation whether critical values in the simulation are within the normal or pathologic range allows diagnostic differentiation. (**c**) After the model is found to describe the status of a patient accurately, a therapeutic intervention may be simulated to obtain a prognosis for that intervention. Simulation of adaptation effects is likely to improve the long-term prognosis

Patient-specific modeling is intended to simulate the most likely status of a patient, given the available measurements. If we do not know anything, the patient is considered the normal average because that state is most likely. After having decided on what aspects patient-specific modeling will be focused, the forward model is designed to simulate relevant physiological principles by quantitative equations, which are governed by a set of parameters describing for instance size, structure, and function of the constituting parts (Fig. 2.1a). Starting from known boundary conditions, e.g., in time and space, a crude simulation of the normal state is obtained by forward model calculation. When comparing the results of the latter simulation with known physiological data, many discrepancies are to be expected. Therefore, the forward model is incorporated in a feedback loop, aiming to fit the model to known physiological data by tuning a carefully selected subset of model parameters. Positive criteria for parameter selection are physiological relevance, large sensitivity, and large uncertainty about the value due to lack of information. Thus, a simulation is obtained that may serve as the starting point for patient-specific simulation.

For patient-specific simulation, the same strategy may be used as for obtaining the basic simulation of the normal state. In contrast with average physiological behavior, for a specific patient, there is not as much quantitative information available. With less information, reliability of the estimate can be maintained only if the number of adjustable parameters is reduced to those parameters that describe patient's pathology best.

Currently, there is a tendency in patient-specific modeling to demand more information to be measured with application of modern technology. Nevertheless, for reasons of efficiency and for minimizing load to the patient, it is important to use the scarcely available, expensive information about the specific patient with utmost efficiency. We think that much efficiency can be gained by application of physical, physiologic, and pathophysiologic principles, to be incorporated in the model. The gain in model quality is illustrated by the example below, where a pathologic state is described by estimating the value of a single causal parameter.

We assume that most pathology has a causal focus that leads to a syndrome, reflecting the sum of resulting processes and compensations. For example, a stenotic aortic valve hampers left ventricular outflow, resulting in hypertrophy of the left ventricle, which, on its turn, hampers diastolic filling and other abnormalities. In modeling terms, change of a single pathologic parameter, i.e., narrowing of the open aortic valve, causes many other parameters such as left ventricular mass and stiffness to change according to standard physiological principles. Instead of fitting all changing parameters, we may adjust only the single pathologic parameter while using known physiological principles to simulate further consequences. Comparing effects of these consequences with measured data may result in a more reliable estimate of the few causal pathologic parameters than as would be obtained with more conventional estimation of all deviant parameters separately.

Following the latter strategy, we propose to include the process of adaptation in the patient-specific simulation, implying that the model adjusts properties like size and structure of the subsystems to changes in chronic load, which are generated by

the model itself (Fig. 2.1b). Thus, the model becomes self-structuring. For example, if blood pressure increases chronically, load of the left ventricle will increase too. According to known physiological principles, the increase of mechanical load results in increase of tissue mass (hypertrophy) of that ventricle. The latter increase will decrease mechanical load per mass of tissue, thus closing a control loop for mass of the left ventricular wall. Eventually, a new steady state is reached.

By inclusion of adaptation in the model, the number of model parameters is reduced considerably, since many parts of the circulation have the same type of tissue in common. For instance, geometry of the heart chambers and blood vessels is largely determined by adaptation properties of myocardial tissue and vascular tissue, respectively.

Patient-specific modeling is intended to estimate prognostic outcomes (Fig. 2.1c). For simulation of a prognosis, there will be no role for parameter fitting, since measurements about future are not available. Incorporation of adaption in the model remains important because intended interventions will change the distribution of load, causing long-term compensations. Prognostic outcomes are to be simulated for different types and degrees of therapeutic intervention. The simulation with the best outcome may indicate best treatment.

In this chapter, we discuss the strategy of designing patient-specific models aiming to facilitate diagnosis and treatment. First, a flexible modular setup of modeling is proposed. Next, physiologic mechanisms should be selected for incorporation in the model. Furthermore, the measurement protocol and the proper set of parameters should be chosen for fitting the model to available patient data. Incorporation of modeling adaptation of tissues to chronic mechanical load is presented as a major issue, aiming to restrict the number of estimated parameters to a minimum. Although the proposed principles will hold generally for patient-specific modeling, we have focused our examples on modeling of the cardiovascular system.

2.2 Cardiovascular Forward Models

Forward models generate simulations by straightforward calculation using a model with known parameters, known boundary conditions in space, and known starting conditions. Here, we focus on modeling hemodynamics and mechanics of the cardiovascular system on a beat-to-beat basis. The cardiovascular system encompasses the heart, blood vessels, valves, and nervous communications. Most models described in the literature focus on a part of the cardiovascular system. Electrical activation of the atrial myocyte has been modeled by Luo and Rudy [30, 39], attributing a large role to currents through channels in membranes. Several modifications were proposed to accommodate the behavior of ventricular myocytes in the human and in other species ([45], Chap. 3). Moving to a higher level of integration, the cardiac tissue was modeled by mutual connection of

myocytes, thus simulating propagation of a depolarization wave through cardiac tissue ([25, 44], Chaps. 2 and 9). Shortly after depolarization of the myocyte, a pulse of intracellular calcium causes temporary cross-bridges between actin and myosin, resulting in the systolic pulse of mechanical stress and strain [38]. Within a cardiac wall, myocytes are arranged in fibers, forming a distinct helical structure [42]. Stress and strain delivered by the myocytes are transferred to the myofiber structure, forming the myocardial tissue. Finite element models are developed to simulate how the work as delivered by the myofibers is converted to pump work of the left ventricle, sometimes combined with a right ventricle [15, 20, 24, 50]. In a few instances, the finite element representation of cardiac chambers was incorporated in a model of circulatory hemodynamics ([21, 24, 41], Chaps. 8–10), thus providing a more realistic estimate of the hemodynamic boundary condition. Finite element models are advantageous in their ability to analyze regional differences in load and performance of the cardiac wall, at the cost, however, of a large computational effort. When not being interested in regional differences, the relation between mean myofiber mechanics and pump function can be described accurately by the much simpler and (more than 1,000 times) faster one-fiber model of cardiac chamber mechanics [1, 29].

Besides for the heart, models have also been developed for spatial and temporal flow profiles in blood vessels (Chap. 6). Blood flow pulses, generated by the heart, are propagated as pressure-flow waves along the compliant arteries [51]. At bifurcations and other irregularities, these waves are partially reflected. In the microcirculation, vessel diameters are so small that viscous effects of blood prevail over inertial effects. Consequently, the microcirculation behaves macroscopically like a peripheral resistance with compliance. About the venous side of the circulation, not much is known, but on a physical basis, one may expect that contraction of the atria causes variations in flow and pressure, resulting in propagation of pulse waves upstream along the veins.

Although the function of a heart valve is simply conduction of flow in forward direction and blockade of flow in backward direction, finite element models have been developed to understand flow patterns and pressure gradients in and around the valves [23]. Models of aortic valve hemodynamics have helped to understand how this valve closes efficiently at the end of systole [49]. The mitral valve is more complicated because their leaflets are attached to actively contracting papillary muscles. For better understanding of the pathologic mitral valve, flow phenomena in and around the normal mitral valve have been modeled to serve as reference. When relating pressure gradient to flow without a need for knowing local flow phenomena, much simpler models can be used. Following the Navier–Stokes equation for pressure drop in a flow field, pressure drop is a summation of inertial effects, steady-state acceleration (Bernouilli effect), and viscous effects. Vortices distal to a valve are responsible for further loss of energy. Human heart valves are so large that viscous effects are of minor importance. Besides simulating forward flow, such models also can describe backward flow (regurgitation) through a leaking valve with formation of vortices and turbulence inclusive [10].

2.3 Integration to a Comprehensive Circulatory System

Patient-specific simulation requires that a wide variety of measurements can be combined to estimate the mechanical and hemodynamic status of heart and circulation as a whole. For that purpose, models of heart chamber, blood vessels, and valve have to be integrated into a comprehensive model. Models integrating many parts into a complete system are relatively scarce. One of the earliest models of a comprehensive cardiovascular system has been designed in the group of Guyton [17, 31]. This model focused on blood pressure and flow control. Several models [18, 33, 37, 43, 46] have been designed to simulate the closed-loop circulation on a beat-to-beat basis. All these models suffer from the major problem that uncertainties of the parameter values in each subsystem add up to such a high level of overall inaccuracy that the reliability of the simulation is severely affected. After all, for a patient-specific simulation, values should be attributed to all these parameters. Measurement of so many parameter values is not realistic when being confined to common clinical methods. Somehow, the number of parameters with patient-specific values should be limited, while the simulation as a whole should still be realistic.

In modeling hemodynamics and mechanics of heart and circulation, we propose a modular setup of the model. With the simplest set of modules, the circulation can already be simulated as a realistic working system. When focusing on specific parts of the system, modules should allow replacement by more detailed ones, having implemented desired specific aspects. Such a plug-in modular setup requires clear definition of input and output for the separate modules.

The CircAdapt model [3, 29] has been designed to act as backbone for a modular setup in modeling heart and circulation. In this model, the whole circulation is composed of a limited number of module types, i.e., chambers, valves, tubes, and resistances (Fig. 2.2a). Atria and ventricles are represented by chambers having a wall, composed of contractile myocardial tissue. Large arteries and veins are represented by nonlinearly elastic tubes that can conduct pressure waves. Tubes and chambers can be connected by valves, whose effective orifice area depends on direction and magnitude of flow through the valve and on pressure drop over the valve. Peripheral vascular beds of the various organs may be simulated by a resistance connecting the arterial module to the venous module. Besides organs, tissues may also be handled as modules. Myocardial tissue is simulated by a nonlinearly elastic material harboring myofibers that contract after depolarization. Vascular tissue is considered nonlinearly elastic.

In the basic version of the CircAdapt model, the ventricular section is described by the TriSeg model, where left ventricular free wall, septum, and right ventricular wall meet in a common junction line, thus forming left and right ventricular cavity. Furthermore, the whole heart is encapsulated in an elastic pericardial chamber (Fig. 2.2a). Sections of the CircAdapt model can be replaced easily. For example, when incorporating a finite element model of the left ventricle as a module, first both ventricles are handled as uncoupled chambers (Fig. 2.2b), thus readily neglecting direct mechanical ventricular interaction. For a chamber, the CircAdapt model

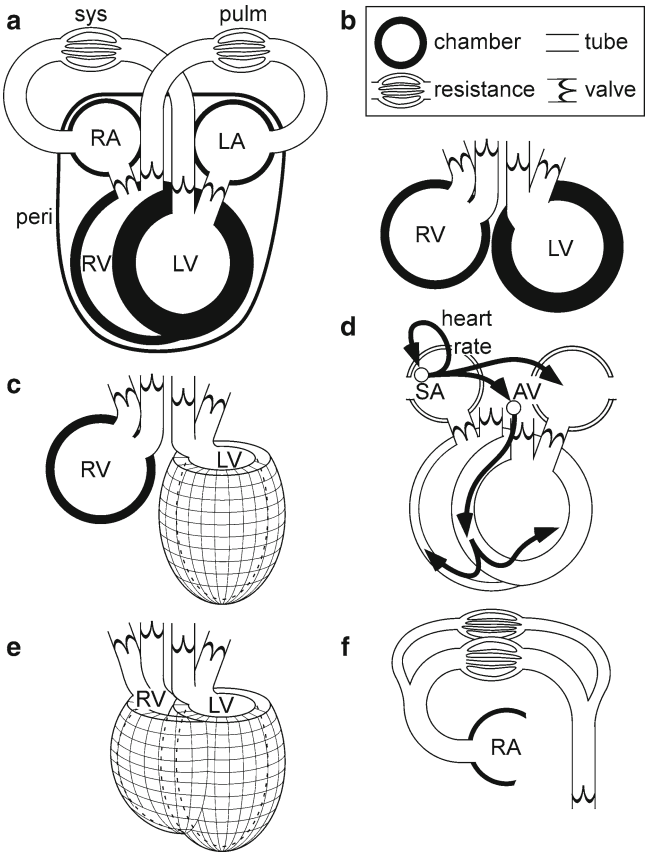

Fig. 2.2 Modular setup to model the complete circulation. (**a**) The CircAdapt model describes pressures and flows in heart and circulation. Meaning of symbols: L/R A/V = left/right atrium/ventricle; peri = pericardium; sys, pulm = systemic, pulmonary circulation. Four modules are used, i.e., contractile chambers, nonlinearly elastic tubes, valves, and peripheral resistances. The TriSeg module describes LV–RV interaction. (**b**) To prepare incorporation of a finite element model of the left ventricle, the TriSeg module may be replaced by simpler, but less accurate independent ventricles. (**c**) Based on (**b**), the LV may be replaced by the finite element model. (**d**) The sequence of electrical depolarization may be included. SA, AV = sinoatrial and atrioventricular nodes. (**e**) Replacement of the TriSeg module by a finite element representation of both coupled ventricles. (**f**) Replacement of the single-channel systemic circulation module by a more complex, multiple-organ representation

requires cavity pressure to be known as a function of volume only. Next, the single left ventricular chamber can be replaced by a finite element model of that chamber. The latter module should be designed so that pressure is delivered as a function of cavity volume (Fig. 2.2c). The sequence of depolarization is modeled by a set of delay times for electrical conduction (Fig. 2.2d). In a more sophisticated ventricular section, the pair of ventricles can be replaced by a finite element model of the coupled ventricles (Fig. 2.2e). Furthermore, the simple description of the whole

systemic circulation (Fig. 2.2f) may be replaced by a realistic tree of arteries and veins feeding and draining the different organs, respectively. The blood vessels may be designed to propagate pressure waves and reflect these waves at bifurcations. Because the backbone of CircAdapt requires very little computational effort, it can be used conveniently for setting realistic hemodynamic boundary conditions to the more detailed versions of subsystems [22].

The modular setup is advantageous because the various modules such as blood vessels and chambers are composed of a few types of tissues. Parameters related to the tissue are therefore largely general, resulting in great reduction of the number of unknown parameters. An important problem remains, however. Geometry of the different components of the circulatory system varies per individual. Accurate measurement of all these dimensions is impractical, even often impossible in a regular clinical setting. Along the lines of abovementioned strategy on patient-specific modeling, we propose to solve the latter problem by attributing properties of adaptation to mechanical load for the different tissues.

2.4 Adaptation Rules

Adaptation is a property attributed to the tissue. For a given tissue, various types of load or concentrations may be sensed and compared with tissue-specific set points. Following the physiological principle that both sensing of load and the resulting compensatory actions take place in and around the same cell, we assume that a discrepancy between actual load and its set point causes an adaptive action in the direct environment of the location where the load has been sensed. Different tissue types will have different adaptation rules. Currently, we confine ourselves to sensing of mechanical load and the resulting adaptation effects such as growth or changes in structure or function. The adaptation effects will change dimensions and structure of heart and blood vessels, so that the sensed discrepancies between actual and referenced levels of load are counteracted, thus closing the loop of control by adaptation (Fig. 2.1b). If adaptation is complete, a stationary state will be reached with load near the set-point values, implying that load is uniformly distributed over the tissues. Adaptation appears the driving force to self-organization of the constituting elements of the circulation. Because the set points of load mark the range of optimal performance of the tissue, in its adapted state, the tissue works in the optimal range. Consequently, it is to be expected that the whole organ is likely to work near its optimum range too.

Geometries and functional properties of the different parts of the cardiovascular system are regulated by a few properties that have the constitutive tissues in common. By a first simplistic approach, within the cardiovascular system we distinguish two main types of tissue, i.e., the nonlinearly elastic vascular tissue and the actively contracting myocardium. In Fig. 2.3 and the section below, adaptive actions for myocardial tissue are summarized.

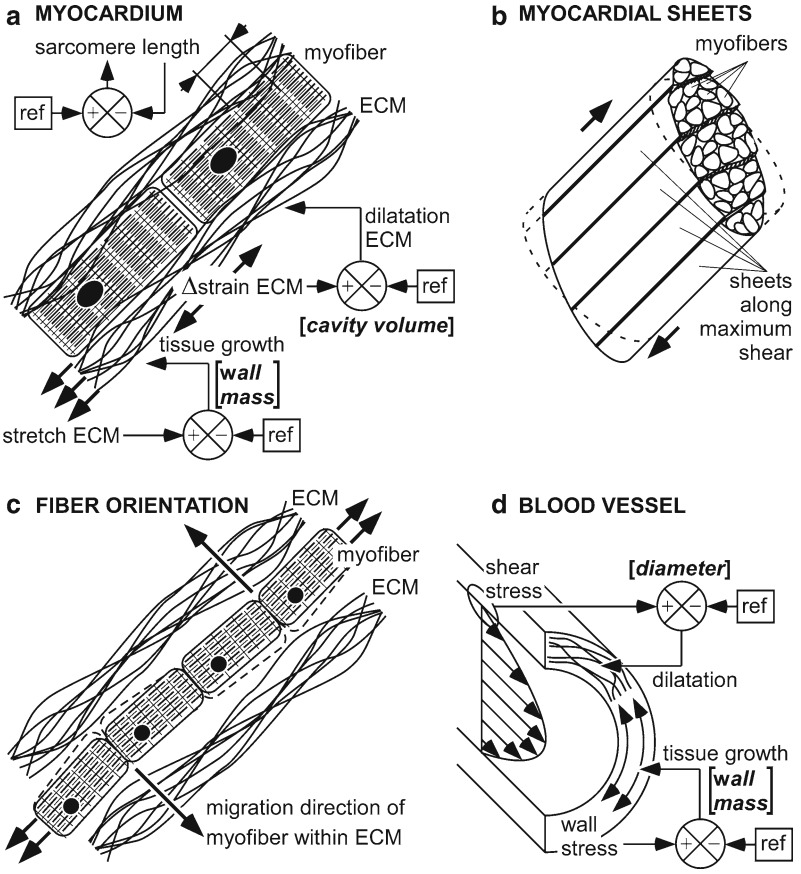

Fig. 2.3 Modeling adaptation of tissues to mechanical load. (**a**) Myocardium consists of myocytes, forming a network of myofibers, embedded in an extra-cellular matrix of collagen fibers (ECM). Sarcomere length is maintained in the working range. Stretch of the ECM induces growth of tissue mass (hypertrophy). A large strain range during ejection causes the ECM to soften, resulting in dilatation of the heart cavity. (**b**) A cylindrical section of myocardium is subject to deformation during the cardiac cycle. Planes of sheets are parallel to the myofibers with the extra condition that sheet orientation is so that shear between the sheets is maximum. (**c**) A series of myocytes, forming a myofiber, tends to straighten by systolic stress. The resulting forces on the ECM, perpendicular to the myober cause the myofiber to migrate through the ECM. (**d**) Model of the blood vessel wall. Similar to the myocardial ECM, wall stress causes tissue mass to grow. Furthermore, shear stress along the tube interior, invoked by flow, causes the blood vessel to dilate

For the myocardium, roughly two types of hypertrophy are distinguished [12, 36, 40]. Pressure overload induces concentric hypertrophy, characterized by thickening of the wall, while cavity volume remains unaffected. Volume overload induces eccentric hypertrophy, characterized by thickening of the wall and proportional increase of inner diameter. At first sight, these adaptive actions suggest that both systolic stress and strain are sensed to induce adaptive changes in wall mass and cavity diameter, finally resulting in fixed levels of systolic stress and strain. Although the proposed

mechanism that systolic stress induces growth of myocardial mass seems logic, at a closer look, the proposed mechanism appears not likely because hypertrophy did not correlate well with changes in systolic stress [13, 32]. A better candidate for control of myocardial mass appears a pathway through sensing diastolic stress or stretch in the extracellular matrix [13, 19, 35]. According to this hypothesis, excess of the diastolic stress over a set-point value would induce growth of myocardial mass (Fig. 2.3a). Therefore, increase of volume load would stretch the wall, thereby inducing wall mass to increase. Similarly, an increase of afterload would hamper full ejection, resulting in an increase of end-systolic volume. With unchanged venous return, next beat will start with increased cavity volume, thus also causing stretch of the wall, resulting in increase of wall mass. Therefore, the proposed adaption rule that stretch of the extracellular matrix causes increase of wall mass is in agreement with induction of hypertrophy by both volume load and pressure load, respectively.

Apparently, increase of preload and afterload both induce hypertrophy of the myocardial wall, although the type of hypertrophy is different. Differentiation between concentric and eccentric hypertrophy is obtained by postulating the adaptation rule that high strain during the cardiac cycle causes the myocardial tissue to soften (Fig. 2.3a), resulting in dilatation of the cavity [14]. With the latter rule, volume load induces dilatation, thus fulfilling the conditions of eccentric hypertrophy. With pressure load, systolic strain is not increasing, implying that cavity size remains relatively unaffected. The resulting hypertrophy is therefore concentric.

The sarcomere is the basic unit that is responsible for myocardial contraction. The working range of sarcomere length seems to be narrow [16], indicating the presence of a control mechanism for sarcomere length (Fig. 2.3a). Although the rule is simple, the mechanism of this adaptive control is not clear. Sarcomere length may be adjusted by adding more sarcomeres in series or by slippage of myocytes in the structure of the myocardial tissue [34].

In modeling the heart with its myofiber structure in three dimensions, myofiber orientation must be known for implementation in the related finite element model. Measurement of fiber orientation is practically impossible in the living heart. With utmost effort, fiber orientation may be determined with MRI diffusion tensor imaging [47], but even then, accuracy is likely not to be sufficient for reliable calculation of local stress and strain in the myocardium [6, 8]. Since fiber orientation cannot be measured reliably, we search to estimate the distribution of fiber orientation by assuming proper adaptation rules. It has been suggested that the myofiber would search for a direction with an optimal strain level [4], but a more likely candidate is directioning by stress along the myofiber, which rule is equivalent with directioning by transverse shear strain at the beginning of systole [24] (Fig. 2.3c). With this adaptation rule, the myofiber searches for straight pathways of systolic stress. If the myofibers were not straight before contraction, the extracellular matrix around the myofibers would be deformed in systole, thus imposing stresses perpendicular on the myofibers. With the proposed adaptation rule, we assume that the active myofiber migrates through the passive matrix structure until the oblique stress component disappears. As a result, myofiber pathways tend to follow straight (geodesic) pathways in systole, while maintaining their straightness in diastole.

In myocardial tissue, the myofibers are arranged in sheets [26] (Fig. 2.3b). Sheets facilitate cross-deformation of the myocardium. Although sheet orientation appeared not reproducible interindividually [9] in dogs, we attempted to search an adaptation rule for it. Because myofibers are contained in sheets, sheet planes are indeed always parallel to the orientation of myofibers. Given the latter constraint, sheets were observed to have formed along the plane through the myofibers oriented so that shear is maximum [2]. Theoretically, two different plane orientations that satisfy shear to be maximum can be found, albeit these maxima might be different in height. Both maxima result in two nearly perpendicular solutions for sheet orientation, explaining the finding of large interindividual differences. On photographs of cross-sections of myocardial tissue, both solutions appear realistic, even near a single location, as shown by the existence of sheet boundaries that cross about perpendicularly.

Morphologically, blood vessels are composed of three layers, the intima, the media, and the adventitia. For simplicity, we consider the wall as a single entity (Fig. 2.3d). Shear stress induced by blood flowing along the inner wall is claimed to control vascular diameter [7]. With increase of flow, shear stress increases, invoking dilatation of the wall. As a result, flow velocity and shear stress along the inner wall surface decrease, counteracting the originally sensed increase of shear stress. Thus, the control loop for vessel diameter is closed. It should be mentioned, however, that the mechanism is more complicated. In small blood vessels, the level of shear rate is about fixed and universal, but in large vessels, this rate appears much smaller. For instance, in mice as well as elephant, peak aortic velocity is about 1 m/s, whereas aortic diameters are very different [11]. Therefore, the level of mean shear rate in the aorta of small animals is much larger than that in large animals. Since viscosity of blood is not very different among the different species, the level of shear stress along the inner wall is also very different. It has also been found that within the same individual, mean shear rate is smaller in the large arteries than in the small ones. Apparently, interindividually as well as intraindividually, for the smaller blood vessels, shear stress controls diameter, whereas for the larger arteries, there is an additional mechanism making the blood vessel somehow more sensitive to shear stress. Besides adaptation of diameter, a blood vessel adapts its wall thickness to transmural pressure, so that wall stress remains about constant.

2.5 Examples of Patient-Specific Modeling

2.5.1 Reference State

Patient-specific modeling is directed to estimate the most likely status of the patient, considering all useful information that is available by clinical observation. Focusing on mechanics and hemodynamics, we use the CircAdapt model as

Table 2.1 Parameter values for a normal circulation

General hemodynamics		
Mean blood pressure (92 mmHg)	12.2	kPa
Mean blood flow at rest/exercise	85/255	ml/s
Cycle time (1/HR) at rest/exercise	850/425	ms
Blood vessels		
Shear rate in large blood vessels	60	s^{-1}
Wall stress	700	kPa
Sarcomere		
Maximum strain	0.23	–
Mean sarcomere length	2.0	μm
Maximum passive stress	7.5	kPa
Maximum active stress	60	kPa

a basis for modeling the dynamics of the whole circulation. Before any observation on the patient is made, the patient is most likely to be normal. For a normal healthy person, mean aortic blood pressure, cardiac output, and heart rate were set to the general average (Table 2.1). During the resting state, blood-vessel diameter adapted to accommodate the set point for shear rate, which is equivalent with keeping the level of shear stress fixed. At a state of moderate exercise, cardiac output and heart rate were multiplied by 3.0 and 2.0, respectively. Then, for the blood vessels, wall thickness adapted to accommodate wall stress. For the heart walls, cavity volume and wall thickness adapted to accommodate myofiber strain and passive myofiber stress. Mean sarcomere length was maintained. Valve diameters were set equal to that of the connected large blood vessels. In Fig. 2.4, resulting hemodynamic signals are shown as a function of time during the cardiac cycle for the left side of the heart at rest. This normal state was used as starting condition for patient-specific modeling.

2.5.2 Non-invasively Obtained LV Pump Function and Myofiber Function

A set of noninvasive measurements was used to investigate to what extent left ventricular function was affected in normal elderly people [27]. In this study, a group of healthy elderly volunteers (60–74 years) was compared with a group of healthy young volunteers (19–26 years). Systolic and diastolic blood pressures were measured by use of an arm cuff (Fig. 2.5, upper left panel). With MRI tagging [5], rotation and contraction of each section were quantified in five to seven short-axis slices of the left ventricle as a function of time. Torsion of the LV was quantified as the base-to-apex gradient of rotation, multiplied by the outer radius of the left ventricle. From the MRI data, LV cavity and wall volumes were estimated as a function of time. In a model of adaptation of fiber orientation to deformation of the

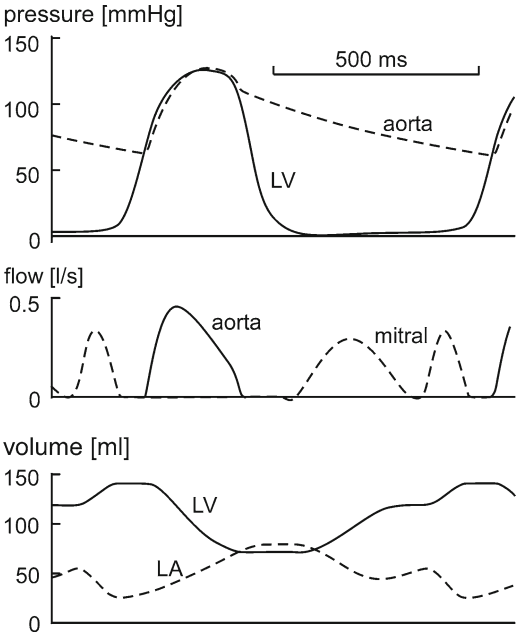

Fig. 2.4 Normal pressures, flows and volumes of the left heart, simulated with the CircAdapt model

LV, for the given LV geometry the transmural distribution of fiber orientation was estimated in a simulation of the beating heart, using the adaptation rules as mentioned in relation to Fig. 2.3a. [4, 24]. From the directly measured torsion and volume decrease during the ejection phase, together with estimated myofiber orientation, the transmural difference of myofiber strain was quantified (Fig. 2.5, lower left panel).

In a closer look, from these noninvasively obtained data, the systolic pressure–volume and stress–strain relations could be estimated too (Fig. 2.5, upper right panel). The CircAdapt model was fit by patient-specific adjustment of arterial wall stiffness, peripheral resistance, LV reference volume, and duration of systolic activation. By this fit, difference between simulated and measured values of the following variables was minimized: systolic and diastolic arterial pressure, ejection time, and end-diastolic LV volume. Measured values of heart rate, stroke volume, and wall mass were substituted directly in the model. It was concluded that with noninvasive techniques, estimates were obtained of the transmural difference of myofiber strain, time courses of mean myofiber stress and strain, and time courses of pressure and volume of the left ventricle (Fig. 2.5, lower right panel). From this study, it was concluded that in the elderly shortening of the myofibers in the subendocardium was 21% less than in the subepicardium, as compared with the young reference group, where this difference was not significant [48].

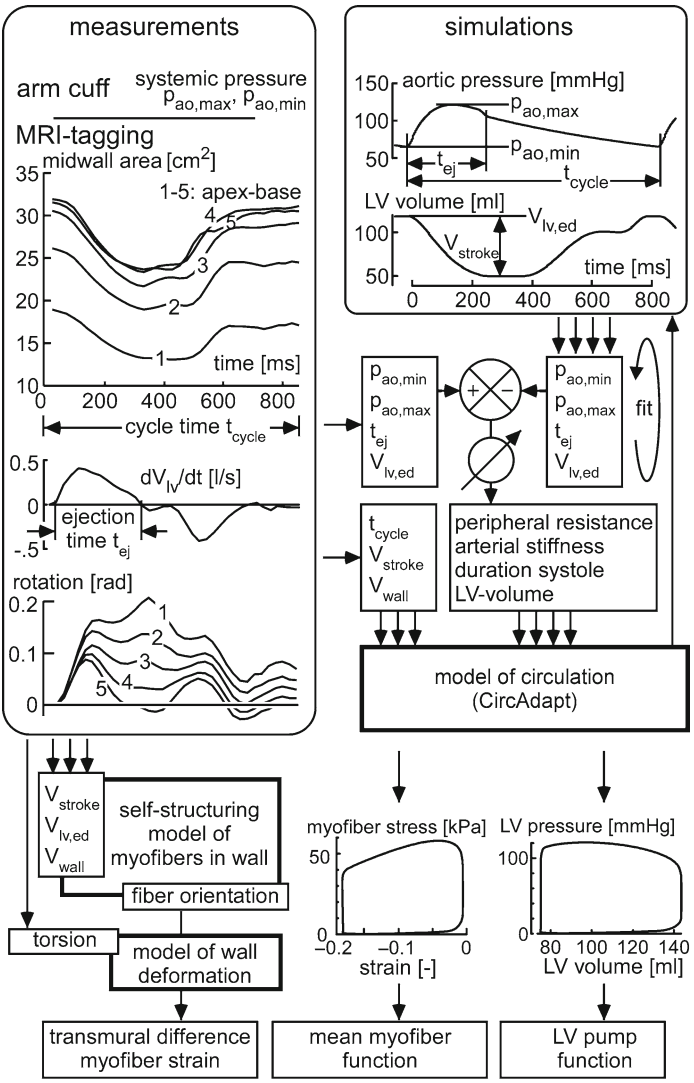

Fig. 2.5 Patient-specific modeling of LV mechanics and hemodynamics, rendering transmural differences in myofiber strain and pump function of the left ventricle. With MRI-tagging, stroke volume V_{stroke}, LV end-diastolic volume $V_{lv,ed}$ and wall volume V_{wall} are determined. Using adaptation of fiber orientation by systolic straightening (Fig. 2.3c), torsional deformation of the LV wall is modeled. Torsion, measured with MRI tagging, renders an estimate of the transmural difference of myofiber strain in the LV wall. With the CircAdapt model, parameters are adjusted for a best fit between measured and simulated aortic pressure, ejection time and end-diastolic LV volume. Cycle time t_{cycle}, V_{stroke}, and V_{wall} are substituted directly. As a result, time courses of LV pressure and volume and LV myofiber stress and strain are simulated, thus estimating function of LV myocardium and LV pump function

2.5.3 Complete Pressure–Volume Loop of the Left Ventricle

Estimation of diastolic LV pressure by non-invasive means is a challenge. Clinically, noninvasiveness is important because measurements can be repeated with fewer burdens to the patient to monitor the status of a patient in time. Realistic estimates of LV pressure can be made, following the principles as outlined below (Fig. 2.6). With 2D-echocardiography, LV wall mass and cavity volume at the beginning and end of ejection are measured. Cardiac output is calculated by multiplication of heart rate with stroke volume, as derived from 2D-echocardiography. With the pulsed Doppler ultrasound technique, flow velocity in the orifice of the aortic valve is measured. Systemic peripheral resistance and aortic stiffness are adjusted so that maximum and minimum aortic pressures match measured systolic and diastolic arterial pressure. Aortic orifice, and intensity and duration of LV contraction are adjusted so that amplitude, shape, and duration of aortic flow velocity match the measurements. Thus, the systolic time course of LV pressure is known. A more difficult problem is to determine diastolic LV pressure.

Flow velocity in the mitral valve orifice is measured in the same session as that measurement in the aortic valve orifice. Assuming that the valves are working properly, effective mitral valve orifice area equals cardiac output divided by mean mitral flow velocity. Commonly, mitral flow velocity is characterized by an early filling peak, the E-wave that immediately follows mitral valve opening and an atrial peak, the A-wave, which is related to atrial contraction. The width of the E-wave depends on the characteristic oscillation frequency of the system formed by the inertia of the blood in the mitral valve orifice and the combined compliance of left atrium and left ventricle. The narrower the E-wave is, the less compliant the ventricle should be. Knowing LV compliance and the time course of LV volume, information is obtained about diastolic pressure changes.

Because so many steps are to be made and so many cross-relations are to be expected to influence the estimate, we have used the complete CircAdapt model (Fig. 2.2a) to fit simulated values with the measured values by proper variation of the adjustable parameters (Table 2.2). As a result, a time course of LV pressure is obtained, satisfying all measurements simultaneously. Predicted LV pressure and invasively measured LV pressure were found to agree closely in systole as well as diastole (Fig. 2.6, lower panels).

2.5.4 Delay of the LV Activation in Left Bundle Branch Block

For proper cardiac pump function, the left and right ventricle should be activated about simultaneously. With left bundle branch block (LBBB), the left ventricle cannot be activated directly from the AV-node because of a conductance block. Then, activation of the LV occurs through the right ventricle by tissue conduction,

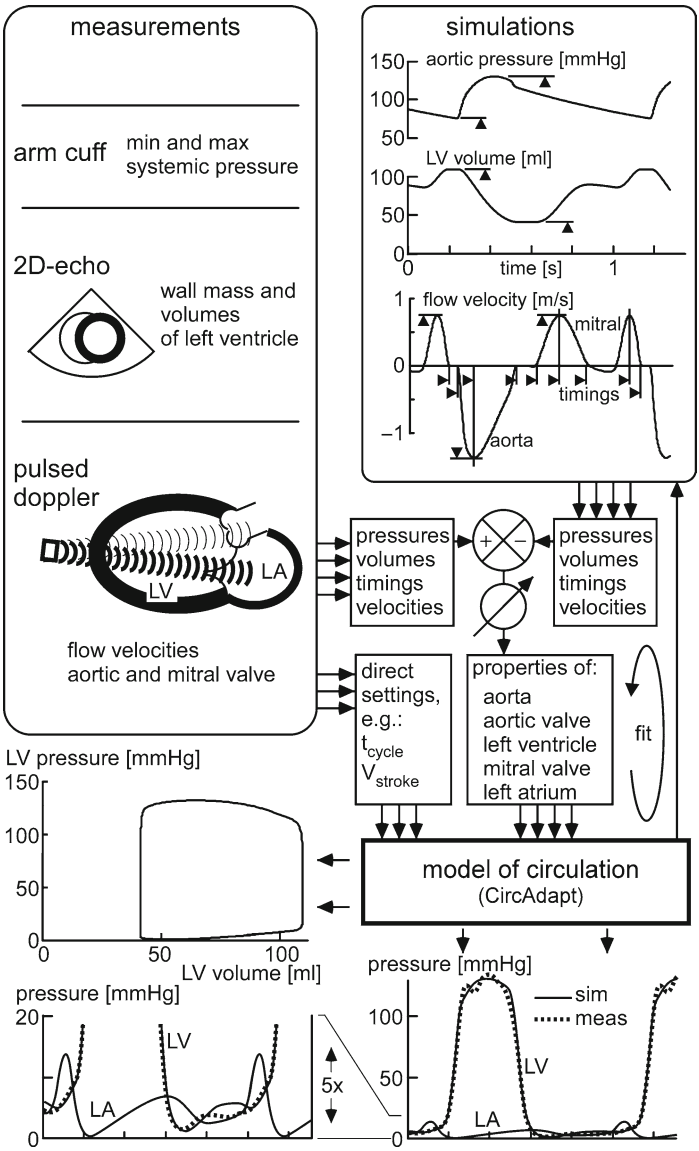

Fig. 2.6 Non-invasive estimation of complete LV pressure–volume loop, including diastolic pressure. Systolic LV function is obtained similar to the situation, indicated in Fig. 2.5. The CircAdapt model is used to estimate the dynamics of LV filling, where an important role is attributed to compliance of the LV and to inertia of the mitral valve tract. Simulation and measurements were fit on timing and amplitudes of flow phenomena, as detected by ultrasonic Doppler measurements of aortic and mitral flow velocity, and as indicated by the triangular arrowheads in the upper right panel. LV pressure and volume are estimated as a function of time. For this patient, predicted pressure has been compared with invasively measured pressure. As can be seen in the lower left enlargement, measured and estimated diastolic pressure closely agree. The model also provides an estimate of LA pressure

Table 2.2 Measured variables and adjusted parameters for patient-specific fit

Systolic aortic pressure	Systemic peripheral resistance
Diastolic aortic pressure	Arterial stiffness
Aortic peak velocity	Aortic valve diameter
Flow rise time	Rise time of LV contraction
Duration of ejection	Duration of myocardial systole
Shape factor of aortic flow velocity curve	LV contractility
Duration of isovolumic relaxation phase	Decay time of relaxation
Mitral E-wave velocity	Mitral valve diameter
Mitral A-wave velocity	Atrial stiffness
Width of E-wave	Ventricular stiffness
End-diastolic LV volume	LV reference volume

which is much slower than regular conduction. The delay between LV activation relative to RV activation can be estimated electrically, but it cannot be easily determined what effects are to be expected hemodynamically. Quantification of the delay of contraction may be derived by comparing the instants of pressure rise in left and right ventricle, respectively [28] (Fig. 2.7, lower left panel). These measurements are not simple due to their invasiveness.

Asynchrony of left and right ventricular contraction can be recognized also by detection of abnormal motion of the septum at the onset on systole (Fig. 2.7), using ultrasonic M-mode echocardiography. In a patient-specific simulation, the TriSeg module (Fig. 2.2a) was used to simulate ventricular interaction. By this model, motion of the septum relative to that of the left ventricle was simulated. In an experiment on a dog, septal motion was measured directly with M-mode echocardiography. In the model, the delay of LV activation was adjusted until simulated and measured septal displacement matched best. As a result, left and right ventricular pressures were simulated as a function of time. In the experiment, left and right ventricular pressures were also measured directly with catheter-tip manometers. Simulated and measured pressure agreed in shape (Fig. 2.7, lower left panel), indicating that aberrations in septal motion can be used to quantify the delay between left and right ventricular pressure noninvasively.

2.6 Discussion

A strategy for patient-specific modeling has been described. Although the proposed principles of this strategy will hold for a wide field of applications, we have focused our examples on modeling the cardiovascular system.

The design of the applied patient-specific model depends on available measurements and on the target parameter that should be quantified. The set of target parameters is a main determinant of the system to be simulated. The set of measured variables and signals determine the extension of the model by which these variables can be simulated as well. Comparison of true measurements and simulated

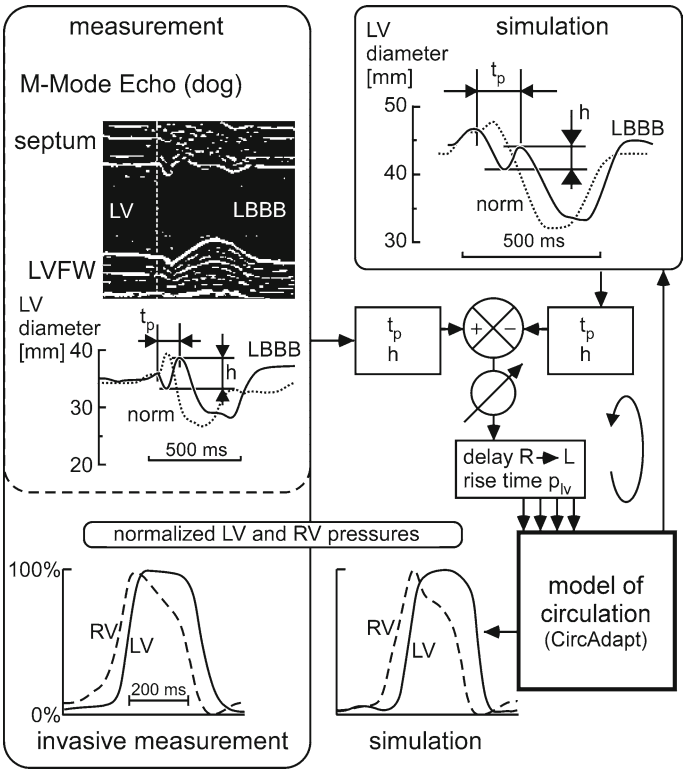

Fig. 2.7 Noninvasive estimation of left to right ventricular pressure delay in a dog heart with left bundle branch block (LBBB). With M-mode echocardiography, septal motion is quantified. Delay of electrical activation and rise-time of myocardial mechanical activation were adjusted for best match between measured and simulated septal motion as characterized by indicators t_p and h. LBBB induces a typical oscillation during ejection, as compared with normal contraction (*dotted lines*). Simulated and invasively measured LV and RV pressure agreed quite well

measurements is used to fit unknown, hidden parameters that are needed for estimating the set of target parameters.

Incorporation of adaptation rules for chronic mechanical load of heart and blood vessels appears an important tool to obtain a realistic simulation of the normal state of the circulation. Geometry of heart chambers and blood vessels appear to become physiologic by self-structuring of the model. In addition, pressure and flow signals appear physiologic without many precautions. In most pathologies, a single defect results in variation of many structural parameters due to adaptation effects. The model is designed to deal with these mutually related effects. For prognosis of a therapeutic intervention, inclusion of adaptation is also advantageous to estimate long-term effects of changes in mechanical load due to the applied intervention. Incorporation of adaptation rules greatly reduces the amount of parameters that should be found by fitting. Consequently, the fit of the remaining smaller set of parameters is more stable and reliable. For myocardium and blood vessel walls, we

have proposed adaptation rules that apparently work, but we must realize that we may not understand the real mechanism of adaptation.

In a few examples, we have shown that bringing together noninvasively measured information gathered from different modalities can render estimates of hidden variables that normally require invasive measurements. For instance, the transmural difference in myofiber shortening can be estimated non-invasively with MRI-tagging. By adding noninvasive arm-cuff measurements of systolic and diastolic pressure, available information appears sufficient to estimate the pressure–volume loop of the left ventricle and the stress–strain loop of the related myofibers. In addition, when combining measurements obtained in standard noninvasive cardiologic measuring protocol, i.e., measurement of blood pressure, ultrasonic echocardiography, and pulsed Doppler of the aortic and mitral valve, estimates can be obtained of diastolic left ventricular pressure. Currently, measurement of the latter variable requires invasive techniques. It is therefore to be expected that patient-specific modeling will increase clinical possibilities to monitor variables in patients, which are currently not easily accessible for that purpose due to required invasiveness.

Patient-specific models will become increasingly important. Given the wide variety of applied measuring techniques, the structure for patient-specific modeling should be flexible. In this respect, the trial with the CircAdapt model of the whole circulation shows that its modular setup is very convenient. Modules can be added to accommodate specific measurements. Modules can be replaced by more detailed ones, if that is required by the focus of clinical attention. The environment of remaining modules is used to render the necessary physiologic boundary conditions for the more detailed module in focus. Because there is not much experience with predictive medicine, much work has to be done to evaluate its potentials and limitations in treatment planning.

References

1. Arts, T., P. H. M. Bovendeerd, et al. (1991). “Relation between left ventricular cavity pressure and volume and systolic fiber stress and strain in the wall.” *Biophys J* **59**: 93–103.
2. Arts, T., K. D. Costa, et al. (2001). “Relating myocardial laminar architecture to shear strain and muscle fiber orientation.” *Am J Physiol* **280**: H2222–H2229.
3. Arts, T., T. Delhaas, et al. (2005). “Adaptation to mechanical load determines shape and properties of heart and circulation, the CircAdapt model.” *Am J Physiol Heart Circ Physiol* **288**: 1943–1954.
4. Arts, T., F. W. Prinzen, et al. (1994). “Adaptation of cardiac structure by mechanical feedback in the environment of the cell, a model study.” *Biophys J* **66**: 953–961.
5. Axel, L. and L. Dougherty (1989). “MR imaging of motion with spatial modulation of magnetization.” *Radiology* **171**: 841–845.
6. Bovendeerd, P. H. M., T. Arts, et al. (1992). “Dependence of left ventricular wall mechanics on myocardial fiber orientation: a model study.” *J Biomech* **25**: 1129–1140.
7. Brownlee, R. D. and B. L. Langille (1991). “Arterial adaptations to altered blood flow.” *Can J Physiol Pharmacol* **69**(7): 978–983.

8. Chadwick, R. S. (1982). "Mechanics of the left ventricle." *Biophys J* **39**: 279–288.
9. Costa, K. D., Y. Takayama, et al. (1999). "Laminar fiber architecture and three-dimensional systolic mechanics in canine ventricular myocardium." *Am J Physiol* **276**(2 Pt 2): H595–H607.
10. Cupps, B. P., P. Moustakidis, et al. (2003). "Severe aortic insufficiency and normal systolic function: determining regional left ventricular wall stress by finite-element analysis." *Ann Thorac Surg* **76**(3): 668–675; discussion 675.
11. Dawson, T. H. (2001). "Similitude in the cardiovascular system of mammals." *J Exp Biol* **204**(Pt 3): 395–407.
12. Devereux, R. B. and M. J. Roman (1999). "Left ventricular hypertrophy in hypertension: stimuli, patterns, and consequences." *Hypertens Res* **22**(1): 1–9.
13. Donker, D. W., J. G. Maessen, et al. (2007). "Impact of acute and enduring volume overload on mechanotransduction and cytoskeletal integrity of canine left ventricular myocardium." *Am J Physiol Heart Circ Physiol* **292**(5): H2324–H2332.
14. Emery, J. L., J. H. Omens, et al. (1997). "Strain softening in rat left ventricular myocardium." *J Biomech Eng* **119**(1): 6–12.
15. Guccione, J. M., K. D. Costa, et al. (1995). "Finite element stress analysis of left ventricular mechanics in the beating dog heart." *J Biomech* **28**: 1167–1177.
16. Guccione, J. M., W. G. O'Dell, et al. (1997). "Anterior and posterior left ventricular sarcomere lengths behave similarly during ejection." *Am J Physiol* **272**: H449–H477.
17. Guyton, A. C., J. P. Montani, et al. (1988). "Computer models for designing hypertension experiments and studying concepts." *Am J Med Sci* **295**(4): 320–326.
18. Hann, C. E., J. G. Chase, et al. (2006). "Integral-based identification of patient specific parameters for a minimal cardiac model." *Comput Methods Programs Biomed* **81**(2): 181–192.
19. Holmes, J. W. (2004). "Candidate mechanical stimuli for hypertrophy during volume overload." *J Appl Physiol* **97**(4): 1453–1460.
20. Kerckhoffs, R. C., A. D. McCulloch, et al. (2008). "Effects of biventricular pacing and scar size in a computational model of the failing heart with left bundle branch block." *Med Image Anal* **13**, 362–369.
21. Kerckhoffs, R. C., M. L. Neal, et al. (2007). "Coupling of a 3D finite element model of cardiac ventricular mechanics to lumped systems models of the systemic and pulmonic circulation." *Ann Biomed Eng* **35**(1): 1–18.
22. Kerckhoffs, R. C. P., Omens, J. H., McCulloch, A. D. and Mulligan, L. J. (2010) Ventricular dilation and electrical dyssynchrony synergistically increase regional mechanical nonuniformity but not mechanical dyssynchrony: A computational model." *Circulation: Heart Failure* **3**, 528–536.
23. Kim, H. J., I. E. Vignon-Clementel, et al. (2009). "On coupling a lumped parameter heart model and a three-dimensional finite element aorta model." *Ann Biomed Eng* **37**(11): 2153–2169.
24. Kroon, W., T. Delhaas, et al. (2009). "Computational analysis of the myocardial structure: adaptation of cardiac myofiber orientations through deformation." *Med Image Anal* **13**(2): 346–353.
25. Kuijpers, N. H., H. M. Ten Eikelder, et al. (2008). "Mechanoelectric feedback as a trigger mechanism for cardiac electrical remodeling: a model study." *Ann Biomed Eng* **36**(11): 1816–1835.
26. LeGrice, I. J., B. H. Smaill, et al. (1995). "Laminar structure of the heart: ventricular myocyte arrangement and connective tissue architecture in the dog." *Am J Physiol* **269**: H571–H582.
27. Lumens, J., T. Delhaas, et al. (2006). "Impaired subendocardial contractile myofiber function in asymptomatic aged humans, as detected using MRI." *Am J Physiol Heart Circ Physiol* **291**(4): H1573–H1579.
28. Lumens, J., T. Delhaas, et al. (2008). "Modeling ventricular interaction: a multiscale approach from sarcomere mechanics to cardiovascular system hemodynamics." *Pac Symp Biocomput* **13**: 378–389.
29. Lumens, J., T. Delhaas, et al. (2009). "Three-wall segment (TriSeg) model describing mechanics and hemodynamics of ventricular interaction." *Ann Biomed Eng* **37**(11): 2234–2255.
30. Luo, C. H. and Y. Rudy (1994). "A dynamic model of the cardiac ventricular action potential. II. After depolarizations, triggered activity, and potentiation." *Circ Res* **74**(6): 1097–1113.

31. Milhorn, H. T., Jr., R. Benton, et al. (1965). "A mathematical model of the human respiratory control system." *Biophys J* **5**: 27–46.
32. Nguyen, T. N., A. C. Chagas, et al. (1993). "Left ventricular adaptation to gradual renovascular hypertension in dogs." *Am J Physiol* **265**(1 Pt 2): H22–H38.
33. Olansen, J. B., J. W. Clark, et al. (2000). "A closed-loop model of the canine cardiovascular system that includes ventricular interaction." *Comput Biomed Res* **33**(4): 260–295.
34. Olivetti, G., J. M. Capasso, et al. (1990). "Side-to-side slippage of myocytes participates in ventricular wall remodeling acutely after myocardial infarction in rats." *Circ Res* **67**(1): 23–34.
35. Omens, J. H. (1998). "Stress and strain as regulators of myocardial growth." *Prog Biophys Mol Biol* **69**(2–3): 559–572.
36. Opie, L. H., P. J. Commerford, et al. (2006). "Controversies in ventricular remodelling." *Lancet* **367**(9507): 356–367.
37. Pennati, G., F. Migliavacca, et al. (1997). "A mathematical model of circulation in the presence of the bidirectional cavopulmonary anastomosis in children with a univentricular heart." *Med Eng Phys* **19**(3): 223–234.
38. Rice, J. J., F. Wang, et al. (2008). "Approximate model of cooperative activation and crossbridge cycling in cardiac muscle using ordinary differential equations." *Biophys J* **95**(5): 2368–2390.
39. Rudy, Y. and J. R. Silva (2006). "Computational biology in the study of cardiac ion channels and cell electrophysiology." *Q Rev Biophys* **39**(1): 57–116.
40. Sasayama, S., J. Ross, et al. (1976). "Adaptations of the left ventricle to chronic pressure overload." *Circ Res* **38**: 172–178.
41. Sermesant, M., P. Moireau, et al. (2006). "Cardiac function estimation from MRI using a heart model and data assimilation: advances and difficulties." *Med Image Anal* **10**(4): 642–656.
42. Streeter, D. D. (1979). Gross morphology and fiber geometry of the heart. In R. M. Berne, editor. *The cardiovascular system, the heart*, vol. 1. Bethesda, Maryland, USA, Am Physiol Soc: 61–112.
43. Sun, Y., M. Beshara, et al. (1997). "A comprehensive model for right-left heart interaction under the influence of pericardium and baroreflex." *Am J Physiol* **272**(3 Pt 2): H1499–H1515.
44. Ten Tusscher, K. H., O. Bernus, et al. (2006). "Comparison of electrophysiological models for human ventricular cells and tissues." *Prog Biophys Mol Biol* **90**(1–3): 326–345.
45. Ten Tusscher, K. H. and A. V. Panfilov (2006). "Cell model for efficient simulation of wave propagation in human ventricular tissue under normal and pathological conditions." *Phys Med Biol* **51**(23): 6141–6156.
46. Thomas, J. D., J. Zhou, et al. (1997). "Physical and physiological determinants of pulmonary venous flow: numerical analysis." *Am J Physiol* **272**(5 Pt 2): H2453–H2465.
47. Tseng, W. Y., T. G. Reese, et al. (1999). "Cardiac diffusion tensor MRI in vivo without strain correction." *Magn Reson Med* **42**(2): 393–403.
48. Van der Toorn, A., P. Barenbrug, et al. (2002). "Transmural gradients of cardiac myofiber shortening in aortic valve stenosis patients using MRI-tagging." *Am J Physiol* **283**: H1609–H1615.
49. Van Steenhoven, A. A. and M. E. H. Van Dongen (1979). "Model studies of the closing behavior of the aortic valve." *J Fluid Mech* **90**: 21–32.
50. Wang, V. Y., H. I. Lam, et al. (2009). "Modelling passive diastolic mechanics with quantitative MRI of cardiac structure and function." *Med Image Anal* **13**(5): 773–784.
51. Womersley, J. R. (1957). "Oscillatory flow in arteries: the constrained elastic tube as a model of arterial flow and pulse transmission." *Phys Med Biol* **2**(2): 178–187.

Chapter 3
Patient-Specific Modeling of Structure and Function of Cardiac Cells

Frank B. Sachse

3.1 Introduction

Cardiovascular diseases (CVDs) are the major cause of death in the developed world. Also, CVDs produce significant economic burden on society [37]. Development and implementation of approaches for prevention, diagnosis, and treatment of CVDs constitute large-scale and long-term efforts of healthcare systems, industry, and academia. Despite significant advances in technologies such as cardiac imaging and medical devices in the last decades, there are still major gaps in our basic knowledge of CVDs and their diagnosis and treatment, in particular, in individual patients.

Recently, patient-specific modeling has been suggested to support established diagnostic and therapeutic approaches in various medical disciplines [46], including cardiology and cardiac surgery. Patient-specific modeling is commonly based on clinical image data and/or physiological data from an individual patient, which are applied with methods of computational engineering, mathematical analysis, and computer visualization with the goal to understand mechanisms of disease, monitor patients, and evaluate treatment options specifically for this subject. Patient-specific modeling of the cardiovascular system is an active and diverse field of research covering molecular to multiorgan level [54]. Research foci at the macroscopic level include modeling of tissue electrophysiology, whole-heart electromechanics, valve mechanics, and blood flow. Patient-specific modeling at the microscopic and molecular level is still in its infancy but promises to provide valuable information on very basic mechanisms of, for instance, genetic diseases and their effects at cellular and tissue level. Promising applications of patient-specific cellular modeling are the tailoring of specialized pharmaceuticals, e.g., ion-channel blockers, parameterization of medical devices, e.g., biventricular pacemakers, treating the

F.B. Sachse (✉)
Nora Eccles Harrison Cardiovascular Research and Training Institute, and Bioengineering Department, University of Utah, 95 South 2000 East, 84112, Salt Lake City, UT, USA
e-mail: fs@cvrti.utah.edu

R.C.P. Kerckhoffs (ed.), *Patient-Specific Modeling of the Cardiovascular System: Technology-Driven Personalized Medicine*, DOI 10.1007/978-1-4419-6691-9_3,

CVD of an individual patient by taking his/her genotype and phenotype into account, and advanced diagnosis, e.g., quantitatively characterizing stages of heart failure based on the remodeling of cellular microstructure and protein distributions.

In order to appreciate the potential and issues of patient-specific cellular modeling, the following sections provide an overview of cardiac cells, their structure, function, and diseases. Methods for microscopic imaging of cardiac cells are presented based on fluorescence labeling. Approaches for functional modeling of cardiac cells are detailed. Studies on ion-channel mutations in humans and their effect on electrophysiology of cardiac myocytes serve as examples for patient-specific modeling of cell function. Furthermore, structural modeling approaches based on microscopic imaging and image processing are presented. In the final section, a perspective on potential clinical applications and implementation of patient-specific cellular modeling is given.

3.2 Cardiac Cells

The main function of the cardiac ventricles and atria is to pump blood by their mechanical contraction and relaxation. Ventricles and atria are composed of muscle tissues specialized for this mechanical activity and its coordination by electrical signaling. Cardiac tissues are a composite of various cell types including myocytes, fibroblasts, neuronal and endothelial cells. Structural and functional properties of these cells vary significantly during development and aging, among species and tissue types, and in the heart. This short overview focuses on myocytes and fibroblasts, which are the dominant cell types in heart.

Myocytes are the volumewise dominating cells in cardiac tissue. The phenotype of cardiac myocytes is diverse and depends on location in the tissue, functional role, and species. Their functional role is primarily force generation that causes mechanical contraction of the cell and tissue. As in other striated muscle cells, force is generated by molecular interactions of actin and myosin filaments, which are assembled in the so-called sarcomeres. The energy carrier for this actin–myosin interaction, the so-called cycling of cross-bridges or actin-activated myosin II ATPase cycle, is adenosine triphosphate (ATP), which is produced in the mitochondria by oxygenation of nutrients. Force generation in myocytes is initiated and controlled by electrical activity of the cell. The signal transduction from electrical activity to force generation is based on calcium fluxes. Processes underlying this signaling are summarized by the term excitation-contraction coupling (ECC).

Electrical signaling in cardiac tissue can be observed at various levels: (1) At myocyte level, electrical signaling initiates and controls contractility. The primary electrical signal initiating ECC is the depolarization of the myocyte membrane (sarcolemma). Various proteins in the sarcolemma, internal membranes, and intracellular compartments contribute to electrical signaling and ECC. (2) At level of cell clusters, coupling via so-called gap junction channels in the sarcolemma serves for synchronizing electrical and mechanical activity of neighboring myocytes.

Gap junction channels provide for low-resistance electrical pathways between myocytes. (3) At macroscopic level, electrical signaling enables synchronized activity of different compartments of the heart. The structural basis for this synchronization of compartments comprises the excitation and conduction system composed of specialized myocytes, e.g., the sinoatrial and atrioventricular node, bundle branches, and Purkinje fibers.

Myocytes of the excitation and conduction system are structurally and functionally distinct from myocytes of the working myocardium. The latter are the major force generators in the heart. Myocytes of the ventricular myocardium are cylindrically shaped with irregular, flat ends. Locally, these cells are commonly aligned in such a manner that their long axes are parallel. Mammalian ventricular myocytes exhibit invaginations of the sarcolemma, the so-called transverse tubular system [10, 42], which serves for synchronization of ECC and is the site of multiprotein signaling complexes. Volume and length of atrial myocytes are, in general, smaller. While differences of myofilament volume density between atrial and ventricular myocytes are small, ventricular myocytes exhibit a significantly larger volume density of mitochondria.

Fibroblasts are by number the dominant cells in many types of cardiac tissue [66]. Their volume is much smaller than myocyte volume. For instance, in rat ventricle, the ratio of myocyte to fibroblast volume was estimated to be 59.7:1 [56]. Their functional role is primarily production of extracellular matrix (ECM) proteins such as collagen and elastin. Some cardiac pathophysiologies, e.g., myocardial infarction and inflammation, are associated with activation of fibroblasts and alterations of their phenotype. Fibroblast activation can lead to fibrosis, hypertrophy, and heart failure. Fibroblasts, in contrast to myocyte, are nonexcitable but can be electrically coupled to myocytes and thus contribute to tissue electrophysiology in various manners.

The space between cardiac cells is called the interstitial space. Interstitial fluid and the ECM occupy it. The fluid is transport medium for nutrients, metabolites, salts, hormones, enzymes, and neurotransmitters. The interstitial space is connected via clefts in the endothelium of capillaries with the vascular space, which enables flux of plasma into and out of interstitial space primarily due to pressure gradients.

3.3 Cardiovascular Diseases and Cellular Phenotype

Various diseases affect the heart. These can be caused extrinsically (outside of the heart) or intrinsically. They can affect all regions of the heart including coronary arteries, valves, and muscle. In this overview, we focus on genetic diseases, congenital heart defects, and coronary artery diseases.

Gene mutations can cause a variety of cardiac diseases [3]. Mutations in the coding region of a protein can affect its function, e.g., loss or gain of function, and/or trafficking. Mutations in the promoter region of a protein can cause its overexpression or underexpression. Ion-channel mutations (channelopathies) and their effects on cellular and tissue electrophysiology are extensively examined in clinical

and basic research. A plethora of mutations of cardiac ion channels have been identified, which are associated with symptoms including sudden cardiac death, atrial fibrillation, and developmental abnormalities. For instance, mutations of the gene SCN5A, which encodes the alpha subunit of the voltage-gated sodium channel underlying fast inward sodium current, are accounted for the Brugada, Romano–Ward, and related arrhythmia syndromes [3, 52]. Loss-of-function KCNJ2 mutations underlie the Andersen–Tawil syndrome [49, 62]. The KCNJ2 gene encodes Kir2.1 subunits, which assemble homotetramerically or heterotetramerically with other Kir2.x subunits to form channels that conduct the inward rectifier potassium current. KCNQ1 gain-of-function mutations can cause atrial fibrillation and short QT syndrome [24]. Coassembly of KCNQ1 and KCNE1 subunits forms ion channels that conduct the slow delayed rectifier potassium current. Similarly, loss- and gain-of-function KCNH2 mutations can cause long and short QT syndrome, respectively [48, 58]. KCNH2 encodes the alpha subunit of ion channels conducting the delayed rectifier cardiac potassium current. The rare Timothy syndrome is caused by mutations of CACNA1C gene [67], which encodes the L-type calcium channel $Ca_v1.2$ alpha-1 subunit. The mutations affect inactivation of the ion channel, which plays a major role in ECC of cardiac myocytes [68]. Timothy syndrome is associated with arrhythmias and structural defects of the heart. Several mutations have been identified, which indirectly modulate ion channel function. These mutations are in regulatory proteins, e.g., phospholamban and junctin, and scaffolding proteins, e.g., A-kinase-anchoring proteins and ankyrin-B.

Genetic causes can also underlie congenital heart defects, which reflect abnormalities of heart development and are present at birth. Also, virus infections and environmental conditions have been suggested to cause congenital heart defects. In most cases, however, the cause of congenital heart defects is not known. Open heart reconstructive surgery in the neonatal period is the state-of-the-art approach to repair heart defects including hypoplastic left heart syndrome, Tetralogy of Fallot, transposition of great arteries, and truncus arterious [69]. Untreated congenital heart defects can lead to heart failure.

Coronary artery disease is the most common type of CVDs. It is typically caused by plaque buildup in the vessels that supply the heart muscle. This process termed atherosclerosis can lead to stiffening of the vessel wall, stenosis and even complete blocking of the vessels. Increased risk of coronary artery disease is associated with diabetes, high blood pressure, smoking, alcohol abuse, and abnormal cholesterol levels. Treatment options include lifestyle modifications, risk factor management, pharmacologic therapy, and surgical interventions such as coronary artery bypass graft surgery, angioplasty, and stenting. Coronary artery disease can lead to myocardial ischemia, infarction, and congestive heart disease. Myocardial ischemia has significant implications on cellular metabolism, electrophysiology, and viability, in particular, of myocytes with high metabolic demand. Prolonged interruption of blood flow, due to coronary artery disease or other reasons, causes apoptosis and necrosis.

In the past, studies on disease-associated remodeling of heart anatomy and function were focused on characterizing alterations at macroscopic level. Newer concepts of cardiac remodeling focus on the pivotal role of remodeling at microscopic

level. These concepts suggest that remodeling of metabolism, structure, and function at microscopic level constitute the basic mechanisms underlying macroscopic remodeling and heart failure. Structural remodeling at microscopic level includes altered shape, volume, and arrangement of cells and cellular compartments as well as density and distribution of proteins. For instance, in a canine model of pacing-induced heart failure, myocytes exhibited increased size, decreased density of L-type calcium channels, and an irregular, sparse t-system [19]. Similar alterations of the t-system have been reported in chronically ischemic porcine myocytes [22] and indicated for failing human myocytes [31, 33, 39, 73].

Diseased associated functional remodeling at cellular level include altered electrical and ECC signaling. Various changes in the action potential shape result from alterations in the expression and function of proteins in diseased cells. Prominent causes for these alterations are genetic diseases that were discussed previously in this section. However, alterations can also be a consequence of other disease types. For instances, reduction of potassium currents is a common theme in hypertrophied and failing ventricular myocardium in animals models. In these disease models, hypertrophy and heart failure were induced by pacing protocols, surgical, and pharmacological interventions. Several studies demonstrated that ECC is altered in diseased cells. For instance, calcium events are dyssynchronous in failing myocytes [22, 39].

3.4 Imaging of Cardiac Cells

Optical microscopy is the major imaging modality in studies at cellular scale. A general advantage of this modality is that it allows for imaging of living preparations [15]. Here, we focus on scanning confocal microscopy [9], which offers three-dimensional imaging of cellular structure and function at sub-micrometer resolution. Confocal microscopy necessitates a fluorescent dye or autofluorescent material in the imaged region. Fluorescent dyes or materials can be excited by light, e.g., from a laser, of a specific wavelength, which causes emission of light of a different wavelength. Some dyes can be attached to molecules such as antibodies.

The spatial resolution, i.e., separability of neighboring objects in the image data, is much higher with confocal microscopy systems than with standard optical microscopes. Nevertheless, the spatial resolution of confocal systems can still pose difficulties in image analysis depending on the size and shape of imaged structures. A measure of the separability is the Rayleigh criterion. Resolution can be estimated by analysis of the response of an imaging system to given signal sources.

In general, the response g of a confocal (or other) imaging system to given sources can be described by convolution of the sources f with the point spread function (PSF) h and the space vector $\mathbf{x}$ [20]:

$$g(x) = (f \times h)(x) = \iiint_{-\infty}^{\infty} f(x')h(x - x')\mathrm{dx}'. \tag{3.1}$$

In this approximation, it is assumed that the response is linear and invariant with respect to translation. The resolution can be derived from measured PSFs [5], which are the image of a subresolution region of fluorescent dye, for instance, glass beads with a diameter of <0.1 μm and surface coated with dye. PSFs of confocal systems typically display directional anisotropy with the full width at half maximum 2–3 times larger in direction of the laser beam than orthogonal to it [5, 59, 60, 64]. Spatial resolutions of state-of-the-art confocal systems are ~0.3 μm in horizontal (orthogonal to the laser) and ~1 μm in vertical (parallel to the laser) direction for excitation and emission wavelengths close to 500 nm and using a lens with a numerical aperture of 1.4.

A limitation of confocal microscopy is depth-dependent attenuation of signal intensity. This attenuation is an inherent property of confocal imaging systems. It can be described as a function of attenuation coefficients for exciting light α_{exc} and emitted light α_{emi}:

$$\ln \frac{I(0)}{I(z)} = (\alpha_{exc} + \alpha_{emi})z \tag{3.2}$$

with the depth z. Commonly, wavelengths and thus attenuation coefficients of the exciting and emitted light differ. Some confocal imaging systems allow for automated attenuation correction.

Various fluorophores are available for labeling of cellular structures and proteins [15]. A natural fluorophore is green fluorescent protein (GFP), which is expressed in jellyfish. GFP can be added or inserted to the coding sequence of proteins, which allows for imaging of expression, trafficking and localization of these GFP fusion proteins. Man-made fluorophores include fluorescein isothiocyanate (FITC) and the Alexa, Rhodamine, and DyLight Fluor families. Fluorophores can be conjugated to various molecules including antibodies for labeling of proteins and dextran of different molecular weights. The latter is membrane impermeable and allows for labeling of the extracellular space.

Structural labeling approaches have been complemented with functional labeling, e.g., of membrane voltage, intracellular calcium, and pH. Di-4-anepps and di-8-anepps are well-established membrane voltage-sensitive dyes, which respond with a ~10% intensity change per 100 mV [11, 17]. Fura-2 and Indo-1 are popular indicators of the intracellular calcium concentration [18]. SNARF-1 allows for imaging of intracellular pH [4, 8].

Recent confocal microscopy systems enable simultaneous imaging of several fluorophores, e.g., to study colocalization of proteins and structures. Separation of the fluorophores is possible due to differences in the wavelengths of their excitation and/or emissions. Excitation of fluorophores can be simultaneously or individually. Further separation of fluorophores can be achieved by filtering of emitted light, e.g., with absorptive and dichroic filters. These approaches are, in particular, useful for acquisition of structural together with functional information.

3.5 Modeling of Cardiac Cells

3.5.1 Functional Modeling

3.5.1.1 Development and Implementation of Functional Models

In general, the first step in development of a functional model of cardiac (and other) cells is its design, which can be based on biophysical, experimental and theoretical insights. Most often, existing models are selected, extended or integrated for development of a new model. Selection of the model is commonly based on its ability in reconstruction of the measured data, assumed similarity between the existing model and model in development, feasibility of implementation, and computational demands.

The next step in model development is the parameterization of the model components. Only some simple models allow parameterization by direct calculation based on features in measured data. The parameterization is commonly an optimization problem, which requires the definition of a cost function describing the fit of simulated data to given data. Commonly, the parameterization is performed with numerical approaches. Typical numerical approaches include the steepest decent, conjugate gradient, Nelder–Mead method, and simulated annealing [50]. Simulated annealing is a stochastic method capable of revealing the global minimum of a cost function also in cases where it exhibits many local minima. Recently, a further stochastic optimization technique, the particle swarm optimization, has been suggested for model parameterization [63]. All these methods require frequent execution of the model with varying parameters. Model parameterization can be a time consuming process. The quality of its results is dependent on the ability of the model in reconstruction of the measured data and their quality.

Most models of cell function consist of sets of ordinary differential equations, which are solved with numerical methods, for instance, Euler and Runge–Kutta methods [50]. For solving models that are based on partial differential equations, finite difference and finite element methods are the most common numerical approaches [53].

3.5.1.2 Models of Cardiac Cells

Electrophysiological modeling of cardiac cells is an established field of research [53]. Electrophysiological models provide a mathematical description of ion transport through membranes and between cellular compartments and allow for reconstruction of measured data such as membrane currents and voltages. A major motivation to develop these descriptions has been to test hypotheses on basic biophysical mechanisms underlying electrical signaling in cardiac cells, either in an a-posteriori manner to explain experimental data or in a predictive manner to probe cellular behavior under specific conditions.

Commonly, electrophysiological models of cardiac cells are not created from scratch, but by re-parameterization and integration of existing models of ion channels, transporters and exchangers, e.g., the established Hodgkin–Huxley or Markov models of ion channels. The parameterization of electrophysiological cell models is commonly based on data measured using a variety of experimental preparations and techniques. Experimental techniques include whole-cell and patch-clamp approaches. Standard experimental preparations are native cells isolated from tissue, membrane patches, and protein expression systems such as bacteria, yeast, and frog oocytes.

Electrophysiological models have been developed for a variety of cardiac cells including ventricular and atrial myocytes [28, 40], Purkinje cells [70], sinus and atrioventricular node cells [26], and fibroblasts [56]. Some of these models reconstruct electrophysiology of human myocytes (Fig. 3.1). The models integrate descriptions of major currents through membrane proteins. These models can serve as a basis for personalized modeling, in particular, of diseased cells, by parameter adjustment and/or replacement of model components.

Electrophysiological cell models constitute a major tool to study effects of ion channel mutations. Commonly, an existing model is adjusted by either reparameterization or substitution of model components that describe the affected protein. For instance, effects of Timothy syndrome have been modeled by reparameterization of a model component describing currents through $Ca_v1.2$ channels, in particular, with respect to the disease caused voltage-dependent inactivation of these ion channels [68]. Short QT and other effects related to a KCNH2 gain of function mutation have

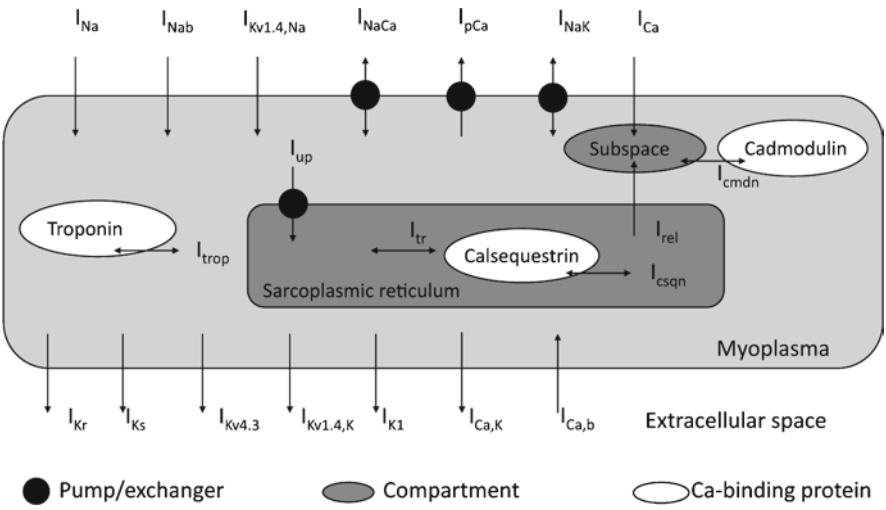

Fig. 3.1 Schematic of electrophysiological model of human ventricular myocyte [28]. Ion currents are depicted by *arrows*. The model includes descriptions of sodium, potassium, and calcium currents through the membrane. Furthermore, the model specifies calcium currents between intracellular compartments and calcium binding to various proteins

been studied by re-parameterization of the related model component [72]. Effects of the Andersen–Tawil syndrome on cellular and tissue electrophysiology have been studied in a human electrophysiological cell model by substitution of its Kir2.x current model [49, 62]. A difficulty of this approach is related to potential cellular remodeling in response to the mutation. This remodeling is commonly not characterized, and thus, its effects on cellular electrophysiology are not considered in most experimental studies.

Models of ECC in cardiac myocytes describe a signaling cascade starting with electrical activation and causing force development in the myofilaments followed by cell contraction. Most models implement a mechanism called calcium-induced calcium release, which is based on the experimental findings that extracellular calcium ions carried by voltage-gated L-type calcium channels into the cell interior can trigger calcium release from the sarcoplasmic reticulum through ryanodine receptors (RyRs). Models differ significantly in their focus, scale, and detail in reconstructing the ECC signaling cascade. Biophysically detailed models off ECC have been developed to describe the unit events underlying calcium transients, i.e., sparks produced by calcium release from the sarcoplasmic reticulum through RyR channels. Some models of ECC have a partial overlap with electrophysiological and force development models as those typically include a description of calcium transients and binding of calcium to troponin C (Figs. 3.1 and 3.2).

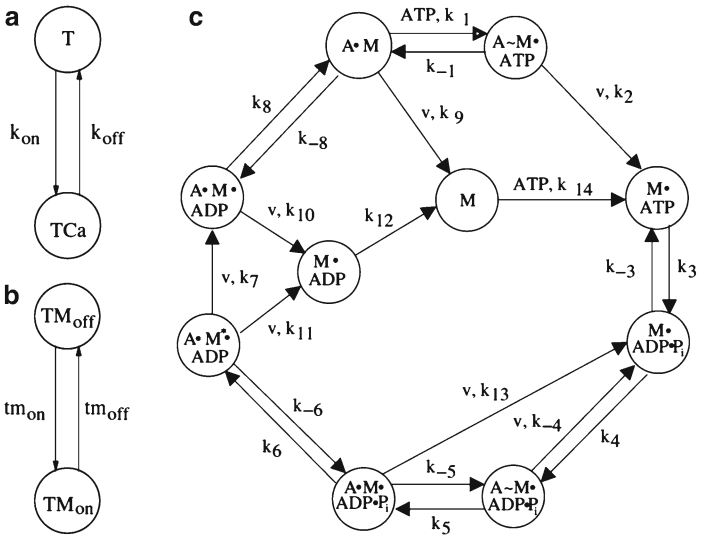

Fig. 3.2 State diagram of a biophysically detailed model of force development [55]. (**a**) Two state variables, T and TCa, describe the calcium binding to troponin C. (**b**) Two state variables, TM_{on} and TM_{off}, describe the configuration of tropomyosin. (**c**) Ten state variables detail the actin–myosin interaction and ATP hydrolysis. M and A symbolize myosin and actin, respectively. ATP, ADP, and P_i represent adenosine triphosphate, adenosine diphosphate, and phosphate, respectively. States transitions are depicted by *arrows*, strong binding by a *closed circle*, and weak binding by a *tilde*. The *arrows* are labeled with rates coefficients, which are functions of e.g. ATP concentration, cross-bridge density XB, and sarcomere stretch velocity

Biophysically realistic models of cellular force generation apply the calcium transient as modulator for actin–myosin interactions. Models differ in their level of detail in the description of the underlying processes. Detailed models describe cellular force generation starting with the binding of calcium to troponin C resulting in shifting of the troponin–tropomyosin complex followed by structural changes of the tropomyosin–actin configuration, which allow the binding of myosin heads to actins. Simplified models lump and/or neglect some of these processes. An example for a detailed model is shown in Fig. 3.2 [55]. The model has three compartments, which cover the binding of intracellular calcium to troponin C, conformational changes of tropomyosin, and the actin–myosin interactions. The model applies as input the concentration of intracellular calcium, the sarcomere stretch, and the sarcomere stretch velocity. Major model output is the normalized cellular tension. Furthermore, the model provides information on protein state probabilities, calcium binding to troponin C, and ATP hydrolysis.

Integration of the described models allows for comprehensive description of cellular physiology. An example is the integration of electrophysiological and force generation models, which can be used to study effects of electrophysiological alterations, such as mutations of ion channels and related to pharmacologic therapy, on force generation. Integration of models, e.g., of electrical conduction and passive mechanics of tissue, allows for description of processes beyond the cellular scale toward modeling of a complete organism. Major challenges of model integration include design and implementation of mode interfaces, efficient numerical solution of combined models, and handling of model inconsistencies. An example for inconsistencies in a combined electrophysiological and force generation model is the multiple but different description of calcium binding to troponin C. Resolution of this type of inconsistency might necessitate model adaption or redesign.

Most functional models have been implemented in programming languages such as Fortran, C, and Matlab. Specialized languages have been developed for model implementation, for instance, the languages CellML [35, 36] and SBML [25], both based on the XML markup language. Software packages for cellular modeling and simulation include CESE [44], COR [13], JSim [30], Neuron [7], OpenCell (formerly PCEnv) [47], QuB [43], and Virtual Cell [61]. The list includes tools originally developed for modeling of ion channels and various cell types beyond those found in the heart.

3.5.2 Structural Modeling

3.5.2.1 Development of Structural Models

This section describes image-based approaches for structural modeling of cardiac cells. The focus is on data from confocal microscopy, which are applied to reconstruct imaged objects using methods of digital image processing. Confocal microscopy has limitations with respect to spatial resolution, signal-to-noise ratio, and

depth-dependent signal attenuation. Image processing can be applied to improve image quality [59]. The section starts with an introduction of image processing techniques, which are typically performed before application of the data in development of structural models and quantitative image analysis. Typical formats for the processing and application of image data are introduced.

3.5.2.2 Image Processing

Imaging can be described as convolution of spatially distributed signal sources with a PSF (Eq. 3.1). Various methods for deconvolution of image data exist including Wiener and Fourier filtering, least squares regularization, and Bayesian approaches [6]. A standard approach is the iterative Richardson–Lucy algorithm [51]. Implementations of deconvolution algorithms are available in Matlab (The Mathworks, Inc., Natick, MA) and specialized packages for microscopic image data processing, e.g., Volocity (Perkin Elmer, MA), Huygens (Scientific Volume Imaging, The Netherlands), and Autoquant X (Media Cybernetics, Bethesda, MD).

Image data can exhibit background intensities that do not stem from the labeled proteins or structures. The background intensities can be caused by autofluorescence and offsets in the signal detection and amplification of the imaging system. Common image processing strategies to remove background intensities include their regionwise detection, interpolation of the intensities over the image volume, and their subtraction from the image intensities.

Depth-dependent attenuation of signal intensity is a process that affects both excitation and emitted light (3.2). It can be measured by analysis of signal intensities measured along the laser beam direction in image regions that were homogeneously labeled and should exhibit identical densities of the fluorescent marker. Intensities along this direction can be fit to a mono- or biexponential function. This procedure yields a slicewise scaling depth-dependent factor.

Various approaches exist for segmentation of image data [16, 53]. The segmentation of microscopic images of cardiac cells and tissues yields regions that typically consist of cells, membranes, cellular compartments, or protein clusters. A simple approach to segmentation is thresholding of the image intensities. The approach yields segments, which are either within or outside of the thresholds. More advanced approaches include region growing, which iteratively assembles image segments starting from given points. The points identify image segments, which are then extended using thresholding in their neighborhood. Commonly, the approaches are applied on filtered images to reduce effects of image artifacts, in particular noise, on the segmentation procedure. The repertoire of approaches includes manual segmentation methods such as interactively deformable surfaces.

Image analysis methods range from simple counting of image segments and integration of signal intensities to complex tasks such as pattern recognition and topological characterization of image segments. Analysis of images from confocal microscopy can yield quantitative information on cells and their microstructure as

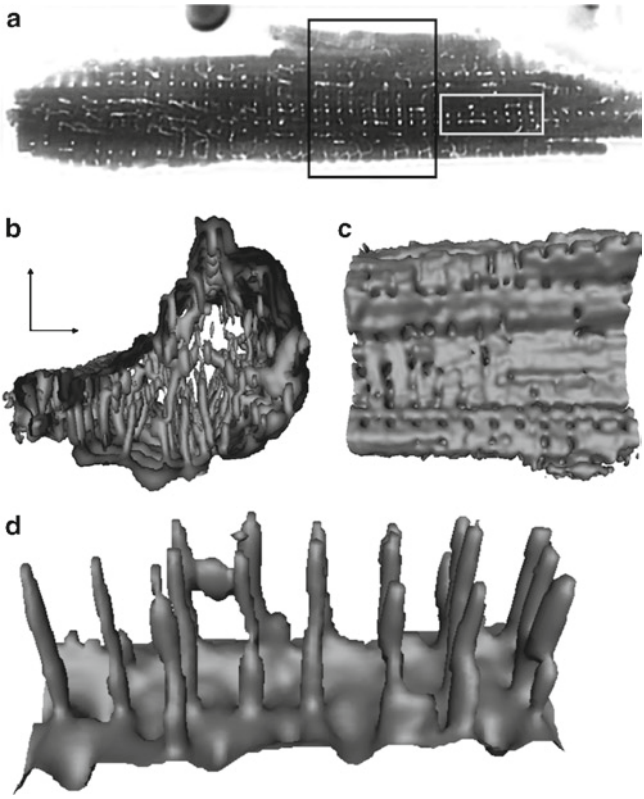

Fig. 3.3 Microstructure of cardiac ventricular myocytes [60]. (**a**) Cross-sectional image showing the transverse tubular system in an isolated cell. (**b**) 3D visualization of cell interior reveals the arrangement of the transverse tubular system. (**c**) A view from exterior on the sarcolemma indicates that t-tubule opening are partly regularly organized. (**d**) Some regions exhibit regularly spaced t-tubules of simple topology

well as on protein densities and their spatial distribution. Quantitative information that can be extracted from segmented images of cardiac cells and tissue includes geometrical parameters of the transverse tubular system (Fig. 3.3), such as length, diameter, and volume of tubules [60], and of the myocytes, such as their length, width, height, and volume [34] (Fig. 3.4). Image analysis can also yield information on protein distributions, e.g., of caveolin-3, sodium–calcium exchange, and RyRs [29, 57, 65].

Of particular interest with respect to patient-specific modeling is the data that can be used in the parameterization and validation of functional models. These data provide the basis for modeling of disease states, which can be associated with significant alterations of cell structure and protein distributions.

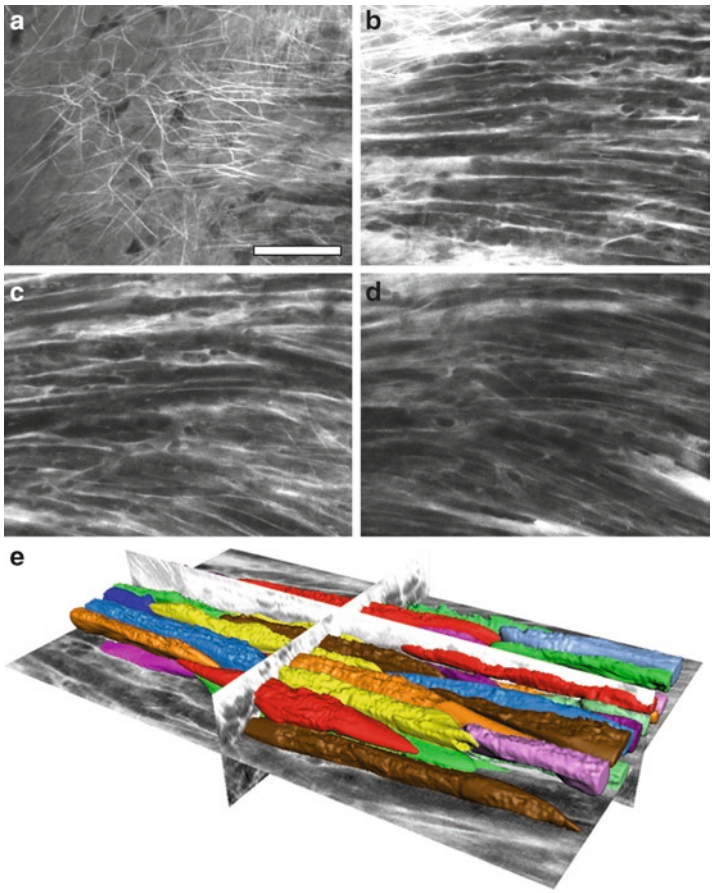

Fig. 3.4 Imaging and modeling of cardiac tissue [34]. The microscopic images are from (**a**) the epicardial surface and a depth of (**b**) 10 μm, (**c**) 20 μm, and (**d**) 30 μm into atrial myocardium. (**e**) A model of atrial myocyte cluster was created from the three-dimensional image stack. The model includes 17 complete and 21 partial myocytes. Scale: 50 μm in (**a**) applies to (**a–d**)

3.5.2.3 Model Representation

Confocal imaging systems commonly export image data in two- and three-dimensional matrices. Generally, results of image processing are provided in this format. Other formats can be more efficient with regard to applications in modeling and simulation. A common format in many applications in image processing and biomedical modeling is the cubic voxel mesh, which can be directly derived from the image matrices and allows for simple conversion to models of various spatial resolutions. A frequently applied format type for visualization of models are surface meshes, e.g., with triangular elements generated with the marching cubes algorithm [38].

The algorithm generates meshes of triangles approximating isointensity surfaces with subvoxel resolution. Modifications of the original algorithm assured closeness of the generated surfaces and permitted subvoxel resolution by adjusting positions of mesh nodes based on edge-wise interpolation of intensities [21]. Further formats for model representation include point sets and meshes of finite elements of variable size and polynomial degree.

3.6 Clinical Perspective

Commonly, modeling of cardiac cells is based on data from animal experimental studies. Most of these experimental studies are based on the excision of the heart followed by dissection or cell isolation procedures using enzymes such as collagenase and protease. Of specific interest for patient-specific modeling of cardiac cells and clinical applications are biopsy techniques, which allow for minimal-invasive extraction of samples from a patient's heart. A variety of myocardial biopsy techniques are established in clinical diagnosis. Biopsies can be performed during cardiac catheterization or surgical procedures. Samples obtained by myocardial biopsy can be labeled and imaged using the methods described above.

Alternatives to biopsy techniques are approaches for labeling and imaging of cells and tissues that can be applied in situ and in vivo. Fiber-optics confocal microscopes have been developed for applications ranging from in situ imaging in small animals to clinical diagnosis of various diseases [1, 2, 12, 14, 23, 27, 45]. Difficulties of their application for imaging of cells and tissues in situ are related to the complicated access to organs inside of a body, the small depth penetration of confocal imaging, and the necessity to provide for fluorescent dyes in the imaged region. Combination of fiber-optics microscopy with endoscopic and catheter technology allows for steering of imaging probes into a patient's heart. Methods for fluorescent labeling and local dye delivery have been developed, which can be applied to provide information on structure and function of living cardiac cells and tissues at submicrometer resolution (Figs. 3.4 and 3.5) [34].

Advancements in various aspects of patient-specific modeling of cells can be expected by high-throughput DNA-sequencing platforms [41]. These are now commercially available and allow for subject-specific screening of mutations and polymorphisms. The genomic data can be applied for characterization of functional and structural consequences of these mutations and polymorphism using experimental approaches. For instance, functional consequences of ion-channel mutations can be characterized using site-directed mutagenesis [32], systems for protein expression in cells, and whole-cell voltage clamping systems [71]. Site-directed mutagenesis allows for creation of a defined mutation in the coding region of an ion channel protein. The protein is then expressed in a cell, e.g., frog oocyte. Patch-clamp techniques are applied to characterize electrophysiological properties of the ion channel.

Advancements in imaging, image processing, and screening technology indicate that cellular cardiac modeling will soon reach out beyond its established role as a research tool and establish a new role in clinical diagnosis and therapy. Several data

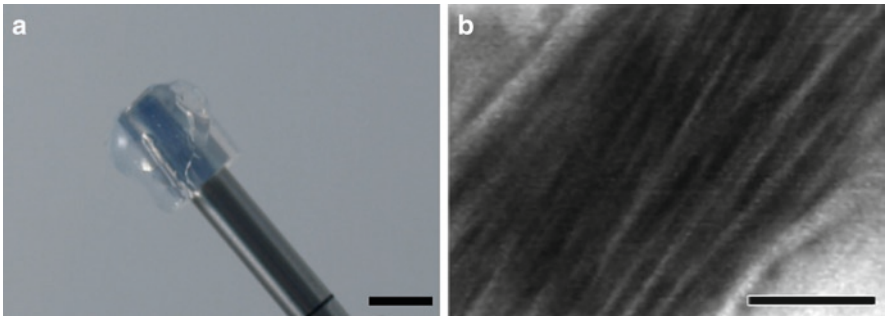

Fig. 3.5 Imaging of microstructure of cardiac tissue with fiber-optics confocal microscopy system (Leica FCM 1000) [34]. (**a**) A dye carrier was attached to a confocal microprobe (M/30). The dye carrier consists of hydrogel loaded with fluorescent dye. (**b**) Image of atrial tissue acquired with the modified microprobe. Scale: 5 mm in (**a**) and 50 μm in (**b**)

sources can provide input for patient-specific modeling of cardiac cells. Image data obtained from myocardial biopsy samples and catheter-based confocal microscopy can be processed using the previously described methods to yield parameters and geometries for modeling. DNA-sequencing platforms can identify mutations and polymorphisms in a patient. Functional consequences of a number of mutations have been already established and described in models.

Major challenges in the integration of patient-specific cellular modeling into a clinical environment are associated with patient safety and assessing its benefits versus costs. The development of clinically feasible protocols for data acquisition, analysis, and interpretation will be crucial. It can be expected that establishing this new technology will require extensive training of medical personnel. It will necessitate that most of the processes underlying model generation and simulation are automated. Most methods used in these processes, e.g., digital image processing and computational modeling of cellular electrophysiology, are already well established in applications beyond academic research. However, usage in clinical applications will require careful validation of the methods and assessment of their limitations.

Acknowledgments This work has been supported by National Heart, Lung, and Blood Institute grant R01 HL094464, the Richard A. and Nora Eccles Fund for Cardiovascular Research, and awards from the Nora Eccles Treadwell Foundation.

References

1. Anandasabapathy, S. 2008b. Novel endoscopic techniques for the detection of Barrett's dysplasia. *Gastrointest Cancer Res,* 2**,** 81–4.
2. Anandasabapathy, S. 2008a. Endoscopic imaging: emerging optical techniques for the detection of colorectal neoplasia. *Curr Opin Gastroenterol,* 24**,** 64–9.
3. Ashcroft, F. M. 2000. *Ion channels and disease*, San Diego, CA, Academic Press.

4. Bassnett, S., Reinisch, L. & Beebe, D. C. 1990. Intracellular pH measurement using single excitation-dual emission fluorescence ratios. *Am J Physiol Cell Physiol,* 258(27)**,** C171–8.
5. Bolte, S. & Cordelieres, F. P. 2006. A guided tour into subcellular colocalization analysis in light microscopy. *J Microsc,* 224**,** 213–32.
6. Boutet de Monvel, J., Le Calvez, S. & Ulfendahl, M. 2001. Image restoration for confocal microscopy: improving the limits of deconvolution, with application to the visualization of the mammalian hearing organ. *Biophys J,* 80**,** 2455–70.
7. Brette, R., Rudolph, M., Carnevale, T., Hines, M., Beeman, D., Bower, J. M., Diesmann, M., Morrison, A., Goodman, P. H., Harris, F. C., Jr., Zirpe, M., Natschlager, T., Pecevski, D., Ermentrout, B., Djurfeldt, M., Lansner, A., Rochel, O., Vieville, T., Muller, E., Davison, A. P., El Boustani, S. & Destexhe, A. 2007. Simulation of networks of spiking neurons: a review of tools and strategies. *J Comput Neurosci,* 23**,** 349–98.
8. Buckler, K. J. & Vaughan-Jones, R. D. 1990. Application of a new pH-sensitive fluoroprobe (carboxy-SNARF-1) for intracellular pH measurement in small, isolated cells. *Pflüger? Arch,* 417**,** 234–9.
9. Diaspro, A. 2002. *Confocal and two-photon microscopy: foundations, applications, and advances,* New York, Wiley.
10. Fawcett, D. W. & McNutt, N. S. 1969. The ultrastructure of the cat myocardium. I. Ventricular papillary muscle. *J Cell Biol,* 42**,** 1–45.
11. Fluhler, E., Burnham, V. G. & Loew, L. M. 1985. Spectra, membrane binding, and potentiometric responses of new charge shift probes. *Biochemistry,* 24**,** 5749–55.
12. Flusberg, B. A., Cocker, E. D., Piyawattanametha, W., Jung, J. C., Cheung, E. L. M. & Schnitzer, M. J. 2005. Fiber-optic fluorescence imaging. *Nat Methods,* 2**,** 941–50.
13. Garny, A., Noble, D., Hunter, P. J. & Kohl, P. 2009. CELLULAR OPEN RESOURCE (COR): current status and future directions. *Philos Transact A Math Phys Eng Sci,* 367**,** 1885–905.
14. Goetz, M., Hoffman, A., Galle, P. R., Neurath, M. F. & Kiesslich, R. 2006. Confocal laser endoscopy: new approach to the early diagnosis of tumors of the esophagus and stomach. *Future Oncol,* 2**,** 469–76.
15. Goldman, R. D. & Spector, D. L. 2005. *Live cell imaging, a laboratory manual,* Cold Spring Harbor, NY, Cold Spring Harbor Laboratory Press.
16. Gonzalez, R. C. & Woods, R. E. 1992. *Digital image processing,* Reading, MA, Addison-Wesley.
17. Gross, E., Bedlack, R. S., Jr. & Loew, L. M. 1994. Dual-wavelength ratiometric fluorescence measurement of the membrane dipole potential. *Biophys J,* 67**,** 208–16.
18. Grynkiewicz, G., Poenie, M. & Tsien, R. Y. 1985. A new generation of Ca^{2+} indicators with greatly improved fluorescence properties. *J Biol Chem,* 260**,** 3440–50.
19. He, J. Q., Conklin, M. W., Foell, J. D., Wolff, M. R., Haworth, R. A., Coronado, R. & Kamp, T. J. 2001. Reduction in density of transverse tubules and L-type Ca^{2+} channels in canine tachycardia-induced heart failure. *Cardiovasc Res,* 49**,** 298–307.
20. Hecht, E. 1987. *Optics*, Reading, MA, Addison-Wesley Publishing Company.
21. Heiden, W., Goetze, T. & Brickmann, J. 1991. 'Marching-Cube'-Algorithmen zur schnellen Generierung von Isoflaechen auf der Basis dreidimensionaler Datenfelder. *In:* Fruehauf, M. & Goebel, M. (eds.) *Visualisierung von Volumendaten.* Berlin, Heidelberg, New York: Springer.
22. Heinzel, F. R., Bito, V., Biesmans, L., Wu, M., Detre, E., von Wegner, F., Claus, P., Dymarkowski, S., Maes, F. & Bogaert, J. 2008. Remodeling of T-tubules and reduced synchrony of Ca^{2+} release in myocytes from chronically ischemic myocardium. *Circ Res,* 102**,** 338–46.
23. Hoffman, A., Goetz, M., Vieth, M., Galle, P. R., Neurath, M. F. & Kiesslich, R. 2006. Confocal laser endomicroscopy: technical status and current indications. *Endoscopy,* 38**,** 1275–83.
24. Hong, K., Piper, D. R., Diaz-Valdecantos, A., Brugada, J., Oliva, A., Burashnikov, E., Santos-de-Soto, J., Grueso-Montero, J., Diaz-Enfante, E., Brugada, P., Sachse, F., Sanguinetti, M. C. & Brugada, R. 2005. De novo KCNQ1 mutation responsible for atrial fibrillation and short QT syndrome in utero. *Cardiovasc Res,* 68**,** 433–40.

25. Hucka, M., Finney, A., Sauro, H. M., Bolouri, H., Doyle, J. C., Kitano, H., Arkin, A. P., Bornstein, B. J., Bray, D., Cornish-Bowden, A., Cuellar, A. A., Dronov, S., Gilles, E. D., Ginkel, M., GOR, V., Goryanin, II, Hedley, W. J., Hodgman, T. C., Hofmeyr, J. H., Hunter, P. J., Juty, N. S., Kasberger, J. L., Kremling, A., Kummer, U., Le Novere, N., Loew, L. M., Lucio, D., Mendes, P., Minch, E., Mjolsness, E. D., Nakayama, Y., Nelson, M. R., Nielsen, P. F., Sakurada, T., Schaff, J. C., Shapiro, B. E., Shimizu, T. S., Spence, H. D., Stelling, J., Takahashi, K., Tomita, M., Wagner, J. & Wang, J. 2003. The systems biology markup language (SBML): a medium for representation and exchange of biochemical network models. *Bioinformatics,* 19**,** 524–31.
26. Inada, S., Hancox, J. C., Zhang, H. & Boyett, M. R. 2009. One-dimensional mathematical model of the atrioventricular node including atrio-nodal, nodal, and nodal-his cells. *Biophys J,* 97**,** 2117–27.
27. Inoue, H., Kudo, S. E. & Shiokawa, A. 2004. Novel endoscopic imaging techniques toward in vivo observation of living cancer cells in the gastrointestinal tract. *Dig Dis,* 22**,** 334–7.
28. Iyer, V., Mazhari, R. & Winslow, R. L. 2004. A computational model of the human left-ventricular epicardial myocyte. *Biophys J,* 87**,** 1507–25.
29. Jayasinghe, I. D., Cannell, M. B. & Soeller, C. 2009. Organization of ryanodine receptors, transverse tubules, and sodium–calcium exchanger in rat myocytes. *Biophys J,* 97**,** 2664–73.
30. JSIM. 2010. *JSim Home Page* [Online]. Available: http://nsr.bioeng.washington.edu/jsim/ [Accessed].
31. Kaprielian, Z., Imondi, R. & Runko, E. 2000. Axon guidance at the midline of the developing CNS. *Anat Rec,* 261**,** 176–97.
32. Karp, G. 2005. *Cell and molecular biology: concepts and experiments*, Hoboken, NJ, Wiley.
33. Kostin, S., Scholz, D., Shimada, T., Maeno, Y., Mollnau, H., Hein, S. & Schaper, J. 1998. The internal and external protein scaffold of the T-tubular system in cardiomyocytes. *Cell Tissue Res,* 294**,** 449–60.
34. Lasher, R. A., Hitchcock, R. W. & Sachse, F. B. 2009. Towards modeling of cardiac microstructure with catheter-based confocal microscopy: a novel approach for dye delivery and tissue characterization. *IEEE Trans Med Imaging,* 28**,** 1156–64.
35. Lloyd, C. M., Halstead, M. D. & Nielsen, P. F. 2004. CellML: its future, present and past. *Prog Biophys Mol Biol,* 85**,** 433–50.
36. Lloyd, C. M., Lawson, J. R., Hunter, P. J. & Nielsen, P. F. 2008. The CellML model repository. *Bioinformatics,* 24**,** 2122–3.
37. Lopez, A. D., Mathers, C. D., Ezzati, M., Jamison, D. T. & Murray, C. J. L. 2006. *Global burden of disease and risk factors*, New York, Oxford University Press.
38. Lorensen, W. E. & Cline, H. E. 1987. Marching cubes: a high resolution 3d surface construction algorithm. *Comput Graph,* 4**,** 163–9.
39. Louch, W. E., Bito, V., Heinzel, F. R., Macianskiene, R., Vanhaecke, J., Flameng, W., Mubagwa, K. & Sipido, K. R. 2004. Reduced synchrony of Ca^{2+} release with loss of T-tubules – a comparison to Ca^{2+} release in human failing cardiomyocytes. *Cardiovasc Res,* 62**,** 63–73.
40. Luo, C. & Rudy, Y. 1991. A model of the ventricular cardiac action potential. Depolarization, repolarization, and their interaction. *Circ Res,* 68**,** 1501–26.
41. Mardis, E. R. 2006. Anticipating the 1,000 dollar genome. *Genome Biol,* 7**,** 112.
42. McNutt, N. S. & Fawcett, D. W. 1969. The ultrastructure of the cat myocardium. II. Atrial muscle. *J Cell Biol,* 42**,** 46–67.
43. Milescu, L. S., Akk, G. & Sachs, F. 2005. Maximum likelihood estimation of ion channel kinetics from macroscopic currents. *Biophys J,* 88**,** 2494–515.
44. Missan, S. & McDonald, T. F. 2005. CESE: cell electrophysiology simulation environment. *Appl Bioinformatics,* 4**,** 155–6.
45. Muldoon, T. J., Anandasabapathy, S., Maru, D. & Richards-Kortum, R. 2008. High-resolution imaging in Barrett's esophagus: a novel, low-cost endoscopic microscope. *Gastrointest Endosc,* 68**,** 737–44.

46. Neal, M. L. & Kerckhoffs, R. 2010. Current progress in patient-specific modeling. *Brief Bioinform,* 11(1)**,** 111–26.
47. Opencell. 2010. Available: http://www.cellml.org/tools/downloads/opencell [Accessed].
48. Perrin, M. J., Subbiah, R. N., Vandenberg, J. I. & Hill, A. P. 2008. Human ether-a-go-go related gene (hERG) K^+ channels: function and dysfunction. *Prog Biophys Mol Biol,* 98**,** 137–48.
49. Plaster, N. M., Tawil, R., Tristani-Firouzi, M., Canun, S., Bendahhou, S., Tsunoda, A., Donaldson, M. R., Iannaccone, S. T., Brunt, E., Barohn, R., Clark, J., Deymeer, F., George, A. L., Jr., Fish, F. A., Hahn, A., Nitu, A., Ozdemir, C., Serdaroglu, P., Subramony, S. H., Wolfe, G., Fu, Y. H. & Ptacek, L. J. 2001. Mutations in Kir2.1 cause the developmental and episodic electrical phenotypes of Andersen's syndrome. *Cell,* 105**,** 511–9.
50. Press, W. H. 1992. *Numerical recipes in C: the art of scientific computing,* Cambridge; NY, Cambridge University Press.
51. Richardson, W. H. 1972. Bayesian-based iterative method of image restoration. *J Opt Soc Am,* 62**,** 55–9.
52. Ruan, Y., Liu, N. & Priori, S. G. 2009. Sodium channel mutations and arrhythmias. *Nat Rev Cardiol,* 6**,** 337–48.
53. Sachse, F. B. 2004. *Computational cardiology: modeling of anatomy, electrophysiology, and mechanics,* Heidelberg, Springer.
54. Sachse, F. B. & Seemann, G. 2009. Special issue: functional imaging and modelling of the heart. *Med Image Anal,* 13**,** 345.
55. Sachse, F. B., Glänzel, K. & Seemann, G. 2003. Modeling of protein interactions involved in cardiac tension development. *Int J Bifurcat Chaos,* 13**,** 3561–78.
56. Sachse, F. B., Moreno, A. P. & Abildskov, J. A. 2008. Electrophysiological modeling of fibroblasts and their interaction with myocytes. *Ann Biomed Eng,* 36**,** 41–56.
57. Sachse, F. B., Savio-Galimberti, E., Goldhaber, J. I. & Bridge, J. H. 2009. Towards computational modeling of excitation-contraction coupling in cardiac myocytes: reconstruction of structures and proteins from confocal imaging. Pac Symp Biocomput, 14, 328–39.
58. Sanguinetti, M. C. & Tristani-Firouzi, M. 2006. hERG potassium channels and cardiac arrhythmia. *Nature,* 440**,** 463–9.
59. Savio, E., Goldhaber, J. I., Bridge, J. H. B. & Sachse, F. B. 2007. A framework for analyzing confocal images of transversal tubules in cardiomyocytes. *Lect Notes Comput Sci,* 4466**,** 110–19.
60. Savio-Galimberti, E., Frank, J., Inoue, M., Goldhaber, J. I., Cannell, M. B., Bridge, J. H. & Sachse, F. B. 2008. Novel features of the rabbit transverse tubular system revealed by quantitative analysis of three-dimensional reconstructions from confocal images. *Biophys J*, 95(4)**,** 2053–62.
61. Schaff, J. & Loew, L. M. 1999. The virtual cell. *Pac Symp Biocomput, 5*, 228–39.
62. Seemann, G., Sachse, F. B., Weiss, D. L., Ptacek, L. J. & Tristani-Firouzi, M. 2007. Modeling of IK1 mutations in human left ventricular myocytes and tissue. *Am J Physiol Heart Circ Physiol,* 292**,** H549–59.
63. Seemann, G., Lurz, S., Keller, D. U. J., Weiss, D. L., Scholz, E. P. & Dössel, O. 2008. Adaption of mathematical ion channel models to measured data using the particle swarm optimization. *IFMBE Proc, 22,* 2507–10.
64. Soeller, C. & Cannell, M. B. 1999. Examination of the transverse tubular system in living cardiac rat myocytes by 2-photon microscopy and digital image-processing techniques. *Circ Res,* 84**,** 266–75.
65. Soeller, C., Jayasinghe, I. D., Li, P., Holden, A. V. & Cannell, M. B. 2009. Three-dimensional high-resolution imaging of cardiac proteins to construct models of intracellular Ca^{2+} signalling in rat ventricular myocytes. *Exp Physiol,* 94**,** 496–508.
66. Souders, C. A., Bowers, S. L. & Baudino, T. A. 2009. Cardiac fibroblast: the renaissance cell. *Circ Res,* 105**,** 1164–76.
67. Splawski, I., Timothy, K. W., Sharpe, L. M., Decher, N., Kumar, P., Bloise, R., Napolitano, C., Schwartz, P. J., Joseph, R. M., Condouris, K., Tager-Flusberg, H., Priori, S. G., Sanguinetti, M. C.

& Keating, M. T. 2004. Ca(V)1.2 calcium channel dysfunction causes a multisystem disorder including arrhythmia and autism. *Cell,* 119**,** 19–31.
68. Splawski, I., Timothy, K. W., Decher, N., Kumar, P., Sachse, F. B., Beggs, A. H., Sanguinetti, M. C. & Keating, M. T. 2005. Severe arrhythmia disorder caused by cardiac L-type calcium channel mutations. *Proc Natl Acad Sci U S A,* 102**,** 8089–96.
69. Stark, J. F., de Leval, M. R., Tsang, V. T. & Courtney, M. 2006. Surgery for congenital heart defects. pp. 754
70. Stewart, P., Aslanidi, O. V., Noble, D., Noble, P. J., Boyett, M. R. & Zhang, H. 2009. Mathematical models of the electrical action potential of Purkinje fibre cells. *Philos Transact A Math Phys Eng Sci,* 367**,** 2225–55.
71. Stuehmer, W. & Parekh, A. B. 1995. Electrophysiological recordings from xenopus oocytes. *In:* Sakmann, B. & Neher, E. (eds.) *Single-channel recordings.* 2 ed. New York and London: Plenum Press.
72. Weiss, D. L., Seemann, G., Sachse, F. B. & Dossel, O. 2005. Modelling of short QT syndrome in a heterogeneous model of the human ventricular wall. *Europace,* 7 Suppl 2**,** 105–17.
73. Wong, C., Soeller, C., Burton, L. & Cannell, M. B. 2001. Changes in transverse-tubular system architecture in myocytes from diseased human ventricles. *Biophys J,* 80**,** 588A.

Chapter 4
Studies of Therapeutic Strategies for Atrial Fibrillation Based on a Biophysical Model of the Human Atria

Laurent Uldry, Nathalie Virag, Jean-Marc Vesin, and Lukas Kappenberger

4.1 Introduction

Atrial fibrillation (AF), the most common sustained form of cardiac arrhythmia, is an endemic disease with an increasing prevalence [14, 32]. Its polymorphic dynamical nature severely hampers the development of a single therapy effective in all individual patients [23, 24]. The limited understanding of the AF mechanisms indicates a clear medical need for improving current therapies, adapting them to various AF dynamics that can be found in different patient populations, and selecting the therapy that is optimal for an individual patient.

Several guidelines for the management of idiopathic AF have been proposed and provide a basis for the treatment of AF in clinical settings [19]. For paroxysmal and persistent AF, ventricular rate control and/or rhythm control (reduction of paroxysms) strategies are proposed, while for patients with permanent AF, the objective is sinus rhythm restoration. Pharmacological therapy with an antiarrhythmic drug is an important part of any rhythm control strategy. Restoration of sinus rhythm can also be achieved by electrical cardioversion, delivering an intracardiac or external electrical shock, a difficult task being the maintenance of sinus rhythm after successful cardioversion. Other treatments have been directed at eliminating the triggers and modifying the AF electrophysiological substrate. Catheter ablation of AF has now become almost a standard procedure for patients with paroxysmal or idiopathic AF, especially for patient with focal triggers. Surgical ablation procedures, such as the maze procedure, are currently performed in patients undergoing concomitant open heart surgery. In addition to pharmacological or ablation therapies, some of the recent pacemakers and defibrillators have incorporated different features to prevent or terminate AF, such as overdrive pacing or antitachycardia pacing (ATP). However, no clinical study has yet proven the long-term clinical benefit.

Computer modeling of biophysical phenomena has gained increasing importance for research in physiology and biology, and the recent improvements in computational

N. Virag (✉)
Medtronic Europe Sàrl, Route du Molliau, Tolochenaz CH-1131, Switzerland
e-mail: nathalie.virag@medtronic.com

R.C.P. Kerckhoffs (ed.), *Patient-Specific Modeling of the Cardiovascular System: Technology-Driven Personalized Medicine*, DOI 10.1007/978-1-4419-6691-9_4,

speed have enabled *in silico* experiments in highly detailed and realistic biophysical models. The use of such models overcomes some of the limitations encountered in *in vivo* experimental or clinical research, by providing an access to all variables of interest at any temporal or spatial scales and by allowing the possibility of performing and repeating the experiments under controlled conditions. Existing biophysical models differ in the trade-off made between accuracy of the representation and the computational load: the more detailed the model, the greater the computational complexity. The choice of a specific model is dependent on the question to be answered. For instance, a model can be modified to selectively reproduce the physiological parameters of a specific type of patient and, likewise, targeted modeling research can be conducted to find a dedicated treatment for the patient. The ability to accurately reproduce a specific physiological response in a model will, as a result, depend on the ability to implement all features that are pertinent to the application considered.

This chapter describes how a biophysical model of human atria can be used to simulate various types of AF dynamics and, on the basis of this, to evaluate and develop therapeutic strategies. Integrated functional computer modeling is considered today as a potentially effective solution for translational research in which the research results can be translated into clinically applicable therapeutic options [14].

The elements of the biophysical model of AF are described in Sect. 4.2. Next, in Sect. 4.3, specific variants of the model are presented, aimed at modeling different AF dynamics based on different tissue properties. These models were developed to reproduce the various dynamical mechanisms of AF suggested as being responsible for its polymorphic nature [23]. This section also describes the database of simulated episodes of AF used in the various applications. Different therapies were subsequently tested on the specific AF dynamics. With this multifaceted approach, a large series of experiments could be conducted on a substrate corresponding to the physiological settings of a specific patient. The examples of model-based analysis and applications included in this chapter are: a study of the conditions leading to the spontaneous termination of AF (Sect. 4.4), the optimization of ablation patterns (Sect. 4.5), and the preliminary results of a study on the feasibility of therapeutic pacing for AF (Sect. 4.6).

4.2 Computer Modeling of AF

Several computer models of the human atria have been developed over the last decades. Moe et al. developed the first model of AF in 1964 using cellular automata [22]. About 40 years later, more sophisticated models that take into account a detailed description of the atrial cellular membrane kinetics together with several aspects of the complex atrial anatomy were conceived [8, 28, 36, 38]. In 2000, Harrild and Henriquez presented the first membrane-based model of 3D conduction in a realistic human atrial geometry [8]. However, the model's heavy

computational demand precluded its use in studies on abnormal activation sequences. The design of simplified models that retain the salient features of atrial anatomy and electrophysiology has allowed the large-scale simulation of abnormal reentrant processes such as atrial arrythmias [36, 38] and associated therapies such as AF ablation [5, 28].

4.2.1 Biophysical Model of Human Atria

The biophysical model used in the material presented in this chapter was developed by the Lausanne Heart Group (http://www.lausanneheart.ch) with the aim of simulating several types of dynamics of AF and associated therapies such as ablation and pacing. This objective required the simulations of long periods of AF on a computer (several minutes or even hours of real-time AF); hence, it was designed such that the main aspects of a human atrial geometry were accounted for, while keeping computational load tractable [5, 38]. The model consists of three main components (Fig. 4.1): (1) realistic atrial geometry, (2) electrical propagation in the atrial tissue represented by a grid of atrial units, interconnected via resistors representing the interconnections of the myocytes at the gap junctions, and (3) atrial membrane kinetic model.

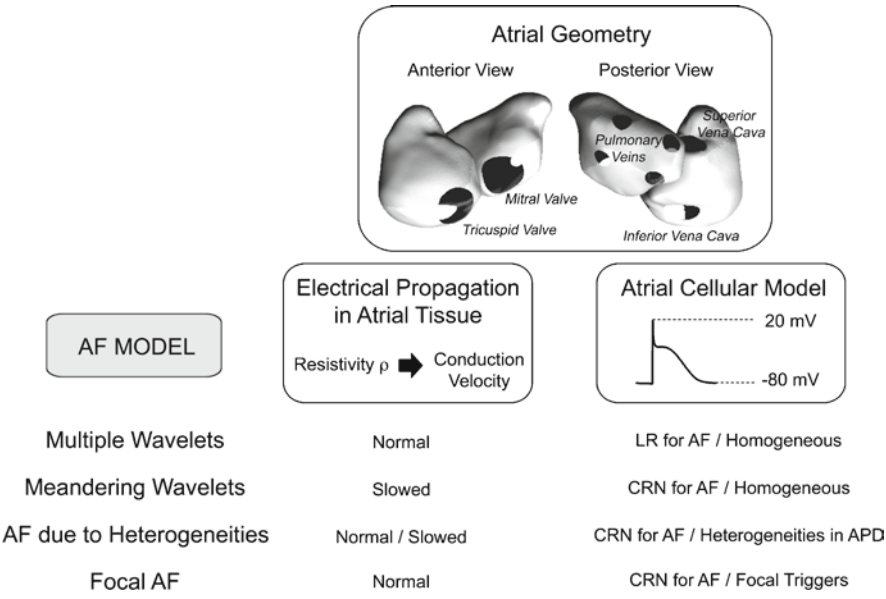

Fig. 4.1 The biophysical model of AF and its different components: (1) atrial geometry, (2) atrial tissue, and (3) atrial cellular model. Using the same geometry, AF models with different dynamics were realized by varying the properties of the atrial substrate

4.2.1.1 Atrial Geometry

Existing computer models of the atria extract the information about anatomy from several sources: commercially available, published atrial datasets [8, 28] or basic considerations from anatomy textbooks or devoted literature on atrial dimensions, atrial muscle bundles and strands, and propagation velocities [8, 36]. The geometry used in our model was derived from magnetic resonance images of the human atria segmented slice by slice, with 1 mm spacing [38]. These images formed the basis for a 3D atrial surface on which surface smoothing was applied to construct a mesh of 100,000 triangular elements (400 μm resolution). The model was given a realistic size and geometry, but the thickness of the atrial wall was taken to be infinitesimal (monolayer model). The resulting atrial geometry with the orifices for the valves and veins is presented in Fig. 4.1, illustrating the tricuspid valve, the two venae cavae and the coronary sinus in the right atrium (RA), the mitral valve and the four pulmonary veins in the left atrium (LA).

A thick-walled variant of this geometry was also constructed [35]. However, the increased computational load of this variant precluded its use in large-scale evaluations such as the ones presented in this chapter. This variant was used during incidental checks on the nature of the results obtained using the monolayer geometry.

4.2.1.2 Electrical Propagation in Atrial Tissue

The mathematical formulation of the electrical propagation on the grid of atrial units interconnected via resistors has been described previously [38]. In the simplest version of the model, these resistors were all given an equal value, resulting in a surface with intrinsic homogeneous, isotropic properties. More sophisticated versions including anisotropy and heterogeneities in conductivity were also developed [11]. Fast conduction systems such as the Bachmann's bundle, the crista terminalis, and the pectinate muscles were also included if deemed essential for a specific experiment [35].

4.2.1.3 Atrial Cellular Model

A dynamical activation model, based on membrane channel ion kinetics, was assigned to each atrial unit of the grid. In a first step, a variant of the Luo and Rudy ventricular model (LR) [20] was used, adapted to atrial cellular properties [18]. In a second step, the kinetics of a dedicated atrial cellular model, the Courtemanche–Ramirez–Nattel model (CRN) [3], was implemented. This model has a much heavier computational load than the LR-model. In these two models, channel conductances could be adjusted to mimic specific substrate conditions present during AF. In the simplest variant, all cells were assigned homogeneous intrinsic kinetics properties. More sophisticated versions included heterogeneities in the membrane properties [12].

4.2.2 Modeling Different Types of AF

Atrial arrhythmias were initiated in the biophysical model of AF in a similar way as in clinical experiments, i.e., using a programmed stimulation protocol or a burst-pacing protocol. Burst pacing at 20 Hz near the sinoatrial node was eventually selected because it does not require any adjustment of timing of the stimulation protocol. In our baseline model of healthy atria, most of the attempts to initiate arrhythmias either failed or produced unstable reentrant waves that terminated after a few seconds. Conditions favorable for the perpetuation of AF were created in a model of pathologic atrial tissue. While using the same atrial geometry, different types of sustained AF dynamics could be obtained by using the basic atrial kinetics models modified to take into consideration the electrical remodeling observed during AF and by varying the cellular or conduction properties to modify the atrial substrate, as summarized in Fig. 4.1. These models correspond to the different AF pathophysiologies proposed as being the cause of AF in the human heart [14].

4.2.2.1 Multiple Wavelet AF

The first AF model was based on a homogeneous atrial tissue using the LR model adjusted to mimic electrical remodeling as observed in patients suffering from permanent AF, such as a shortening of the action potential duration [13]. The resulting AF dynamics revealed multiple reentrant wavelets (three to eight), continuously changing in size and direction due to functional or anatomical reentries [13]. This reentry can be described by the multiple wavelet hypothesis formulated by Moe et al. [22]. It corresponds to the observations made in human mapping experiments, classified as type III AF, by Konings et al. [17]. In this variant of our model, AF was sustained for more than 10 min, which is the longest simulation ever performed in a biophysical model of AF. These conditions were chosen as a basis to test therapeutic interventions.

4.2.2.2 Meandering Wavelet AF

The second AF model was based on a homogeneous atrial tissue having an overall slower propagation. It uses the CRN model adjusted to reproduce the restitution properties measured in human atrial cells during permanent AF [13, 34]. The resulting AF dynamics revealed several meandering wavelets (one to four), commonly accompanied by shifting leading circles. This dynamics corresponds to type I or type II AF as described by Konings et al. [17]. AF was not sustained for more than 40 s. These model specifications were chosen as a basis for studying spontaneous AF termination.

4.2.2.3 Heterogeneities

Other AF models were developed in which different types of heterogeneities were introduced. Patchy heterogeneities in the cellular membrane properties (with a characteristic length scale of 2 cm) were introduced, which led to different AF dynamics [12]. A cholinergic AF model resulted in dominant mother rotors, supporting the hypothesis in which a single source of stable reentrant wave front maintains a fibrillatory activity [15, 37]. Similarly, a model variant was created including patchy heterogeneities in action potential duration [7].

4.2.2.4 Focal AF

The last AF model presented here was based on a mechanism different from that of functional reentry: the multiple source hypothesis, which postulates that a small number of foci is needed to maintain fibrillatory activity. It is now known that these foci of rapid ectopic activity, often located inside the pulmonary veins, play a pivotal role in the initiation of AF in humans [9]. In order to study this particular situation, a model variant was developed that included several focal sources of rapid discharge (placed mainly in the pulmonary veins region) [10]. This model was used to study the mechanisms of ablation of focal sources.

4.2.3 Link to Clinical Data

The link between computer simulations and clinical data is crucial for the validation of computer modeling assumptions and for the translation of research results into clinically relevant applications. First, in the computer modeling experiments, direct access to transmembrane potentials was available. This transmembrane potential was color-coded, red representing a value of 20 mV, and blue the resting potential of −80 mV. The complete distribution of instantaneous transmembrane potentials over the atrial surface was depicted as potential maps.

Electrical activity of the atria can also be recorded by electrodes in contact with the atrial wall (endocardial electrograms). This is the type of signals recorded during electrical mapping, either by catheter-guided electrodes during an electrophysiogical study or an ablation procedure or by the electrodes of an implantable device (pacemaker or defibrillator). In our simulations, local endocardial electrograms at virtual electrodes positioned at 1 mm from the atrial surface were computed using a current source approximation [11]. These simulated electrograms were in agreement with measured electrical mapping data during AF. The advantage of simulations like these is that high-resolution maps over the entire atrial surface can be

produced, with maps that are unperturbed by any ongoing ventricular activity, movement artifacts, or recording noise.

Finally, the standard 12-lead surface electrocardiogram is the most commonly used noninvasive tool for diagnosing cardiac arrhythmias. In our study, it was simulated using a thorax model involving the geometries of a healthy subject's torso, lungs, heart, and blood cavities derived from magnetic resonance images and using an equivalent double layer source model to compute the atrial components of the electrocardiograms [35]. The inclusion of the volume conduction model resulted in electrocardiographic signals that are in all aspects similar to those observed clinically.

4.3 Therapeutic Strategies for AF

4.3.1 Modeling AF Therapies

A computer model able to simulate sustained AF with realistic properties offers the possibility of evaluating different therapies for AF. In atrial models, pharmacological interventions were simulated by modulating the ion kinetics of the atrial units [16]. The effectiveness of surgical or catheter ablation line patterns was simulated by modifying the conduction (via the resistivity) of the cardiac cells located on the ablation line [5]. Therapeutic pacing, as in overdrive or ATP protocols, was simulated by injecting intracellular current in 3 mm^2 areas at different locations [33]. Model-based studies of defibrillation have been mostly developed in ventricular models [31].

4.3.1.1 AF Database

The evolving nature of AF was taken into consideration by performing multiple simulations for each of the therapeutic strategies studied. After the initiation of AF by means of rapid pacing, the evolving nature was accounted for by randomly selecting several moments in the ongoing sustained simulated AF (Fig. 4.2) and storing the subsequent episodes in a database. This methodology adds a statistical dimension to the analysis. In our studies on AF ablation [5, 30] and pacing of AF [33], up to 50 different instantaneous transmembrane potentials maps were taken as initial conditions for the application of the therapies. These snapshots correspond to different states of activity in the tissue, such as the number of wavelets and their spatial distribution. A similar approach was also used for the study of spontaneous termination of AF, where the elements of the database were chosen as initial conditions from which the system evolved freely until termination [34].

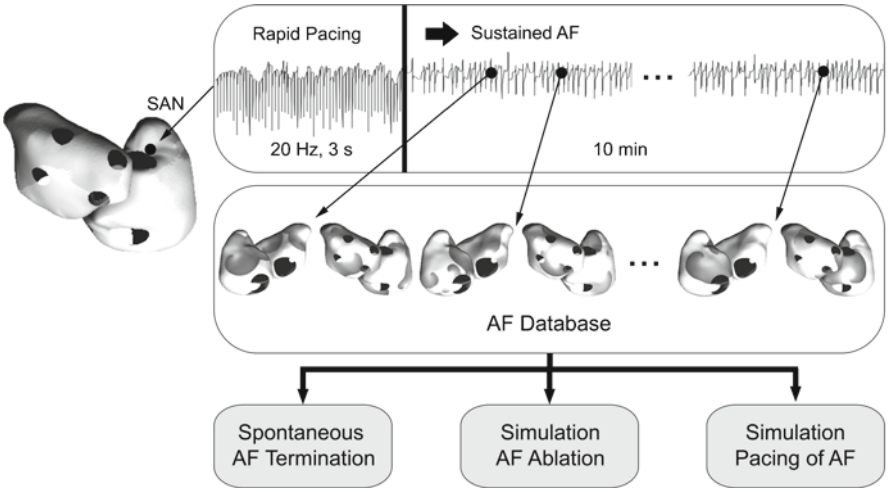

Fig. 4.2 Creation of an AF database for the simulation of spontaneous termination and therapeutic strategies for AF. AF was initiated with a rapid pacing at the sinoatrial node (SAN) region at 20 Hz during 3 s. When pacing was stopped, sustained AF was obtained, and the AF database was constructed by randomly selecting instantaneous transmembrane potential maps at different time instants. A black-and-white scale was used here, *black* representing a value of 20 mV and *white* the resting potential of −80 mV

4.4 Spontaneous Termination of AF

4.4.1 Simulation of Spontaneously Terminated Episodes

Spontaneous termination of AF is frequently observed in patients, and this also took place in our computer simulations. In patients, within the first 24 h, up to 50% of cases with a new onset of AF revert to sinus rhythm. However, if the AF episode lasted for more than 7 days, the chance of spontaneous cardioversion was greatly reduced [19]. So far the mechanisms of this termination are not fully understood. Identification of the spontaneous termination mechanisms could lead to a better understanding of AF and therefore to the development of more effective therapies. It is, however, difficult to study spontaneous AF termination episodes in any detail since they are transient and sometimes very short. Clinical studies have been conducted mostly on paroxysmal AF observed from 24-h Holter recordings [27], mapping experiments [25], or from data collected from implantable devices. The use of a biophysical model allows the generation of a high number of spontaneously terminated AF episodes in a spatially more complete way than is possible in clinical settings [34]. For the study presented below, 50 episodes of spontaneous termination in both the LR and the CRN models were observed, and the mechanisms of termination could be studied in detail during the 8 s preceding termination.

4.4.2 Temporal Scales of Termination

To assess the time scales involved in the AF termination process, the following parameters were assessed: the duration of the AF episode, the temporal evolution of AF cycle length (AFCL), and the AF dynamics characterized by the number of wave fronts (#WF) present in the atria [34]. Each measure was systematically performed globally in both atria, and separately in the RA and the LA (Fig. 4.3). In the LR model, mean AF episode duration was 58.5 ± 56.2 s. AFCL and #WF started to increase on a global scale at about 1,600 ms prior to termination, for both the RA and the LA. However, a consistently higher #WF was found in the RA, while instants with faster AF (shorter AFCL) were observed in the LA. In the CRN model, mean AF episode duration was 8.5 ± 7.1 s and therefore shorter than for the LR model. The AFCL started to increase about 3 s before termination on a global scale but 800 ms earlier in the LA than in the RA. In a similar way, #WF started to decrease 1,800 ms earlier in the LA than in the RA. An asymmetry in dynamics between atria, even for a homogeneous substrate, was observed in the CRN model. Clinical observations in humans indicate that distinct frequency changes in the

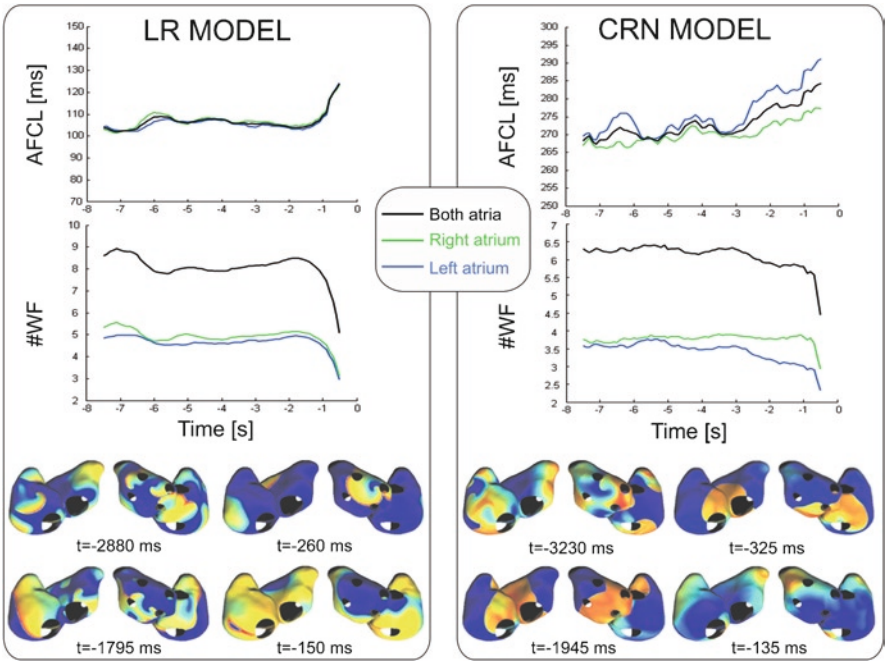

Fig. 4.3 Spontaneous termination in the Luo-Rudy (LR) and the Courtemanche–Ramirez–Nattel (CRN) models. The mean temporal evolution of AFCL and #WF during the 8 s preceding termination are shown for the two different models. For each model, instantaneous transmembrane potential maps for an example of AF termination episode are also presented. A color scale was used here, *red* representing a value of 20 mV and *blue* the resting potential of −80 mV

process of spontaneous termination occur during the last few seconds before termination [27]. Ndrepepa et al. showed that the earliest detectable event prior to AF termination occurred on average 4 s before termination with a significant increase of cycle length in the LA first of all, followed by an increase in the RA about 1 s later [25]. In our simulations, a similar observation was made when using the CRN kinetics model. However, when using a model with a different AF dynamics, the LR model, the temporal dynamics of the spontaneous termination was different. Further investigations will be devoted to the precise description and understanding of these mechanisms.

4.4.3 Spatial Scales of Termination

The spatial aspect of termination was assessed through a visual inspection of the extinction of the last active reentrant wave front before AF termination. In most cases, this last wave front was annihilated by one or several collisions, generating a larger wave front resembling normal activation, which died out in one of the extremities of the geometry. Therefore, the extinction site was the location where AF terminated, but not necessarily where electrical activity died.

In the LR model, no significant difference ($p = 0.1096$) was found between the number of episodes with an extinction site in the left atrium (21/50, 42%) and the number of episodes terminating in the right atrium (29/50, 58%). Therefore, AF based on multiple wavelets reentries did not terminate predominantly at a specific anatomic location on the atrium.

In the CRN model, significantly fewer episodes ($p < 0.001$) terminated in the LA (9/50, 18%) compared to the RA (41/50, 82%). This is very different from what has been observed in the LR model using the same atrial geometry. The role of atrial geometry still needs to be analyzed further. Model-based analysis is essential for understanding the spatial patterns involved in AF termination and its dependence on the underlying dynamics. This is a field where computer modeling offers unique possibilities since these detailed observations cannot be easily performed in clinical studies based on surface electrocardiograms or mapping data with a limited number of electrodes.

4.5 Ablation of AF

Surgical ablation of AF aims at creating lines of block to interrupt electrical conduction and to prevent the AF reentrant process, the gold standard being the Maze III procedure developed by Cox et al. [4]. This complex ablation procedure has proven to be effective in treating chronic AF, but it can be time-consuming and associated with a risk of serious complications. Therefore, less-invasive radiofrequency catheter ablation alternatives were developed and investigated clinically.

However, the ideal location and number of ablation lines, their best connection, and appropriate length still remain to be determined.

Different ablation patterns were systematically studied in the biophysical model of chronic AF. For each pattern evaluated, results were averaged over 10–40 AF initial conditions on which a specific ablation pattern was applied instantaneously. The simulation results confirmed that the most complex ablation patterns led both to the best success rate and shortest time to AF termination. Ablation patterns involving lines in the right or left atrium only led to success ranges of 20–60% and 55–80%, respectively, while those combining lines in both atria showed an increased rate in the range 80–100% [30]. The best results were obtained with the Maze III pattern: 100% success rate in the biophysical model, which is in the upper range of clinical data showing a long-term success rate ranging from 80 to 99% [4]. Figure 4.4 shows an example of AF termination using this ablation pattern. Simulations studies were also directed at finding ablation patterns reproducing the maximum conversion rate of 100% obtained with the Maze III procedure while using a minimum number of lesions [30].

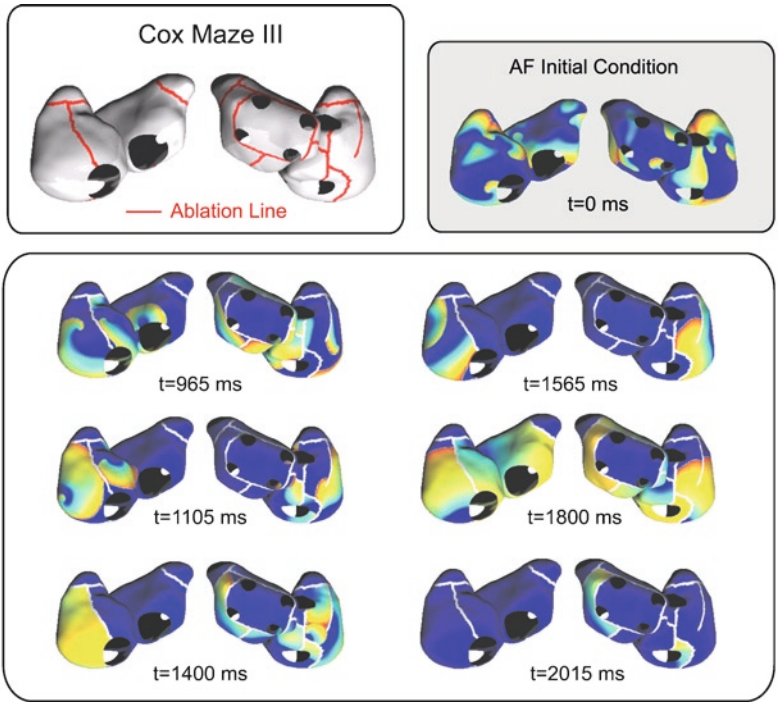

Fig. 4.4 Example of a successful ablation in the biophysical model of AF with the Maze III pattern (represented in the *upper left box*). $t = 0$ ms: AF initial condition, $t = 965$ ms: last reentry in the LA, $t = 1{,}105$ ms: last reentry in anterior RA, $t = 1{,}400$ ms: last reentry in posterior RA, $t = 1{,}565$ ms: uniform propagation wave fronts, $t = 1{,}800$ ms: uniform propagation wave front with prolonged action potential duration, $t = 2{,}015$ ms: final activity just before termination

This was the case for the patterns combining an isolation of the pulmonary veins, the left isthmus line, and the line between vena cavae in the right atrium.

A comparison between in silico ablation results obtained in the biophysical model and *in vivo* data from patients who underwent radiofrequency ablation showed a positive correlation for conversion rates to sinus rhythm and residual atrial flutter [29]. Computer modeling offers the possibility to test ablation line patterns in a reversible way in a human model, to test patterns not generally performed in clinical experiments, to observe the AF termination process in detail, and to study the impact of imperfections that may be present in the ablation lines.

4.6 Pacing of AF

Several ATP techniques such as burst or ramp pacing are currently used clinically to terminate atrial tachycardia or atrial flutter. Pacing treatment has the advantage over electrical cardioversion in that the therapy is painless and the energy cost negligible. However, no ATP therapy has proved to be effective in terminating AF, probably due to its more complex dynamics, the variable number of wavelets and the smaller variable excitable gap [21]. On the other hand, the possibility of local atrial capture by rapid pacing has been shown in animal and human experiments during electrically induced or spontaneous AF [1, 6, 26]. The resulting paced AF cycle length was smaller than the original one and did not lead to termination but sometimes to a loss of capture.

To study these processes, we implemented and tested an ATP algorithm currently used in pacemakers, namely, burst pacing, and determined the optimal pacing sites and pacing periods leading to local capture of AF. We followed a methodology similar to that used in our previous studies on AF ablation, and for each pacing protocol tested, the results were the average values obtained following three different initial AF conditions [33].

4.6.1 Pacing Protocol and Assessment of AF Capture

The pacing protocol is presented in Fig. 4.5. Burst pacing at constant cycle length was applied during 30 s, at 20–110% AFCL with 5% increments. Five pacing sites were evaluated: two sites in the RA, two sites in the LA, and one on the septum between both atria. Capture was defined as the ability of the pacing burst to take control over an area with a radius greater than 2 cm around the pacing site for a minimum of five consecutive beats. This definition was related to local capture around the pacing site, not to the generalized capture of both atria. Three different measures were used to describe the results. The capture interval was the pacing period interval (expressed in percentage of AFCL) for which capture was observed during more than 50% of the

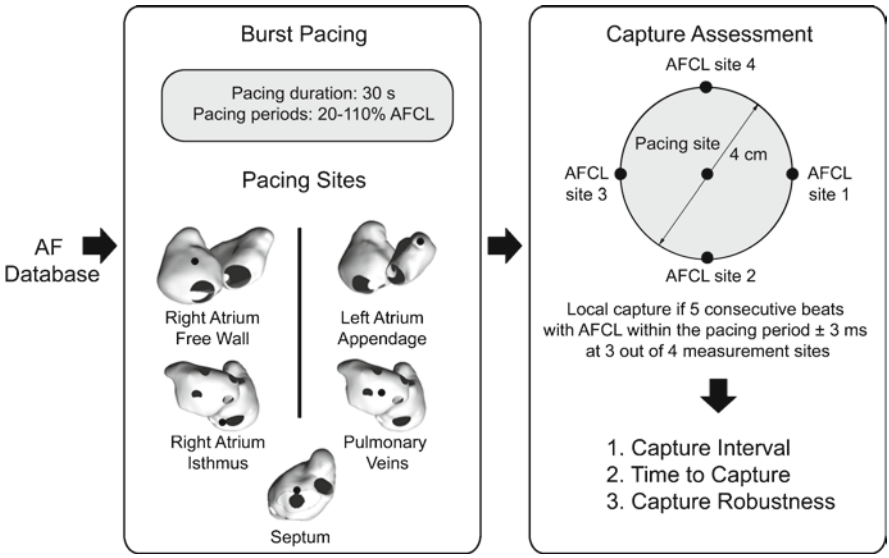

Fig. 4.5 Protocol for the simulation of AF pacing in the biophysical model of AF. Three initial conditions were extracted from the AF database. The burst pacing protocol was then tested at five different pacing sites. Local capture was assessed 2 cm away from the pacing site. Results were averaged on the different AF initial conditions and three measures describing the capture were computed

time. Within this capture interval, time to capture was defined as the duration from the start of ATP pacing to the onset of the first capture episode, thus providing an indication of how rapidly capture was achieved. Finally, capture robustness was used as a measure of the ability to sustain capture, computed as the percentage of time spent in capture between the first capture episode and the end of the pacing protocol.

4.6.2 AF Pacing Results

Capture results for the different pacing sites and the burst pacing protocol are summarized in Fig. 4.6. The optimal pacing period was similar for all pacing sites when computed as a percentage of the AFCL measured at the pacing location (68–83%), except for the isthmus pacing where a very narrow capture interval with only brief episodes of captures was observed. The expression of the capture interval as a percentage of AFCL allowed us to be independent of a specific AF cycle length and to compare results for the different pacing sites, even if longer AFCL were observed at some locations such as the septum. No significant difference was observed between the times to capture at the different pacing locations. Higher capture robustness was found in the right atrial free wall, the left atrial

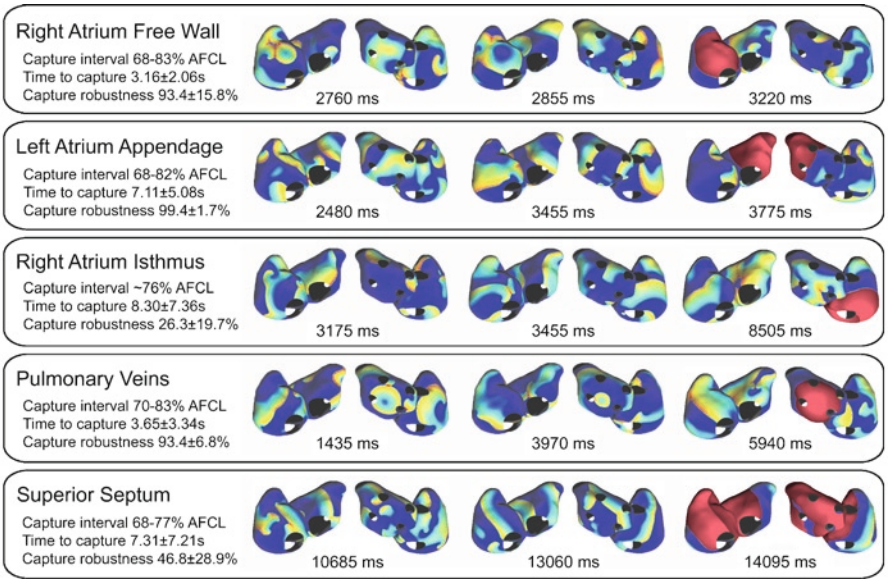

Fig. 4.6 Simulations results for AF pacing. For each of the five pacing sites, capture results are expressed with the capture interval, the time to capture, and the capture robustness. Three instantaneous transmembrane potential maps of AF activity during burst pacing at optimal frequency are also shown. The instantaneous transmembrane potential map on the *right* shows a time instant where the most favorable capture was achieved with the captured wave fronts induced by pacing highlighted in *red*

appendage, and the pulmonary veins compared with the isthmus or the septum. However, when pacing only in one atrium, control in both atria was not observed. Obtaining capture in both atria was found possible only when pacing in the septum, although being far less robust. Figure 4.6 presents the spatial repartition of the wave fronts following capture for the different pacing sites. The wave fronts induced by pacing encompassed for some locations the major part of the paced atrium. However, this was often accompanied by residual waves outside the area of capture. AF termination was not possible due to the fact that a slowing down or an abrupt stop of the pacing protocol allowed these residual wavelets to penetrate the captured area and to reinitiate AF. These observations of capture loss are consistent with experimental data [6]. Taken together, these results suggest that modeling studies can be helpful in the optimization of pacing protocols for AF treatment. We found that ATP algorithms working well for slower atrial tachyarrhythmias cannot be directly transposed to terminate AF, which is faster and less organized. Nevertheless, parameters such as pacing sites and frequencies can be optimized to maximize pacing efficacy. This explorative study was based on three initial conditions. More simulations will be needed to define precisely optimal pacing protocols for AF, and to explain the underlying mechanisms of AF control and pace termination.

4.7 Conclusion

This chapter shows how a biophysical model can be used to increase our understanding of AF. It permits the simulation of different AF dynamics, the evaluation of the mechanisms of spontaneous termination, and the study of currently used therapies for AF. The advantage of a computer modeling approach over clinical experiments lies in the possibility of performing systematic studies at detailed temporal and spatial scales, and thus offering a deeper insight into the underlying pathophysiological processes. While the biophysical model presented here is simplified in many aspects, the simulations are complex enough to reproduce observations made in humans, both in terms of obtained AF dynamics and the effectiveness of therapies. Today, with the emergence of mathematical models of increasing complexity, the challenge remains to reproduce phenomena with the least possible number of relevant parameters and, most importantly, to be able to have a close match to clinical observations [2]. The ability to reproduce a specific AF dynamics corresponding to a single patient makes this modeling framework attractive for dedicated experiments. Hopefully, such an approach will make a better translation of research results into therapeutic options possible. An improved understanding of the initiating and perpetuating factors of AF in individual patients will enhance the development of mechanism-based therapies.

Acknowledgements This study was made possible through grants from the Theo-Rossi-Di-Montelera Foundation, Medtronic Europe, and the Swiss Governmental Commission of Innovative Technologies (CTI). The authors wish to thank Ryan Lahm, Drs. Josée Morisette, and Arthur Stillman who kindly furnished the atrial geometry surface model. The authors also would like to thank Prof. Adriaan van Oosterom for helpful discussions and suggestions regarding the manuscript.

References

1. Allessie M, Kirchof C, Scheffer GJ, Chorro F, and Brugada J. Regional control of atrial fibrillation by rapid pacing in conscious dogs. *Circulation* 1991;84:1689–1697.
2. Coronel R. Myths, metaphors, and mathematical models. *Heart Rhythm* 2007;4:1046–1047.
3. Courtemanche M, Ramirez RJ, Nattel S. Ionic mechanisms underlying human atrial action potential properties: insights from a mathematical model. *Am J Physiol* 1998;275:H301–H321.
4. Cox JL, Schuessler RB, D'Agostino HJ Jr, Stone CM, Chang B-C, Cain ME, Corr PB, Boineau JP. The surgical treatment of atrial fibrillation: III. Development of a definitive surgical procedure. *J Thorac Cardiovasc Surg* 1991;101:569–583.
5. Dang L, Virag N, Ihara Z, Jacquemet V, Vesin J-M, Schlaepfer J, Ruchat P, Kappenberger L. Evaluation of ablation patterns using a biophysical model of atrial fibrillation. *Ann Biomed Eng* 2005;33:465–474.
6. Daoud E, Pariseau B, Niebauer M, Bogun F, Goyal R, Harvey M, Man C, Strickberger SA, Morady F. Response of type I atrial fibrillation to atrial pacing in humans. *Circulation* 1996;94:1036–1040.
7. Fareh S, Villemaire C, Nattel S. Importance of refractoriness heterogeneity in the enhanced vulnerability to atrial fibrillation induction caused by tachycardia-induced atrial electrical remodeling. *Circulation* 1998;98:2202–2209.
8. Harrild D, Henriquez C. A computer model of normal conduction in the human atria. *Circ Res* 2000;87:e25–e36.

9. Haissaguerre M, Jais P, Shah S, Takashi A, Hocini M, Quiniou G, Garrigue S, Le Mouroux A, Le Métayer P, Clémenty J. Spontaneous initiation of atrial fibrillation by ectopic beats originating in the pulmonary veins. *N Engl J Med* 1998; 339:649–666.
10. Haissaguerre M, Lim K-T, Jacquemet V, Rotter M, Dang L, Hocini M, Matsuo S, Knecht S, Jais P, Virag N. Atrial fibrillatory cycle length: computer simulation and potential clinical importance. *Europace* 2007;9:vi64–vi70.
11. Jacquemet V, Virag N, Ihara Z, Dang L, Blanc O, Zozor S, Vesin J-M, Kappenberger K, Henriquez C. Study of unipolar electrogram morphology in a computer model of atrial fibrillation. *J Cardiovasc Electrophysiol* 2003;14:S172–S179.
12. Jacquemet V, Virag N, Kappenberger L. Wavelength and vulnerability to atrial fibrillation: insights from a computer model of human atria. *Europace* 2005;7:S83–S92.
13. Kim B-S, Kim Y-H, Hwang G-S, Pak HN, Lee SC, Shim WJ, Oh DJ, Ru YM. Action potential duration restitution kinetics in human atrial fibrillation. *J Am Coll Cardiol* 2002;39:1329–1336.
14. Kirchhof P, Bax J, Blomstrom-Lundquiest C, Calkins H, Camm AJ, Cappato R, Cosio F, Crijns H, Diener H-C, Goette A, Israel CW, Kuck K-H, Lip GYH, Nattel S, Page RL, Ravens U, Schotten U, Steinbeck G, Vardas P, Waldo A, Wegscheider K, Willems S, Breithardt G. Early and comprehensive management of atrial fibrillation: proceedings from the 2nd AFNET/EHRA concensus conference on atrial fibrillation entitled 'research perspective in atrial fibrillation'. *Europace* 2009;11:860–885.
15. Kneller J, Zou R, Vigmond EJ, Wang Z, Leon LJ, Nattel S. Cholinergic atrial fibrillation in a computer model of a two-dimensional sheet of canine atrial cells with realistic ionic properties. *Circ Res* 2002;90(9):E73–E87.
16. Kneller J, Kalifa J, Zou R, Zaitsev AV, Warren M, Berenfeld O, Vigmond EJ, Leon J, Nattel S, Jalife J. Mechanisms of atrial fibrillation termination by pure sodium channel blockade in an ionically-realistic mathematical model. *Circ Res* 2005;96:35–47.
17. Konings KT, Kirchhof CJ, Smeets JR, Wellens HJ, Penn OC, Allessie MA. High-density mapping of electrically induced atrial fibrillation in humans. *Circulation* 1994;89:1665–1680.
18. Li D, Zhang L, Kneller J, Nattel S. Potential ionic mechanism for repolarization differences between canine right and left atrium. *Circ Res* 2001;88:1168–1175.
19. Lip GYH, Tse H-F. Management of atrial fibrillation. *Lancet* 2007;370:604–618.
20. Luo C-H, Rudy Y. A model of the ventricular cardiac action potential. *Circ Res* 1991; 68:1501–1526.
21. Mitchell ARJ, Spurrell PAR, Cheatle L, Sulke N. Effect of atrial antitachycardia pacing treatment in patients with an atrial defibrillator: randomized study comparing subthreshold and nominal pacing outputs. *Heart* 2002;87:433–437.
22. Moe GK, Rheinbold WC, Abildskov JA. A computer model of atrial fibrillation. *Am Heart J* 1964;67:200–220.
23. Nattel S. New ideas about atrial fibrillation 50 years on. *Nature* 2002;415:219–226.
24. Nattel S, Opie LH. Controversies in atrial fibrillation. *Lancet* 2006;367:262–272.
25. Ndrepepa G, Weber S, Karch MR, Schneider MAE, Schreieck J, Schomig A, Schmitt C. Electrophysiologic characteristics of the spontaneous onset and termination of atrial fibrillation. *Am J Cardiol* 2002;90:1215–1220.
26. Pandozi C, Bianconi L, Villani M, Castro A, Altamura G, Toscano S, Jesi AP, Gentilucci G, Ammirati F, Lo Bianco F, Santini M. Local capture by atrial pacing in spontaneous chronic atrial fibrillation. *Circulation* 1997;95:2416–2422.
27. Petrutiu S, Sahakian AV, Swiryn S. Abrupt changes in fibrillatory wave characteristics at the termination of paroxysmal atrial fibrillation in humans. *Europace* 2007;9:466–470.
28. Reumann M, Bohnert J, Seeman G, Osswals B, Doössel O. Preventive ablation strategies in a biophysical model of atrial fibrillation based on realistic anatomical data. *IEEE Trans Biomed Eng* 2008;55:399–406.
29. Ruchat P, Dang L, Schlaepfer J, Virag N, von Segesser LK, Kappenberger L. Use of a biophysical model of atrial fibrillation in the interpretation of the outcome of surgical ablation procedures. *Eur J Cardiothorac Surg* 2007;32:90–95.
30. Ruchat P, Virag N, Dang L, Schlaepfer J, Pruvot E, Kappenberger L. A biophysical model of atrial fibrillation ablation: what can a surgeon learn from a computer model? *Europace* 2007; 9:vi71–vi76.

31. Skouibine K, Trayanova NA, Moore P. Success and failure of the defibrillation shocks: insights from a simulation study. *J Cardiovasc Electrophysiol* 2000;11:785–796.
32. Steinberg JS. Atrial fibrillation: an emerging epidemic? *Heart* 2004;90:239–240.
33. Uldry L, Virag N, Kappenberger L, Vesin J-M. Optimization of antitachycardia pacing protocols applied to atrial fibrillation: insights from a biophysical model. *Proceedings of the 31st Annual International Conference of IEEE EMBC 2009*:3024–3027, September 2009.
34. Uldry L, Virag N, Jacquemet V, Vesin J-M, Kappenberger L. Spontaneous termination of atrial fibrillation: study of the effect of atrial geometry in a biophysical model. *Proceedings of the 31st Annual International Conference of IEEE EMBC 2009*:4504–4507, September 2009.
35. Van Oosterom A, Jacquemet V. Genesis of the P wave: atrial signal as generated by the equivalent double layer source model. *Europace* 2005;7:S21–S29.
36. Vigmond EJ, Ruckdeschel R, Trayanova N. Reentry in a morphologically realistic atrial model. *J Cardiovasc Electrophysiol* 2001;12:1046–1054.
37. Vigmond EJ, Tsoi V, Kuo S, Arvalo H, Kneller J, Nattel S, Trayanova N. The effect of vagally induced dispersion of action potential duration on atrial arrhythmogenesis. *Heart Rhythm* 2004;1:334–344.
38. Virag N, Jacquemet V, Henriquez CS, Zozor S, Blanc O, Vesin J-M, Pruvot E, Kappenberger L. Study of atrial arrhythmias in a computer model based on magnetic resonance images of human atria. *Chaos* 2002;12:754–763.

Chapter 5
Patient-Specific Modeling for Critical Care

Maxwell Lewis Neal

5.1 Introduction

Decision-making in critical care occurs on a time scale of hours, minutes, or even seconds and requires synthesizing large amounts of patient-specific (PS) data. It is therefore sensible to make use of PS modeling applications in critical care since they offer tools for integrating disparate data into a single system view and leverage computing power to provide decision support information in a timely manner. PS modeling can be used to aid diagnosis, to estimate occult physiological variables, and to test potential therapies in silico before administering them to a patient. They can therefore help clinicians determine what happened to the patient in the past, what is happening in the present, and what will happen in the future.

PS models are computational representations of human anatomy, physiology, or pathology that are tuned to match data from one individual as opposed to data from a population. These models supply clinicians with decision support information that is applicable to a single patient rather than a patient group. Generally, PS modeling systems developed for critical care scenarios must be computationally tractable enough to provide this decision support information in real or near-real time. This is an important distinction between critical care PS models and those developed for less time-sensitive scenarios (such as predicting a patient's response to cardiac resynchronization therapy, for example (Chap. 10, [18, 19])). Because computational timeliness is an issue, critical care PS models are usually limited to algebraic or ordinary differential equations (ODEs) and are optimized to simulate only those PS features that are essential for providing accurate decision support information. Hence, researchers in critical care PS modeling often adopt a "simple first" approach to model development. The goal of this approach is to identify effective, "minimal models" that keep computational burdens small but still provide accurate decision support information. Minimal models also have the advantage of being easier to

M.L. Neal (✉)
Department of Medical Education and Biomedical Informatics, University of Washington, 1959 NE Pacific Street, Box 357240, Seattle, WA 98195-7240, USA
e-mail: mneal@uw.edu

R.C.P. Kerckhoffs (ed.), *Patient-Specific Modeling of the Cardiovascular System: Technology-Driven Personalized Medicine*, DOI 10.1007/978-1-4419-6691-9_5,

understand and use once deployed. This advantage is crucial because in time-sensitive scenarios, it is essential to optimize not only the computational overhead of the modeling system being used but also the user's interaction with the system.

Critical care environments are often data-rich, since clinicians must monitor unstable patients thoroughly and continuously. Therefore, critical care PS modelers have the advantage of access to large amounts of detailed physiological data. Modelers can leverage this abundance to create PS simulations that are accurate on a high-resolution time scale, a luxury often unavailable outside the critical care setting. By representing a patient systemically, rather than in a reductionist manner, PS models can coalesce these large critical care datasets into a single, coherent picture of a patient's status. For example, given a PS hemodynamic model, ECG signals can be used to drive the simulated heart, from which the blood flow can be obtained. The latter can be constrained by afterload data derived from the patient's arterial catheter.

Despite over a century of quantitative biological modeling, only recently has the store of biological knowledge and computational power become sufficient to achieve the long-sought goal of applying PS quantitative modeling to real-time clinical decision-making. The first section of this chapter describes several examples of recent PS modeling applications in critical care, some of which are based on models created decades earlier. Working from these examples, the second section describes the major challenges currently faced by researchers in critical care PS modeling.

5.2 Examples of Patient-Specific Modeling in Critical Care

Although the field of applied PS modeling is relatively young, some important examples of applications in critical care exist. Many involve simulating cardiovascular or blood glucose dynamics, as these systems must be managed closely in the critical care environment.

5.2.1 Hemodynamic Models

Maintaining a patient's hemodynamic homeostasis is a primary task in critical care, and it is not surprising that many critical care PS models simulate cardiovascular dynamics. Figure 5.1a shows a basic example of a hemodynamic model used for estimating a patient's systemic vascular resistance (SVR). Given its simplicity, one may not think of this as a PS model in the modern sense, but it is nonetheless a computational representation of a patient's physiology, which is parameterized to match PS pressure and flow data. This particular model is based on the fluid analog of Ohm's Law. As Ohm's Law relates voltage and current to electrical resistance, the fluid analog relates a pressure difference and fluid flow to fluid resistance. This model,

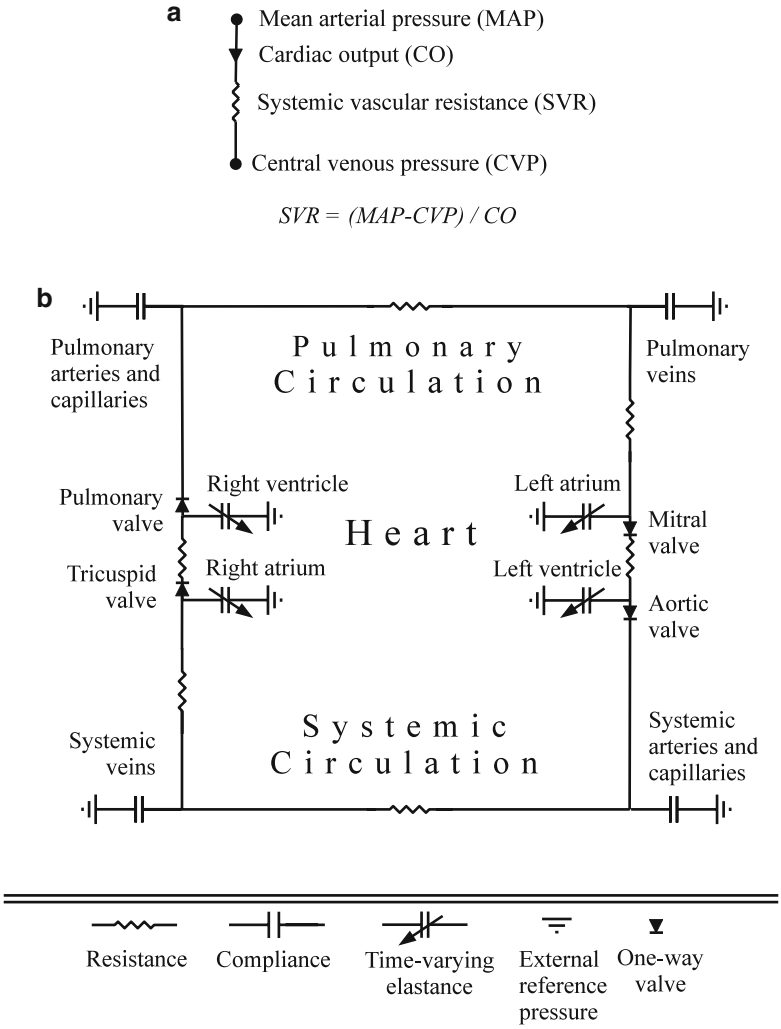

Fig. 5.1 Lumped-parameter, hemodynamic models. (**a**) A simple electrical analog model of blood flow through the systemic vasculature for estimating systemic vascular resistance. (**b**) A more complex electrical analog model that simulates blood pressures, flows, and volumes throughout the cardiovascular system

which has been in use for decades, treats the systemic vasculature as a single resistive element. It is computationally simple and provides an estimate of an important physiological variable that helps medical decision-making.

Figure 5.1b illustrates a more complicated hemodynamic model based on fluid analogs of electrical transmission laws. The model uses a collection of Windkessel ("wind-chamber," see below) compartments [10, 32] to simulate segments in the circulation that not only provide energy loss via resistive pathways but also energy

storage via vessel compliance. This kind of formulation allows the modeler to account for blood volumes (analogous to electrical charge) throughout circulatory compartments along with blood pressures and flows. Although this model does not directly correspond to any published PS modeling application, it is used here to illustrate a common modeling technique used in hemodynamic simulations. The code for the model in Fig. 5.1b includes a set of algebraic equations and ODEs that are solved using numerical, as opposed to analytical, methods. In the interest of model sharing and reproducibility, this code is presented in the appendix. It is written in the Mathematical Modeling Language (MML) used for simulations within the free JSim environment [17]. A digital copy of the original model file is also available from the author upon request.

The hemodynamic modeling techniques used to create the models in Fig. 5.1 are by no means new (see, for example, [30]). These so-called "lumped parameter" models (they lump groups of resistive and/or capacitive elements together) have been used in the past to estimate cardiac output (CO) [8, 25, 38], to study the effects of orthostatic stress on the cardiovascular system [15], to analyze the Valsalva and Forced Vital Capacity maneuvers [23], to predict hemodynamics in traumatic brain injury patients [37] (see below), and to create educational tools in physiology [7, 34]. However, it is only within the last 10–20 years that computing power has increased to the point where models of this complexity can be solved within a time frame that is realistic for critical care decision-making.

5.2.1.1 Cardiac Output Estimation

The gold-standard measurement of CO is thermodilution, a procedure that requires an indwelling catheter. Therefore, less-invasive means of obtaining accurate CO would substantially reduce patient health risks. Emphasizing this fact, Kouchoukos et al. [20] referred to the creation of a reliable, noninvasive continuous CO measurement technique as an "El Dorado." Several researchers have explored the use of models like those in Fig. 5.1 for estimating cardiac output (CO) from more readily available, less risky continuous measurements like arterial blood pressure (ABP) and heart rate (HR).

The origins of the hemodynamic models applied to the problem of CO estimation can be traced to work done by Otto Frank over 100 years ago [10, 32]. In 1899, Frank published the first major quantitative study that related systemic arterial system properties to arterial pressures and flows. His widely used Windkessel model, which simulates a compliant, fluid-filled chamber, laid the foundation for much of the hemodynamic modeling work that has followed, including model-based CO estimation studies.

One of the first PS model-based CO estimation methods to emerge was that of Wesseling et al. [38]. Their "Model Flow" method relies on a simple three-element Windkessel model of blood flow out of the left ventricle and into the systemic circulation. In order to compute a continuous CO estimate, this method relies on PS age, ABP, and HR data along with an initial CO measurement used to calibrate the model.

A recent study by De Wilde et al. [8] also describes the development of a model-based CO estimation technique called Hemac that is similar to the Wesseling

Model Flow method. Whereas the Model Flow method uses an aortic pressure–volume relationship (compliance) based on population-averaged in vitro data, the Hemac method bases the relationship on PS data obtained from in vivo measurements on the aorta. In a recent clinical study, authors showed that the Model Flow and Hemac CO estimation methods were more accurate than three other methods not based on models, including the commercially available LiDCO CO estimation system [22]. However, this particular study was limited to 24 surgical patients without congestive heart failure, with normal heart rhythm and reasonable peripheral circulation. Indeed, one of the current challenges in the field of CO estimation is to demonstrate a method's utility across a broad spectrum of patient conditions.

Neal and Bassingthwaighte [25] have also recently published a model-based CO and total blood volume estimation method using a hemodynamic model similar to the one in Fig. 5.1b. Based on the work of Lu et al. [23], their model was constructed using a network of Windkessel compartments that simulate blood pressures, flows, and volumes in a 21-segment representation of the cardiovascular system. The authors created an algorithm that tuned this hemodynamic model to match a baseline set of hemodynamics from a given subject. The tuned parameters were then used in an open-loop version of the model to estimate CO from mean ABP and HR data obtained from single subjects. Unlike other CO estimation techniques, this method does not require an invasively obtained ABP curve, but uses mean ABP instead, which can be estimated noninvasively. Although the Neal and Bassingthwaighte CO estimation method provided good estimates of CO in preclinical studies, the tuning procedure used to match baseline PS data took hours to compute using commercially available desktop processing power. This bottleneck must be removed either through an increase in computational power or a simplification of the tuning process and/or model design before such a method becomes viable in a critical care setting.

Exemplified by the Neal and Bassingthwaighte model, one of the major challenges in PS modeling lies in creating computationally efficient tuning methods for matching model output to PS data. These methods can be time-intensive, since multiple model runs are often required to complete the tuning process. Researchers have addressed this issue recently and created methods for reducing the burden of parameter tuning in detailed hemodynamic models [14, 29]. These methods are discussed below in Sect. 5.3, "Current challenges."

5.2.1.2 Simulating Response to Traumatic Brain Injury

Hemodynamic PS modeling has also been applied to the treatment of traumatic brain injury in pediatric patients. Wakeland et al. [37] developed a six-compartment ODE-based model that simulates blood pressures, volumes, and flows in intracranial arteries, capillaries, and volumes. The model also simulates the aggregated CSF volume, brain tissue volume, and (if applicable) intra- and extracranial hematoma volumes. In a clinical study, researchers used this model to anticipate individual patients' responses to head of bed tilt and respiratory rate change therapies. They first tuned the model to PS hemodynamic data obtained from an initial instance of

one of these physiological challenges. Then, using the newly parameterized model, they simulated the effects of future challenges, and compared the model's predictions of intracranial pressure with data from actual challenges performed during the same therapy session (within 2–3 h) and in subsequent sessions performed on other days. The researchers demonstrated that their PS modeling system could be implemented in a critical care environment and used to make predictions about individual patient's responses to traumatic brain injury therapy. However, they obtained only modest success when they validated model predictions against data from nine pediatric ICU patients. Model predictions made within a single therapy session were favorable in 27% of these cases, and those made between sessions were favorable in 10% of cases. Wakeland et al. propose that their system may be improved by adding more physiological detail to their model and by incorporating higher resolution clinical data. Additionally, as in the Neal and Bassingthwaighte model, the Wakeland et al. PS modeling application requires a significant amount of time for model tuning (in excess of 20 min) and stands to benefit from more efficient tuning methods and increases in computing power.

5.2.2 Models of Glucose and Insulin Dynamics

The management of blood glucose levels in ICU patients is also a major challenge in critical care. Even nondiabetic patients can suffer from hyperglycemia in the ICU, a condition that worsens hospital outcomes due to increased susceptibility to infection, myocardial infarction, and other illnesses. At the same time, improper treatment of hyperglycemia can result in hypoglycemia, which is also associated with impaired outcomes.

5.2.2.1 Controlling Blood Glucose Levels

PS models have recently been applied to predict and control blood glucose levels in ICU patients at risk for hyper- and hypoglycemia. Van Herpe et al. [36] developed a system for predicting blood glucose levels in ICU patients based on system identification techniques. In this method, the underlying physiological system responsible for glucose dynamics is treated as a black box, and optimization methods are used to find an empirically-based, single-equation model that accurately relates a set of input data (initial blood glucose levels, body temperature, flow of carbohydrate calories, etc.) to output data (predicted blood glucose levels). They demonstrated that an adaptive modeling system that alters their model to account for PS features was more accurate in predicting future blood glucose values in the ICU.

In 2008, Chase and colleagues [5] published a clinical validation study assessing the impact on patient mortality of a PS model-based glucose control system implemented in an ICU. They showed that their "Specialised Relative Insulin Nutrition Tables" (SPRINT) system reduced the hospital mortality of ICU patients by 26%

for those staying 3 days or more. Mortality was reduced by 32% for patients staying 4 days or more and 35% for patients staying 5 days or more. This study provides an important example of a PS modeling application that has passed through the processes of design, development, preclinical testing and clinical testing and emerged as a valuable tool for the ICU. Time will tell whether SPRINT is widely adopted as a standard of care.

There are several important features of the SPRINT system that contribute to its success. First, the system is based on a time-tested model of insulin and glucose dynamics called the Bergman minimal model [2, 3]. This ODE-based model simulates time courses of insulin and glucose following injection of insulin into a patient's bloodstream. By tuning the model parameters to match PS data obtained from intravenous glucose tolerance tests, the model provides indexes of a patient's insulin sensitivity, glucose effectiveness, and first-phase insulin response. These three model parameters provide the ICU clinician with a thorough view of a patient's glucose homeostasis, and can help guide the administration of insulin for controlling blood glucose levels.

The Bergman model's simplicity has likely contributed to its viability and adoption as a clinical and educational tool. SPRINT is based on an extended Bergman model but is still simple enough to be translated into a paper-based protocol in an ICU. Thus, no interaction with a computer is required to employ the SPRINT system and model results can be retrieved immediately. As shown by the reductions in mortality of the large patient population studied by Chase et al., this minimal approach to PS modeling can prove effective despite its simplicity.

To further illustrate the value of blood glucose modeling, researchers have recently found that the insulin sensitivity variable computed by the SPRINT model can be used as a negative predictor of sepsis in ICU patients [28]. This provides an example of how PS modeling can help clinicians with challenging diagnostic tasks and also demonstrates an important, perhaps overlooked value in model-based estimation of physiological variables. As surrogates for unavailable or overly risky in vivo measurements, these variables can be used as additional biomarkers to aid clinical diagnoses and prognoses. To provide a second example, Neal and Bassingthwaighte found that their model-derived total blood volume loss estimates predicted survival/nonsurvival following severe hemorrhage in pigs [25]. Obtaining an actual total blood volume measurement on a person (or a pig) in a critical care scenario is not feasible; therefore, clinicians have no way of knowing the predictive value of this variable for survival, time to death, etc. However, a model-based estimate of total blood volume can be used as a surrogate measurement and can be tested for its predictive value, as can any other physiological variable computed by a PS model.

5.3 Current Challenges

Although much progress has been made in applying computational PS modeling systems to challenges in critical care, these applications have yet to become widely adopted standards. Considering the computational power presently available to

clinicians and the fact that PS models used in critical care must often rely on time-tested, minimal models, it is somewhat surprising that more success stories of applied PS modeling in critical care do not exist. The field of PS modeling as a whole is young, and researchers face many challenges in translating modeling work performed in the biomedical research realm into useful, clinically validated tools.

5.3.1 Clinical Validation

Many current efforts in PS modeling for critical care are at the stage where computationally timely models have been built and can be parameterized to match individual patient data, but have yet to be validated against large-n clinical data sets [27]. These kinds of validation studies can be financially and temporally expensive since they require IRB approval, patient recruitment, and data collection. It is only after data have been collected from human subjects that the iterative cycle of refining the PS modeling application under development begins.

During the validation process researchers often find that their models need to be revised to generate accurate simulations. This process can involve increasing the model's detail, replacing/editing components of the model, or testing out an entirely new model design. Such revisions can be cumbersome and difficult, especially with models of higher complexity. Currently, researchers have access to few tools that would make the revision of more complex models less cumbersome and error-prone. The potential utility of a modular modeling approach that addresses these issues is discussed below in the "Model interoperability" section.

As discussed by Neal and Kerckhoffs [27], even when researchers are able to successfully test and validate their PS models against a significant number of patients, the question remains whether their system, once deployed, will actually effect clinical decision-making and improve patient outcomes. Whereas large-n validation studies have been the traditional endpoint of biosimulation modeling research, PS modelers will be faced with the additional task of deploying PS modeling systems into a clinical setting and demonstrating their effectiveness as decision support tools. The process does not end there, however. In order for a PS modeling system to become a standard of care it will require approval by the FDA, or similar regulatory agencies in other countries as a medical device.

5.3.2 Timely Tuning Methods

One of the challenges in using more modern, detailed physiological models to simulate PS phenomena lies in tuning the models to match PS data. Whereas a simple fluid dynamics model like that of Wesseling et al. [38] has a minimum number of free parameters to adjust, a more sophisticated, multicompartment model like that of Neal and Bassingthwaighte requires tuning scores of parameter values. In lieu of this computational hurdle, researchers have created more streamlined tuning

procedures for multicompartment hemodynamic models. For example, Pope et al. [29] employed parameter sensitivity and subset selection methods to reduce the complexity of a multicompartment cardiovascular model used to identify biomarkers that distinguish between healthy young and elderly populations. Additionally, Hann et al. [14] developed an "integral-based parameter identification method" that can be used to quickly and accurately tune a minimal cardiovascular model to match PS data. This integral-based approach was also applied in creating the successful SPRINT system discussed above. Models that employ adaptation rules also seem promising in reducing the number of parameters (Chap. 2).

5.3.3 Variability in Patient Anatomy, Physiology and Clinical Scenario

Each patient in a critical care scenario is unique, and the importance of developing accurate, automated tuning algorithms that account for differences between patients cannot be overstated. However, if a patient presents with a feature that violates the underlying assumptions of a model, often the only way to account for this abnormality is to change the equations of the model itself. For example, suppose a clinician would like to use a cardiovascular model such as that in Fig. 5.1b to simulate the hemodynamics of an infant undergoing surgery to repair Tetralogy of Fallot. In this case, the patient's anatomy is different from the anatomy assumed in the computational model, due to a ventricular septal defect and overriding aorta. The clinician will require a new model that includes an abnormal arrangement of blood flow before and possibly after the surgical procedure (because the end goal of some heart defect surgeries is a noncanonical arrangement of blood flow). Furthermore, if a cardiopulmonary bypass (CPB) machine is employed during the surgical procedure, the simulation must account for its use as well. None of these conditions would be present in a model that assumes canonical cardiovascular anatomy. Therefore, given the anatomical and physiological variation present in humans and the variation in clinical scenarios between patients, there is a general challenge to devise a modeling approach that can readily account for this diversity. This challenge must be addressed if PS modeling is to realize its full potential in critical care.

There are two solutions to this challenge: precoordination and postcoordination of models. Pre-coordinating models to account for the variations in blood flow described above would require modeling each possible noncanonical blood flow arrangement ahead of time, either using separate models for each arrangement, or model "switches" that toggle between flow arrangements in a single model. This solution requires model developers to anticipate every possible noncanonical arrangement of blood flow whether due to patient anatomy or the application of artificial shunting mechanisms (such as a CPB machine). The approach presents a potentially intractable combinatorial problem, given the number of separate models or switchable model subcomponents that must be created to account for all blood flow arrangements.

A more scalable, manageable, and flexible approach to this complex problem is to postcoordinate the models. In this approach, users have access to a repository of

smaller, interoperable, modular models that can be recombined "on the fly" to simulate a wide variety of PS conditions. For example, if a patient goes on CPB, a CPB module can be retrieved from the repository, and then merged with a PS systemic circulation model (perhaps extracted from the system in Fig. 5.1b) to simulate the rerouting of the patient's blood flow through the bypass machine. As a design principle, modularity is a time-tested method of dealing with complexity [1], and it has been leveraged in a myriad of industrial fields to organize and optimize the creation of complex products [33]. A modular approach to PS modeling would theoretically provide a means for clinicians to create PS models across a wide spectrum of clinical cases. In the next section, I provide more details on biosimulation model interoperability and its applicability in creating PS models for critical care.

5.3.4 Model Interoperability

Because modelers usually choose to code in whatever simulation language is most comfortable for them, published physiological models that may have applicability in critical care are coded in a variety of languages for a variety of simulation platforms. Consequently, these models are not readily shareable or reproducible between research groups. Model code often languishes on laboratory hard drives when it could be built upon and/or repurposed to address clinically relevant problems. Some researchers have tackled this issue and developed methods that facilitate the reuse of published biosimulation models. For example, systems biologists, who focus on modeling chemical networks, have created a number of standards for model reproduction among their research community. The Systems Biology Markup Language (SBML [16]), an XML-based model description format, is one such standard that acts as a *lingua franca* for encoding chemical network models. Using a common set of SBML parsing and simulation tools, systems biologists can readily reuse models coded by independent research groups. The systems biology community has also created other standards for curating published models in a centralized database [21] and for describing the tasks required for the reproduction of published model results [24].

This work within the systems biology community is an example of a success story in addressing the larger issue of biosimulation model interoperability. However, a standard like SBML does not scale beyond the chemical network domain. Furthermore, most of the modeling applications described above simulate phenomena at the tissue or organ level. Therefore, as discussed by Neal and Kerckhoffs [27], to encourage model interoperability, the PS modeling community needs standards for describing, curating, and reproducing models that scale beyond chemical networks to include higher levels of biological organization. These standards can be applied not only as part of the modular, postcoordination PS modeling approach described above but also to encourage model reuse and development among the greater modeling community.

Currently, the most ambitious attempt to create a model description standard that applies across physical modeling scales and modeling languages is the Semantic Simulation (SemSim) approach [26]. In this approach, the codewords and mathematical

dependencies of existing biosimulation models are annotated against concepts in standardized reference sources like the Foundational Model of Anatomy (FMA, [31]), the Gene Ontology (GO, [13]), the Chemical Entities of Biological Interest (ChEBI) ontology [9], and the Ontology of Physics for Biology (OPB, [6]). Once annotated within the SemSim format, physiological models become semantically interoperable, allowing for more automation of common modeling tasks. When a user combines multiple SemSim models, the merged model not only compiles, but also is biologically meaningful. For example, a user may want to combine a heart model with a systemic circulatory model. Suppose both models include a codeword that gives values for left ventricular (LV) outflow but in the heart model this codeword is a variable output, whereas LV outflow is a static parameter in the systemic circulatory model. Semantic interoperability helps automate the merging of these models into a biologically meaningful result. Cast in the SemSim format, a computer can recognize that both models simulate LV outflow, and thus, the user may want to couple the models at that point so that LV outflow from the heart model replaces the static LV outflow codeword in the systemic circulatory model. Without semantic composability, there is no way to automate this merging process beyond simply copying blocks of code from one model into another, and in doing so, there is no guarantee that the result will be biologically consistent. With semantic interoperability, a computer can recognize that having two different codewords that simulate the same physical property is contradictory, and can prompt the user to resolve the contradiction, thus retaining biological meaning in the merged model.

Semantic interoperability is just one level of model interoperability and is an important step in reaching even higher, more powerful levels of interoperability. The US military, specifically the Simulation Interoperability Standards Organization (SISO), has been researching this issue to optimize the creation of defense-related simulations. Tolk et al. [35] define six levels of interoperability for simulation systems: technical, syntactic, semantic, pragmatic, dynamic, and conceptual.

- *Technical interoperability*. A protocol exists for exchanging data (bits) between participating model components.
- *Syntactic interoperability*. A common data format is applied to share information between model components.
- *Semantic interoperability*. The meaning of the data is shared between model components.
- *Pragmatic interoperability*. The use of the data (i.e., the context of its application) is shared between model components.
- *Dynamic interoperability*. Components react to time-dependent changes in their internal assumptions and constraints. The effect of the system's operation is shared between model components.
- *Conceptual interoperability*. Model components share a common understanding of the assumptions and constraints of a simulation's abstraction of reality.

Presently, most interoperability solutions in software engineering and simulation only provide the technical and syntactic levels. However, researchers are now exploring how Semantic Web technologies can help realize semantic and pragmatic interoperability for simulations [4, 11, 12, 26].

The issue of model interoperability has been stressed here because to fully tap the potential of PS modeling in critical care, modeling applications must be able to account for unforeseen patient conditions, must be designed for use by nonengineers, and must be optimized for efficiency. A modular approach using minimal, optimized, interoperable models is the most logical design paradigm that addresses all of these issues. Although a challenging area of research, model interoperability is a potentially powerful catalyst for the development of PS modeling in critical care. A modular modeling approach will also help streamline the cumbersome, iterative model design cycle discussed above by eliminating common hand-coding tasks and coding-related errors.

This being said, modular PS modeling has its own limitations to consider as well. While researchers can validate single standalone models against empirical data, there is no way to do this for all the possible recombinations of model components from a repository of modular models. Therefore, while the individual component models that comprise a composite PS model may be validated individually, the composite model may not. Validating all the possible model recombinations from a repository of model components is not tractable. Therefore, clinicians composing novel PS models "on the fly" must realize that such models may not have been tested against empirical data prior to use. Instead of attempting to validate all possible recombinations of the model repository components, a modular modeling system will have to be validated by analyzing whether the composite models *as a group* successfully matched empirical data, improved patient outcomes, etc. Furthermore, because modular modeling allows the user to create novel models, flexible, adaptable parameter tuning programs will also be required to match model output to patient data.

5.4 Vision for the Future

Much work remains before more PS modeling systems become standards of care in critical care environments. With access to sophisticated modeling tools and scores of published models, many modelers have begun testing their work in preclinical and/or clinical settings. Thus, many PS modeling efforts are at the validation stage, one of the main challenges that researchers currently face in PS modeling in general. However, PS modeling researchers must ultimately go beyond the traditional endpoints of modeling research so they not only demonstrate that their models are valid but also that their modeling systems actually improve medical decisions and patient outcomes when implemented in a critical care environment.

Another research area that must be explored before PS modeling becomes a standard of care involves identifying the optimal means of deploying and using a PS modeling system in the clinical environment. If a modeling system requires in-depth quantitative knowledge of the model(s) involved in simulating patient dynamics, specialized technicians will be required to manipulate the system. In this case it may be most logical for clinical centers to develop modeling cores with members specializing in PS modeling applications. Alternatively, if a modeling system does not

require in-depth, technical knowledge to tune and execute, specialization may not be required. In this case, critical care physicians and nurses will be able to use the modeling systems themselves (as is the case with the SPRINT protocol). Initially, PS modeling systems will focus on delivering accurate PS information to the clinician, and usability improvements will occur later, as the utility of such systems is demonstrated. Once demonstrated, we will likely see interface improvements that make PS modeling accessible to a broad spectrum of users.

Acknowledgments My thanks to Dr. Daniel Cook who provided valuable suggestions for improving this chapter. This work was supported by American Heart Association Award 09PRE210064.

References

1. Baldwin, C.Y. and K.B. Clark, *Design Rules Volume I: The Power of Modularity*. 2000, Cambridge: The MIT Press. 471.
2. Bergman, R.N., *Minimal model: perspective from 2005.* Hormone Research, 2005. 64: p. 8–15.
3. Bergman, R.N. et al., *Quantitative estimation of insulin sensitivity.* American Journal of Physiology- Gastrointestinal and Liver Physiology, 1979. 236(6): p. 667.
4. *BOMs Homepage*. http://www.boms.info/. Accessed 2009.
5. Chase, J.G. et al., *Implementation and evaluation of the SPRINT protocol for tight glycaemic control in critically ill patients: a clinical practice change.* Critical Care, 2008. 12(2): p. R49.
6. Cook, D.L. et al., *Bridging Biological Ontologies and Biosimulation: The Ontology of Physics for Biology*, American Medical Informatics Association Annual Symposium Proceedings. Washington, D.C., 2008: p. 136–140.
7. *CVSim*. http://www.physionet.org/physiotools/cvsim/. Accessed 2009.
8. De Wilde, R.B.P. et al., *An evaluation of cardiac output by five arterial pulse contour techniques during cardiac surgery.* Anaesthesia, 2007. 62(8): p. 760.
9. Degtyarenko, K. et al., *ChEBI: a database and ontology for chemical entities of biological interest.* Nucleic Acids Research, 2007. 36, Database issue: p. D344–D350.
10. Frank, O., *Die grundform des arteriellen pulses.* Zeitschrift Fur Biologie, 1899. 37: p. 483–526.
11. Gennari, J.H. et al., *Integration of multi-scale biosimulation models via light-weight semantics.* Pacific Symposium on Biocomputing, 2008. 13: p. 414–425.
12. Gennari, J.H. et al., *Using Multiple Reference Ontologies: Managing Composite Annotations.* Proceedings of the International Conference on Biomedical Ontology. Buffalo, NY., 2009: p. 83–86.
13. *Gene Ontology*. http://www.geneontology.org/. Accessed 2009.
14. Hann, C.E. et al., *Integral-based parameter identification for long-term dynamic verification of a glucose-insulin system model.* Computer Methods and Programs in Biomedicine, 2005. 77(3): p. 259–270.
15. Heldt, T. et al., *Computational modeling of cardiovascular response to orthostatic stress.* Journal of Applied Physiology, 2002. 92(3): p. 1239.
16. Hucka, M. et al., *The systems biology markup language (SBML): a medium for representation and exchange of biochemical network models.* Bioinformatics, 2003. 19(4): p. 524–531.
17. *J Sim Home Page*. http://physiome.org/jsim/index.html. Accessed 2009.
18. Kass, D.A., *Cardiac resynchronization therapy.* Journal of Cardiovascular Electrophysiology, 2005. 16 Suppl 1: p. S35–S41.
19. Kerckhoffs, R.C.P. et al., *Effects of biventricular pacing and scar size in a computational model of the failing heart with left bundle branch block.* Medical Image Analysis, 2009. 13(2): p. 362–369.

20. Kouchoukos, N.T., L.C. Sheppard, and D.A. McDonald, *Estimation of stroke volume in the dog by a pulse contour method.* Circulation Research, 1970. 26(5): p. 611.
21. Le Novere, N. et al., *Minimum information requested in the annotation of biochemical models (MIRIAM).* Nature Biotechnology, 2005. 23(12): p. 1509–1515.
22. *LiDCO Cardiac Sensor Systems for measuring Cardiac Output*. http://lidco-ir.co.uk/. Accessed 2009.
23. Lu, K. et al., *A human cardiopulmonary system model applied to the analysis of the Valsalva maneuver.* American Journal of Physiology - Heart and Circulatory Physiology, 2001. 281(6): p. H2661–H2679.
24. *MIASE - Minimum Information About a Simulation Experiment*. http://www.ebi.ac.uk/comp-neur-srv/miase/. Accessed 2009.
25. Neal, M.L. and J.B. Bassingthwaighte, *Subject-specific model estimation of cardiac output and blood volume during hemorrhage.* Cardiovascular Engineering, 2007. 7(3): p. 97–120.
26. Neal, M.L. et al., *Advances in semantic representation for multiscale biosimulation: a case study in merging models.* Pacific Symposium on Biocomputing , 2009. 14: p. 304–315.
27. Neal, M.L. and R.C. Kerckhoffs, *Current progress in patient-specific modeling.* Briefings in Bioinformatics, 2010. 11(1): p. 111–126.
28. Parente, J. et al. *Model Based Insulin Sensitivity As A Metabolic Marker For Sepsis In The ICU*. 2008.
29. Pope, S.R. et al., *Estimation and identification of parameters in a lumped cerebrovascular model.* Mathematical BioSciences and Engineering, 2008. 6(1): p. 93–115.
30. Rideout, V.C., *Mathematical and computer modeling of physiological systems*. NJ, USA: Prentice Hall. 1991.
31. Rosse, C. and J.L.V. Mejino, *A reference ontology for bioinformatics: the foundational model of anatomy.* Journal of Biomedical Informatics, 2003. 36: p. 478–500.
32. Sagawa, K., R.K. Lie, and J. Schaefer, *Translation of Otto Frank's paper "Die Grundform des Arteriellen Pulses" Zeitschrift fur Biologie 37: 483–526 (1899).* Journal of Molecular and Cellular Cardiology, 1990. 22(3): p. 253–277.
33. Sanchez, R. and J.T. Mahoney, *Modularity, flexibility, and knowledge management in product and organization design.* Strategic Management Journal 1996. 17(Winter 1996): p. 63–76.
34. Schwid, H.A., *Anesthesia simulators: technology and applications*. The Israel Medical Association Journal. IMAJ-RAMAT GAN-, 2000. 2(12): p. 949–953.
35. Tolk, A., S.Y. Diallo, and C.D. Tunista, *Applying the Levels of Conceptual Interoperability Model in Support of Integratability, Interoperability, and Composability for System-of-Systems Engineering.* Journal of Systemics, Cybernetics and Informatics, 2008. 5(5): p. 65–74.
36. Van Herpe, T. et al., *An adaptive modeling approach for predicting the glycemia of critically ill patients.* Physiological Measurement, 2006. 27: p. 1057–1069.
37. Wakeland, W. et al., *Assessing the prediction potential of an in silico computer model of intracranial pressure dynamics.* Critical Care Medicine, 2009. 37(3): p. 1079–1089.
38. Wesseling, K.H. et al., *Computation of aortic flow from pressure in humans using a nonlinear, three-element model.* Journal of Applied Physiology, 1993. 74(5): p. 2566–2573.

Chapter 6
Biomechanical Analysis of Abdominal Aortic Aneurysms

Lambert Speelman, Mariëlle Bosboom, Geert W.H. Schurink, and Frans N.v.d. Vosse

6.1 Abdominal Aortic Aneurysm

The aorta is the largest artery in the human body, transporting oxygenized blood directly from the left ventricle of the heart to the rest of the body. An aortic aneurysm is a local dilation in the aorta of more than 1.5 times the original diameter [27]. Although aneurysms can be present in every part of the aorta, the majority of the aortic aneurysms are situated in the abdominal aorta (AAA, Fig. 6.1), below the level of the renal arteries and above the aortic bifurcation to the common iliac arteries [7]. A diameter of 3 cm or more is generally used as indication for an AAA (abdominal aortic aneurysm). In most AAAs, thrombus is found between the perfused flow lumen and the aortic wall. Thrombus is a fibrin structure with mainly blood cells, platelets, and blood proteins, which is deposited onto the vessel wall [21].

AAAs occur mostly in the elderly population. In the Western world, the prevalence of AAA in people over 65 years of age is 4–8% in men and 1–2% in women [13, 38]. Risk factors for AAA include advanced age, male gender, smoking, hypertension, positive family history, and atherosclerosis [31, 38].

AAAs are generally asymptomatic, until rupture of the AAA wall occurs. This can lead to a large abdominal bleeding and death within a short period of time. A ruptured AAA typically presents itself with acute abdominal pain and is, in most cases, combined with hemodynamic shock. The overall mortality rate for ruptured AAAs is around 90%, as a large group of patients with a ruptured AAA does not reach the hospital in time [3]. For those who reach the hospital in time, the mortality rates are as high as 50% [5, 26]. The overall mortality of AAA remains very high due to the fact that most AAAs are asymptomatic and therefore unknown. Screening programs have been proposed previously for men between 65 and 75 years old, who have ever smoked [28, 47]. Although screening can indeed reduce the AAA-related mortality by 50%, the costs per life year remain considerable [28].

L. Speelman (✉)
Biomechanics Laboratory, Department of Biomedical Engineering, Erasmus Medical Center Rotterdam, PO Box 2040, Ee2322, 3000 CA Rotterdam, The Netherlands
e-mail: l.speelman@erasmusmc.nl

R.C.P. Kerckhoffs (ed.), *Patient-Specific Modeling of the Cardiovascular System: Technology-Driven Personalized Medicine*, DOI 10.1007/978-1-4419-6691-9_6,

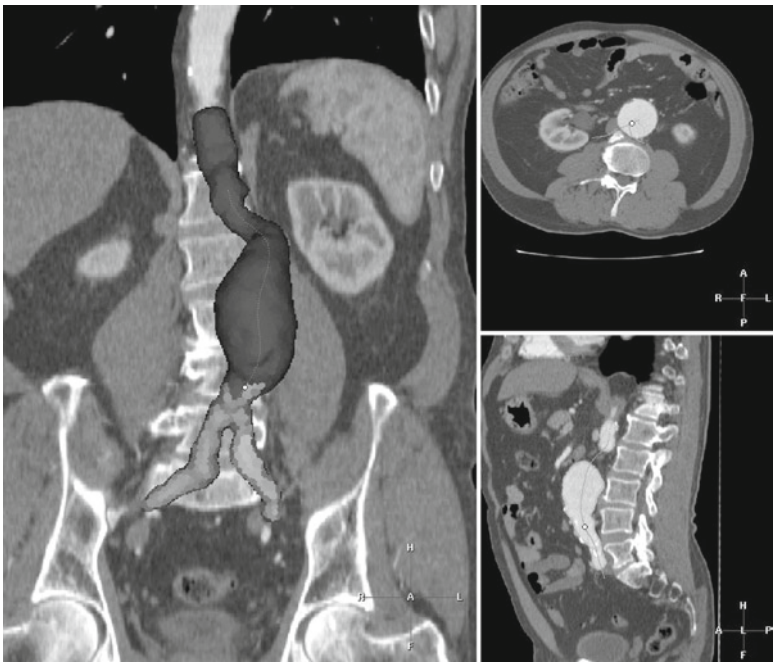

Fig. 6.1 Graphical representation of an abdominal aortic aneurysm

The main treatment option is to exclude the aneurysm wall from the systemic pressure, using a vascular graft. In open repair, a regular graft is sutured to healthy parts of the aorta by means of transabdominal surgery. This major surgical procedure has a 30-day mortality rate of about 5% [18]. Endovascular repair is an established alternative to open repair and is performed by placement of a stent graft in the AAA, via a small incision in the groin. It is associated with a lower perioperative mortality and a shorter recovery period than open repair [18]. Also in the long term, aneurysm-related mortality is lower for endovascular repair [33]. However, complications such as incomplete sealing, migration, kinking, or material failure of the stent graft may occur during the procedure or sometime afterward [41]. This leads to an elevated pressure inside the aneurysm and, in the worst case, rupture of the AAA wall [64]. Therefore, patients who underwent endovascular repair remain under surveillance, to evaluate the status of the stent graft on a regular basis [41].

6.2 AAA Risk Stratification

To determine when an AAA requires surgical intervention, the risk of AAA rupture should carefully be weighed against the risk of the operative procedure. In current clinical practice, the risk of rupture is based on the maximum anterior–posterior

diameter, and an elective repair procedure is initiated when the diameter reaches 5.5 cm or when the diameter grows more than 1 cm per year [19]. In 1977, 24,000 nonspecific autopsy reports were studied, and 473 nonresected AAAs were found, of which 118 were ruptured [8]. Of the 265 aneurysms smaller than 5.0 cm, 12.8% were ruptured, indicating that for a significant number of small AAAs, the elective repair threshold of 5.5 cm in diameter is too high. Previously, rupture rate of large AAAs with medical contraindication or patient refusal for elective repair was studied [30]. The 1-year incidence of probable rupture was 9% for AAAs with diameters 5.5–5.9 cm. This increased to 33% for AAAs more than 7 cm in diameter. Although the 1-year incidence is substantially for AAAs over 5.5 cm in diameter, the majority of patients with large aneurysms will not (yet) experience rupture. These patients would be subjected to unnecessary surgical risks in case of elective AAA repair. For more accurate rupture risk stratification, patient-specific parameters, other than the diameter, have to be considered.

Besides maximum diameter, it is advised to include the growth in diameter in the decision for AAA repair [19, 63]. When a patient is known to have an AAA, follow-up is, in most cases, done by the ultrasound examination to evaluate the maximum diameter and the diameter growth. The AAA growth is believed to increase with the initial diameter of the AAA [46, 57]. However, a large variation in growth rate is found between AAAs. While some AAAs remain stable for a considerable period of time, others show a strong increase in diameter in a short period or grow discontinuously, with alternating periods of growth and shrinkage [29, 58]. Prediction of the future expansion rate of an AAA in an early stage can be used to optimize the follow-up schedule and intervention plans for each patient.

So far, both aneurysm rupture and growth are unpredictable by the diameter alone. Better predictors for rupture and growth are required and may be found in a more extended patient-specific analysis, based on biomechanical information.

6.3 AAA Biomechanical Analysis

From a biomedical engineering point of view, mechanical forces play an imminent role in rupture of the AAA wall. When the stress on the AAA wall, caused by the blood pressure, locally exceeds the strength of the wall, rupture of the wall occurs. The law of Laplace states that the wall stress (σ) in a thin-walled cylinder linearly increases with increasing radius (r) and transmural pressure (P), and decreases for increasing wall thickness (h):

$$\sigma = \frac{P \bullet r}{h} \tag{6.1}$$

Due to the complex geometry of most AAAs, the wall stress is determined by the local AAA geometry and wall thickness, and can therefore not be predicted by the law of Laplace, or based on simplified geometrical models [25]. The 3D wall stress distribution of the AAA wall can be computed using the finite

element method. A 3D model of the AAA first has to be created, based on 3D imaging. The derivation of this model is called segmentation and meshing of the AAA. The finite element model of the AAA comprises small subsections, the so-called finite elements. The wall stress computations are based on conservation of mass and momentum (second law of Newton) for all finite elements in the model. Boundary conditions are required to solve the complex system of conservation laws. These comprehend, in addition to the applied pressure on the inner surface of the AAA model, complete fixation of the most proximal and distal planes of the model. Also, a choice of material models for the components in the model is required to solve the computational system.

Several research groups have previously focused on AAA wall stress, computed with a finite element model, as a clinical measure for aneurysm rupture risk [15, 37, 49, 59]. Early patient-specific wall stress computations have shown that peak wall stress for ruptured and symptomatic AAAs was significantly higher than that of electively repaired or asymptomatic AAAs [15, 49]. In most cases, the segmentation of the AAA is performed manually, and labor-intensive procedures are followed to generate the finite element model. Also, as in every model, simplifications and assumptions are made concerning factors that are difficult or impossible to determine, like local wall thickness and initial wall stress. The incorporation of thrombus and calcifications is also ignored in most cases, as the correct implementation in the analysis is not known. It is unclear to what extent these simplifications or assumptions influence the resulting wall stress on a patient-specific basis. This, and the fact that the derivation of the 3D model is complex and labor-intensive, dissuades an easy translation to a clinical environment. The focus of the remainder of this chapter is on optimization and standardization of AAA wall stress analyses for future diagnostic purposes.

For the purpose of a future introduction of wall stress analyses as a clinical diagnostic tool, Philips Healthcare (Best, the Netherlands) developed a software package HemoDyn, in collaboration with the University Medical Center Utrecht (the Netherlands), Philips Research (Paris, France), Eindhoven University of Technology, and Maastricht University Medical Center [6, 10, 11, 16, 36, 42, 43]. This package is developed within the Philips ViewForum environment, which is widely used for visualization and analysis of medical images within clinical centers. HemoDyn uses automatic segmentation and meshing procedures and is used in the majority of the research presented here. Other comparable initiatives to create automatic procedures for AAA wall stress computations are currently being developed.

6.3.1 Wall Stress Reproducibility

HemoDyn uses automatic segmentation and meshing procedures to minimize the user input in the wall stress analysis [6]. Based on the selection of only three points in the lumen of the AAA in the Computed Tomography Angiography (CTA) data

of the patient (one starting point at the level of the lowest renal branch and two end points in the iliac arteries, proximal to the aortic bifurcation), automatic centerline tracking and subsequent 3D segmentation of the lumen and the thrombus is performed. This highly automated process should increase the stability and reproducibility of the wall stress analyses. Inter- and intraoperator reliability of peak wall stress was previously evaluated, using a manual segmentation procedure with ten AAAs [23]. Interoperator variation was found over 100% between the lowest and highest stress value for the same patient. A double analysis on ten patients by one operator resulted in differences up to 40%.

Reproducibility of the AAA wall stress was determined using HemoDyn, by evaluating CTA data of 20 patients by three different operators [43]. Two operators performed the analyses five times. The intraoperator intraclass correlation coefficient (ICC) of the peak wall stress was 0.73 and 0.79, while the interoperator ICC was 0.71. This approached the findings of the aforementioned study [23]. The 99-percentile wall stress proved to be a more reproducible wall stress parameter than peak wall stress (intraoperator ICC 0.94, 0.94 and interoperator ICC 0.95). The 99-percentile wall stress is computed as the highest wall stress in the AAA wall after exclusion of 1% of the wall, containing the highest stresses [43]. This is illustrated in Fig. 6.2, in a typical histogram of the wall stress of an AAA. The number of nodes between the 99-percentile wall stress and the peak wall stress occupies only 1% of the total wall surface. Small subtle shape changes induced by the segmentation of different operators, strongly influences this part of the histogram, while this effect was significantly lower for the 99-percentile wall stress.

A strong linear relation between the 99-percentile wall stress and the maximum AAA diameter for the 20 patients analyzed indicates that the 99-percentile wall

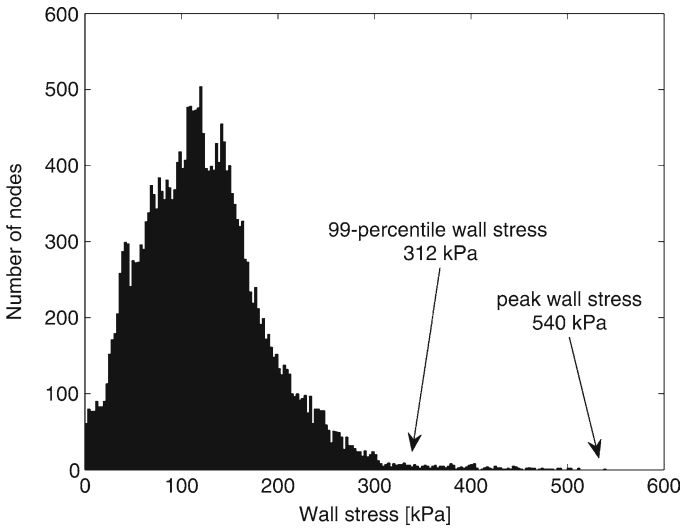

Fig. 6.2 Typical AAA wall stress histogram indicating the 99-percentile and peak wall stress

stress can still discriminate between AAAs of different sizes. It is, therefore, a more robust and reproducible stress parameter than the peak wall stress.

6.3.2 Initial Stress

During CTA imaging, the AAA is subjected to a time-averaged blood pressure and is therefore not stress free. However, until recently, all patient-specific wall stress studies ignored this fact and applied a systolic blood pressure directly to the geometry derived from the CTA data (conventional method). The Backward Incremental (BI) method was introduced by de Putter et al. (2007), to account for the initial stress in AAAs [10]. The BI method was validated by showing a strong correspondence between the computed systolic and diastolic AAA geometries and the systolic and diastolic geometries from gated MRI measurements in three AAAs. It was also shown that, when using the BI method, the wall motion as computed with AAA wall stress analyses, significantly better corresponded to the gated MRI wall motion for ten patients [34].

For a complete description of the BI method, the reader is referred to [42]. In the same study, the effect of neglecting the initial stress on the AAA wall stress of patient-specific AAA models using the BI method was investigated [42]. The 99-percentile wall stress was computed with and without initial stress, using both a linear and nonlinear material model for the AAA wall. The results clearly showed that ignoring initial stress, as is the case in the conventional method, leads to an overestimation of the systolic aneurysm volume and a change in surface curvature (Fig. 6.3). This leads to a change in wall stress for each AAA, although this change was different for each patient. This indicates that no general correction factor can be used to estimate the effect on the wall stress. Therefore, initial stress cannot be omitted in patient-specific wall stress studies.

6.3.3 Intraluminal Thrombus

As previously indicated, the majority of the AAAs contain thrombus, defined as an accumulation of blood cells, platelets, and blood proteins, which is deposited on the inside of the aneurysm wall. The volume and thickness of thrombus have previously been indicated to influence the growth rate and rupture risk of AAAs [20, 63]. Recently, mechanical tests have resulted in a lower stiffness of the thrombus than was previously assumed [2, 52]. Van Dam et al. (2008) found thrombus shear moduli around 2 kPa [52], while Wang et al. (2001) presented up to 180 kPa for thrombus [61]. In the light of these recent results, the mechanical role of thrombus was evaluated by computing wall stress with and without thrombus in idealized axisymmetric AAA models with various thrombus stiffnesses and volumes, and in 30 patient-specific AAA models [45]. Additionally, the growth rate of these AAAs was prospectively monitored and a comparison was made between the growth rate of AAAs with relative small and large thrombi.

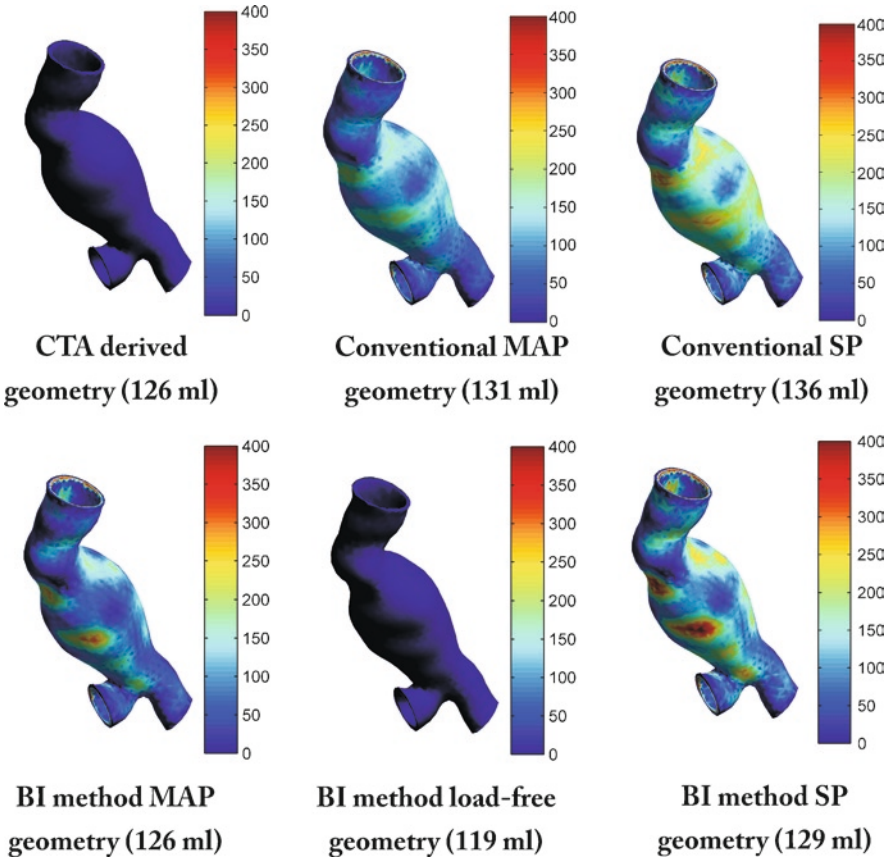

Fig. 6.3 The AAA wall stress distributions for one AAA at mean arterial pressure (MAP) and peak systolic pressure (SP) with the conventional method (*top*) and with the BI method (*bottom*). Also the CTA-derived geometry and the backward computed load-free geometry are displayed. The volume of each geometry is displayed in milliliters

The results from the idealized AAA model showed that the decrease in wall stress due to the presence of thrombus strongly depends on the shear modulus and volume of the thrombus. The relation between the decrease in wall stress and the shear modulus was found to be nonlinear; the decrease in wall stress is less influenced by a change in shear modulus at higher shear moduli. The recently reported shear moduli based on shear and compression experiments were found to be in the order of 10 kPa [24], or even lower [2, 52]. However, the same studies also reported considerable variations in shear modulus, indicating that between and within different thrombi, the shear modulus may vary markedly. Considering that the resulting wall stress is strongly influenced by the shear modulus, the choice of using an average shear modulus for each thrombus in AAA wall stress analyses may therefore not be valid.

A considerable variation in effect was found in the patient data. Likely, not only the amount of thrombus influences the wall stress but also the geometry of the AAA and the thrombus. Therefore, to estimate the effect of thrombus on the patient-specific

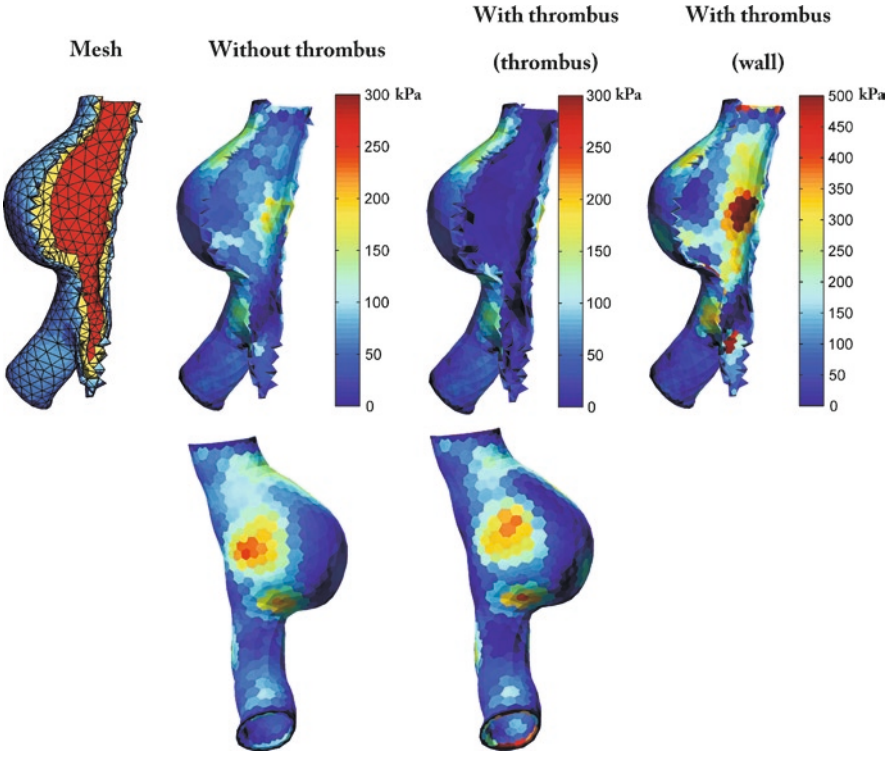

Fig. 6.4 AAA wall stress distribution with and without thrombus

wall stress, idealized models are inadequate, and patient-specific models are required (Fig. 6.4). The diameter growth rate was significantly higher in the group with a large thrombus ($p<0.01$). This supports findings from previous research on the relation between thrombus and AAA growth [63]. The wall stress was significantly lower for the large thrombus group when thrombus was incorporated ($p<0.01$). This suggests that diameter growth of AAAs is not instigated by the stress in the wall. In earlier research, thrombus thickness was identified as one of the parameters that lowers the strength of the AAA wall [55, 60]. If this wall weakening is the basis for AAA growth, this may explain the increased growth for AAAs with a relative large thrombus. Future research may evaluate the relation between the amount of thrombus, wall weakening and the growth in diameter of AAAs.

6.3.4 Material Properties

The choice of material model that is used for the aneurysm wall in the finite element models can have a strong impact on the resulting wall stress. Extensive mechanical testing on a large data set has resulted in a commonly used hyper-elastic,

nonlinear material model for the AAA wall in general [40]. It was shown that the wall stresses only changed by 4% or less when the parameters of the material model were changed within the 95% confidence intervals for the studied patient population.

However, a considerable variation was shown in parameters on a patient-specific scale. A first step in determining patient-specific material parameters was done recently [53]. Distensibility and compliance of AAAs were determined in vivo for ten patients by simultaneously measuring pressure and volume changes of the AAA, based on dynamic MRI measurements. A strong linear relation between pressure and volume was found. This enables a direct computation of the compliance, being the slope of the pressure–volume relation. The stiffness or Young's modulus of the AAA wall can then be estimated, under the assumptions of a uniform 2 mm wall thickness and incompressibility. Accurate measurements were obtained in eight patients, resulting in Young's moduli between 5.5 and 12.9 MPa [53]. Due to the linear relation between pressure and volume, it suffices to know the diastolic and systolic blood pressure and volumes, by means of dynamic imaging, to estimate the patient-specific AAA stiffness. Future developments of this noninvasive method may result in local nonlinear and even anisotropic material properties, by evaluating the local wall deformation patterns instead of the total AAA volume.

6.3.5 Future Directions

The previous sections have described the current status of several important parameters in patient-specific AAA wall stress analyses. However, further evaluation of these parameters may increase sensitivity and specificity of wall stress as a clinical parameter in diagnosis of AAA.

The 99-percentile wall stress showed to be more robust and less sensitive to the variations introduced by different operators. However, a patient study is required to establish the clinical relevance of the 99-percentile wall stress in the rupture risk stratification, by comparing the 99-percentile wall stress for ruptured and nonruptured AAAs.

Also, further evaluation of the mechanical material models for the AAA wall and the thrombus is required. It is extremely difficult to evaluate the properties of the constituents separately. Local nonlinear and nonisotropic material behavior may be determined by evaluating the local wall deformation patterns. However, higher resolution 3D imaging is an important requisite for this analysis. Developments in dynamic MRI and CT may facilitate these patient-specific analyses. Furthermore, advances in (3D) ultrasound may attribute to determining local mechanical properties in a patient-specific manner.

In the discussed AAA wall stress studies, thrombus in the AAAs has been modeled as a solid structure. Modeling thrombus as a porous material may be more appropriate, considering the poroelastic character of thrombus [1, 4]. In that case,

the pressure can be transferred through the pores of the material. The effect that a poroelastic material model for the thrombus has on the wall stress cannot be predicted on forehand. Parameters like porosity and viscous permeability first need to be determined by experimental testing before wall stress computations can be extended with a porous material model for thrombus. Evaluation of the thrombus deformations over the cardiac cycle using dynamic imaging, in combination with finite element modeling may contribute to this development [48].

6.4 Clinical Application

More insight in the pathogenic pathways of aneurysm formation and progression may be gathered by evaluating circulating biomarker concentrations [17, 50]. Circulation matrix metalloproteinase-9 (MMP-9) concentrations have been investigated most frequently in association with AAA. MMP-9 is involved in the breakdown of the extracellular matrix and, in most studies, was found to be elevated in AAAs compared to healthy subjects [17]. Also, the tissue inhibitor of MMP-1 (TIMP1) was found to be increased in AAA patients compared to healthy controls [35]. The markers of inflammation interleukin-6 (IL-6) and C-reactive protein (CRP) are frequently studied in cardiovascular disease and were found to be elevated in the presence of AAA in most studies [17]. Besides, serum CRP concentration was also associated with the size of AAA [51].

Also, AAA growth was investigated in relation to biomarkers. Again, MMP-9 was correlated with AAA expansion rate [32]. In the same study, it was found that alpha 1-antitrypsin (α1-AT) was weakly correlated with AAA expansion rate [32]. α1-AT is an inhibitor of alpha 1-trypsin that inhibits elastase. Elastase, on its turn, actively breaks down elastic fibers in the aortic wall.

Biomarkers as predictor for AAA rupture have been relatively little investigated. Engström et al. (2004) concluded that the incidence of fatal or repaired AAA was associated with a higher number and levels of inflammation-sensitive plasma proteins [14]. CRP levels in patients with symptomatic or ruptured AAAs were significantly higher than that in patients with an asymptomatic AAA [12]. Also, MMP-1 and MMP-9 were elevated in the plasma of ruptured AAA versus nonruptured AAA and elevation of MMP-9 was associated with ruptured AAA related 30-day mortality [62].

Numerous studies have focused on measuring biomarker concentrations in order to predict AAA presence, growth or rupture, but most studies have not assessed the value of these markers as diagnostic tests for AAA [17, 50, 51, 56]. Biomarkers may play a role in the identification of small AAAs. Additionally, when biomarkers associated with AAA are identified, targeted medical treatment may be developed to slow down AAA progression. For now, sensitivity and specificity appear inadequate for the use of single biomarkers alone in diagnosis [17]. Using multiple biomarkers in combination with other AAA related factors might prove to be of value in the diagnostics of AAA.

A first step to clinical applicability of AAA wall stress analysis was made, by comparing AAA wall stress, growth rate, and biomarker concentrations in the blood of patients [44]. It was hypothesized that AAAs with a high wall stress, relative to the average wall stress at the corresponding diameter, have increased damage and degeneration of the AAA wall. This could reflect on AAA growth and the up- or down-regulation of specific circulating biomarkers. The 99-percentile wall stress was determined with incorporation of the initial stress and a nonlinear material model for the AAA wall, but without thrombus and calcifications. A relative medium or high wall stress was indeed found to be associated with a higher AAA growth rate compared to AAAs with a relatively low wall stress. Also, the MMP-9 concentration, which is involved in the breakdown of the extra cellular matrix, was positively related to AAA growth rate. Although the average concentrations of MMP-9 and CRP (a marker for inflammation) showed an increase for higher relative wall stress, no significant correlation was found between wall stress and biomarkers levels analyzed in this study. Further analysis is warranted to verify the relation between AAA wall stress, growth rate and biomarker concentrations.

6.5 Scope and Limitations

Future diagnostic purposes for AAA wall stress analyses may include an estimation parameter for AAA rupture risk, in addition to the currently used decision parameters, but also the prediction of the AAA growth rate. A dynamic follow-up plan can then be developed based on the computed wall stress. Some patients may require more frequent hospital visits, while others, as their AAA remains stable over a longer period, can suffice with long interval follow-up.

The first step to clinical applicability of wall stress is made. A robust and reproducible stress measure is proposed and important factors influencing the wall stress have been identified. Several limitations and assumptions remain that may improve the stress analysis. One of the major assumptions that is inevitable is that of a constant wall thickness over the whole aneurysm model. It is known that a strong variation in wall thickness exists between, but also within patients [22, 39]. Including the local variation in wall thickness can have a strong effect on the resulting wall stress. Currently, no non-invasive methods are available that can reliably determine the local wall thickness. CTA cannot provide information on the location of the thrombus–wall transition and therefore no wall thickness can be determined. Most MRI protocols can also not be used due to chemical shift artifacts, caused by the transition between water-rich and fat-rich tissues, and due to the large voxel size, relative to the expected wall thickness. Black-blood MRI sequences may reach sufficient resolution, but no discrimination between wall and thrombus can yet be made with this protocol, and thus no wall thickness can be measured in the presence of thrombus. Although ultrasound evaluation can be used to determine the local AAA wall thickness, the wall thickness cannot be determined over the whole AAA. Using intravascular ultrasound (IVUS), a complete wall thickness map can be made, but

this medical imaging technique is expensive, time-consuming and is considered as an intervention. This makes IVUS unsuitable for follow-up of AAA patients. Developments in (3D) ultrasound imaging and advanced MRI sequences may in the future facilitate non-invasive local wall thickness measurements of AAAs.

Another limitation is the mechanical material model that is used for the AAA wall and the thrombus. Extensive mechanical testing has resulted in a commonly used hyper-elastic, nonlinear material model for the average AAA wall [40]. However, considerable variation in AAA wall stiffness was observed. In studies evaluating thrombus material properties, a wide spread in mechanical behavior was found between and within the tested thrombi [52, 61]. This hampers the use of a single shear modulus for both wall and thrombus in patient-specific wall stress analyses. By using dynamic MRI measurements to determine the distensibility of the AAA in combination with simultaneous pressure recordings, van't Veer et al. (2008) determined patient-specific Young's moduli for the AAA wall noninvasively [53]. Future developments of this method may result in local nonlinear and even anisotropic material properties, by evaluating the local wall deformation patterns instead of the total AAA volume. Also patient-specific material properties of thrombus may be determined by evaluating the thrombus deformations over the cardiac cycle in dynamic MRI measurements [48].

In most AAAs, calcifications are present in the wall of the aneurysm. Research on these calcifications using high-resolution micro-CT revealed that what appears as a solid, uniform calcification in normal resolution CTA images, may in fact be a complex arrangement of smaller calcified areas [9]. This means that it is of little use to accurately model the shape and the material interface of the calcification, based on the normal CTA image data. The resolution is too low to capture the required details. Future research should therefore focus on accurately establishing the material properties of calcified regions and on experimentally assessing the rupture potential of the calcifications, the material interface and the surrounding non-calcified tissue.

Most biomechanical considerations of AAAs have focused on computing stresses acting on the aneurysm wall, and not on the wall strength. This is, however, an equally important part in rupture risk prediction, since rupture occurs when the stresses exceed the strength of the wall. If only the wall stress is considered and a certain stress threshold is determined that indicates a high risk of rupture, this corresponds with the choice of a uniform failure strength throughout the AAA. Vande Geest et al. (2006) proposed a Rupture Potential Index (RPI), which combines the wall stress computed with finite element analysis and the wall strength, estimated with a seven parameter statistical model (age, gender, family history of AAA, smoking status, AAA size, local diameter, and local thrombus thickness) [54, 55]. The results suggested that the peak RPI may be better able to identify those AAAs at high risk of rupture than maximum diameter or peak wall stress alone. Future developments in medical imaging quality to obtain local wall thickness may also add to this strength estimation. The clinical relevance of this method for rupture assessment has yet to be validated; however, its success could aid clinicians in decision-making and AAA patient management [54].

6.6 Clinical Perspectives

Although future research is required to further increase the accuracy of the wall stress analyses, the currently available model is close to be clinically applicable. However, the clinical relevance, which is much more important, has only been touched swiftly. A significant positive stress–diameter relation was identified, and it was shown that a relative high wall stress was associated with a higher growth rate. The ultimate question whether AAA rupture risk can be predicted based on wall stress cannot (yet) be answered. However, tools have been created, and important factors have been identified in the process of wall stress computations. The road is now free to investigate the clinical relevance of wall stress with respect to AAA rupture risk and growth. As more and more AAA patients in follow-up are followed using CTA instead of ultrasound, the basis of this study is already present. Continuous follow-up with CTA of a large group of patients can give insight in the relation of AAA wall stress and growth rate. As AAA rupture is a relatively rare phenomenon, especially in the combination with recent prerupture CTA imaging, a large prospective patient study is required. The @neurist program can therefore be taken as an example (see http://www.aneurist.org). This program integrates biomedical information for the management of cerebral aneurysms. A large collaboration between multiple health organizations in several countries created an infrastructure for combining data of cerebral aneurysms with the goal to provide individualized aneurysm rupture predictions. Such an infrastructure may also be of high value in the rupture risk estimation of AAAs.

6.7 Conclusion

Although the basis for AAA wall stress to be incorporated in clinical diagnostics has been created, the clinical relevance of AAA wall stress is still unknown. Based on the research discussed here, one can conclude that a standardized AAA wall stress analysis using automatic segmentation is required. Additionally, initial stress and material nonlinearity are undisputable elements in the finite element simulations. To be able to conclude on the role of thrombus, future research on the material properties and interface with the surroundings is required. Patient-specific cardiac gated imaging may play an important role in the determination of the material properties. Also, developments in the wall strength estimation are essential for accurate risk estimation. With the foundation that has been laid, the road is open for profound patient studies to evaluate the clinical relevance of AAA wall stress in relation to the AAA rupture risk and growth rate.

References

1. Adolph, R., Vorp, D.A., Steed, D.L., Webster, M.W., Kameneva, M.V., Watkins, S.C.: Cellular content and permeability of intraluminal thrombus in abdominal aortic aneurysm. J. Vasc. Surg. **25**(5), 916–926 (1997)

2. Ashton, J.H., vande Geest, J.P., Simon, B.R., Haskett, D.G.: Compressive mechanical properties of the intraluminal thrombus in abdominal aortic aneurysms and fibrin-based thrombus mimics. J. Biomech. **42**(3), 197–201 (2009)
3. Basnyat, P.S., Biffin, A.H., Moseley, L.G., Hedges, A.R., Lewis, M.H.: Mortality from ruptured abdominal aortic aneurysm in Wales. Br. J. Surg. **86**(6), 765–770 (1999)
4. Boschetti, F., di Martino, E., Gioda, G.: A poroviscoelastic model of intraluminal thrombus from abdominal aortic aneurysms. Proceedings of the 2007 Summer Bioengineering Conference, Keystone CO (2007)
5. Bown, M.J., Sutton, A.J., Bell, P.R., Sayers, R.D.: A meta-analysis of 50 years of ruptured abdominal aortic aneurysm repair. Br. J. Surg. **89**(6), 714–730 (2002)
6. Breeuwer, M., de Putter, S., Kose, U., Speelman, L., Visser, K., Gerritsen, F., Hoogeveen, R., Krams, R., van den Bosch, H., Buth, J., Gunther, T., Wolters, B., van Dam, E., van de Vosse, F.: Towards patient-specific risk assessment of abdominal aortic aneurysm. Med. Biol. Eng. Comput. **46**(11), 1085–1095 (2008)
7. Crawford, E.S., Cohen, E.S.: Aortic aneurysm: a multifocal disease. Arch. Surg. **117**(11), 1393–1400 (1982)
8. Darling, R.C., Messina, C.R., Brewster, D.C., Ottinger, L.W.: Autopsy study of unoperated abdominal aortic aneurysms. The case for early resection. Circulation **56**(Suppl 3), II161–II164 (1977)
9. de Putter, S., van de Vosse, F.N., Breeuwer, M., Gerritsen, F.A.: Local influence of calcifications on the wall mechanics of abdominal aortic aneurysm. Prog. Biomed. Opt. Imaging **7**(2), 61432E.1–61432E.11 (2006)
10. de Putter, S., Wolters, B.J., Rutten, M.C., Breeuwer, M., Gerritsen, F.A., van de Vosse, F.N.: Patient-specific initial wall stress in abdominal aortic aneurysms with a backward incremental method. J. Biomech. **40**(5), 1081–1090 (2007)
11. Delingette, H.: Modélisation, déformation et reconnaissance d'objets tridimensionnels a l'aide de maillages simplexes. Ph.D. thesis, Ecole Centrale de Paris (1994)
12. Domanovits, H., Schillinger, M., Mullner, M., Holzenbein, T., Janata, K., Bayegan, K., Laggner, A.N.: Acute phase reactants in patients with abdominal aortic aneurysm. Atherosclerosis **163**(2), 297–302 (2002)
13. Eckstein, H.H., Bockler, D., Flessenkamper, I., Schmitz-Rixen, T., Debus, S., Lang, W.: Ultrasonographic screening for the detection of abdominal aortic aneurysms. Dtsch. Arztebl. Int. **206**(41), 657–663 (2009)
14. Engstrom, G., Borner, G., Lindblad, B., Janzon, L., Lindgarde, F.: Incidence of fatal or repaired abdominal aortic aneurysm in relation to inflammation-sensitive plasma proteins. Arterioscler. Thromb. Vasc. Biol. **24**(2), 337–341 (2004)
15. Fillinger, M.F., Raghavan, M.L., Marra, S.P., Cronenwett, J.L., Kennedy, F.E.: In vivo analysis of mechanical wall stress and abdominal aortic aneurysm rupture risk. J. Vasc. Surg. **36**(3), 589–597 (2002)
16. Gérard, O., Billon, A.C., Rouet, J.M., Jacob, M., Fradkin, M., Allouche, C.: Efficient model-based quantification of left ventricular function in 3-d echocardiography. IEEE Trans. Med. Imaging **21**(9), 1059–1068 (2002)
17. Golledge, J., Tsao, P.S., Dalman, R.L., Norman, P.E.: Circulating markers of abdominal aortic aneurysm presence and progression. Circulation **118**(23), 2382–2392 (2008)
18. Greenhalgh, R.M., Brown, L.C., Kwong, G.P., Powell, J.T., Thompson, S.G.: Comparison of endovascular aneurysm repair with open repair in patients with abdominal aortic aneurysm (EVAR trial 1), 30-day operative mortality results: randomised controlled trial. Lancet **364**(9437), 843–848 (2004)
19. Greenhalgh, R.M., Forbes, J.F., Fowkes, F.G., Powel, J.T., Ruckley, C.V., Brady, A.R., Brown, L.C., Thompson, S.G.: Early elective open surgical repair of small abdominal aortic aneurysms is not recommended: results of the UK small aneurysm trial. Eur. J. Vasc. Endovasc. Surg. **16**(6), 462–464 (1998)
20. Hans, S.S., Jareunpoon, O., Balasubramaniam, M., Zelenock, G.B.: Size and location of thrombus in intact and ruptured abdominal aortic aneurysms. J. Vasc. Surg. **41**(4), 584–588 (2005)

21. Harter, L.P., Gross, B.H., Callen, P.W., Barth, R.A.: Ultrasonic evaluation of abdominal aortic thrombus. J. Ultrasound Med. **1**(8), 315–318 (1982)
22. Hellenthal, F.A., Geenen, I.L., Teijink, J.A., Heeneman, S., Schurink, G.W.: Histological features of human abdominal aortic aneurysm are not related to clinical characteristics. Cardiovasc. Pathol. **18**(5), 286–293 (2008)
23. Heng, M.S., Fagan, M.J., Collier, J.W., Desai, G., McCollum, P.T., Chetter, I.C.: Peak wall stress measurement in elective and acute abdominal aortic aneurysms. J. Vasc. Surg. **47**(1), 17–22 (2008)
24. Hinnen, J.W., Rixen, D.J., Koning, O.H., van Bockel, J.H., Hamming, J.F.: Development of fibrinous thrombus analogue for in-vitro abdominal aortic aneurysm studies. J. Biomech. **40**(2), 289–295 (2007)
25. Hua, J., Mower, W.R.: Simple geometric characteristics fail to reliably predict abdominal aortic aneurysm wall stresses. J. Vasc. Surg. **34**(2), 308–315 (2001)
26. Johnston, K.W.: Ruptured abdominal aortic aneurysm: six-year follow-up results of a multicenter prospective study. J. Vasc. Surg. **19**(5), 888–900 (1994)
27. Johnston, K.W., Rutherford, R.B., Tilson, M.D., Shah, D.M., Hollier, L., Stanley, J.C.: Suggested standards for reporting on arterial aneurysms. J. Vasc. Surg. **13**(3), 452–458 (1991)
28. Kim, L.G., Ra, P.S., Ashton, H.A., Thompson, S.G.: A sustained mortality benefit from screening for abdominal aortic aneurysm. Ann. Intern. Med. **146**(10), 699–706 (2007)
29. Kurvers, H., Veith, F.J., Lipsitz, E.C., Ohki, T., Gargiulo, N.J., Cayne, N.S., Suggs, W.D., Timaran, C.H., Kwon, G.Y., Rhee, S.J., Santiago, C.: Discontinuous, staccato growth of abdominal aortic aneurysms. J. Am. Coll. Surg. **199**(5), 709–715 (2004)
30. Lederle, F.A., Johnson, G.R., Wilson, S.E., Ballard, D.J., Jordan, W.D., Blebea, J., Littooy, F.N., Freischlag, J.A., Bandyk, D., Rapp, J.H., Salam, A.A.: Rupture rate of large abdominal aortic aneurysms in patients refusing or unfit for elective repair. JAMA **287**(22), 2968–2972 (2002)
31. Lederle, F.A., Johnson, G.R., Wilson, S.E., Chute, E.P., Littooy, F.N., Bandyk, D., Krupski, W.C., Barone, G.W., Acher, C.W., Ballard, D.J.: Prevalence and associations of abdominal aortic aneurysm detected through screening. Ann. Intern. Med. **126**(6), 441–449 (1997)
32. Lindholt, J.S., Vammen, S., Fasting, H., Henneberg, E.W., Heickendorff, L.: The plasma level of matrix metalloproteinase 9 may predict the natural history of small abdominal aortic aneurysms. A preliminary study. Eur. J. Vasc. Endovasc. Surg. **20**(3), 281–285 (2000)
33. Lovegrove, R.E., Javid, M., Magee, T.R., Galland, R.B.: A meta-analysis of 21,178 patients undergoing open or endovascular repair of abdominal aortic aneurysm. Br. J. Surg. **95**(6), 677–684 (2008)
34. Merkx, M.A., van't Veer, M., Breeuwer, M., Bosboom, E.M., van de Vosse, F.N.: Importance of initial stress incorporation in abdominal aortic aneurysm wall motion: dynamic MRI validated finite element analysis. J. Biomech. **42**(14), 2369–2373 (2009)
35. Nakamura, M., Tachieda, R., Niinuma, H., Ohira, A., Endoh, S., Hiramori, K., Makita, S.: Circulating biochemical marker levels of collagen metabolism are abnormal in patients with abdominal aortic aneurysm. Angiology **51**(5), 385–392 (2000)
36. Ollabarriaga, S.D., Rouet, J.M., Fradkin, M., Breeuwer, M., Niessen, W.J.: Segmentation of thrombus in abdominal aortic aneurysms from CTA with non-parametric statistical grey level appearance modeling. IEEE Trans Med Imaging **24**(4), 477–485 (2005)
37. Papaharilaou, Y., Ekaterinaris, J.A., Manousaki, E., Katsamouris, A.N.: A decoupled fluid structure approach for estimating wall stress in abdominal aortic aneurysms. J. Biomech. **40**(2), 367–377 (2007)
38. Pleumeekers, H.J., Hoes, A.W., van der Does, E., van Urk, H., Hofman, A., de Jong, P.T., Grobbee, D.E.: Aneurysms of the abdominal aorta in older adults. The Rotterdam study. Am. J. Epidemiol. **142**(12), 1291–1299 (1995)
39. Raghavan, M.L., Kratzberg, J., de Tolosa, E.M.C., Hanaoka, M.M., Walker, P., da Silva, E.S.: Regional distribution of wall thickness and failure properties of human abdominal aortic aneurysm. J. Biomech. **39**(16), 3010–3016 (2006)

40. Raghavan, M.L., Vorp, D.A.: Toward a biomechanical tool to evaluate rupture potential of abdominal aortic aneurysm: identification of a finite strain constitutive model and evaluation of its applicability. J. Biomech. **33**(4), 475–482 (2000)
41. Sandford, R.M., Bown, M.J., Sayers, R.D., Fishwick, G., London, N.J., Nasim, A.: Endovascular abdominal aortic aneurysm repair: 5-year follow-up results. Ann. Vasc. Surg. **22**(3), 372–378 (2008)
42. Speelman, L., Bosboom, E.M., Schurink, G.W., Buth, J., Breeuwer, M., Jacobs, M.J., van de Vosse, F.N.: Initial stress and nonlinear material behavior in patient-specific AAA wall stress analysis. J. Biomech. **42**(11), 1713–1719 (2009)
43. Speelman, L., Bosboom, E.M., Schurink, G.W., Hellenthal, F.A., Buth, J., Breeuwer, M., Jacobs, M.J., van de Vosse, F.N.: Patient-specific AAA wall stress analysis: 99-percentile versus peak stress. Eur. J. Vasc. Endovasc. Surg. **36**(6), 668–676 (2008)
44. Speelman, L., Hellenthal, F.A., Pulinx, B., Bosboom, E.M., van de Vosse, F.N., Jacobs, M.J., Breeuwer, M., van Sambeek, M.J.H.M., Wodzig, W.K.W.H., Schurink, G.W.: The influence of wall stress on AAA growth and biomarkers. Eur. J. Vasc. Endovasc. Surg. **39**(4), 410–416 (2010)
45. Speelman, L., Schurink, G.W., Bosboom, E.M., Buth, J., Breeuwer, M., van de Vosse, F.N., Jacobs, M.J.: The mechanical role of thrombus on the growth rate of an AAA. J. Vasc. Surg. **51**(1), 19–26 (2010)
46. Stonebridge, P.A., Draper, T., Kelman, J., Howlett, J., Allan, P.L., Prescott, R., Ruckley, C.V.: Growth rate of infrarenal aortic aneurysms. Eur. J. Vasc. Endovasc. Surg. **11**(1), 70–73 (1996)
47. Thanos, J., Rebeira, M., Shragge, B.W., Urbach, D.: Vascular ultrasound screening for asymptomatic abdominal aortic aneurysm. Healthc. Policy **4**(2), 75–83 (2008)
48. Truijers, M., Fillinger, M.F., Renema, K.W., Marra, S.P., Oostveen, L.J., Kurvers, H.A., Schultzekool, L.J., Blankensteijn, J.D.: In-vivo changes in abdominal aortic aneurysm thrombus volume during the cardiac cycle. J. Endovasc. Ther. **16**, 314–319 (2009)
49. Truijers, M., Pol, J.A., Schultzekool, L.J., van Sterkenburg, S.M., Fillinger, M.F., Blankensteijn, J.D.: Wall stress analysis in small asymptomatic, symptomatic and ruptured abdominal aortic aneurysms. Eur. J. Vasc. Endovasc. Surg. **33**(4), 401–407 (2007)
50. Urbonavicius, S., Urbonaviciene, G., Honore, B., Henneberg, E.W., Vorum, H., Lindholt, J.S.: Potential circulating biomarkers for abdominal aortic aneurysm expansion and rupture – a systematic review. Eur. J. Vasc. Endovasc. Surg. **36**(3), 273–280 (2008)
51. Vainas, T., Lubbers, T., Stassen, F.R., Herngreen, S.B., Dieijen-Visser, M.P., Bruggeman, C.A., Kitslaar, P.J., Schurink, G.W.: Serum C-reactive protein level is associated with abdominal aortic aneurysm size and may be produced by aneurysmal tissue. Circulation **107**(8), 1103–1105 (2003)
52. van Dam, E.A., Dams, S.D., Peters, G.W., Rutten, M.C., Schurink, G.W., Buth, J., van de Vosse, F.N.: Non-linear viscoelastic behavior of abdominal aortic aneurysm thrombus. Biomech. Model. Mechanobiol. **7**(2), 127–137 (2008)
53. van't Veer, M., Buth, J., Merkx, M., Tonino, P., van den Bosch, H., Pijls, N., van de Vosse, F.N.: Biomechanical properties of abdominal aortic aneurysms assessed by simultaneously measured pressure and volume changes in humans. J. Vasc. Surg. **48**, 1401–1407 (2008)
54. vande Geest, J.P., di Martino, E.S., Bohra, A., Makaroun, M.S., Vorp, D.A.: A biomechanics-based rupture potential index for abdominal aortic aneurysm risk assessment: demonstrative application. Ann. N. Y. Acad. Sci. **1085**, 11–21 (2006)
55. vande Geest, J.P., Wang, D.H., Wisniewski, S.R., Makaroun, M.S., Vorp, D.A.: Towards a noninvasive method for determination of patient-specific wall strength distribution in abdominal aortic aneurysms. Ann. Biomed. Eng. **34**(7), 1098–1106 (2006)
56. Vega de Céniga, M., Esteban, M., Quintana, J.M., Barba, A., Estallo, L., de la Fuente, N., Viviens, B., Martin-Ventura, J.L.: Search for serum biomarkers associated with abdominal aortic aneurysm growth – a pilot study. Eur. J. Vasc. Endovasc. Surg. **37**(3), 297–299 (2009)
57. Vega de Céniga, M., Gomez, R., Estallo, L., de la Fuente, N., Viviens, B., Barba, A.: Analysis of expansion patterns in 4–4.9 cm abdominal aortic aneurysms. Ann. Vasc. Surg. **22**(1), 37–44 (2008)

58. Vega de Céniga, M., Gomez, R., Estallo, L., Rodriguez, L., Baquer, M., Barba, A.: Growth rate and associated factors in small abdominal aortic aneurysms. Eur. J. Vasc. Endovasc. Surg. **31**(3), 231–236 (2006)
59. Venkatasubramaniam, A.K., Fagan, M.J., Mehta, T., Mylankal, K.J., Ray, B., Kuhan, G., Chetter, I.C., McCollum, P.T.: A comparative study of aortic wall stress using finite element analysis for ruptured and non-ruptured abdominal aortic aneurysms. Eur. J. Vasc. Endovasc. Surg. **28**(2), 168–176 (2004)
60. Vorp, D.A., Lee, P.C., Wang, D.H., Makaroun, M.S., Nemoto, E.M., Ogawa, S., Webster, M.W.: Association of intraluminal thrombus in abdominal aortic aneurysm with local hypoxia and wall weakening. J. Vasc. Surg. **34**(2), 291–299 (2001)
61. Wang, D.H., Makaroun, M.S., Webster, M.W., Vorp, D.A.: Mechanical properties and microstructure of intraluminal thrombus from abdominal aortic aneurysm. J. Biomech. Eng. **123**(6), 536–539 (2001)
62. Wilson, W.R., Anderton, M., Choke, E.C., Dawson, J., Loftus, I.M., Thompson, M.M.: Elevated plasma mmp1 and mmp9 are associated with abdominal aortic aneurysm rupture. Eur. J. Vasc. Endovasc. Surg. **35**(5), 580–584 (2008)
63. Wolf, Y.G., Thomas, W.S., Brennan, F.J., Goff, W.G., Sise, M.J., Bernstein, E.F.: Computed tomography scanning findings associated with rapid expansion of abdominal aortic aneurysms. J. Vasc. Surg. **20**(4), 529–535 (1994)
64. Wolters, B.J., Emmer, M., Rutten, M.C., Schurink, G.W., van de Vosse, F.N.: Assessment of endoleak significance after endovascular repair of abdominal aortic aneurysms: a lumped parameter model. Med. Eng. Phys. **29**(10), 1106–1118 (2007)

Chapter 7
The Cardiac Atlas Project: Towards a Map of the Heart

Michael Backhaus, Jae Do Chung, Brett R. Cowan, Carissa G. Fonseca, Wenchao Tao, and Alistair A. Young

7.1 Introduction

Although much is known about the pathophysiological cellular processes underlying heart disease, little is known about how the heart remodels structurally and functionally during the development of disease, and how particular presentations of disease fit into the spectrum of functional manifestations across patient groups. If clinicians were able to map the structure and function of the heart in a standard way, they would be able to characterize a particular patient's function with the range of functional characteristics derived from large populations of patients. This would enable more precise quantification of the type and severity of disease, as well as more robust measures of evaluation of the effects of treatment.

A major goal of computational biology is the development of mathematical and computer models that integrate observations from many studies into quantitative, self-consistent, and comprehensive descriptions [1, 32]. Many groups have begun to construct physiological databases, linked with anatomical, functional, and clinical data gleaned from a variety of sources. This information must be integrated across many scales, from molecular interactions to organ system function. Several initiatives have begun in this vein, centering on different organ systems and pathology targets. Projects include the Integrative Biology Project [14], the ECG signal database [20], the Cardiac Gene Expression database [6], the Medical Image File Archive Project [18], anatomical ontology databases such as the Foundational Model of Anatomy [11], Informatics for Integrating Biology and the Bedside [12], and the Physiome Project [1].

The establishment of large imaging databases is essential for the development and validation of these physiological models. Multidimensional image data provide the ability to customize biomechanical and physiological parameters to a particular patient's anatomy and cardiac performance. Large population based databases also enable statistical models of normal and pathological function to be developed,

A.A. Young (✉)
Department of Anatomy with Radiology, University of Auckland, 85 Park Road, Auckland 1142, New Zealand
e-mail: a.young@auckland.ac.nz

R.C.P. Kerckhoffs (ed.), *Patient-Specific Modeling of the Cardiovascular System: Technology-Driven Personalized Medicine*, DOI 10.1007/978-1-4419-6691-9_7,

which, in turn, facilitates better tools for construction of computational models from image data. Computational atlases refer to a set of maps that relate scientific information to spatial coordinates at a series of scales, from genotype to phenotype. These rely on computational and informatics infrastructure which facilitates patient-specific analysis as well as population-based statistical analysis.

In the brain, methods are well advanced to provide a detailed statistical map of brain morphology, and the infrastructure for building atlases and computational anatomy tools are well developed. For example, the Center for Computational Biology at UCLA [8] provides "middleware" applications and software required to provide secure, Web-based access to the underlying computational and network resources, including the International Consortium for Brain Mapping [15]. The Biomedical Informatics Research Network (BIRN) [3] provides a number of tools to facilitate collaborative research among neuroscientists and medical scientists, making use of computational and networking technologies and addressing issues of user authentication, data integrity, security, and data ownership. These tools, and those of the Cancer Biomedical Informatics Grid (CaBIG) [5], are being exploited by the Cardiovascular Research Grid [7] to create an infrastructure for sharing cardiovascular data and data analysis tools.

The Cardiac Atlas Project (CAP) is a worldwide collaborative project to establish a standardized database of cardiovascular imaging examinations together with derived analyses, for the purposes of statistical characterization of global and regional heart function abnormalities. By merging data from many different sources in a standardized manner, the CAP aims to provide the research community with a valuable resource for the study of heart disease. This chapter describes the infrastructure and analysis methodologies employed in the design and construction of the CAP database and client software. We also outline the standard procedures for data upload and access.

7.2 Cardiovascular Magnetic Resonance Imaging

Cardiovascular magnetic resonance (CMR) imaging provides an abundant source of detailed, quantitative data on heart structure and function. Advantages of CMR include its noninvasive nature, well-tolerated and safe (nonionizing) procedures, ability to modulate contrast in response to several mechanisms, and ability to provide high-quality functional information in any plane and any direction. Its three-dimensional (3D) tomographic nature allows excellent views of the entire heart, irrespective of cardiac orientation and cardiac chamber shape (Fig. 7.1). CMR imaging has provided detailed information on 3D ventricular shape and geometry [42, 45], regional systolic [55] and diastolic [30] strain, material microstructure [33, 47], blood flow [36], perfusion [41], and viability [37, 48]. It is considered the most accurate method to measure ventricular volumes and systolic function [42]. The high precision and accuracy of CMR [27, 39] has led to its increasing application worldwide in cardiovascular research trials and clinical practice.

The Society for Cardiovascular Magnetic Resonance teaching atlas [2], created in 1999 and updated in 2007, comprises a comprehensive range of CMR images of

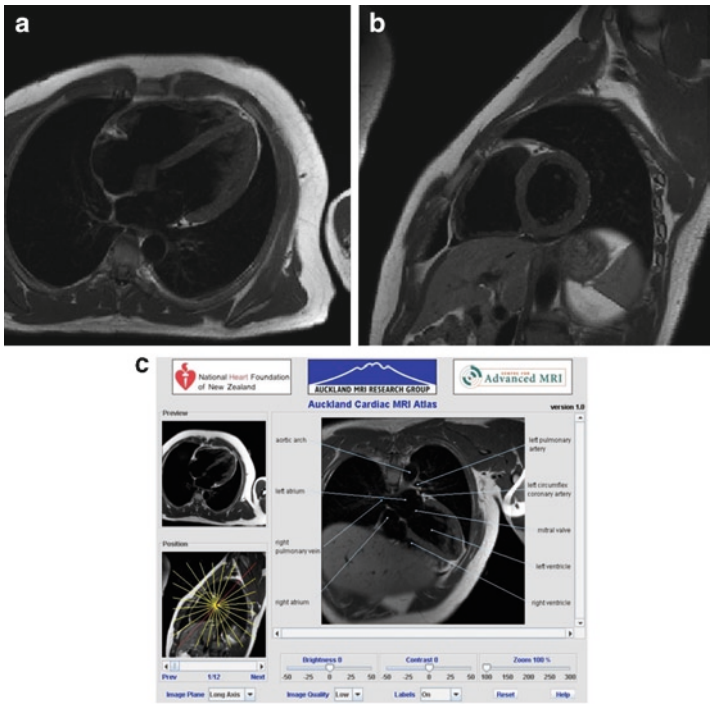

Fig. 7.1 Black blood anatomical images from the SCMR atlas. (**a**) Long-axis slice; (**b**) short-axis slice; (**c**) annotated long-axis slice with applet navigation and viewing tools [26]

a single healthy volunteer, including SSFP cine function images, myocardial tagging images, T1 anatomical images, and phase-contrast flow images (Fig. 7.1). This can be viewed as one end of a variety of "atlas" tools. At the other end lie population -based atlases comprising many thousands of patient studies. But before these population-based atlases can be used in clinical practice, we must formulate a standard coordinate system for the heart, which enables the registration of many cases to a common anatomically based target.

7.3 Mapping Shape and Motion

Analysis of the ~500 images that result from a typical imaging study has generally been limited to global estimates of mass and volume, which are very useful in the clinic. However, these images also provide detailed information on shape and function during diastole and systole, which can be combined with other imaging or clinical data to yield greater understanding of the underlying disease processes.

Model-based analysis tools allow the calculation of standard cardiac performance indices such as left ventricular mass and volume, as well as detailed assessment of regional wall motion in a standard coordinate system, by efficient customization of a

mathematical model to patient images using guide-point modeling [52]. The main advantage of the modeling approach is that this enables quantitative parameterization of regional heart wall motion, in a way that facilitates statistical comparison of cases drawn from different patient populations [25]. The mathematical model also provides a mechanism for the integration and comparison of information from different imaging protocols, such as late gadolinium enhancement [40, 44] and displacement encoding [51, 54].

In addition to the traditional mass and volume analysis, the mathematical model allows detailed evaluation of regional wall motion and shape characteristics. Figure 7.2 shows a bull's-eye map of regional wall thickness at end systole,

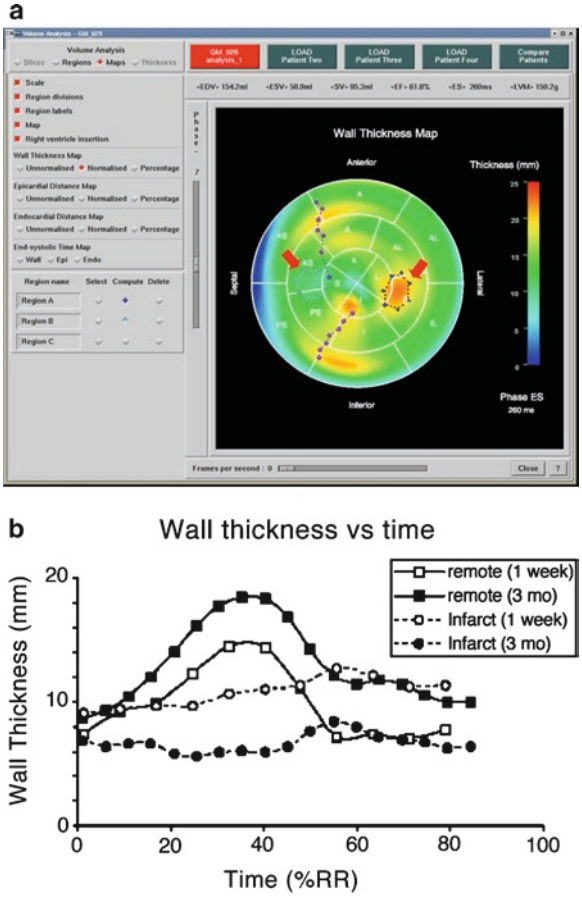

Fig. 7.2 Wall thickness in all regions of the heart can be determined from the mathematical model. (**a**) Bull's-eye plot of wall thickness in each region of the LV, with user defined regions (*arrows*) allowing interactive calculation of wall thickness within a nonstandard region. (**b**) Wall thickness vs. time in a patient at 1 week and 3 months after a first time myocardial infarction, showing wall thinning in the infarct zone due to remodeling, together with functional augmentation in the remote zone [33] (data courtesy Professor Lou Dell'Italia, University of Alabama, Birmingham, Alabama, USA)

together with plots of wall thickness against time. Figure 7.2b shows an example of remodeling in infarcted and remote zones in a patient at 1 week and 3 months after myocardial infarction.

7.4 Population Models

Model-based image analysis procedures provide a powerful mechanism for the fast, accurate assessment of CMR data, and facilitate biophysical analyses and standardized functional mapping procedures. Since the mathematical models employed for motion analysis are registered to the anatomy of the heart, they can be used to derive statistical descriptions of characteristic patterns of regional heart wall motion in health and disease. This leads to the identification of differences in the characteristic pattern of regional wall motion between disease or treatment groups.

However, the differences in regional wall motion parameters between groups are difficult to characterize succinctly due to their multidimensional nature. Many parameters are required to describe regional performance (including regional myocardial strain, rotation, and displacement). One powerful technique is principal component analysis (PCA), which describes the major sources of variation within a multidimensional dataset, by decomposing the variability into a set of orthogonal components (known as "modes") [29]. Thus, a database of models of heart shape and motion can be characterized by a set of orthogonal modes and their associated variance. The modes are ranked in order of highest to lowest variability, thereby showing which variations are most strongly present in the data and which variations can be neglected. This reduces the number of significant parameters by distinguishing the modes that truly differentiate the groups and eliminating modes that are insignificant. Given two such database distributions, describing different patient groups, statistical comparisons can then be made to determine the differences in shape and motion between the two groups. Similarly, given a new case, a comparison could be made with the database distributions to see which database best describes the patient's cardiac performance.

7.4.1 Parametric Distribution Models

By customizing mathematical models of the anatomy and function of the heart to individual cases, it is possible to construct parameter variation models describing the distribution of regional cardiac shape and function across patient subgroups. Cootes et al. [29] pioneered the application of Point Distribution Models in computer vision problems. Homologous landmarks (i.e., the points which are aligned to match corresponding features in the shape) were used to characterize shape and shape variations with the aid of a PCA. Since mathematical models, represented by

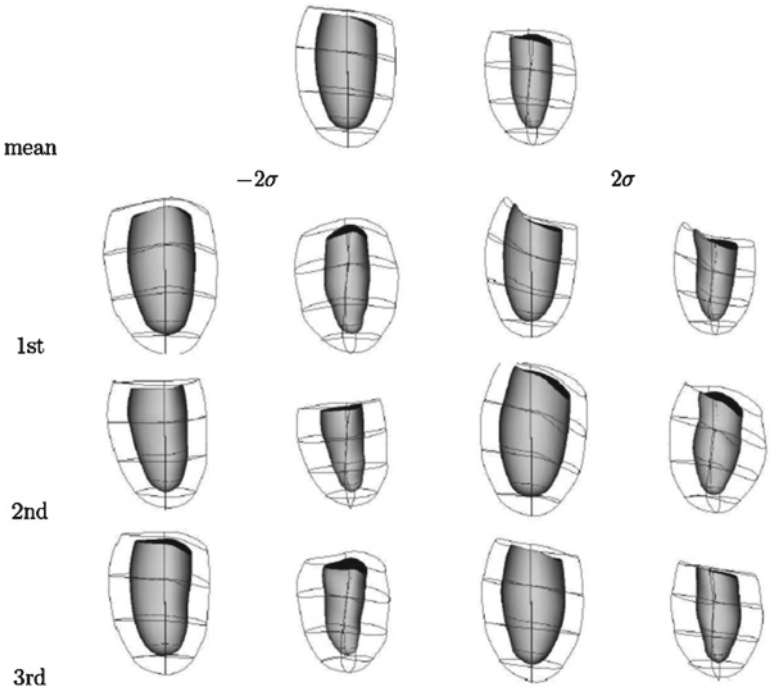

Fig. 7.3 Principal components of shape and motion showing mean (*top*) and first three modes plus and minus two standard deviations [28]

the model parameters, are a complete and efficient characterization of cardiac shape and motion, parameters of the model form homologous landmarks that can then be analyzed using PCA (Fig. 7.3).

7.4.2 Clinical Functional Modes

Although the PCA provides orthogonal (i.e., mathematically uncoupled) modes of deformation, the modes may not correspond to any intuitive or simple deformation. In an attempt to provide more clinically understandable modes of deformation, Remme et al. [46] described a set of "clinical" modes of variation. The deformation modes were chosen to decompose the motion into clinically meaningful components, including apex-base shortening, wall thickening, and ventricular torsion [46]. Figure 7.4a shows the definition of the modes of ventricular deformation, and Fig. 7.4b shows the distribution of the amount of each mode in a group of 15 healthy volunteers relative to a group of 30 patients with type II diabetes with clinical evidence of diastolic dysfunction but normal systolic chamber function [46]. The results show clear difference

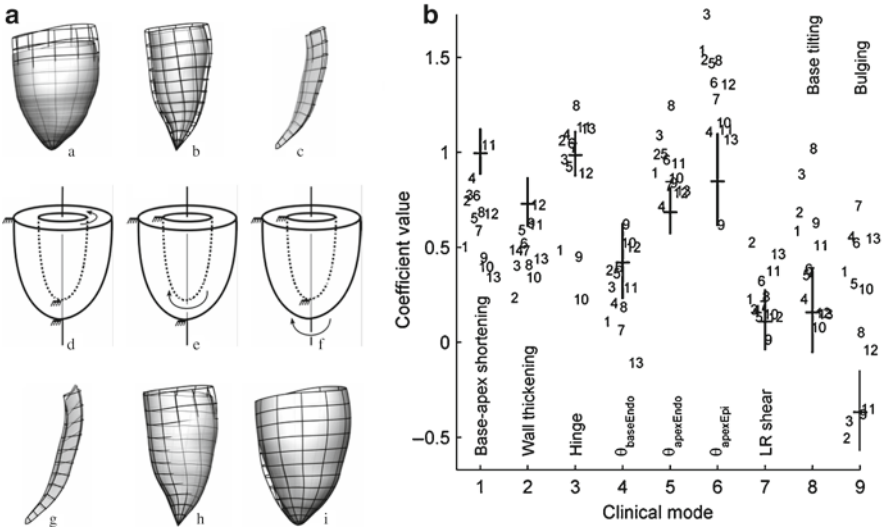

Fig. 7.4 (**a**) Definition of nine clinical modes of heart deformation. (**b**) Distribution of amount of motion in each clinical mode in patients with type II diabetes (numbers) compared with normal volunteers (mean and SD shown as cross hairs) [35]

in systolic modes of function, when there was no clinical evidence of systolic dysfunction (as measured by ejection fraction).

7.5 Data Fusion

The mathematical model of the heart enables registration and fusion of data from different imaging modalities and protocols. In one study, model-based methods for mapping regional strain and wall motion in relation to tissue characterization maps were developed and applied to a mouse model of reperfused myocardial infarction [53]. MRI tissue tagging was analyzed in each short and long-axis image using a semiautomated active contour process, and the 3D motion reconstructed with the aid of the finite element model [54] (Fig. 7.5, iii–iv), resulting in a dynamic model of the LV deformation. The Lagrangian Green strain components between end diastole and each subsequent time were calculated at specific finite element material points using standard methods of continuum mechanics [31]. Previous validation experiments using a deformable silicone gel phantom have shown that this procedure produces accurate, unbiased estimates of displacement and shortening [54].

Infarcted regions, as defined by regions of late gadolinium enhancement [37], were outlined on each image in the short-axis stack (Fig. 7.5, v–vi). The image coordinates of the contours were then transformed into 3D magnet coordinates using the 3D location of the image planes. The magnet coordinates were then transformed into a bull's-eye plot of the left ventricle (Fig. 7.5, vii). A convex perimeter

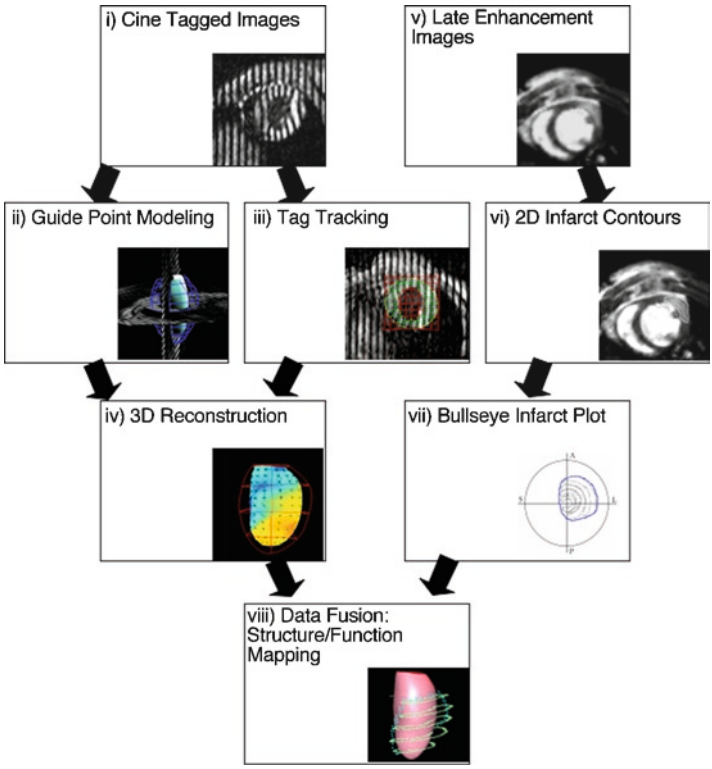

Fig. 7.5 Flow chart of the modeling and data fusion process

was manually drawn on the bull's-eye map so as to enclose the hyperenhancement contours (Fig. 7.5, vii). The bull's-eye coordinates of the perimeter were then converted to 3D cardiac coordinates and projected in the transmural direction onto the midwall surface of the LV finite element model. This allowed the calculation of the 3D infarct geometry in finite element material coordinates. The 3D infarct geometry was fixed onto the dynamic finite element model at end diastole, and allowed to deform with the beating model during systole and diastole (Fig. 7.5, viii).

Material points within the finite element model were assigned to regions relative to the 3D infarct geometry as follows. Points within the 3D infarct geometry were denoted *infarct*, points within 1.0 mm of the 3D infarct geometry (but outside it) were denoted *adjacent*, and all other points were denoted *remote*. This procedure also allowed calculation of the percentage myocardium in the infarct, adjacent, and remote zones, respectively. Since the models were defined in a coordinate system aligned with each heart, a material point could be mapped onto the corresponding material point at each time point during remodeling. The material points of the 3D infarct geometry at day 1 could thus be mapped into the baseline, days 7 and 28 models to give an approximate corresponding region for comparison purposes (Fig. 7.6).

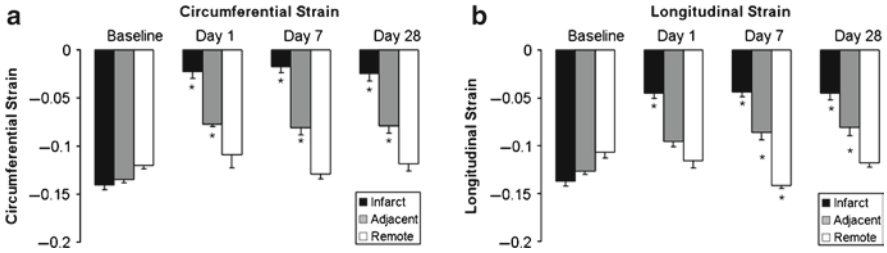

Fig. 7.6 Green strain components (no units) in infarcted, adjacent and remote zones over time after myocardial infarction. $*p<0.05$ vs. baseline, Scheffé test. (**a**) Circumferential shortening strain; (**b**) longitudinal shortening strain [36]

7.6 The CAP Databases

CMR images used by the CAP are stored in a production and a research database. The design and application of these databases are described in the following two sections. The CAP research database is hosted at the Diagnostic Cardiovascular Imaging section of UCLA Radiology (USA) and the Bioengineering Institute of the University of Auckland (NZ). It is based on the open source DICOM Clinical Manager system *dcm4chee* [10] and is used for implementation of research tasks, e.g., data mining, 3D modeling and metadata management.

7.6.1 Production Database (CCB)

The CAP production database is hosted by the UCLA Laboratory for NeuroImaging (LONI) and is an extension of existing brain mapping infrastructure, which has been modified for use with cardiac images. The purpose of this database is to provide a mechanism by which approved third-party users can access the deidentified data and derived information. The LONI Image Data Archive (IDA) is a server farm consisting of Linux computers running the MySQL database engine and Tomcat web application servers with a built-in load balancer that manages the requests to the web servers. The database schema is composed of a standard core plus a set of modules that can be customized to meet the needs of a particular project. Core components include project-, subject-, and study-related elements. Extensions are used to store visit-, protocol-, assessment-, and additional subject-related metadata. The IDA database has been extended to enable the storage and browsing of time-resolved cardiovascular MRI data.

Through a WEB interface, users can upload, query, and visualize CAP imaging data (Fig. 7.7a, b).

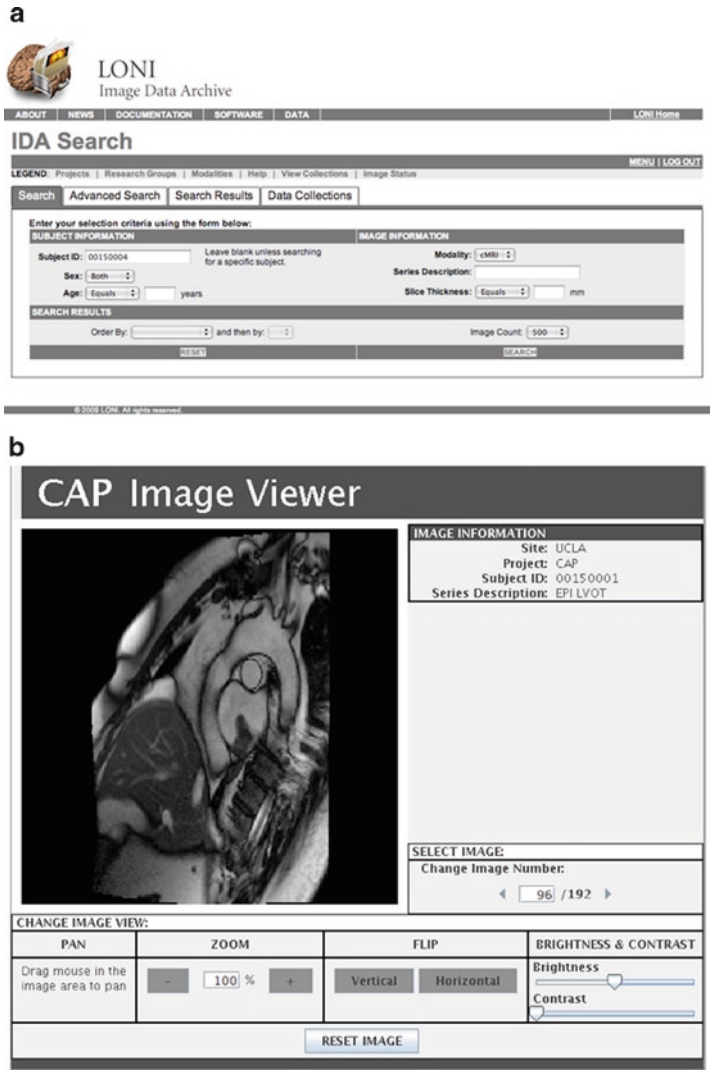

Fig. 7.7 (**a**) Query form in IDA for CAP Database. (**b**) Image Viewer in IDA for the Production CAP Database

7.6.2 Research Database

The CAP research database is developed as a branch to the DICOM archive and image manager dcm4chee. It is implemented as a JEE and JMX system, which is deployed within the JBoss Application Server [16] to provide a number of clinical services (DICOM, WADO, RID, HL7, etc.).

To allow the user to search for specific MR image values (e.g., timing, spacing, and sampling values), we have extended dcm4chee to facilitate storage of DICOM Image Model Attributes as defined in the DICOM Base Standard. While the DICOM Standard covers all public (even-numbered) attributes, vendors of MRI scanners often use additional private (odd-numbered) attributes to capture vendor-specific values. Private attributes differ between vendors and depend on the scanner model and software version used to capture the images. To provide the ability to search on private attributes, we have implemented the storage of image attributes in an XML format and a search function utilizing XPath queries.

3D models generated with the CAP Client software can be uploaded and stored in the research database. The models are linked to CMR images and contours in a relational database schema, allowing for searching results in the web application, listing images used by model, models using a given image, and models available for a patient.

In managing the hosting of the database-, application- and web-server, several IT issues had to be considered. The system has been set up as a multitier architecture hosted in a cluster of virtual machines, providing a secure, fast and scalable service oriented architecture [50]. 2TB of CMR images are stored on a redundant network file system, while incremental backups to an off-site location provide full disaster recovery. The servers are monitored for availability of services and file systems. User access is controlled through firewall rules filtering IP addresses and ports, as well as secure authentication using X.509 server certificates and Transport Layer Security (TLS) encryption for the web application.

7.7 The CAP Client

The CAP includes the development of a client-side software tool that can be used to visualize the MRI data stored in the CAP database and to generate patient-specific mathematical models from those data (Fig. 7.8). The client software is currently still under development, but a functional version (0.2, as of February 2010) of the software can be freely downloaded from the project website. The CAP client is open source under the Mozilla tri-license, and its source code is being hosted at SourceForge.net.

The main features of the CAP Client are as follows:

Database access. The Client can retrieve CMR data from the database located across the network. The CAP Client is also capable of uploading models generated from such data to the database.

Visualization. The Client offers various visualization capabilities that can be used for the visualization of 2D CMR images, 3D Visualization of the mathematical model constructed from the CMR images, and 4D Visualization (3D Visualization with time as the fourth dimension).

Model fitting. The Client can be used to fit a mathematical model to a series of CMR images with minimal human intervention, thus enabling a large set of data to be automatically fitted to appropriate models and parameters. The

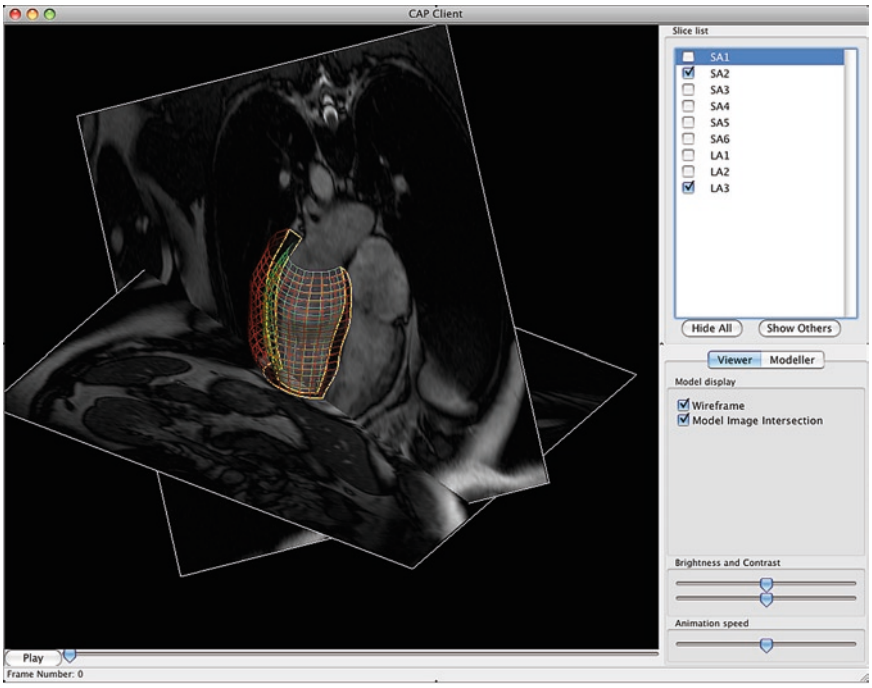

Fig. 7.8 Screenshot of the CAP Client showing fitted model in relation to long-axis and short-axis images

Client software must also provide a means for the human user to be able to interactively and graphically modify the relevant model parameters.

Statistical analysis. The Client must provide the necessary tools to allow statistical analysis of the data. This will be used for the generation of the parametric distribution models.

Cross-platform. The Client must be able to run on the Windows, Mac OS X, and Linux platforms.

The CAP Client is being developed using the C++ programming language on top of the CMGUI visualization library [9] and wxWidgets GUI Toolkit. These design choices were made for the following design criteria – performance, portability, and extensibility. First, the decision to use the C++ programming language was made mainly because of performance requirements, as the CAP Client performs a fair amount of numerical computation in real time and also requires real-time rendering of graphics. The use of cross-platform libraries helped the development of a portable software package, thus enabling the CAP client to run on all of the major operating systems. The development of the CAP Client has been greatly aided by the powerful features the CMGUI library offers, such as 3D visualization of finite element models and mathematical field visualization and manipulation. Also, as the

extensibility of the software is of great importance, the software was written using software engineering techniques such as Object Oriented Design, Design Patterns, and Unit Testing.

7.8 CAP Data Access

7.8.1 Upload and Deidentification

All data are deidentified before upload into the CAP database using HIPAA compliant tools developed by the CCB [17]. All images and associated information is stripped of any identifying information, including names, addresses, and all identifiers using the following algorithm:

1. Split by tag: DICOM tags that have allowed tag numbers are left unchanged. These include tags that contain unique identifiers that are not to be encrypted, dates, trusted binaries, and trusted strings.
2. Split by VR: DICOM tags not selected in step (1) are included in the dataset if they have an allowed *Value Representation* (VR). Numbers, times, and small code strings are typically left unchanged. Strings and binaries are not.
3. Encrypt: DICOM tags not selected in step (1) or (2) are either encrypted or discarded.
4. Replace: Out of all the DICOM tags in steps (1) and (2) the values of specified tags are replaced. Physician names as well as patient names are replaced with empty strings, and the patient identifier is replaced with a user-specified code. Default values for missing tags are also set.

Each study is assigned a CAP code before upload into the CAP database. The CAP does not have access to the keys which can associate CAP codes with the contributing study identifiers. These are held by the contributing studies. The deidentifying process has been validated with studies acquired from a variety of MR scanners, including GE, Siemens, and Philips. The deidentification algorithm has also been enhanced to handle derived (segmented) images with contours information embedded in the DICOM header.

7.8.2 Ownership and Control of Data Use

Cardiovascular imaging data and derived results have been contributed to CAP by several Contributing Studies, including MESA [26] and DETERMINE [35]. Each Contributing Study has supported collection of data from participants in a well-controlled manner, which provides a valuable scientific resource. The Contributing Studies have made a substantial long-term contribution in collecting the data. This contribution includes the design of recruitment, inclusion and exclusion criteria,

ensuring high quality of data, ensuring the participants are well-characterized, as well as significant resources spent on acquisition of the data. All data contributed to CAP are therefore considered the property of the Contributing Study. The data can only be used for purposes approved explicitly by the Contributing Study, on a case-by-case basis. All Research Projects which propose to make use of the data arising from the Contributing Study must be approved by the Contributing Study steering committee or nominee. Only those participants with informed consent compatible with the data use will be made available to CAP Users. No data can be distributed to any other entity or any individual in a manner not previously approved by the Contributing Study.

7.8.3 Protocols for Users

All Users who wish to use data from CAP are required to submit a Research Project to the CAP Steering Committee. The committee will review the proposal and assess its eligibility with respect to the goals of the CAP project. If approved, CAP will liaise with each of the Contributing Studies whose data are required for the Research Project. Each Contributing Study (or nominee) will then review the proposal and assess its eligibility with respect to the goals of the Contributing Study. If the proposal is approved by the Contributing Study, the User will be required to sign and abide by a Data Distribution (DDA) agreement for each of the Contributing Studies involved. A separate DDA is required for each Contributing Study because the terms and conditions which govern the use of the data are specific to the goals and rationale of each Contributing Study. Further details of CAP policies and procedures can be found at www.cardiacatlas.org.

7.8.4 Informed Consent and Institutional Review Board Approval

The CAP seeks to promote the development of valuable discoveries and inventions beneficial to the public health based upon use of the CAP repository of valuable data. All Contributing Studies must have local Institutional Review Board approval for the contribution of deidentified data into databases, for the purpose of cardiac research at this time and in the future. Only data from those participants who have provided informed consent will be included in the CAP database. All data are deidentified in a manner compliant with the HIPAA privacy rule. The deidentification of data occurs before inclusion in CAP data servers, so CAP never has access to original identifiers for the Contributing Study. This means there is no way CAP personnel or Users can identify individual participants. All CAP personnel and Users will not attempt at any time to identify participants.

7.9 Conclusions and Future Work

7.9.1 Grid Enabling

The CAP seeks to federate cardiovascular modeling software and data resources to make them available to the cardiovascular research community *via* the Cardiovascular Research Grid (CVRG) [7]. CVRG provides infrastructure tools in the cardiovascular domain to enable researchers to easily access distributed resources through standardized interfaces, based on tools developed in the BIRN [43] and caBIG [34] projects. The CAP database will be interfaced with the CVRG-Core, and modified to implement interfaces and mechanisms compatible with CVRG enabled analysis tools. The CAP client software will also be grid-enabled, in order to be used in standard CVRG workflows, including a portal component to enable interaction with other resources on the grid. The parametric modeling tools and associated ontological schema that are being developed by CAP will be designed to facilitate data fusion between different imaging protocols and modalities as well as other data sources.

7.9.2 Ontologies

The data provided in the CAP database (CV images and derived morphological information including contours and parametric geometry descriptions) will be classified and described in a standardized way. This will occur through registration of an information model and associated semantic annotations, expressed in the Web Ontology Language (OWL) [19], at the National Center for Biomedical Ontologies (NCBO) [4]. This provides a formalized description of the information provided, so that grid-enabled tools can query and access data of the correct type, and databases can declare what type of data are available. A top-level ontology [28] will provide axiomatic theories for the integration of existing domain ontologies, such as the Foundational Model of Anatomy (FMA) for anatomical data [11], RadLex ontology for radiological data [21], Annotation and Image Markup (AIM) for tagging of image regions using RadLex terms [38], Systems Biology Ontology (SBO) for the modeling framework [22], Information Artifact Ontology (IAO) for image attributes [13], Phenotypic Quality Ontology (PATO) for phenotype annotation [49], and Systematized Nomenclature of Medicine – Clinical Terms (SNOMED CT) for clinical terms [24]. The use of these ontologies will allow data and derived results from several studies to be collated in a standardized manner to achieve meta- or subgroup analyses. Where gaps occur, suggested terms will be proposed based on feedback from the radiological and cardiological communities. This feedback will be obtained using online resources such as the NCBO BioPortal [4] and WebProtégé [23].

References

1. ABI Physiome Home Page. Available at http://www.physiome.org.nz/
2. AMRG Cardiac Atlas (SCMR). Available at http://atlas.scmr.org/
3. Biomedical Informatics Research Network Home Page. Available at http://www.nbirn.net/
4. Bioportal 2.0 Home Page. Available at http://www.bioontology.org/tools/alpha.html
5. Cancer Biomedical Informatics Grid Home Page. Available at http://cabig.nci.nih.gov
6. Cardiac Gene Expression Home Page. Available at http://www.cage.wbmei.jhu.edu/
7. Cardiovascular Research Grid Home Page. Available at http://www.cvrgrid.org/. Accessed August 1, 2009
8. Center for Computational Biology Home Page. Available at http://www.loni.ucla.edu/ccb
9. cmGUI Home Page. Available at http://www.cmiss.org/cmgui
10. The DCM4CHE Open Source PACS Home Page. Available at http://www.dcm4che.org
11. Foundational Model of Anatomy Home Page Available at http://sig.biostr.washington.edu/projects/fm/AboutFM.html
12. Informatics for Integrating Biology and Bedside Home Page. Available at http://www.i2b2.org/
13. Information Artifact Ontology Project Page. Available at http://code.google.com/p/information-artifact-ontology/
14. Integrativebiology Project Home Page. Available at http://www.integrativebiology.ox.ac.uk/
15. International Consortium for Brain Mapping Available at http://www.loni.ucla.edu/ICBM
16. JBoss Application Server. Available at http://labs.jboss.com/
17. LONI De-identification Debablet. Available at http://www.loni.ucla.edu/Software/DiD
18. Medical Image File Archive Project Home Page. Available at http://dpi.radiology.uiowa.edu/mifar/index.php
19. OWL Web Ontology Language. Available at http://www.w3.org/TR/owl-features/
20. PhysioNet Home Page. Available at http://www.physionet.org/
21. Radlex RSNA Page. Available at http://www.rsna.org/radlex/
22. Systems Biology Ontology Home Page. Available at http://www.ebi.ac.uk/sbo/
23. WebProtégé Home Page. Available at http://protegewiki.stanford.edu/index.php/WebProtege
24. Amanda R: Towards semantic interoperability in healthcare: ontology mapping from SNOMED-CT to HL7 version 3. Hobart: Australian Computer Society, Inc., 2006
25. Augenstein KF, Young AA: Finite element modeling for three-dimensional motion reconstruction and analysis. Dordrecht: Kluwer Academic, 2001
26. Bild DE, et al.: Multi-ethnic study of atherosclerosis: objectives and design. Am J Epidemiol 156:871–881, 2002
27. Bottini PB, Carr AA, Prisant LM, Flickinger FW, Allison JD, Gottdiener JS: Magnetic resonance imaging compared to echocardiography to assess left ventricular mass in the hypertensive patient. Am J Hypertens 8:221–228, 1995
28. Burek P, Hoehndorf R, Loebe F, Visagie J, Herre H, Kelso J: A top-level ontology of functions and its application in the Open Biomedical Ontologies. Bioinformatics 22:e66–73, 2006
29. Cootes TF, Hill A, Taylor CF, Halsam J: The use of active shape models for locating structures in medical images. Image Vis Comput 12:355–366, 1994
30. Fonseca CG, Oxenham HC, Cowan BR, Occleshaw CJ, Young AA: Aging alters patterns of regional nonuniformity in LV strain relaxation: a 3-D MR tissue tagging study. Am J Physiol Heart Circ Physiol 285:H621–630, 2003
31. Fung YC: Foundations of solid mechanics. Englewood Cliffs: Prentice Hall, 1965
32. Grenander U, Miller MI: Computational anatomy: an emerging discipline. Q J Appl Math 56:627–694, 1998
33. Hsu EW, Muzikant AL, Matulevicius SA, Penland RC, Henriquez CS: Magnetic resonance myocardial fiber-orientation mapping with direct histological correlation. Am J Physiol 274:H1627–1634, 1998
34. James JC, Terry FH, Olivier B, Brian D, Grace AS, Martin R: The caBIG terminology review process. J Biomed Inform 42:571–580, 2009

35. Kadish AH, et al.: Rationale and design for the Defibrillators to Reduce Risk by Magnetic Resonance Imaging Evaluation (DETERMINE) trial. J Cardiovasc Electrophysiol 20:982–987, 2009
36. Kilner PJ, Yang GZ, Wilkes AJ, Mohiaddin RH, Firmin DN, Yacoub MH: Asymmetric redirection of flow through the heart. Nature 404:759–761, 2000
37. Kim RJ, et al.: The use of contrast-enhanced magnetic resonance imaging to identify reversible myocardial dysfunction. N Engl J Med 343:1445–1453, 2000
38. Kundu S, et al.: The IR Radlex Project: an interventional radiology lexicon--a collaborative project of the Radiological Society of North America and the Society of Interventional Radiology. J Vasc Interv Radiol 20:S275–277, 2009
39. Myerson SG, Bellenger NG, Pennell DJ: Assessment of left ventricular mass by cardiovascular magnetic resonance. Hypertension 39:750–755, 2002
40. Oshinski JN, Yang Z, Jones JR, Mata JF, French BA: Imaging time after Gd-DTPA injection is critical in using delayed enhancement to determine infarct size accurately with magnetic resonance imaging. Circulation 104:2838–2842, 2001
41. Panting JR, et al.: Abnormal subendocardial perfusion in cardiac syndrome X detected by cardiovascular magnetic resonance imaging. N Engl J Med 346:1948–1953, 2002
42. Pattynama PM, De Roos A, Van der Wall EE, Van Voorthuisen AE: Evaluation of cardiac function with magnetic resonance imaging. Am Heart J 128:595–607, 1994
43. Philip MP: Building cyber-infrastructure for the biomedical informatics research network. Washington, DC: IEEE Computer Society, 2006
44. Rehwald WG, Fieno DS, Chen EL, Kim RJ, Judd RM: Myocardial magnetic resonance imaging contrast agent concentrations after reversible and irreversible ischemic injury. Circulation 105:224–229, 2002
45. Reichek N: Magnetic resonance imaging for assessment of myocardial function. Magn Reson Q 7:255–274, 1991
46. Remme EW, Young AA, Augenstein KF, Cowan B, Hunter PJ: Extraction and quantification of left ventricular deformation modes. IEEE Trans Biomed Eng 51:1923–1931, 2004
47. Scollan DF, Holmes A, Winslow R, Forder J: Histological validation of myocardial microstructure obtained from diffusion tensor magnetic resonance imaging. Am J Physiol 275:H2308–2318, 1998
48. Wagner A, et al.: Contrast-enhanced MRI and routine single photon emission computed tomography (SPECT) perfusion imaging for detection of subendocardial myocardial infarcts: an imaging study. Lancet 361:374–379, 2003
49. Washington N, et al.: NLP and Phenotypes: using Ontologies to link Human Diseases to Animal Models. Dagstuhl: Schloss Dagstuhl – Leibniz-Zentrum fuer Informatik, 2008
50. Yang TH, et al.: A scalable multi-tier architecture for the National Taiwan University Hospital Information System based on HL7 Standard. Washington, DC: IEEE Computer Society, 2006
51. Young AA, Axel L: Three-dimensional motion and deformation of the heart wall: estimation with spatial modulation of magnetization – a model-based approach. Radiology 185:241–247, 1992
52. Young AA, Cowan BR, Thrupp SF, Hedley WJ, Dell'Italia LJ: Left ventricular mass and volume: fast calculation with guide-point modeling on MR images. Radiology 216:597–602, 2000
53. Young AA, et al.: Reperfused myocardial infarction in mice: 3D mapping of late gadolinium enhancement and strain. J Cardiovasc Magn Reson 8:685–692, 2006
54. Young AA, Kraitchman DL, Dougherty L, Axel L: Tracking and finite element analysis of stripe deformation in magnetic resonance tagging. IEEE Trans Med Imaging 14:413–421, 1995
55. Young AA, Kramer CM, Ferrari VA, Axel L, Reichek N: Three-dimensional left ventricular deformation in hypertrophic cardiomyopathy. Circulation 90:854–867, 1994

Chapter 8
In Vivo Myocardial Material Properties and Stress Distributions in Normal and Failing Human Hearts

Jonathan F. Wenk, Zhihong Zhang, Guangming Cheng, Kay Sun, Joseph C. Walker, David A. Saloner, Mark B. Ratcliffe, and Julius M. Guccione

8.1 Introduction

A noninvasive method for estimating myocardial material properties in vivo would be of great value in the design and evaluation of new surgical and medical strategies to treat and/or prevent heart failure. Once the material properties for the myocardium are established, the effect of therapeutic changes on regional geometry (i.e., surgical remodeling) and/or material properties (i.e., medicine, gene therapy, and cell therapy) can be evaluated and the success or failure of a proposed therapy predicted. With clinical experience, such a method could be used as a diagnostic modality to risk stratify patients early after a myocardial infarction (MI) who are at risk for adverse remodeling and the development of heart failure.

The distributions of three-dimensional (3D) stress (and strain) are determined by: (1) the 3D geometry and fibrous architecture of the ventricular walls; (2) the boundary conditions imposed by the ventricular cavity and pericardial pressures and structures like the fibrous valve ring skeleton at the base of the ventricles; and (3) the 3D mechanical properties of the myofibers and their collagen interconnections in the relaxed end-diastolic and actively contracting end-systolic states [10, 21]. Formulating a mathematical model for interpreting these distributions in such a complex and constantly changing mechanical system is clearly very difficult. Solution of the governing equations of equilibrium for a body with such a complex geometry, boundary conditions, and material properties requires computational techniques. *The most versatile of these techniques is the finite element (FE) method*, in which the dependent variables are discretized by piecewise polynomial approximations over finite subdomains (elements) and expressed in terms of parameter values at inter-element connection points (nodes). In the analysis of geometrically complex

J.F. Wenk (✉)
Department of Veterans Affairs Medical Center, Building 2, Room 106, 4150 Clement Street, San Francisco, CA 94121, USA
e-mail: jonathan.wenk@va.gov

R.C.P. Kerckhoffs (ed.), *Patient-Specific Modeling of the Cardiovascular System: Technology-Driven Personalized Medicine*, DOI 10.1007/978-1-4419-6691-9_8,

3D domains, the FE method operates on discrete, geometrically approximate models (meshes) that can be refined both locally and globally to insure a high degree of accuracy in the numerical results.

Previous FE studies of the left ventricle (LV) have validated stress calculations by showing good agreement with myocardial deformations (strains) measured with implanted markers [3, 11, 30, 39, 41]. However, this is invasive and is limited to few simultaneous LV locations (usually only two). In a pioneering study, Moulton et al. [24] used tagged magnetic resonance (MR) images to determine isotropic, diastolic material properties in a two-dimensional (2D) FE analysis of beating canine hearts. Using a more realistic material law, Okamoto et al. [29] determined anisotropic myocardial material properties in a 3D FE model using tagged MR images. However, the experimental preparation and loading conditions were unphysiological to create significant transverse shear strain. Since then, Guccione et al. [12] successfully modeled end-isovolumic systole in an ovine model of MI and determined material parameters that reproduced circumferential stretching (as measured with 2D-tagged MRI) in the infarct borderzone (BZ). This FE study successfully revealed that the mechanism of circumferential stretching in the infarct BZ during isovolumic systole related to impaired contractile function in that region. However, the FE model was validated against only two measurements of strain in the anterior and posterior BZ and lacked measurements of ovine material properties and fiber architecture. More recently, our laboratory used cardiac catheterization, MR imaging with myocardial tissue tagging [13], MR diffusion tensor imaging [42], and a finite element (FE) method [6] to measure regional systolic myocardial material properties in the beating hearts of four sheep with LV aneurysm [43] and six sheep with LV aneurysm repaired surgically [44]. With knowledge of these myocardial material properties, we were able to quantify the effect of aneurysm plication on regional myocardial stress distributions. Although our previous studies [43, 44] represented significant advancements in FE modeling of hearts with MI, because of long computation times, they both employed a manually directed pseudo-optimization.

In a recent study [38], we performed an explicit FE model-based formal optimization of regional myocardial contractility in a sheep with LV aneurysm using tagged MR images and cardiac catheterization pressures. From the tagged MR images, 3D myocardial strains, LV volumes, and geometry for the animal-specific 3D FE model of the LV were calculated, while the LV pressures provided physiological loading conditions. Active material parameters (T_{max_B} and T_{max_R}) in the noninfarcted myocardium adjacent to the aneurysm (BZ) and the myocardium remote from the aneurysm were estimated by minimizing the errors between FE model-predicted and measured systolic strains and LV volumes using the success response surface method for optimization. The significant depression in optimized T_{max_B} relative to T_{max_R} was confirmed by direct ex vivo force measurements from skinned fiber preparations. The objective of the study in this chapter is to apply our method to the noninvasive study of myocardial material properties in a normal human subject and a patient with diastolic heart failure.

8.2 Left Ventricular Diastolic Function

The increasing recognition of the importance of diastolic dysfunction has led to a need for new methods not only to evaluate diastolic function, but also to provide insight into the underlying causes of this abnormality. Although some investigators have gone as far as to dismiss the existence of altered stiffness in patients with diastolic heart failure [5], a recent study demonstrated significant abnormalities in passive stiffness in patients with heart failure and a normal ejection fraction [49]. Specifically, the diastolic pressure–volume relation (assessed by means of cardiac catheterization and echocardiography) was shifted up and to the left in the patients with diastolic heart failure when compared with controls. This study, and others, confirms the central role that the material properties of the heart have in the pathogenesis of diastolic dysfunction.

Echocardiography is currently the most widely used diagnostic modality for assessing diastolic function. Echo-Doppler measurement of transmitral blood flow patterns are now supplemented by tissue Doppler echocardiography (TDE) and pulmonary venous inflow patterns, to measure LV diastolic function. Normally, early flow (E wave) is higher than that associated with atrial contraction (A wave) with a systolic dominant pulmonary inflow pattern. Mild diastolic dysfunction is typically associated with a reversal of the *E*/*A* ratio [45]. However, the *E*/*A* ratio in dilated cardiomyopathy may range between complete A wave dominance that suggests decreased ventricular compliance and a "pseudonormalized" (E wave dominance) or restrictive pattern in more severe cases of diastolic dysfunction [35]. Mitral flow patterns can also be difficult to interpret because of confounding factors including atrial pressure, ventricular relaxation time, and mitral regurgitation [40]. In addition, aging is associated with a decrease in the *E*/*A* ratio possibly related to increasing myocardial fibrosis with age [4]. TDE may provide useful quantitative measures of diastolic material properties. For instance, TDE may be superior in the measurement of diastolic filling pressure [32] and diastolic stiffness associated with myocardial stunning and reperfused MI [36]. However, echocardiographic measures have significant limitations as well. Another study of patients with diastolic heart failure concluded that standard echo-Doppler indices of diastolic function correlate poorly with LV diastolic pressure transients. Thus, the diagnosis of diastolic heart failure cannot be made on the basis of a single echo-Doppler parameter but, rather, all parameters must be examined in concert and used in combination with clinical observations [1].

8.2.1 Methodology for Model Generation and Strain Calculation in the Left Ventricle

Tagged MRI [2, 48] is a valuable technique for noninvasively assessing the regional mechanical function of the LV wall. Analysis of wall motion abnormalities

with dobutamine stress echocardiography and cine-MRI are established methods of detecting myocardial ischemia, but are either semiquantitative or subjective [27, 34]. In tagged MR images, the myocardium appears with a spatially encoded pattern that moves with the tissue (Fig. 8.1) and can be analyzed to compute quantitative measures of regional myocardial contractile performance, such as 3D strain. Quantitative 3D analysis of tagged MRI has shown promise for detecting ischemia and differentiating between viable and nonviable myocardium [7, 19]. Several methods have been developed to quantitatively analyze tagged images [8, 15, 18, 25, 28, 33, 47]. Most techniques first use a tag detection algorithm to extract the positions of taglines in each image in a study. Myocardial motion is then reconstructed by fitting a deformation model to the tagline positions.

A customized version of the MR image tagging postprocessing software, FindTags (Laboratory of Cardiac Energetics, National Institutes of Health, Bethesda, MD), was used to contour the endocardial and epicardial LV surfaces and also to segment the systolic tags for each image slice [14]. Systolic myocardial strains (six Lagrangian Green's strain tensor components in cylindrical coordinates, circumferential, longitudinal, and radial) at midwall and around the circumference in each short-axis slice were calculated from tagline deformation using the four dimensional B-spline-based motion tracking technique [33].

An FE model was created using early diastole as the initial unloaded reference state since the LV pressure is lowest at this point and therefore stress is at a minimum. Surface meshes were then created from the LV contours to replicate the in vivo geometry and measure end-diastolic and end-systolic volumes (Rapidform,

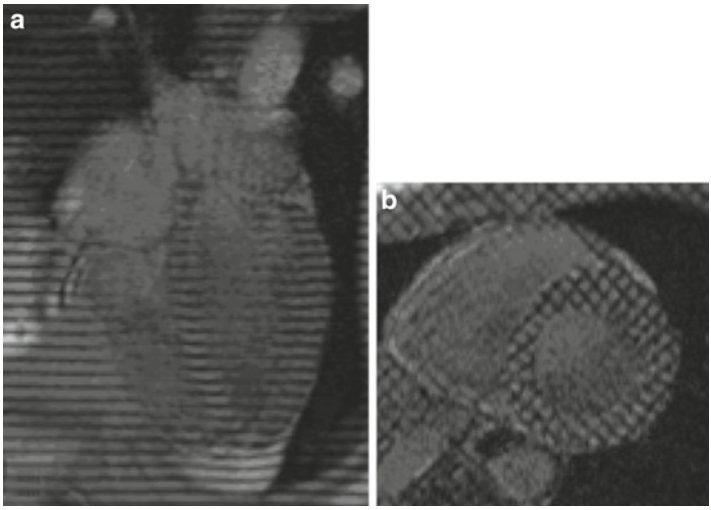

Fig. 8.1 Tagged long-axis (**a**) and short-axis (**b**) magnetic resonance images from a normal male human subject

INUS Technology, Inc., Sunnyvale, CA). The spaces between the endocardial and epicardial surfaces were filled with eight-noded trilinear brick elements with a single integration point for computational efficiency to generate a volumetric mesh that is refined into three elements transmurally (Truegrid, XYZ Scientific Applications, Inc., Livermore, CA). The inner endocardial surface was lined with a layer of soft nonstructural shell elements to form an enclosed volume for LV volume measurements.

Cardiac myofiber angles of −37, 23, and 83° were assigned at the epicardium, midwall, and endocardium, respectively [31]. Cross-fiber, in-plane stress equivalent to 40% of that along the myocardial fiber direction was added [43]. Nodes at the LV base were restricted to displace horizontally, and circumferential displacements were constrained at the basal epicardial nodes. The inner endocardial wall was loaded to the measured in vivo end-diastolic and end-systolic LV pressures.

8.2.2 *Left Ventricular Myofiber Stress Distributions in a Normal Human Subject and a Patient with Diastolic Heart Failure*

The 3D stress distributions in the myocardium are important to regional ventricular function because both regional coronary blood flow [17] and myocardial oxygen consumption [37] are influenced by ventricular wall stress. Changes in ventricular wall stress are believed to be stimuli for hypertrophy and remodeling [9]. *There have been no successful methods developed to measure stress in the intact heart wall* – primarily because of its large deformations and the tissue injury caused by implanted transducers [16, 46].

Ventricular wall stress has traditionally been estimated from chamber pressure and radii of curvature using LaPlace's law. However, LaPlace's law is based on a global force balance, which ignores myocardial material properties. Thus, LaPlace's law can be used to estimate only average stress across the full wall thickness in the circumferential and longitudinal directions [23].

Models, using the methodology outlined in the previous section, of the LV in a normal human subject and a patient with diastolic heart failure were generated. The material properties were manually adjusted until the simulated end-diastolic and end-systolic volumes were within a reasonable range of the experiment. Figure 8.2 shows color-coded plots of the 3D distributions of stress in the local muscle fiber direction of the LV for a normal human subject at end-diastole (Fig. 8.2a) and end-systole (Fig. 8.2b). Additionally, Fig. 8.2 shows the corresponding LV myofiber stress distributions in a patient with diastolic heart failure at end-diastole (Fig. 8.2c) and end-systole (Fig. 8.2d). It can be seen that the stress at end-diastole is much higher through the thickness of the LV in the diastolic heart failure case than the healthy case. Notice that the maximum end-diastolic and end-systolic myofiber stress values in the case of diastolic heart failure are nearly twice the normal case.

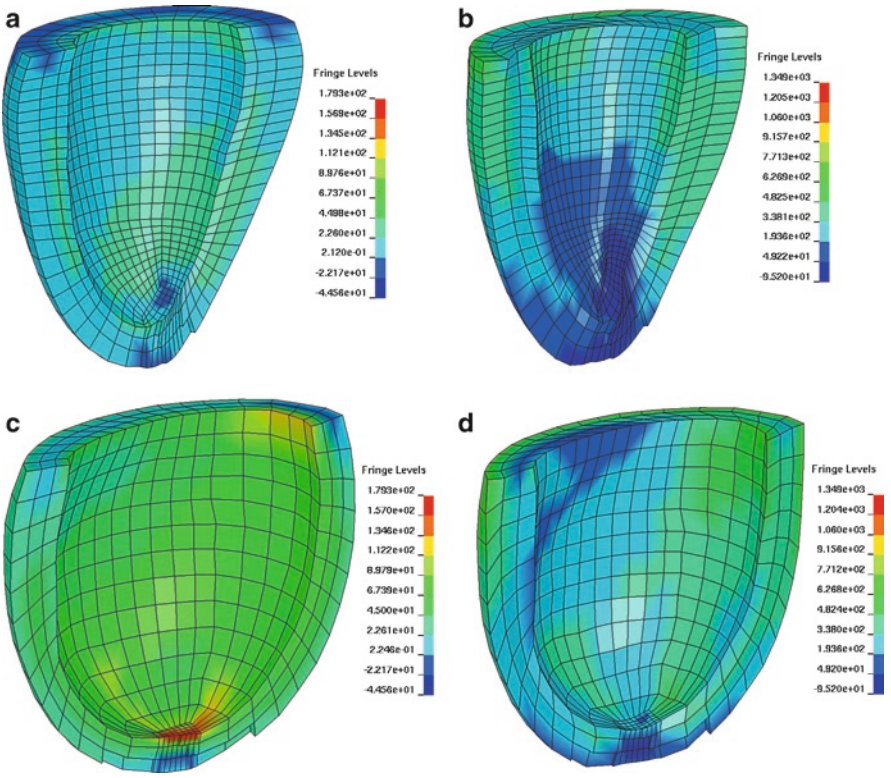

Fig. 8.2 Color-coded myofiber stress distributions in lateral LV wall. (**a**) Normal human subject, end-diastole (max = 6.16 kPa); (**b**) Normal human subject, end-systole (max = 60.9 kPa); (**c**) Patient with diastolic heart failure, end-diastole (max = 17.9 kPa); (**d**) Patient with diastolic heart failure, end-systole (max = 134.9 kPa)

A comparison of the diastolic material properties between healthy and diseased hearts, in terms of parameter values in the constitutive equation, can be somewhat difficult to interpret. A much clearer comparison is shown in Fig. 8.3. Notice the significantly greater myofiber stress at equibiaxial stretches above 1.15 (15% stretch in the fiber and cross-fiber directions) in the case of diastolic heart failure. This implies that the diseased LV wall is stiffer than the healthy LV, which means that it requires a greater load to deform.

The 3D systolic strains for the normal human subject were determined from tagged MR images, as described previously. The circumferential component is shown in Fig. 8.4. The next step in the analysis of the human data will be to use the formal optimization, outlined in the next section, to determine both the passive and active material properties for healthy and dysfunctional myocardium.

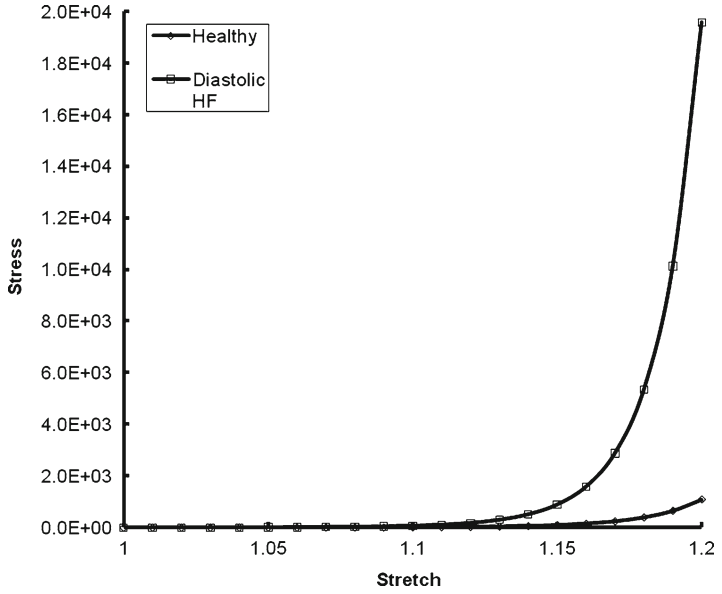

Fig. 8.3 Comparison of myofiber stress vs. stretch ratio relationships during a hypothetical equibiaxial stretch of diastolic myocardium in a healthy LV (model in Fig. 8.2a) and an LV (model in Fig. 8.3a) with diastolic heart failure

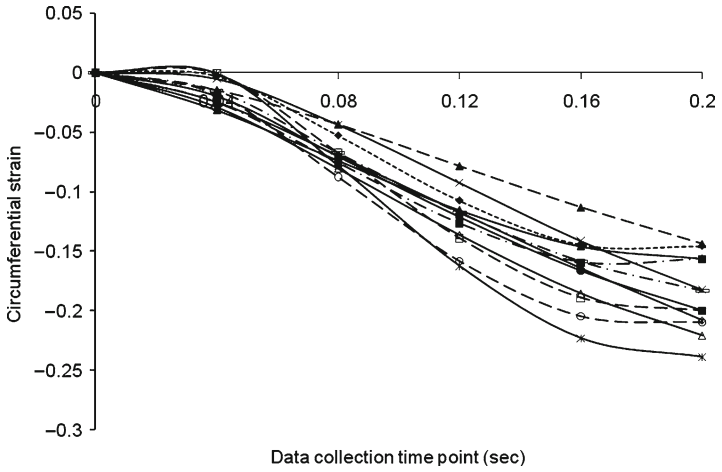

Fig. 8.4 Circumferential strain time course from end-diastole (0 s) to end-systole (0.2 s) at 12 equally spaced midwall points around the circumference in a short-axis slice at mid-ventricle in a normal human subject

8.3 A Computationally Efficient Formal Optimization of Regional Myocardial Contractility

Recently, our laboratory developed a very efficient and fast method to formally optimize regional myocardial contractility from tagged MR images and cardiac catheterization pressures [38]. Our approach was demonstrated for data from sheep, 14 weeks after anteroapical MI. The proposed method involves performing FE simulations using the customized commercial FE solver (LS-DYNA) that was programmed with the passive and active myocardial material laws. The forward FE solutions are fed into the optimization software (LS-OPT), which was customized to determine the systolic myocardial material parameters (T_{max}) using the SRSM approach by targeting the in vivo systolic strains and LV volumes. The in vivo systolic strains and LV volumes were determined from tagged MRI, which also provided the LV endocardial and epicardial contours that were used to generate the FE model. The FE model loading conditions were obtained from cardiac catheterization measurements of LV pressures. Figure 8.5 summarizes the optimization methodology.

Data collected from adult sheep [38] were used to demonstrate the methodology and accuracy of the FE optimization tool. Briefly, the sheep underwent anteroapical myocardial infarct following the procedures described in Markovitz et al. [20]. At 14-week post-MI, a series of orthogonal short- and long-axis tagged MR images were acquired as described previously [13]. The end-diastolic and end-systolic LV pressures were measured with a nonferromagnetic transducer-tipped pressure catheter (model SPC-320; Millar Instruments, Houston, TX) inserted into the LV via sterile neck incisions [13] and used to define the endocardial boundary conditions of the FE model.

A customized version of the MR image tagging postprocessing software, FindTags (Laboratory of Cardiac Energetics, National Institutes of Health, Bethesda, MD), was used to contour the endocardial and epicardial LV surfaces and also to segment the systolic tags for each image slice [14]. Systolic myocardial strains at midwall and around the circumference in each short-axis slice were calculated from tagline deformation using the four dimensional B-spline-based motion tracking technique [33], as shown in Fig. 8.6.

An FE model was created using early diastole as the initial unloaded reference state, since the LV pressure is lowest at this point and therefore stress is at a minimum. From the LV contours at early diastole, aneurysm, remote, and BZ regions were determined based on the ventricular wall thickness. Specifically, the BZ region is defined as the steep transition in wall thickness between remote and aneurysm regions [26]. Surface meshes were then created from the LV contours to replicate the in vivo geometry and measure end-diastolic and end-systolic volumes (Rapidform, INUS Technology, Inc., Sunnyvale, CA). The spaces between the endocardium and epicardium surfaces were filled with eight-noded trilinear brick elements with a single integration point for computational efficiency to generate a volumetric mesh that is refined into three elements transmurally (Truegrid, XYZ

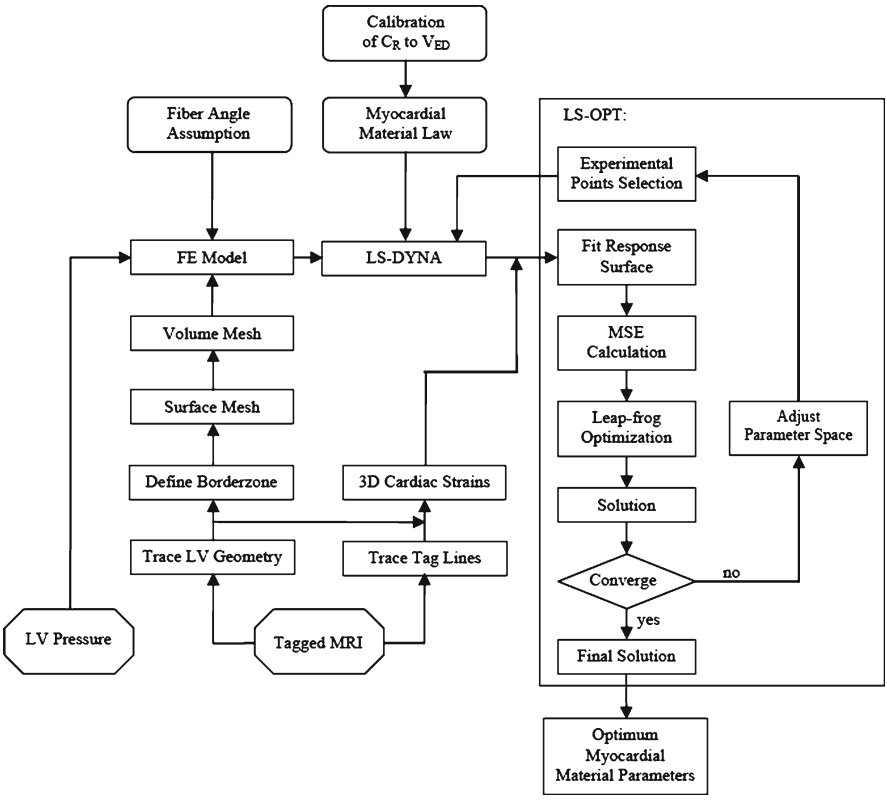

Fig. 8.5 A flowchart illustrating the process involved in determining the optimum myocardial material parameters from tagged MR images and LV pressures from cardiac catheterization (from Sun et al. [38], with permission from ASME)

Scientific Applications, Inc., Livermore, CA). Each zone, remote, BZ, and infarct was assigned to different material properties. The inner endocardial surface was lined with a layer of soft nonstructural shell elements to form an enclosed volume for LV volume measurements. A mesh convergence study determined that 2,496 elements are required and further mesh refinement only results in a 1% change in strain predictions. An example of the endocardial and epicardial surfaces, as well as the 3D mesh, is shown in Fig. 8.7.

Cardiac myofiber angles of −37, 23, and 83° were assigned at the epicardium, midwall, and endocardium, respectively, in the remote and BZ regions [31]. Cross-fiber, in-plane stress equivalent to 40% of that along the myocardial fiber direction was added [43]. At the aneurysm region, fiber angles were set to 0° in order to use experimentally determined aneurysm material parameters with respect to this direction [22]. In other words, the constitutive equation for the aneurysm is in terms of strain components that are referred to in cardiac (i.e., circumferential and longitudinal) coordinates instead of fiber coordinates. Nodes at the LV base were restricted to

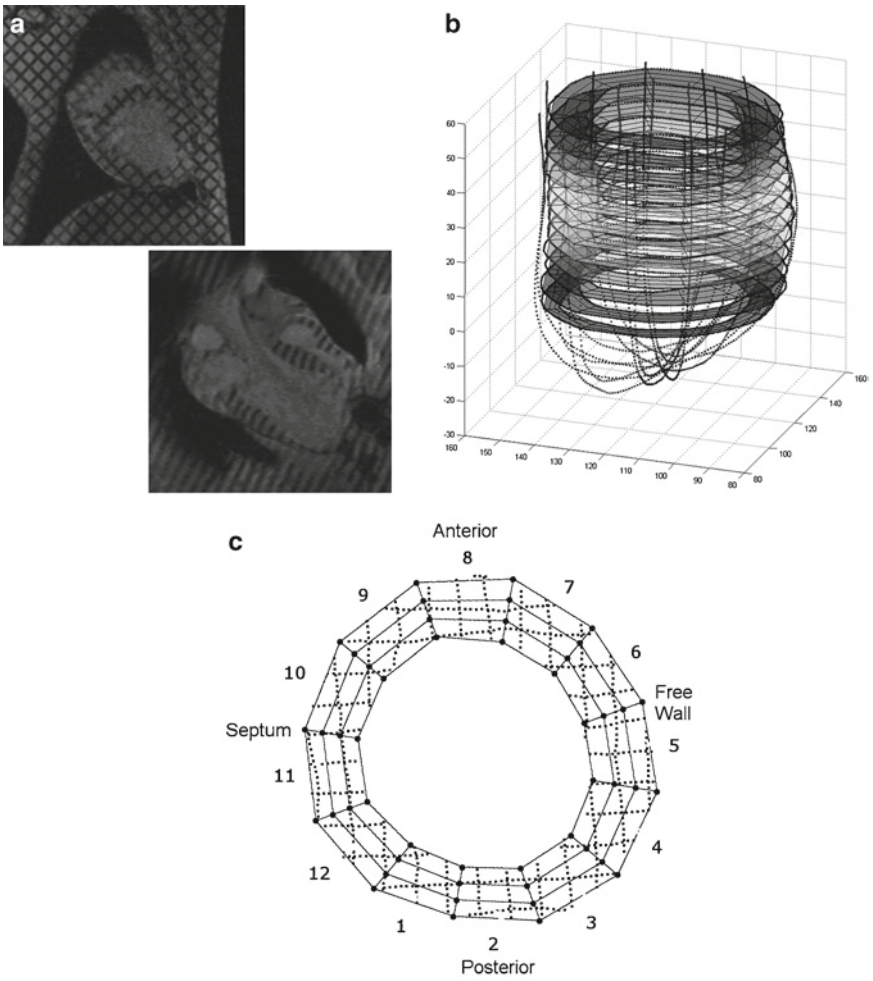

Fig. 8.6 3D cardiac strain analysis from in vivo tagged MR images. Endocardial and epicardial contours as well as segmented taglines were traced from (**a**) short-axis, as well as long-axis, MR images to create, (**b**) a 3D geometry. (**c**) Each short-axis slice was divided into 12 sectors and a 4D B-spline-based motion tracking technique was applied to the tagline (*dotted lines*) deformations to calculate the Lagrangian Green's strains in cylindrical coordinates. For each sector of each short-axis slice, longitudinal, radial, circumferential, and shear strains throughout systole were determined (from Sun et al. [38], with permission from ASME)

displace horizontally, and circumferential displacements were constrained at the basal epicardial nodes. The inner endocardial wall was loaded to the measured in vivo end-diastolic and end-systolic LV pressures.

The minimum of the objective function, consisting of 960 strain and two LV volume data points, was reached in ten iterations. The optimized $T_{\text{max\_R}}$ and $T_{\text{max\_B}}$ (remote and BZ) for this sheep are 190.1 and 60.3 kPa, respectively, with 90%

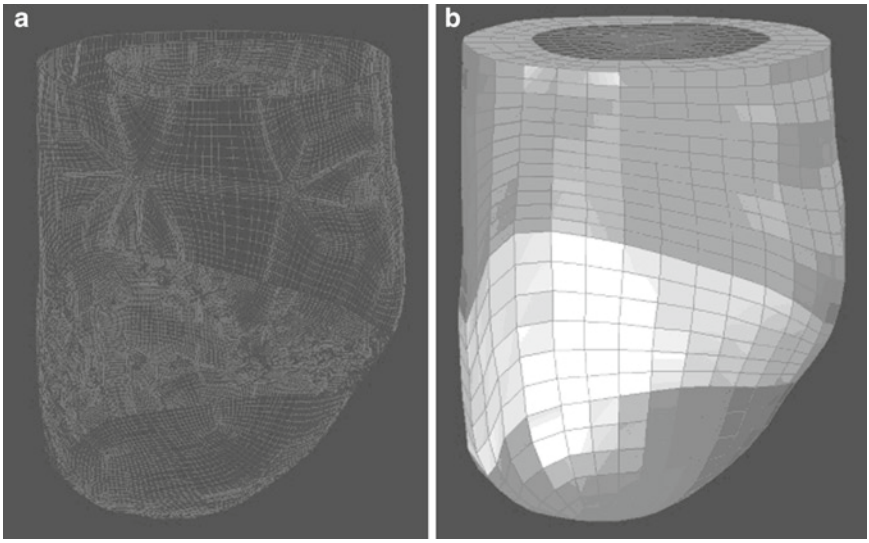

Fig. 8.7 Creation of the FE model of the LV using geometry from in vivo tagged MR images. Endocardial and epicardial contours extracted from short- and long-axis MR images were used to generate (**a**) a surface mesh with three distinct LV regions (remote, BZ, and aneurysm). The surface meshes provide projection surfaces for (**b**) the volumetric mesh, which is refined into three elements transmurally. A layer of shell elements line the endocardial surface and cap off the top of the LV to form a closed volume for LV volume measurements (from Sun et al. [38], with permission from ASME)

confidence intervals at 14.9 and 16.9%, respectively. This represents a decrease in BZ contractility, that is, 3.15 times less than the remote region. V_{SD} was accurately predicted at 110.8 ml, only 4.9% higher than the measured value of 105.6 ml. The predicted systolic strains, using the optimized material parameters, were generally in decent agreement with the in vivo measured strains. The insertion points of the right ventricle (RV) to the LV showed the largest difference between the measured and predicted strains since the RV was not included in the model. The RMS error for the circumferential strain component between the 137 pairs of measured and predicted strains in the remote zone was 0.048, and in the BZ the RMS error was 0.070 with 55 pairs of strain points. Unfortunately, there were no strain measurements in the infarct zone as short-axis MR images were not acquired in that area. The significant depression in optimized T_{max_B} relative to T_{max_R} was confirmed by direct ex vivo force measurements from skinned fiber preparations. In addition, the optimized values of T_{max_B} and T_{max_R} were not overly sensitive to the passive material parameters specified. The computation time of less than 5 h associated with our proposed method for estimating regional myocardial contractility in vivo makes it a potentially very useful clinical tool.

Acknowledgments This research was supported by National Institutes of Health grants R01 HL077921 and HL086400 (Dr. Guccione).

References

1. Aurigemma GP, Zile MR, Gaasch WH. Lack of relationship between Doppler indices of diastolic function and left ventricular pressure transients in patients with definite diastolic heart failure. Am Heart J 2004;148(3):E12.
2. Axel L, Dougherty L. Heart wall motion – Improved method of spatial modulation of magnetization for MR imaging. Radiology 1989;172(2):349–350.
3. Bovendeerd PHM, Arts T, Delhaas T, Huyghe JM, Vancampen DH, Reneman RS. Regional wall mechanics in the ischemic left ventricle: Numerical modeling and dog experiments. Am J Physiol 1996;270(1):H398–H410.
4. Bryg RJ, Williams GA, Labovitz AJ. Effect of aging on left-ventricular diastolic filling in normal subjects. Am J Cardiol 1987;59(9):971–974.
5. Burkhoff D, Maurer MS, Packer M. Heart failure with a normal ejection fraction – Is it really a disorder of diastolic function? Circulation 2003;107(5):656–658.
6. Costa KD, Hunter PJ, Wayne JS, Waldman LK, Guccione JM, McCulloch AD. A three-dimensional finite element method for large elastic deformations of ventricular myocardium. 2. Prolate spheroidal coordinates. J Biomech Eng 1996;118(4):464–472.
7. Croisille P, Moore CC, Judd RM, Lima JAC, Arai M, McVeigh ER, Becker LC, Zerhouni EA. Differentiation of viable and nonviable myocardium by the use of three-dimensional tagged MRI in 2-day-old reperfused canine infarcts. Circulation 1999;99(2):284–291.
8. Denney TS, McVeigh ER. Model-free reconstruction of three-dimensional myocardial strain from planar tagged MR images. J Magn Reson Imaging 1997;7(5):799–810.
9. Grossman W. Cardiac hypertrophy: Useful adaptation or pathologic process? Am J Med 1980; 69:576–584.
10. Guccione J, Mcculloch A. Finite element modeling of ventricular mechanics. Glass l, Hunter P, McCulloch A, eds. Theory of Heart: Biomechanics, Biophysics, and Nonlinear Dynamics of Cardiac Function. New York: Springer, 1991.
11. Guccione JM, McCulloch AD, Waldman LK. Passive material properties of intact ventricular myocardium determined from a cylindrical model. J Biomech Eng 1991;113(1):42–55.
12. Guccione JM, Moonly SM, Moustakidis P, Costa KD, Moulton MJ, Ratcliffe MB, Pasque MK. Mechanism underlying mechanical dysfunction in the border zone of left ventricular aneurysm: A finite element model study. Ann Thorac Surg 2001;71(2):654–662.
13. Guccione JM, Walker JC, Beitler JR, Moonly SM, Zhang P, Guttman MA, Ozturk C, McVeigh ER, Wallace AW, Saloner DA, Ratcliffe MB. The effect of anteroapical aneurysm plication on end-systolic three-dimensional strain in the sheep: A magnetic resonance imaging tagging study. J Thorac Cardiovasc Surg 2006;131(3):579–586, e3.
14. Guttman MA, Zerhouni EA, McVeigh ER. Analysis and visualization of cardiac function from MR images. IEEE Comp Graph Appl 1997;17(1):30–38.
15. Huang JT, Abendschein D, Davila-Roman VG, Amini AA. Spatio-temporal tracking of myocardial deformations with a 4-D B-spline model from tagged MRI. IEEE Trans Med Imaging 1999;18(10):957–972.
16. Huisman RM, Elzinga G, Westerhof N, Sipkema P. Measurement of left ventricular wall stress. Cardiovasc Res 1980;14(3):142–153.
17. Jan KM. Distribution of myocardial stress and its influence on coronary blood flow. J Biomech 1985;18(11):815–820.
18. Kerwin WS, Prince JL. Tracking MR tag surfaces using a spatiotemporal filter and interpolator. Int J Imaging Syst Technol 1999;10(2):128–142.

19. Kramer CM, Rogers WJ, Mankad S, Theobald TM, Pakstis DL. Contractile reserve and contrast uptake pattern by magnetic resonance imaging and functional recovery after reperfused myocardial infarction. J Am Coll Cardiol 2000;36(6):1835–1840.
20. Markovitz LJ, Savage EB, Ratcliffe MB, Bavaria JE, Kreiner G, Iozzo RV, Hargrove WC III, Bogen DK, Edmunds LH Jr. Large animal model of left ventricular aneurysm. Ann Thorac Surg 1989;48(6):838–845.
21. McCulloch A, Waldman L, Rogers J, Guccione J. Large-scale finite element analysis of the beating heart. Crit Rev Biomed Eng 1992;20(5–6):427–449.
22. Moonly SM. Experimental and Computational Analysis of Left Ventricular Aneurysm Mechanics. PhD thesis. San Francisco, CA: University of California, 2003.
23. Moriarty TF. The law of Laplace: Its limitations as a relation for diastolic pressure, volume, or wall stress of the left ventricle. Circ Res 1980;46:321–331.
24. Moulton MJ, Creswell LL, Downing SW, Actis RL, Szabo BA, Pasque MK. Myocardial material property determination in the in vivo heart using magnetic resonance imaging. Int J Card Imaging 1996;12(3):153–167.
25. Moulton MJ, Creswell LL, Downing SW, Actis RL, Szabo BA, Vannier MW, Pasque MK. Spline surface interpolation for calculating 3-D ventricular strains from MRI tissue tagging. Am J Physiol Heart Circ Physiol 1996;270(1):H281–H297.
26. Moustakidis P, Maniar HS, Cupps BP, Absi T, Zheng J, Guccione JM, Sundt TM, Pasque MK. Altered left ventricular geometry changes the border zone temporal distribution of stress in an experimental model of left ventricular aneurysm: A finite element model study. Circulation 2002;106(12 Suppl 1):I168–I175.
27. Nagel E, Lehmkuhl HB, Bocksch W, Klein C, Vogel U, Frantz E, Ellmer A, Dreysse S, Fleck E. Noninvasive diagnosis of ischemia-induced wall motion abnormalities with the use of high-dose dobutamine stress MRI – Comparison with dobutamine stress echocardiography. Circulation 1999;99(6):763–770.
28. O'Dell WG, Moore, C.C., Hunter, W.C., Zerhouni, E.A., and McVeigh, E.R. Displacement field fitting for calculating 3D myocardial deformations from parallel-tagged MR images. Radiology 1995;270:829–835.
29. Okamoto RJ, Moulton MJ, Peterson SJ, Li D, Pasque MK, Guccione JM. Epicardial suction: A new approach to mechanical testing of the passive ventricular wall. J Biomech Eng 2000; 122(5):479–487.
30. Omens JH, Mackenna DA, McCulloch AD. Measurement of strain and analysis of stress in resting rat left-ventricular myocardium. J Biomech 1993;26(6):665–676.
31. Omens JH, May KD, McCulloch AD. Transmural distribution of three-dimensional strain in the isolated arrested canine left ventricle. Am J Physiol 1991; 261(3 Pt 2): H918–H928.
32. Ommen SR, Nishimura RA, Appleton CP, Miller FA, Oh JK, Redfield MM, Tajik AJ. Clinical utility of Doppler echocardiography and tissue Doppler imaging in the estimation of left ventricular filling pressures – A comparative simultaneous Doppler-Catheterization study. Circulation 2000;102(15):1788–1794.
33. Ozturk C, McVeigh ER. Four-dimensional B-spline based motion analysis of tagged MR images: Introduction and in vivo validation. Phys Med Biol 2000;45(6):1683–1702.
34. Picano E, Lattanzi F, Orlandini A, Marini C, Labbate A. Stress echocardiography and the human factor – The importance of being expert. J Am Coll Cardiol 1991;17(3):666–669.
35. Pinamonti B, Dilenarda A, Sinagra G, Camerini F, Alberti E, Lardieri G, Miani D, Morgera T, Perkan A, Salvi A, Giacca M, Mestroni L, Severini G, Falaschi A, Bussani R, Tanganelli P, Silvestri F. Restrictive left-ventricular filling pattern in dilated cardiomyopathy assessed by doppler-echocardiography – Clinical, echocardiographic and hemodynamic correlations and prognostic implications. J Am Coll Cardiol 1993;22(3):808–815.
36. Pislaru C, Bruce CJ, Anagnostopoulos PC, Allen JL, Seward JB, Pellikka PA, Ritman EL, Greenleaf JF. Ultrasound strain imaging of altered myocardial stiffness – Stunned versus infarcted reperfused myocardium. Circulation 2004;109(23):2905–2910.

37. Sarnoff S, Braunwald E, Welch G, Case R, Stainsby W, Macruz R. Hemodynamic determinants of oxygen consumption of the heart with special reference to the tension-time index. Am J Physiol 1958;192:148–156.
38. Sun K, Stander N, Jhun C-S, Zhang Z, Suzuki T, Saeed M, Wallace AW, Tseng EE, Baker AJ, Saloner D, Einstein DR, Ratcliffe MB, Guccione JM. A computationally efficient formal optimization of regional myocardial contractility in a sheep with left ventricular aneurysm. J Biomech Eng 2009;131(11):111001.
39. Usyk TP, Mazhari R, McCulloch AD. Effect of laminar orthotropic myofiber architecture on regional stress and strain in the canine left ventricle. J Elasticity 2000;61:143–164.
40. Vanoverschelde JLJ, Raphael DA, Robert AR, Cosyns JR. Left-ventricular filling in dilated cardiomyopathy – Relation to functional class and hemodynamics. J Am Coll Cardiol 1990;15(6):1288–1295.
41. Vetter FJ, McCulloch AD. Three-dimensional stress and strain in passive rabbit left ventricle: A model study. Ann Biomed Eng 2000;28(7):781–792.
42. Walker JC, Guccione JM, Jiang Y, Zhang P, Wallace AW, Hsu EW, Ratcliffe MB. Helical myofiber orientation after myocardial infarction and left ventricular surgical restoration in sheep. J Thorac Cardiovasc Surg 2005;129(2):382–390.
43. Walker JC, Ratcliffe MB, Zhang P, Wallace AW, Fata B, Hsu EW, Saloner D, Guccione JM. MRI-based finite-element analysis of left ventricular aneurysm. Am J Physiol Heart Circ Physiol 2005;289(2):H692–H700.
44. Walker JC, Ratcliffe MB, Zhang P, Wallace AW, Hsu EW, Saloner DA, Guccione JM. Magnetic resonance imaging-based finite element stress analysis after linear repair of left ventricular aneurysm. J Thorac Cardiovasc Surg 2008;135(5):1094–1102, 1102, e1–2.
45. Wiegers S, Plappert, T, St John Sutton M. Role of echocardiography in the diagnosis and treatment of cardiomyopathies. Poole-Wilson P et al. eds. Heart Failure: Scientific Principles And Clinical Practice. New York: Churchill Livingstone, 1997.
46. Yin FCP. Ventricular wall stress. Circ Res 1986;49:829–842.
47. Young AA, Kraitchman DL, Dougherty L, Axel L. Tracking and finite-element analysis of stripe deformation in magnetic-resonance tagging. IEEE Trans Med Imaging 1995;14(3):413–421.
48. Zerhouni EA, Parish DM, Rogers WJ, Yang A, Shapiro EP. Human-heart: Tagging with MR imaging – A method for noninvasive assessment of myocardial motion. Radiology 1988;169(1):59–63.
49. Zile MR, Baicu CF, Gaasch WH. Diastolic heart failure – Abnormalities in active relaxation and passive stiffness of the left ventricle. N Engl J Med 2004;350(19):1953–1959.

Chapter 9
Modeling of Whole-Heart Electrophysiology and Mechanics: Toward Patient-Specific Simulations

Fijoy Vadakkumpadan, Viatcheslav Gurev, Jason Constantino, Hermenegild Arevalo, and Natalia Trayanova

9.1 Introduction

The practice of cardiovascular care has seen significant advances in the past 40 years with dramatic reduction of mortality from heart diseases. Nevertheless, cardiac diseases remain the leading cause of morbidity and mortality in the developed world and are on the rise in developing countries [37]. It is well recognized that the conventional clinical practice of using population-based metrics to prescribe "one size fits all" treatment methods does not provide optimal health care for many patients because of the individual variability in pathophysiology. Moreover, in many situations, physicians do not have a way of predicting patient responses to various therapeutic interventions, and therefore have to rely on "trial and error" to identify the treatment-response relationship. An emerging paradigm that addresses these challenges is the so-called personalized medicine, which seeks to develop diagnosis and treatment methods that can be tailored by the physician a priori according to the specific needs of an individual patient [25, 44, 52]. Application of such personalized approach to cardiac care can dramatically improve the treatment of heart diseases. To fully utilize the quality and diversity of clinically available data for personalized cardiac care, it is necessary to integrate structural and functional data at molecular, cellular, tissue, and organ level into a consistent framework which can be used to predict the outcomes of therapeutic interventions. Computational modeling provides a powerful tool to perform this data integration [29, 32].

Among the different data collection techniques, imaging has attained special significance due to the recent advances in acquisition technologies. Ex vivo magnetic resonance imaging (MRI) technologies have facilitated the acquisition of geometry and tissue architecture of the heart at very high spatial resolution. Modern ex vivo anatomical MR scanners can image the cardiac histoanatomy of small experimental animals, such as rabbit, with an isotropic resolution in the order of 10^{-5} m [11].

F. Vadakkumpadan (✉)
Institute for Computational Medicine and Department of Biomedical Engineering,
Johns Hopkins University, CSEB Room 218, 3400 N Charles St, Baltimore, MD 21218, USA
e-mail: fijoy@jhu.edu

R.C.P. Kerckhoffs (ed.), *Patient-Specific Modeling of the Cardiovascular System: Technology-Driven Personalized Medicine*, DOI 10.1007/978-1-4419-6691-9_9,

Advanced ex vivo diffusion tensor (DT) MR equipments can measure the diffusivity of water in the tissue with a resolution in the order of 10^{-4} m [20]. The primary eigenvectors of the DTs have been shown to be aligned with the fiber orientations. Evidence also suggests that the secondary and tertiary eigenvectors are oriented normally to the main cell axes, in the myocardial laminar plane and perpendicular to it, respectively. These developments in ex vivo imaging have facilitated the construction of image-based representative models of cardiac structure with unprecedented detail [32, 49]. Similarly, advances in in vivo imaging methods have placed at physicians' disposal the structural details of patient hearts in hitherto unavailable detail. State-of-the-art MRI and computed tomography (CT) methods can image the myocardial geometry of patient hearts at resolutions that are less than a millimeter [15, 30]. Furthermore, it is now feasible to use MRI in combination with late gadolinium enhancement to acquire the geometry of scar and peri-infarct zones of patient hearts with myocardial infarction [39]. These advances have placed image-based modeling at the threshold of patient-specific applications.

The purpose of this chapter is twofold. First, we briefly explain the methods we have developed to construct high-resolution representative models of the whole-heart electrophysiology and electromechanics from images acquired ex vivo. Second, we present a pipeline that we have implemented to estimate patient-specific myocardial fiber orientations from in vivo images. The whole-heart electrophysiology is modeled using a continuum approximation of tissue properties, which accounts for current fluxes in the extracellular and intracellular spaces, transmembrane currents through ionic channels, pumps, and exchangers, as well as changes in ionic concentrations including intracellular calcium cycling. The electromechanical modeling incorporates, in addition to cardiac electrophysiology, representations of the myofilament dynamics, ventricular contraction, and blood flow through the circulatory system. These modeling techniques in combination with the proposed methodology for estimating patient-specific cardiac fiber orientations constitute a step toward personalized simulations of cardiac electrophysiology and mechanics.

In the following, Sect. 9.2 describes our methods for segmenting high-resolution ex vivo images of the heart, Sect. 9.3 describes our methods for generating electrophysiological meshes from segmented images, Sect. 9.4 outlines the generation of mechanical meshes, Sect. 9.5 explains our methodology for simulating cardiac electrophysiology, Sect. 9.6 presents our methodology for simulating cardiac electromechanics, Sect. 9.7 outlines the electrophysiological modeling of an infarcted canine heart, Sect. 9.8 presents the electromechanical modeling of a normal canine heart, and Sect. 9.9 presents our pipeline for generating patient-specific computational cardiac meshes. Section 9.10 concludes the chapter.

9.2 Image Segmentation

To generate image-based models of the heart, it is necessary to classify (or segment) the voxels in the structural MR image into different groups, such as normal tissue, diseased tissue (or infarct), background, etc. We developed a processing pipeline

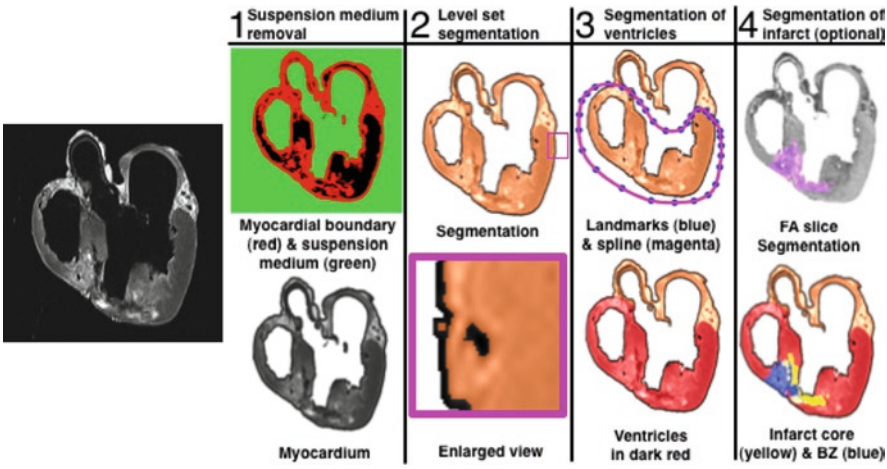

Fig. 9.1 The processing pipeline we have developed to generate computational models of the whole heart from high-resolution ex vivo structural MR images

for the segmentation of the structural MR image as illustrated in Fig. 9.1. The figure shows the results as an example image slice is processed through the steps 1–4 in the pipeline. The original example slice is shown in the leftmost column of the figure. The steps of the pipeline are briefly explained in detail below. More details of our segmentation methodology can be found elsewhere [48, 49].

9.2.1 Suspension Medium Removal

In the first step of our segmentation pipeline, the structural MR image is processed to label and "remove" the voxels corresponding to the cavity content, and the medium in which the heart was suspended during the image acquisition. First, the myocardial boundary of the whole heart is extracted using a combination of two-dimensional (2D) edge detection [24] and three-dimensional (3D) region growing [1]. Next, from the image that represents the myocardial boundary, voxels that correspond to the suspension and cavity medium are extracted using the region-growing algorithm. Finally, the suspension medium is removed from the original structural MR image by assigning the background intensity to all voxels that correspond to the medium. Step 1 in Fig. 9.1 shows the myocardial boundary, suspension medium, and myocardium for the example slice.

9.2.2 Level Set Segmentation

In the next step, a level set method is applied to the image of the myocardium to separate the larger coronary arteries and interlaminar clefts, as well as to refine the myocardial boundary extracted during the previous steps. Level set methods have

the inherent capability to implicitly track complex topologies [21]. This characteristic makes them highly suitable for the delineation of the complex coronary artery network and interlaminar clefts. Step 2 in Fig. 9.1 illustrates the level set segmentation for the example slice.

9.2.3 Segmentation of Ventricles

In the third step of our pipeline, segmentation of the ventricular myocardium is performed. In this step, in each slice, the ventricular portion of the tissue is labeled by fitting a closed spline curve through landmark points placed around the ventricles and along the atrioventricular border. All voxels that belong to tissue inside the curve are marked as ventricular. Step 3 in Fig. 9.1 shows the landmarks, spline, and ventricular myocardium for the example slice. The identification of landmark points is performed manually for a number of slices that are evenly distributed in the image. The landmarks for the remaining slices are obtained by linearly interpolating the manually identified points.

9.2.4 Infarct Segmentation

Frequently, hearts have undergone structural remodeling, most notable infarction. After the delineation of the ventricles, any infarct tissue present is labeled. First, a fractional anisotropy (FA) image is generated from the DTMR image by computing the FA of the DT at each voxel [8]. FA quantifies the degree of anisotropy – of diffusion of water in the tissue – in a single number. The infarct region is characterized by lower anisotropy [12]. On the basis of this difference in FA values, the infarct region is separated from the normal myocardium by applying the level set segmentation to the 3D FA image. Step 4 in Fig. 9.1 shows the segmentation of the FA image slice that corresponds to the example slice. Next, the infarct region is subdivided into two areas: a core, which is assumed to contain inexcitable scar tissue, and a peri-infarct zone, which is assumed to contain excitable but pathologically remodeled tissue, by thresholding the structural MR image based on the intensity values of the voxels. The core has high or low intensity, while the peri-infarct zone has medium intensity [39, 53]. Step 4 in Fig. 9.1 illustrates the final segmentation of the example slice. Once any infarct areas present are identified, segmentation of the structural MR image is complete.

9.3 Electrical Mesh Generation

The electrical mesh is a finite element mesh in which each element is assigned a unit vector that indicates the orientation of myocardial fibers inside that element. We generate the finite element mesh directly from segmented images using commercial

software known as Tarantula (http://www.meshing.at/Spiderhome/Tarantula.html). For details regarding the mesh generation methodology as well as the examination of mesh quality metrics such as aspect ratio, skewness, maximum angle, and minimum angle, the reader is referred to a recent paper [33]. The paper also contains performance metrics of benchmark electrophysiological simulations and a comparison with other mesh generation techniques. The unique advantage of the software is that it can generate unstructured meshes directly from segmented images. Figure 9.2a shows a mesh generated for the processed slice shown in Fig. 9.1. Figure 9.2b presents a small region of the mesh in detail. As the figure illustrates, the interior tissue volume is meshed at low resolution, while the interface between tissue and non-tissue is refined by a factor of about two.

The generation of the electrical mesh is completed by mapping the fiber orientations onto the finite element mesh by interpolating the primary diffusion vectors on the centroids of the elements. First, a reference vector field is constructed by computing the primary eigenvector of each tensor in the previously interpolated DTMR image. This vector field is in the same coordinate system as the finite element mesh. The fiber orientation assigned to an element in the mesh is the direction of that vector in the reference field nearest to the centroid of the element. It must be noted

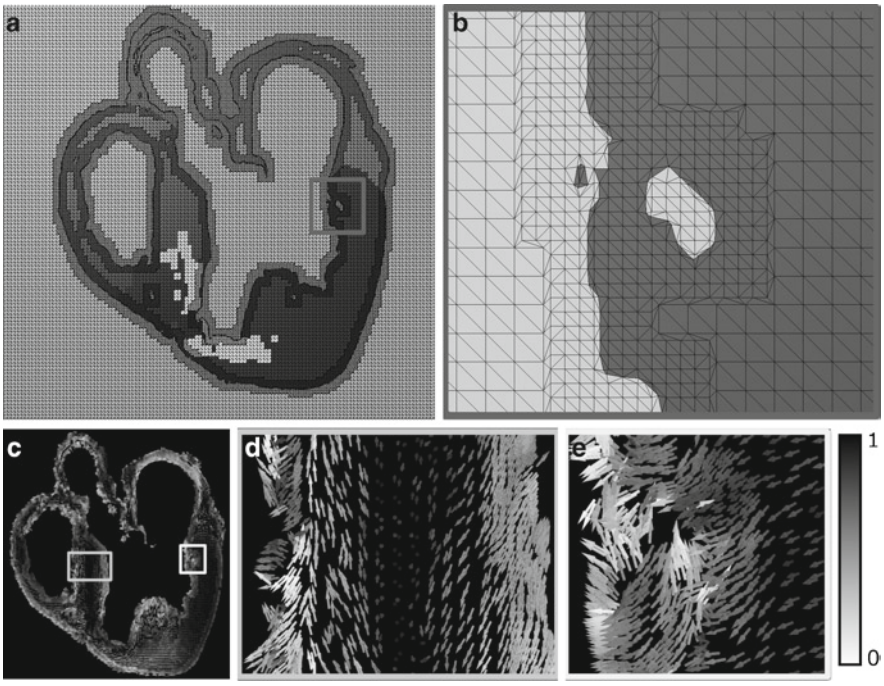

Fig. 9.2 Electrical mesh generation: (**a**) mesh corresponding to the slice shown in Fig 9.1; (**b**) enlarged view of the small region enclosed by the box in (**a**); (**c**) 2D projection, on the *xz* plane, of orientations assigned to the mesh shown in (**a**); (**d**, **e**) show enlarged views of small regions enclosed by the boxes in septum and LV in (**c**), respectively

that the two-step interpolation process correctly handles cases, where two diffusion vectors that form an obtuse angle are close together, because the reference field is constructed based on the interpolation of original diffusion weighted images, and the nearest neighbor interpolation does not involve spatial averaging of multiple vectors. Also, the nearest neighbor interpolation performed here does not produce any artifacts because the spatial resolution of the reference vector field is greater than or equal to that of the mesh in all our data. Figure 9.2c shows the 2D projection, on the *xz* plane, of derived fiber orientations that are mapped to the mesh shown in Fig. 9.2a. The arrows are colored according to the *y* component of the diffusion vectors. Due to the transmural rotation of the fibers [18–20], the arrows are lighter near the epi- and endocardial surfaces, and darker near the midwall. Figure 9.2d shows the enlarged view of a small region in the septum. Since the original slice shown in Fig. 9.1 intersects the septum nearly at a right angle, the rotation of the fibers is evident in Fig. 9.2d: the arrows are longer near the surfaces, where the fibers are oriented in the base–apex direction, and shorter near midwall, where the fibers aligned with the circumferential direction [18–20]. Figure 9.2e shows an enlarged view of a small region in the left ventricular (LV) myocardium. The arrows are densely distributed near the surfaces, demonstrating the higher resolution of the mesh in those regions.

9.4 Mechanical Mesh Generation

In this section, we describe our methods for generating computational meshes for the simulation of cardiac mechanics. The structure of the finite element hexahedral mesh for our mechanical model consists of two 6×6-element layers, as shown in Fig. 9.3a. The portion of the mesh where the two layers are attached formed the LV, the upper detached layer formed the septum, and the remaining lower layer formed

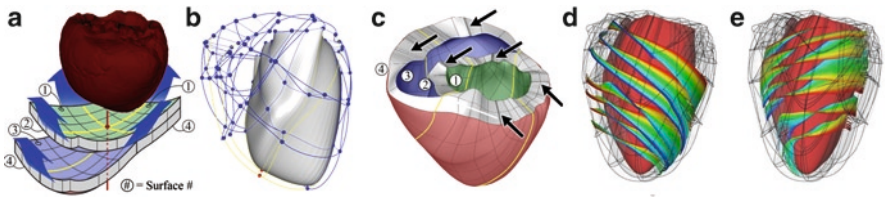

Fig. 9.3 (**a**) Overview of fitting the hexahedral mesh to the geometry obtained from segmenting the MRI scans (*the red mesh*). See text for details. (**b**) Wireframe of the hexahedral mesh. The LV is solid and the RV is transparent. The center node of the *blue surface* (*upper red node*) was positioned to the RV apex. The *yellow lines* correspond to those in panel (**a**). (**c**) Final hexahedral mesh. The *arrows* point to locations where corner elements were removed. Fibers within laminar sheets of normal canine ventricles visualized as streamlines. (**d**, **e**) Visualization of the laminar sheets located near the epicardium and endocardium, respectively. The colors in the sheets trace individual fibers

the right ventricle (RV). Layer surfaces labeled 1–4 in Fig. 9.3a defined the endocardium and epicardium of the ventricles, where surface 1 (green) was the LV endocardium, surfaces 2 and 3 (blue) formed the RV endocardium, and surface 4 (red) defined the epicardium.

To reconstruct the geometry of the mechanical mesh, a least-squares fitting method is used to define the nodal coordinates and their derivatives of the epicardial and endocardial surfaces. This fitting algorithm is described elsewhere [19, 27]. For the nodes that reside within the LV midwall, the spatial coordinates and its derivatives are calculated as the averages of the corresponding nodes on the epicardium and endocardium. To ensure continuity with respect to the global coordinates, all derivatives are defined with respect to arc length, as done by Nielsen et al. [27]. After the fitting, corner elements of the mesh are nearly prisms with two nearly triangular faces, which result in the degeneration of mesh quality. Therefore, the mesh is further refined by decreasing the size of the layers' corner elements and increasing that of the elements adjacent to the corner elements, while retaining the overall shape of the mesh. These smaller corner elements are then removed from the mesh. The arrows in Fig. 9.3c point to the locations of the corner elements. Finally, mesh elements are subdivided to distribute the ventricular volume more evenly among elements. As a result, the initial mesh of 72 elements (Fig. 9.3b) becomes a final hexahedral mesh of 172 elements and 356 nodes (Fig. 9.3c).

The fiber and laminar sheet structural information for the mechanical mesh is obtained from the DTMR image dataset. To this end, tensors and their gradients are defined at each node of the finite element mesh and interpolated within the finite elements using Hermite interpolation. The values at the nodes are computed using a least-squares method, which minimizes the sum of the squared distances between the DTs from the DTMR image and the tensors from the interpolated tensor field. The minimization is performed in the so-called log-Euclidean metric space, which was introduced previously by Arsigny et al. [3]. Since artifacts appear when voxels of MR images represent both ventricular tissue and surrounding media, a regularization of the approximated tensor field was employed to smooth the tensor field and eliminate the partial volume effect on the DTs at the epicardial and endocardial surfaces. The eigenvectors of the tensors in the interpolated tensor field represent the fiber and laminar sheet structure of the reconstructed hearts. Figure 9.3d illustrates the fiber orientations and laminar structure near the epicardium of the anterolateral part of a mechanical mesh that was built using our methods. Figure 9.3e illustrates the fiber orientations and laminar sheets near the endocardium.

9.5 Modeling of Electrophysiology: General Aspects

This section describes the methodology associated with simulating the electrophysiological behavior of the heart. The simulation of propagation of a wave of transmembrane potential is performed by solving a reaction-diffusion partial differential equation (PDE) for the transmembrane potential [31] on the electrical

finite element mesh. This equation describes current flow through cardiac cells that are electrically well connected by means of low-resistance gap junctions, allowing for a continuum representation of current flow in the heart. Cardiac tissue has orthotropic passive electrical conductivities that arise from the cellular organization into fibers and laminar sheets. Global conductivity values are obtained by combining ventricular fiber and sheet organization with myocyte-specific local conductivity values [51]. Current flow in the tissue is driven by active processes of ionic exchange across myocyte membranes (See also Chaps. 3 and 4). These active electrical processes are represented by the ionic model of myocyte membrane behavior, where current flow through ion channels, pumps, and exchangers in the myocyte membrane as well as subcellular Ca cycling between cell compartments and buffers are governed by a set of ordinary differential (ODE) and algebraic equations. Simultaneous solution of the PDE with the set of ionic model equations represents the simulation of electrical wave propagation in the heart. Our laboratory has extensive expertise in simulating electrical activity in the heart using this approach [4, 38, 45], where a biophysical model of myocyte active behavior is combined with a model of cardiac structure and geometry; review of all the modeling details can be found in [31].

9.6 Modeling of Electromechanics: General Aspects

To simulate cardiac electromechanics, the electrical component of the model (described in the previous section) is coupled to a mechanical component. A schematic of the electromechanical model is shown in Fig. 9.4. Physiologically, when an electrical wave propagates through the heart, the depolarization of each myocyte initiates a release of Ca from its intracellular Ca stores, followed by binding of Ca to Troponin C and cross-bridge cycling. The latter forms the basis for contractile protein movement and development of active tension in the cell, ultimately resulting in the deformation of the ventricles. Thus, the intracellular Ca released during the electrical activation couples the electrical and mechanical components. It serves as an input to a biophysical cell myofilament model representing the generation of

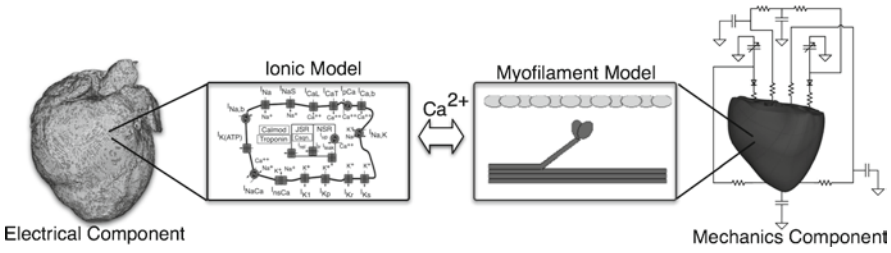

Fig. 9.4 Overall scheme of the image-based electromechanical model

active tension within each myocyte, where a set of ODEs and algebraic equations describe Ca binding to Troponin C, cooperativity between regulatory proteins, and cross-bride cycling.

Contraction of the ventricles arises from the active tension generated by the cardiac cells. Ventricular deformation is described by the equations of passive cardiac mechanics [17, 46, 47], with the myocardium being an orthotropic (due to fiber and laminar sheet organization), hyperelastic, and nearly incompressible material with passive mechanical properties defined by an exponential strain energy function. Simultaneous solution of the myofilament model equations with those representing passive cardiac mechanics on the finite element mechanical mesh constitutes the simulation of cardiac contraction. During contraction, the stretch ratio (i.e., the ratio of myocyte length before and after deformation) and its time derivative affect myofilament dynamics, including length-dependent Ca sensitivity, providing a feedback loop.

Finally, to simulate the cardiac cycle, conditions on chamber volume and pressure are imposed by a lumped-parameter model of the systemic and pulmonic circulatory systems, as shown in Fig. 9.4. The lumped-parameter model is based on the implementation by Kerckhoffs et al. [23], which we modified.

9.7 Cardiac Electrophysiology Modeling Example: Ventricular Tachycardia in the Infarcted Canine Heart

This section presents an example of the image-based electrophysiological model approach described above. It examines ventricular tachycardia (VT) in an image-based 3D model that incorporates accurate infarct geometry and composition. Complex myocardial remodeling that occurs in postinfarcted hearts has been shown to give rise to substrates that could initiate or anchor VT reentrant activity. The degree of myocardial injury in the infarcted region is dependent on tissue proximity from the site of occlusion. Tissue that experiences zero perfusion undergoes cellular necrosis and formation of scar tissue. Infarct-shape analysis has demonstrated that strands of viable tissue within electrically passive scar tissue could provide alternate pathways for propagation. In addition, partial perfusion in the adjacent peri-infarct zone tissue results in ion channel and gap junction remodeling that have been shown to result in slowed conduction and altered action potential morphology. The complexity of tissue remodeling within the infarct has made it difficult to elucidate the specific mechanisms that give rise to postinfarction VT and its morphology.

The model was built using previously described methods from an infarcted canine heart, which was scanned 4-week postinfarction using structural MR and DTMR at a resolution of $350 \times 350 \times 800$ μm^3 and interpolated using cubic splines to a resolution of $200 \times 200 \times 200$ μm^3. The top row in Fig. 9.5 shows the geometry of the model. The ionic kinetics in the normal myocardium and peri-infarct zone were represented by the Luo–Rudy dynamic model [26]. Membrane kinetics in the peri-infarct zone was modified based on data from literature. Previous studies of

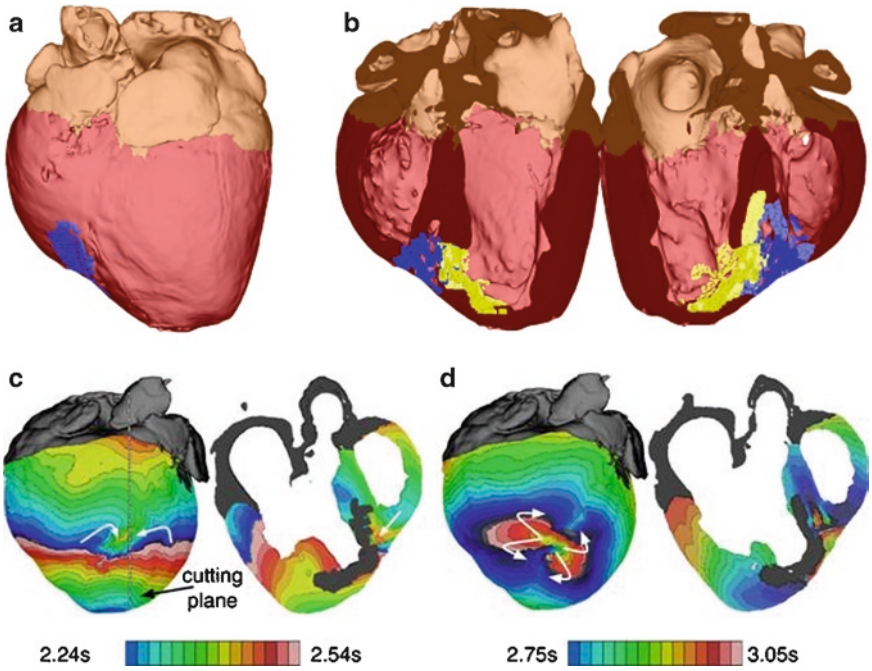

Fig. 9.5 The geometry of the infarcted canine heart model and activation times during VT induction. (**a**) Anterior view of geometry, where the ventricles are colored in *red*, atria in *chocolate brown*, infarct core in *yellow*, and peri-infarct zone in *blue*; (**b**) the geometry split in half along a horizontal view axis plane; (**c**) epicardial and transmural activation times during the fourth pacing stimulus; (**d**) activation map showing the VT circuit

peri-infarct zone in infarcted canine hearts have reported a reduction in peak sodium current to 38% of the normal value [35], in peak L-type calcium current to 31% of normal [13], and in peak potassium currents I_{Kr} and I_{Ks} to 30 and 20% of the maximum [22], respectively. These modifications result in longer action potential duration (APD) and decreased excitability compared to the normal myocardium. To examine the arrhythmogenic propensity of the infarct substrate, an aggressive pacing protocol was delivered from the apex, similar to protocols used for clinical evaluation of patients with myocardial infarction. Pacing commenced at a basic cycle length of 250 ms for five beats (S1); 450 ms after the last S1, six stimuli were delivered at progressively shorter coupling intervals, starting at 190 ms and decreasing in steps of 10 ms. The induced activity was monitored for additional 2.5 s.

The bottom row in Fig. 9.5 illustrates the events that lead to VT induction. It depicts isochrones of activation times for time periods during the fourth stimulus of the aggressive pacing protocol (panel c) and during the resulting VT (panel d). For each activation map, the image on the right presents the intramural activation pattern on a slice through the heart, the location of which is indicated by the white

dotted line on the epicardium in panel c. When the propagating wavefront from the pacing site reaches the peri-infarct zone, conduction significantly slows as compared to the surrounding normal tissue. Faster wavefronts from the normal myocardium converge into the peri-infarct zone laterally (white arrows) activating the entire peri-infarct zone. The transmural view show late activation of the peri-infarct zone due to the wavefront propagating from the normal myocardium. Since the peri-infarct zone has a longer APD, it remains refractory, while the surrounding myocardium is fully recovered. As the pacing rate is increased, the wavefront encounters refractory tissue, resulting in conduction block. This region of block later becomes the conduit for wavefront propagation from the intramural PZ toward the surface. When pacing is completed, the activation from within the peri-infarct tissue develops into an epicardial quatrefoil reentry. The reentry core remains within the peri-infarct and is sustained throughout the simulation with a rotation frequency of 5 Hz.

Previous experimental studies of infarcted canine hearts have reported the induction of VT with epicardial reentry morphology [5]. The simulations revealed that decreased excitability, longer APD, and reduced conduction velocity throughout the peri-infarct zone promoted conduction block and wave break that develops into epicardial reentry. Furthermore, the simulation showed that the site of wave break and reentry formation occurred in both the epicardial and intramural portions of the peri-infarct zone. Thus, this study showcased the utility of image-based computational modeling in predicting sites of reentry formation and maintenance.

9.8 Cardiac Electromechanics Modeling Example: Electromechanical Delay in the Normal Canine Heart

Despite recent advancements in the understanding of the electromechanical activation sequence during normal sinus rhythm, characterization of the spatiotemporal interactions between electrical activation and mechanical contraction throughout the ventricular volume remains incomplete. This stems from the fact that current experimental techniques are limited by their inability to simultaneously evaluate the 3D electrical and mechanical activity of the heart at a high spatiotemporal resolution; therefore, alternative approaches must be undertaken. In this section, the image-based electromechanical model of the normal canine ventricles was employed to obtain insight into the 3D electromechanical activation sequence during the normal sinus rhythm. To do so, we examined the distribution of the electromechanical delay (EMD), the time interval between the onset of myocyte depolarization and that of myofiber shortening, throughout the ventricular volume during the normal sinus rhythm.

Sinus rhythm was simulated by stimulating the endocardial surface at specific locations as if activation originated from the Purkinje network. The timings and locations were adjusted until the activation pattern matched experimental data [14, 43]. We employed the canine ionic model in [16], in which we incorporated an

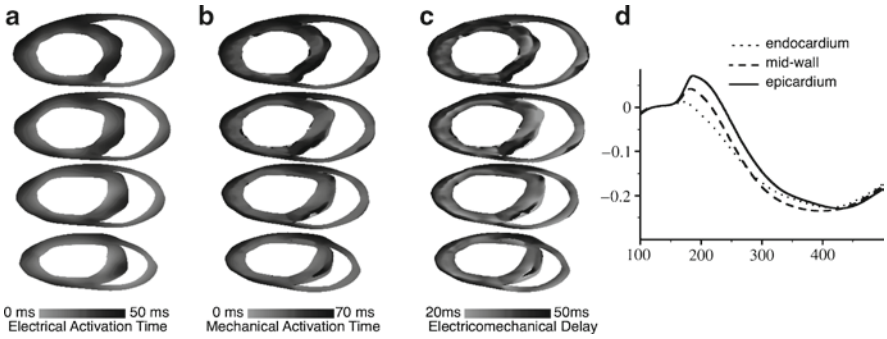

Fig. 9.6 Transmural, short-axis maps of electrical activation (**a**), mechanical activation (**b**), and electromechanical delay (**c**) during sinus rhythm in the normal canine heart. (**d**) Temporal traces of myofiber strain at the LV anterior wall

equation to represent Ca buffering by Troponin C [42]. Myofilament dynamics were governed by the biophysical model [36].

To determine the 3D distribution of EMD, the local time difference between myocyte depolarization and onset of myofiber shortening was calculated throughout the ventricles. Myocyte depolarization is defined as the instant at which the transmembrane potential exceeds 0 mV. Onset of shortening was defined as the instant when local myofiber shortening reaches 10% of its maximal value [41].

Transmural, short-axis maps of the electrical and mechanical activation (i.e., onset of myofiber shortening) times are shown in Fig. 9.6a and b, respectively. Electrical activation generally began from the endocardium and propagated to the epicardium and from the apex to the base; mechanical activation also followed this pattern. Transmural maps of EMD at the same short-axis views are shown in Fig. 9.6c and reveal that there are transmural differences in EMD throughout the LV free wall. EMD at the late-activated epicardium was longer than that at the early activated endocardium. To understand how these transmural differences in EMD arise, temporal traces of transmural myofiber strain at the mid-base of the anterior left ventricle are presented in Fig. 9.6d, and they demonstrate that the late-activated epicardium is prestretched, as indicated by the positive myofiber strain. This prestretch delays the onset of myofiber shortening and results in a prolonged EMD.

Previous experimental studies have shown that during normal sinus rhythm, there are differences in EMD on the epicardium between the apex and base [34, 41]. In addition, a local transmural difference in EMD has been reported at one single location at the anterior wall [6]. Our simulation results further these experimental findings and demonstrate that the 3D distribution of EMD is heterogeneous throughout the ventricular volume in the normal canine heart.

Understanding how this 3D distribution of EMD is altered under diseased conditions, such as dyssynchronous heart failure, and under different loading conditions could be particularly important to improving pacing therapies that aim to recoordinate mechanical contraction, such cardiac resynchronization therapy (CRT). Although CRT has been shown to improve quality of life and reduce hospitalizations [7], a

substantial number of patients do not respond to CRT, making it difficult to justify the expense of its broader application (Chap. 10). Thus, further advancements in optimizing CRT delivery and improving the selection criteria of potential CRT responders will necessitate mechanistic insights into the 3D interaction between electrical activation and mechanical activation under healthy and diseased conditions.

9.9 On the Road to Patient-Specific Modeling

In the preceding sections, we described the methodologies that we have developed to construct representative models of cardiac structure and to study electrophysiological and electromechanical phenomena of the heart by simulating with numerical models. In this section, we present the techniques that we have developed to build models that are based on the specific architecture and electromechanical properties of the patient's diseased heart. Such personalized cardiac models in combination with high-performance computing can provide clinical researchers with quick and noninvasive access to critical information about electrophysiological and electromechanical phenomena and events in the hearts of individual patients. Ultimately, such patient-specific information will aid physicians to arrive at highly personalized decisions for electrophysiological interventions as well as prophylaxis, thereby dramatically improving cardiac healthcare. To illustrate, current radiofrequency ablation approaches to treating ventricular arrhythmia rely solely on the physician's experience in identifying and destroying the arrhythmogenic substrate, a task that is complicated by the variations in the morphology of structural remodeling (infarct) across different patients (Chap. 1). With the aid of realistic patient-specific computational models, physicians will be able to simulate different ablation scenarios, predict the results, and select the optimal intervention.

Despite the potential impact, the application of electrophysiological simulations in personalized treatment is hampered by a significant barrier, namely the lack of technology to acquire the fiber structure of a given patient heart. While advanced MR and CT technologies can acquire the geometry of a patient heart in vivo up to submillimeter resolution [15, 28, 30], there is no practical method that physicians can use for noninvasively acquiring the fiber structure of a living patient heart. This limitation constitutes one of the major obstacles to the application of computational cardiac simulations in the clinical setting. To address this need, we have developed a methodology to predict fiber orientations of a patient heart from geometry acquired in vivo [50].

We hypothesize that fiber orientations of a patient heart can be accurately predicted given the geometry of the patient heart and an atlas human heart. If this hypothesis was proven, it will be possible to estimate fiber orientations of patient hearts from geometries acquired using modern in vivo MRI and CT technologies. We have tested this hypothesis, and developed, using state-of-the-art techniques, a processing pipeline for the estimation of patient-specific fiber orientations. The pipeline involves the use of tools of computational anatomy [9] to morph fiber

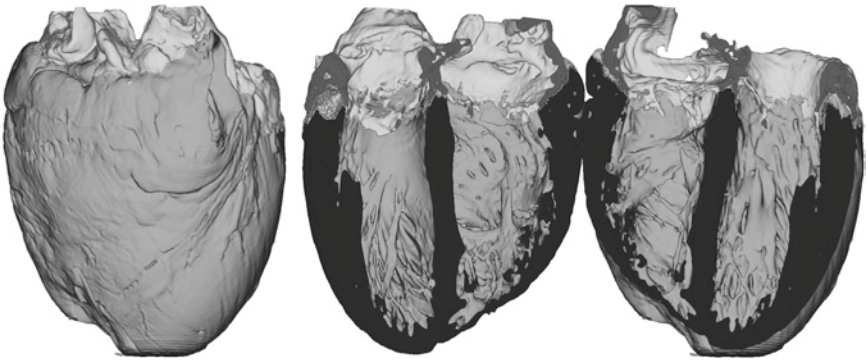

Fig. 9.7 The geometry of the normal human atlas heart. The *left panel* shows the anterior view, and the *right panel* shows the atlas split in half along a horizontal view axis plane. The ventricles appear in *dark gray*, and the atria in *light gray*

orientations of an atlas to match patient geometries (see, e.g., Chap. 7), thereby obtaining patient-specific fiber orientations.

The atlas is a normal human heart whose geometry and fiber orientations are acquired ex vivo using high-resolution ($0.4297 \times 0.4297 \times 1$ mm^3) structural MRI and DTMR image, respectively. The reconstruction of the atlas geometry from the structural data was performed using methods described in the previous section on image segmentation. Figure 9.7 shows the atlas geometry. The reconstruction is highly detailed, retaining finer structures such as trabeculations and papillary muscles. A visualization of the atlas fiber orientations is shown in Fig. 9.8. As expected, the fibers form a counterclockwise helix on the epicardial surface.

9.9.1 Processing Pipeline for Estimating Patient-Specific Fiber Orientations

Figure 9.9a shows the processing pipeline that we have developed to estimate patient-specific fiber orientations of the heart. The pipeline involves three main steps, as shown in the gray blocks in the figure. The following subsections describe these steps and illustrate our methodology by showing how the estimation is performed for an example patient who was scanned using in vivo CT.

9.9.2 Reconstruction of Patient Heart Geometry

In the first step, the patient heart structural MR or CT image is segmented to reconstruct the ventricular myocardium. In this segmentation, the voxels that correspond to the ventricular myocardium of the patient heart are labeled. The labeling is performed

Fig. 9.8 A visualization of the fiber orientations in the normal human heart atlas

by fitting closed splines through a set of landmark points that are semiautomatically placed along the epicardial and endocardial boundaries of the ventricles in the image. All voxels that lie inside the epicardial spline, but outside the endocardial splines are marked as myocardial. Similar to the extraction of ventricles from a high-resolution ex vivo image described previously, the placement of landmark points is performed manually for a number of slices that are evenly distributed in the image. The landmark points for the remaining slices are obtained automatically by linearly interpolating the manually identified points. Figures 9.9b and c illustrate the reconstruction of the ventricular geometry from the in vivo CT image of the example patient. Incidentally, our experiments indicate that the number of image slices for which landmark points need to be placed manually is about 10% of the total number of slices, and the amount of time required for segmenting the myocardium from a typical in vivo image is less than 1 h.

9.9.3 Deformation of Atlas Heart Geometry

In the next step of the pipeline, the ventricular myocardium of the atlas heart is deformed to match the patient heart geometry. This deformation is performed in two phases. The first phase involves an affine transformation based on a set of landmarks points. Five manually identified landmarks, including the LV apex, the right ventriculoseptal junctions located at the base, and the right ventriculoseptal

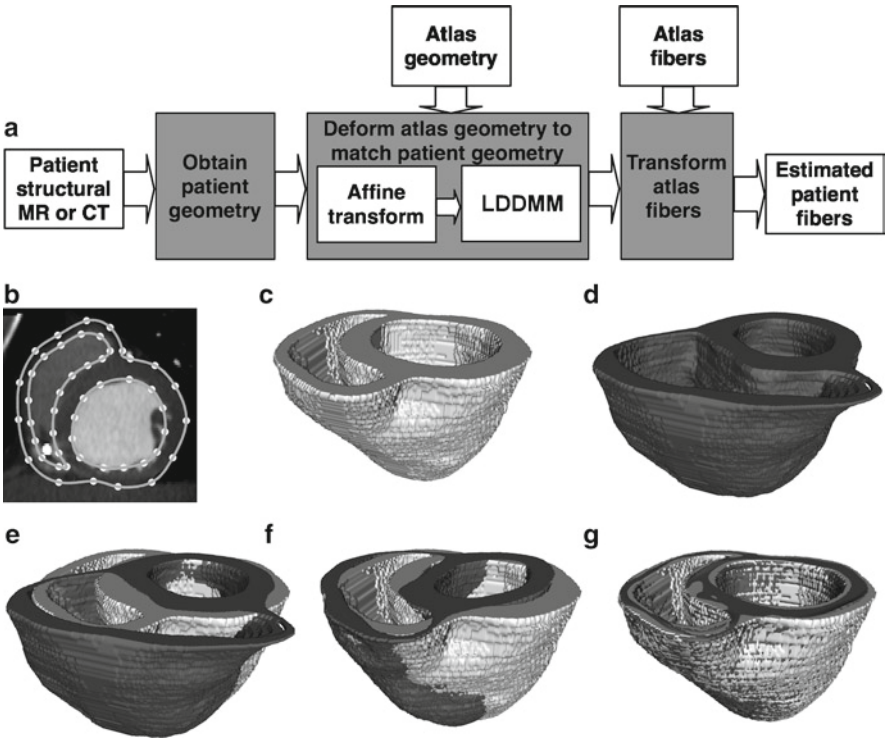

Fig. 9.9 Our methodology for estimating patient-specific myocardial fiber orientations. (**a**) The processing pipeline for the estimation; (**b**) segmentation of an example patient heart image, where splines are shown in *gray* and landmarks in *white*; (**c**) ventricular geometry of the example patient heart; (**d**) the ventricular myocardium of the atlas; (**e**) patient and atlas ventricular geometries superimposed; (**f**) patient geometry and affine transformed atlas geometry; (**g**) patient geometry and atlas geometry after large deformation diffeomorphic metric mapping (LDDMM)

junctions located midway between base and apex are used. Figure 9.9d shows the ventricular myocardium of the atlas heart, which is shown in Fig. 9.7. Figure 9.9e shows the patient geometry from Fig. 9.9c, together with the atlas ventricular myocardium. Figure 9.9f shows the patient geometry and the affine transformed atlas geometry.

The second phase of deformation of atlas geometry involves a high-dimensional nonlinear deformation using an algorithm known as large deformation diffeomorphic metric mapping (LDDMM) [10]. The advantage of the LDDMM algorithm is two-fold. First, it computes transformations that are smooth and invertible (diffeomorphic), thereby preserving the integrity of anatomical structures during deformation. In particular, connected sets remain connected and disjoint sets remain disjoint, smoothness of anatomical structures such as curves and surfaces is preserved, and coordinates are transformed consistently. Secondly the algorithm computes a geodesic, which is the shortest length path in the space of transformations that match the template and target, thereby quantifying the deformation via a scalar metric distance,

and providing a superior registration quality. The deformation of the atlas geometry, using the affine transformation and LDDMM, matches the atlas geometry with the patient geometry. Figure 9.9g shows the patient geometry together with the atlas geometry after LDDMM deformation. The deformed atlas closely matches the patient geometry.

9.9.4 Deformation of Atlas Fiber Orientations

In the final step of the pipeline, the fiber orientations of the patient heart are estimated. This step involves the application of the affine transformation matrix and the deformation field of LDDMM in sequence to deform the DTMR image of the atlas. The deformation of the DTMR image consists of spatial repositioning of the image voxels in accordance with the spatial transformation of geometry images and reorientation of the DTs. The reorientation of the DTs is performed by using the so-called preservation of principal directions method [2]. This method preserves the principal direction of the DT as well as the plane spanned by the largest two eigenvectors, and therefore is well suited for the higher-order transformations that are involved in registering cardiac images. The deformation of the template DTMR image, by repositioning the image voxels and reorienting the DTs, gives an estimate of the patient heart DTs, the primary eigenvectors of which provide an estimate of the patient-specific fiber orientations. Figure 9.10 shows the estimated myocardial fiber orientations of the example patient. As expected, the fiber orientations appear clockwise helically near the endocardium, circumferentially near midwall, and anticlockwise helically near the epicardium.

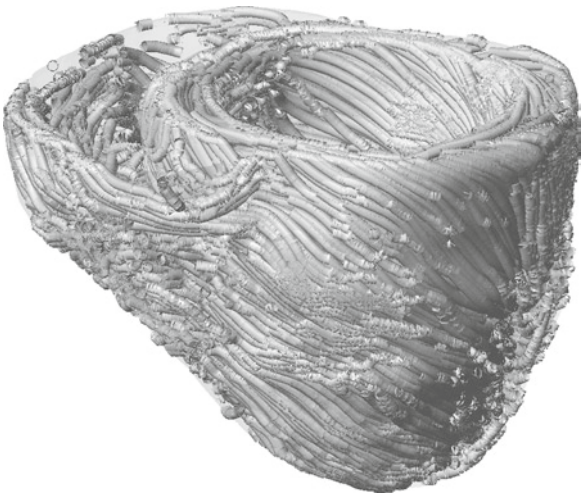

Fig. 9.10 A visualization of the estimated myocardial fiber orientations of the example patient

9.9.5 Pipeline Validation

The pipeline for estimating patient-specific fiber orientations was validated using six normal, one failing, and one infarcted canine hearts, all of which were scanned ex vivo with high-resolution DTMR to obtain ground truth fiber orientations. One normal canine heart was chosen as the "atlas" and the fiber orientations of all other hearts were estimated. The error in estimated fiber orientations was computed as the absolute difference between the inclination angles [40] of estimated orientations and ground truth orientations. It was found that the mean error in the normal, failing, and infarcted cases were 14, 14.3, and 18°, respectively. The overall mean error was 14.8°, which is comparable to the error of 12° in fiber orientations derived from DTMR images [40].

In addition to the above, we conducted simulations of paced propagation with ventricular models built using estimated and ground truth fiber orientations and compared the resulting activation time values. In normal canine hearts, simulations showed a difference of 7.8% in activation timing values between models built using ground truth fiber orientations and those using estimated fiber orientations. In failing and infarcted cases, the differences were 7.7 and 6.2%, respectively. These results show that the estimated fiber orientations can be reliably used in electrophysiological simulations.

9.10 Conclusion

In conclusion, we have developed methods to construct high-resolution representative models of the whole-heart electrophysiology and electromechanics from images acquired ex vivo. Simulations with these models can provide new insights into cardiac function, in health and disease. Building upon our research in constructing representative models of the heart, we have developed a pipeline to create patient-specific computational meshes of the heart from in vivo images. The pipeline involves a method to accurately predict fiber orientations of patient hearts and constitutes a step toward patient-specific models of cardiac electrophysiology.

References

1. Adams, R. and L. Bischof (1994). "Seeded Region Growing." IEEE Transactions on Pattern Analysis and Machine Intelligence **16**(6): 641–647.
2. Alexander, D. C., C. Pierpaoli, et al. (2001). "Spatial Transformations of Diffusion Tensor Magnetic Resonance Images." IEEE Transactions on Medical Imaging **20**(11): 1131–1139.
3. Arsigny, V., P. Fillard, et al. (2006). "Log-Euclidean Metrics for Fast and Simple Calculus on Diffusion Tensors." Magnetic Resonance in Medicine **56**: 411–421.
4. Ashihara, T., J. Constantino, et al. (2008). "Tunnel Propagation of Postshock Activations as a Hypothesis for Fibrillation Induction and Isoelectric Window." Circulation Research **102**(6): 737–745.

5. Ashikaga, H., T. Sasano, et al. (2007). "Magnetic Resonance-Based Anatomical Analysis of Scar-Related Ventricular Tachycardia: Implications for Catheter Ablation." Circulation Research **101**: 939–947.
6. Ashikaga, H., B. A. Coppola, et al. (2008). "Transmural Dispersion of Myofiber Mechanics: Implications for Electrical Heterogeneity In Vivo." Journal of American College of Cardiology **49**(8): 909–916.
7. Auricchio, A., C. Stellbrink, et al. (2003). "Clinical Efficacy of Cardiac Resynchronization Therapy Using Left Ventricular Pacing In Heart Failure Patients Stratified By Severity of Ventricular Conduction Delay." Journal of American College of Cardiology **42**(12): 2109–2116.
8. Basser, P. J. and C. Pierpaoli (1996). "Microstructural and Physiological Features of Tissues Elucidated by Quantitative-Diffusion-Tensor MRI." Journal of Magnetic Resonance **111**(3): 209–219.
9. Beg, M. F., P. A. Helm, et al. (2004). "Computational Cardiac Anatomy Using MRI." Magnetic Resonance in Medicine **52**(5): 1167–1174.
10. Beg, M. F., M. I. Miller, et al. (2005). "Computing Large Deformtion Metric Mppings via Geodesic Flows of Diffeomorphisms." International Journal of Computer Vision **61**(2): 139–157.
11. Burton, R. A. B., G. Plank, et al. (2006). "Three-Dimensional Models of Individual Cardiac Histoanatomy: Tools and Challenges." Annals of the New York Academy of Sciences **1080**: 301–319.
12. Chen, J., S.-K. Song, et al. (2003). "Remodeling of Cardiac Fiber Structure After Infarction In Rats Quantified With Diffusion Tensor MRI." American Journal of Physiology. Heart and Circulatory Physiology **285**(3): H946–H954.
13. Dun, W., S. Baba, et al. (2004). "Dynamic Remodeling of K^+ and Ca^{2+} Currents in Cells that Survived in the Epicardial Border Zone of Canine Healed Infarcted Heart." American Journal of Physiology. Heart and Circulatory Physiology **287:** 1046–1045.
14. Durrer, D., R. T. v. Dam, et al. (1970). "Total Excitation of the Isolated Human Heart." Circulation **41**(6): 899–912.
15. Fayad, Z. A., V. Fuster, et al. (2002). "Computed Tomography and Magnetic Resonance Imaging for Noninvasive Coronary Angiography and Plaque Imaging." Circulation **106**: 2026–2034.
16. Fox, J. J., J. L. McHarg, et al. (2002). "Ionic Mechanism of Electrical Alternans." American Journal of Physiology. Heart and Circulatory Physiology **282**(2): H516–H530.
17. Guccione, J. M., K. D. Costa, et al. (1995). "Finite Element Stress Analysis of Left Ventricular Mechanics in the Beating Dog Heart." Journal of Biomechanics **28**(10): 1167–1177.
18. Helm, P., M. F. Beg, et al. (2005). "Measuring and Mapping Cardiac Fiber and Laminar Architecture Using Diffusion Tensor MR Imaging." Annals of the New York Academy of Sciences **1047**: 296–307.
19. Helm, P. A., H.-J. Tseng, et al. (2005). "Ex Vivo 3D Diffusion Tensor Imaging and Quantification of Cardiac Laminar Structure." Magnetic Resonance in Imaging **54**(4): 850–859.
20. Helm, P. A., L. Younes, et al. (2006). "Evidence of Structural Remodeling in the Dyssynchronous Failing Heart." Circulation Research **98**(1): 125–132.
21. Ibanez, L., W. Schroeder, et al. (2003). The ITK Software Guide: The Insight Segmentation and Registration Toolkit, Albany, NY, Kitware Inc.
22. Jiang, M., C. Cabo, et al. (2000). "Delayed Rectifier K Currents Have Reduced Amplitudes and Altered Kinetics in Myocytes from Infarcted Canine Ventricle." Cardiovascular Research **48**: 34–43.
23. Kerckhoffs, R. C., M. L. Neal, et al. (2007). "Coupling of a 3D Finite Element Model of Cardiac Ventricular Mechanics to Lumped Systems Models of the Systemic and Pulmonic Circulation." Annals of Biomedical Engineering **35**(1): 1–18.
24. Law, M. W. K. and A. C. S. Chung (2007). "Weighted Local Variance-Based Edge Detection and Its Application to Vascular Segmentation in Magnetic Resonance Angiography." IEEE Transactions on Medical Imaging **26**(9): 1224–1241.
25. Lesko, L. J. (2007). "Personalized Medicine: Elusive Dream or Imminent Reality." Clinical Pharmacology and Therapeutics **81**(6): 807–816.

26. Luo, C. and Y. Rudy (1994). “A Dynamic Model of the Cardiac Ventricular Action Potential. I. Simulations of Ionic Currents and Concentration Changes.” Circulation Research **74**: 1071–1096.
27. Nielsen, P. M. F., I. J. Legrice, et al. (1991). “Mathematical Model of Geometry and Fibrous Structure of the Heart.” American Journal of Physiology. Heart and Circulatory Physiology **260**(4): H1365–H1378.
28. Nikolaou, K., T. Flohr, et al. (2004). “Advances in Cardiac CT Imaging: 64-Slice Scanner.” International Journal of Cardiovascular Imaging **20**(6): 535–540.
29. Noble, D. (2002). “Modeling the Heart – From Genes to Cells to the Whole Organ.” Science **295**(5560): 1678–1682.
30. Peters, D. C., D. B. Ennis, et al. (2002). “High-Resolution MRI of Cardiac Function with Projection Reconstruction and Steady-State Free Precession.” Magnetic Resonance in Medicine **48**(1): 82–88.
31. Plank, G., L. Zhou, et al. (2008). “From Mitochondrial Ion Channels to Arrhythmias in the Heart: Computational Techniques to Bridge the Spatio-Temporal Scales.” Philosophical Transactions Series A, Mathematical, Physical, and Engineering Sciences **366**(1879): 3381–3409.
32. Plank, G., R. A. B. Burton, et al. (2009). “Generation of Histo-anatomically Representative Models of the Individual Heart: Tools and Application.” Philosophical Transactions of the Royal Society A **367**(1896): 2257–2292.
33. Prassl, A. J., F. Kickinger, et al. (2009). “Automatically Generated, Anatomically Accurate Meshes for Cardiac Electrophysiology Problems.” IEEE Transactions on Biomedical Engineering **56**(5): 1318–1330.
34. Prinzen, F. W., C. H. Augustijn, et al. (1992). “The Time Sequence of Electrical and Mechanical Activation During Spontaneous Beating and Ectopic Stimulation.” European Heart Journal **13**(4): 535–543.
35. Pu, J. and P. A. Boyden (1997). “Alterations of Na+ Currents in Myocytes from Epicardial Border Zone of the Infarcted Heart A Possible Ionic Mechanism for Reduced Excitability and Postrepolarization Refractoriness.” Circulation Research **81**: 110–119.
36. Rice, J. J., F. Wang, et al. (2008). “Approximate Model of Cooperative Activation and Crossbridge Cycling in Cardiac Muscle Using Ordinary Differential Equations.” Biophysical Journal **95**(5): 2368–2390.
37. Rodgers, A. and P. Vaughan (2002). The World Health Report 2002. Geneva, Switzerland, The World Health Organization.
38. Rodríguez, B., J. C. Eason, et al. (2006). “Differences Between Left and Right Ventricular Anatomy Determine the Types of Reentrant Circuits Induced by an External Electric Shock. A Rabbit Heart Simulation Study.” Progress in Biophysics and Molecular Biology **90**(1–3): 399–413.
39. Schmidt, A., C. F. Azevedo, et al. (2007). “Infarct Tissue Heterogeneity by Magnetic Resonance Imaging Identifies Enhanced Cardiac Arrhythmia Susceptibility in Patients with Left Ventricular Dysfunction.” Circulation **115**(15): 2006–2014.
40. Scollan, D. F., A. Holmes, et al. (1998). “Histological Validation of Myocardial Microstructure Obtained from Diffusion Tensor Magnetic Resonance Imaging.” American Journal of Physiology. Heart and Circulatory Physiology **275**(6): H2308–H2318.
41. Sengupta, P. P., B. K. Khandheria, et al. (2006). “Apex-to-Base Dispersion in Regional Timing of Left Ventricular Shortening and Lengthening.” Journal of American College of Cardiology **47**(1): 163–172.
42. Solovyova, O., L. Katsnelsona, et al. (2002). “Mechanical Inhomogeneity of Myocardium Studied in Parallel and Serial Cardiac Muscle Duplexes: Experiments and Models.” Chaos, Solitons and Fractals **13**(8): 1685–1711.
43. Spach, M. S. and R. C. Barr (1975). “Ventricular Intramural and Epicardial Potential Distributions During Ventricular Activation and Repolarization in the Intact Dog.” Circulation Research **37**(2): 243–257.
44. Thrall, J. H. (2004). “Personalized Medicine.” Radiology **231**: 613–616.

45. Trayanova, N., F. Aguel, et al. (2004). Modeling Cardiac Defibrillation: An Inquiry into Post-shock Dynamics. Cardiac Electrophysiology: From Cell to Bedside, Philadelphia, Saunders, 282–291.
46. Usyk, T. P., R. Mazhari, et al. (2000). "Effect of Laminar Orthotropic Myofiber Architecture on Regional Stress and Strain in the Canine Left Ventricle." Journal of Elasticity **61**: 143–164.
47. Usyk, T. P., I. J. L. Grice, et al. (2002). "Computational Model of Three Dimensional Cardiac Electromechanics." Computing and Visualization in Science **4**(4): 249–257.
48. Vadakkumpadan, F., H. Arevalo, et al. (2008). "Image-Based Models of Cardiac Structure in Health and Disease." Wiley Interdisciplinary Reviews: Systems Biology and Medicine **2**(4): 489–506.
49. Vadakkumpadan, F., L. J. Rantner, et al. (2009). "Image-Based Models of Cardiac Structure with Applications in Arrhythmia and Defibrillation Studies." Journal of Electrocardiology 42(2): 157.e1–157.e10.
50. Vadakkumpadan, F., H. Arevalo, et al. (2009). "Image-Based Estimation of Myocardial Fiber Orientations for Patient-Specific Models of Cardiac Electrophysiology." Heart Rhythm **6**(11): 1688.
51. Vigmond, E., F. Vadakkumpadan, et al. (2009). "Towards Predictive Modelling of the Electrophysiology of the Heart." Experimental Physiology **94**(5): 563–577.
52. Whiteley, P. (2007). The Case for Personalized Medicine. 14th International Tri-Conference on Molecular Medicine, San Francisco, CA, Moscone convention center.
53. Wu, M.-T., W.-Y. I. Tseng, et al. (2006). "Diffusion Tensor Magnetic Resonance Imaging Mapping the Fiber Architecture Remodeling in Human Myocardium After Infarction: Correlation With Viability and Wall Motion." Circulation **114**(10): 1036–1045.

Chapter 10
Personalized Computational Models of the Heart for Cardiac Resynchronization Therapy

Maxime Sermesant and Reza Razavi

10.1 Introduction

Cardiovascular diseases (CVD) are the major cause of morbidity and mortality in the western world. Within CVD, the increasing prevalence of congestive heart failure (CHF) is mainly caused by the steadily increasing number of heart attack survivors. They suffer an important scar burden on their cardiac function due to the infarction. Moreover, CHF has a terrible prognosis with 50% mortality in the first 3 years after diagnosis. Of all CHF patients, those with an additional dyssynchronous contraction have the worst prognosis. Cardiac resynchronization therapy (CRT) involves placing a pacemaker to improve the synchronicity of cardiac contraction. It has recently been shown to be an effective method of treating patients with dyssynchronous CHF, inducing significant reductions in morbidity and mortality in large clinical trials. However, clinical trials have also demonstrated that up to 30% of patients may be classified as nonresponders. There remains major controversy surrounding patient selection and optimization of this expensive treatment (e.g., lead positioning, pacemaker setting). For instance, recent studies showed that patients with heart failure and narrow QRS intervals do not currently benefit from CRT (RethinQ, [3]) and that no single echocardiographic measure of dyssynchrony may be recommended to improve patient selection (PROSPECT, [10]). Therefore, new approaches are needed in order to provide a better diagnosis and characterization of patients while achieving a better planning and delivery of the therapy.

In parallel, the last decades have seen major progress in medical imaging, cardiac modeling, and computational power that make personalized simulations (i.e., using models with patient-specific parameters) achievable. While the scientific importance and enormous clinical potential of this approach have been acknowledged [12, 23], its translation into clinical applications remains largely to be done. We aim to build

M. Sermesant (✉)
Asclepios Team INRIA, 2004 route des Lucioles, 06 902, Sophia Antipolis, France
e-mail: maxime.sermesant@inria.fr

R.C.P. Kerckhoffs (ed.), *Patient-Specific Modeling of the Cardiovascular System: Technology-Driven Personalized Medicine*, DOI 10.1007/978-1-4419-6691-9_10,

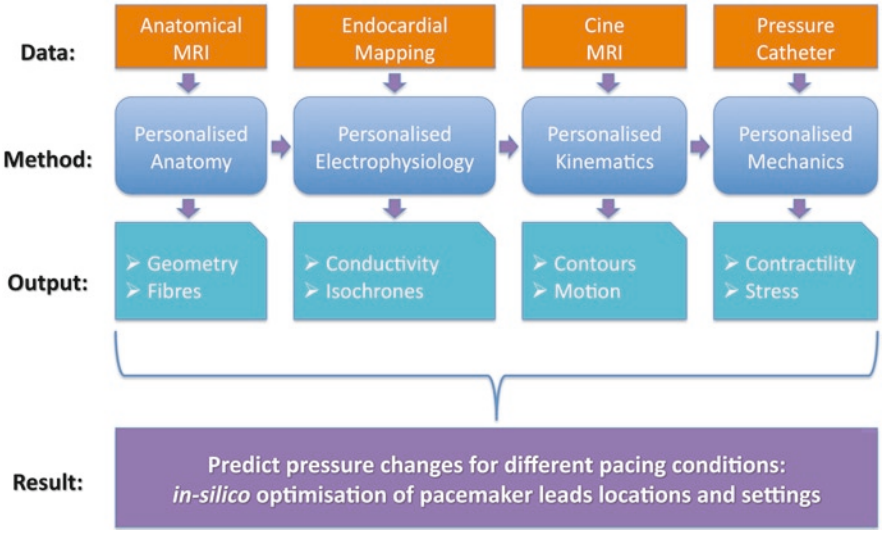

Fig. 10.1 Global scheme of the clinical data used for the personalized models, the generated output maps and parameters, and the resulting predictions [54]

on the major scientific progress that has already been made in cardiac modeling, in order to proceed to the next level and personalize such models to each specific patient using state-of-the-art multimodal imaging. This personalization of models has the potential to have a major impact on clinical practice. Indeed, patient management would be improved by a more accurate diagnosis and characterization, and personalized and predictive therapy planning for that specific patient could be achieved.

In this chapter, we demonstrate a proof of concept on a first case study of how the personalization of an electromechanical model of the heart can predict the changes in cardiac function due to changes in pacing (Fig. 10.1). Such predictions can be used to quantify the improvement in cardiac function that can be expected from CRT and also to optimize the location and delays of the pacemaker leads (stimulation electrodes). In this work we only focus on the acute effects of resynchronization. There is also an important part of the therapy process due to the reverse remodeling of the heart under the new pacing conditions [58], but this is out of the scope of the presented work.

There is a growing body of literature on the functional imaging of the heart, for instance with the measurement of electrical activity, deformation, flows, fiber orientation [15, 28, 31, 32], and on the modeling of the electrical and mechanical activity of the heart [24, 33, 39, 42, 63]. Many of these models are *direct* computational models, designed to reproduce the cardiac activity in a realistic manner, often requiring high computational costs and the manual tuning of a very large set of parameters.

Recently, computational models have been used to simulate CRT on a generic anatomy and compared with animal experiments [26, 27], which provide important insights on the pathophysiology of dyssynchrony. However, in order to translate to the clinics and impact the patient management and the therapy planning, such models

need to be personalized (i.e., with adjusted parameters) to the specificity of each patient, which is still a very challenging task.

The proposed approach involves models whose complexity is directly related to the phenomena observed in clinical data. This is the reason why these models are often simplified compared to the very detailed models available in the literature. The observability of their parameters is crucial in the personalization step. Involving a limited number of parameters can allow their identification from clinical measurements on a specific patient by the resolution of a tractable *inverse* problem (Fig. 10.1).

We illustrate in this chapter the personalization of several components. A preliminary section details the clinical context, the data acquisition, and the data fusion into the same spatio-temporal coordinates. We then present the four sections concerning the personalization of the model anatomy, electrophysiology, kinematics, and mechanics. Finally, we demonstrate this first proof of concept on the prediction of the cardiac function and its agreement to interventional measurements for five different pacing conditions on each of the two clinical cases presented.

10.2 Clinical Context, Data Acquisition, and Fusion

The construction, testing, and personalization of biophysical models rely on the ability to fuse data from an array of sources. For cardiac modeling, the fusion of anatomical, mechanical, and electrical data is of primary importance. This fusion must be both in the spatial and temporal domains. High-quality cardiac anatomical and functional data can be obtained from both computerized tomography and magnetic resonance imaging (MRI). MRI can also be used to obtain functional data such as myocardial wall motion and blood flow. Electrical data can be obtained from catheter-based measurements that are guided using X-ray fluoroscopy.

Spatial fusion of these different data requires an effective image registration strategy. Our solution has focused on the use of the X-ray/MR (XMR) hybrid imaging system that allows the seamless collection of both MRI and X-ray-based data (Fig. 10.2). We have developed a real-time registration solution [48] that allows the spatial integration of MRI-based anatomical and functional data with X-ray-based catheter data, such as intracardial electrical and pressure signals. For the temporal integration, the electrocardiogram (ECG) gives information on the heart rhythm that enables the synchronization of the different datasets.

The first patient of this study is a 60-year-old woman with NYHA class III symptoms. The etiology of heart failure is thought to be dilated cardiomyopathy although cardiac MRI did show two nonviable areas of a moderate size corresponding to the drainage area of the left anterior descending (in the apical and mid-inferoseptal segments) and of the left circumflex coronary artery [mid-inferolateral segment of the left ventricle (LV)], which are consistent with a previous subendocardial infarction. However, there was no flow-limiting disease on coronary angiography. Ejection fraction of the LV was around 30% on maximal tolerated medication. The patient suffers from a left bundle branch block as revealed in the ECG, with in particular a QRS duration of 144 ms (while a normal QRS is less than 100 ms). Echocardiography,

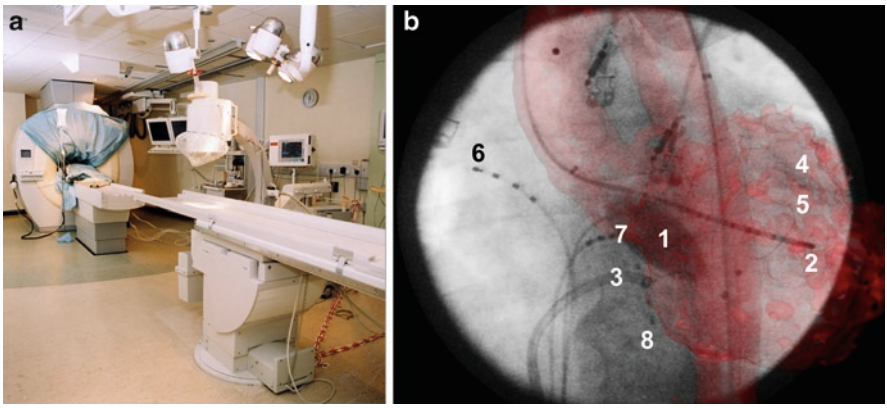

Fig. 10.2 (**a**) XMR suite with the MR scanner and the X-ray C-arm. (**b**) Overlay of MRI-derived left ventricular (LV) surface model onto live X-ray fluoroscopy image. This real-time overlay was used to guide the placement of catheters prior to the start of pacing. The catheters are as follows: (1) St. Jude ESI balloon; (2) LV roving; (3) coronary sinus sheath; (4) coronary venous/epicardial; (5) pressure; (6) high right atrium; (7) His bundle; and (8) right ventricle

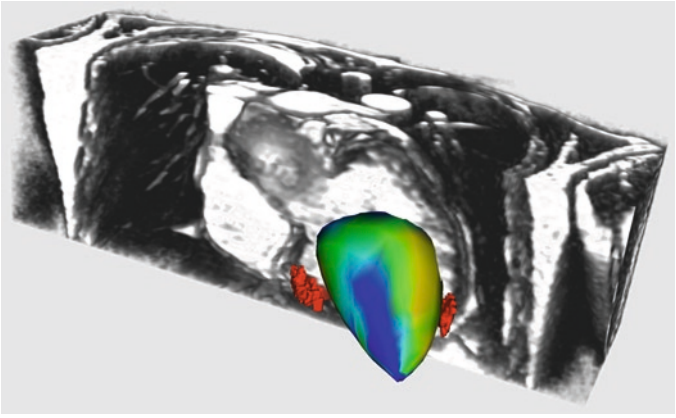

Fig. 10.3 Fusion of late enhancement derived scars (*red surfaces*), anatomical MR (volume rendering) and Ensite isochronal map (colored surface)

including tissue Doppler, confirmed significant mechanical dyssynchrony in keeping with the ECG findings.

The MR examination sequences involve SSFP Cine MR imaging for the estimation of ventricular function and volumes, late enhancement images with gadolinium for scar anatomy, and whole heart 3D navigated free breathing sequences for coronary venous anatomy. The noncontact mapping is performed using the ESI 3000 multielectrode array catheter system (St Jude, Sylmar, CA). This consists of a 64 laser-etched wire braid mounted on an 8 mm balloon. The array records intracavity far-field potentials. The resulting signals are allowing a reconstruction of over 3,000

virtual unipolar electrograms superimposed on a computerized model of the LV, creating both isopotential and isochronal maps. The scar anatomy was manually delineated in late enhancement images. The XMR fusion provides the location of the ESI mapping with respect to the MR-derived information (Fig. 10.3).

10.3 Personalized Anatomy

In this work, the anatomy model we use is limited to the compact biventricular myocardium. As we do not model the valves, we do not simulate the papillary muscles and we only integrate the blood flows in the atria and arteries as preload and afterload boundary conditions. There is an important literature on the segmentation of the heart from medical images, see for instance [14] and references therein. However, to cope with extreme and variable anatomies due to pathologies, we developed a simple yet efficient method, which combines specific image processing tools to extract the biventricular myocardium from Cine-MRI. We segment in the mid-diastolic volume of the cardiac sequence the LV endocardium, the right ventricle (RV) endocardium and the epicardium. To this aim, we developed an interactive tool based on variational implicit functions [62]. This tool allows the user to intuitively model any 3D surface in the 3D scene by placing, moving, or deleting control points inside, on and outside the desired surface [61].

We then extract the surface mesh from the volumetric binary mask and build the volumetric tetrahedral anatomical model from the surface mesh. For personalization of the simulation, each tetrahedron is automatically labeled according to the anatomical region it belongs to (LV, RV, and scar tissue, see Fig. 10.4). The scar label is based on the expert manual delineation on late enhancement MRI. Also, for regional parameter estimation, the mesh was subdivided according to the 17-segment model proposed by the American Heart Association.

The complex cardiac fiber architecture has an important role in the electrical and mechanical functions of the heart. The introduction of the fiber orientation in cardiac electromechanical modeling is essential for simulating properly the cardiac functions.

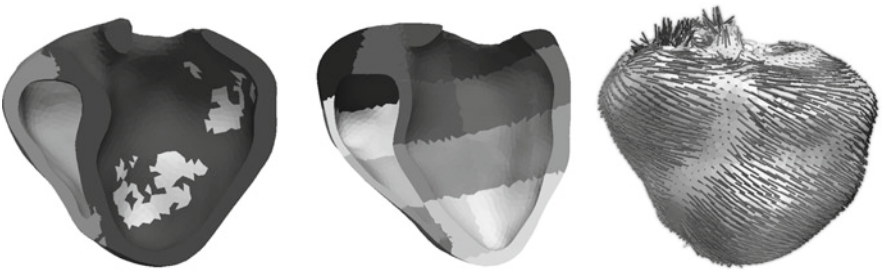

Fig. 10.4 Labeled volumetric mesh. Three main areas are defined. *Left panel*: left ventricle, right ventricle, and scar *(in white)*. *Mid panel*: Additional AHA segments subdivision is also performed for regional personalization. *Right panel*: Fiber orientations assigned to the mesh

The lack of accurate in vivo measurement of these orientations at high resolution [13] yields to using prior knowledge. Synthetic models were built with analytical laws describing general trends of fiber orientations observed in different studies [57]. The complete 3D reconstruction of fiber orientations from histological slices [40] and, more recently, its direct 3D acquisition on ex vivo hearts with diffusion tensor magnetic resonance imaging (DT-MRI) [21] have been used for a more realistic description of the myofiber architecture. However, it still comes from a single subject and thus do not take into account any inter-subject variability. We preferred to use here a statistical atlas of the cardiac fiber architecture [45]. This atlas was computed from a population of ex vivo canine hearts but was showed to be consistent with human hearts [46]. We use this atlas to generate cardiac fiber orientations, by setting the parameters of an analytical model of these fibers according to the angles observed in the atlas (Fig. 10.4, see also Chaps. 7 and 9). The personalized anatomy encompassing a computational mesh of the compact biventricular myocardium and the local fiber orientations is used for the electrophysiology model personalization described in the next section.

10.4 Personalized Electrophysiology

Clinical electrophysiological data currently available only reliably describe the depolarization times, and not the extracellular or transmembrane potentials. So we chose our electrophysiology model accordingly. Modeling the cell electrophysiology (EP) has been an active research area since the seminal work of Hodgkin and Huxley [18]. At the organ level, it involves a cell membrane model embedded into a set of partial differential equations (PDEs) representing a continuum. There are three main categories, in decreasing order of computational complexity.

- Biophysical: Semi-linear reaction-diffusion dynamic PDEs with ionic models (over 50 equations for ions and channels) [2, 30, 41, 43, 59].
- Phenomenological: Semi-linear reaction-diffusion dynamic PDEs with mathematical simplifications of the biophysical models (bidomain, monodomain) [1, 16, 47].
- Eikonal: One static nonlinear PDE for the depolarization time derived from the previous models (Eikonal-Curvature, Eikonal-Diffusion) [11, 25].

Solving the dynamic PDEs is computationally very demanding, due to the space scale of the electrical propagation front being much smaller than the size of the ventricles, and the stability issues of the dynamic aspect. The Eikonal equation is static, and the front can be observed at a larger scale, resulting in much faster computations. An anisotropic multifront fast marching method was developed in order to solve the Eikonal model equations very efficiently [52]. We base our model on the Eikonal diffusion (ED) equation (see [60] for more details on the ED equation and its parameters).

To personalize the electrophysiology model, there are two important adjustments to perform: the onset of the electrical propagation and the local conduction velocity, which corresponds to an apparent conductivity (AC). The idea is to estimate the AC by matching the simulated propagation times of the model to the clinically measured

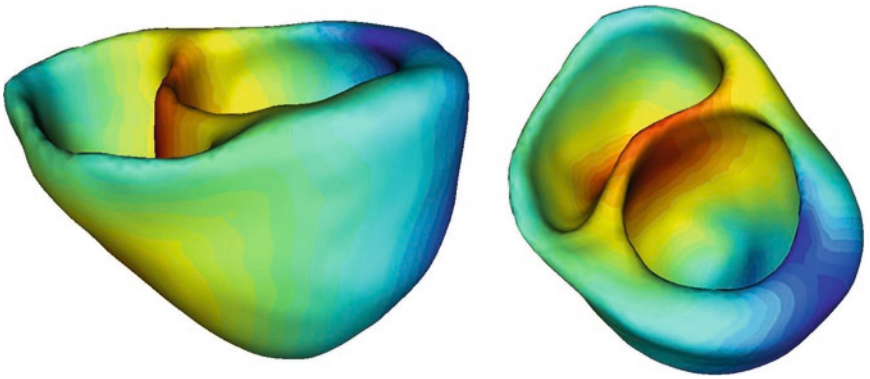

Fig. 10.5 Simulated isochrones on the volumetric mesh, adjusted using the endocardial mapping as reference. Color encodes the depolarization time (*red*: 0 ms, *blue*: 130 ms)

propagation times of the patient. The automatic adjustment method of the AC was designed for surfaces [8, 9, 37].

Such approaches were extended to volumetric models, by using a coupled error criterion both on endocardial depolarization times and QRS duration. When applying this method to the baseline data, we obtain a very good fit to the data with a final mean error that drops to 3.8 ms. The resulting AC map (Fig. 10.5) provides information on some potential Purkinje network (high values) and does seem to correlate with the scars locations (low values).

10.5 Personalized Electromechanical Models

The myocardium constitutive law has to model the active, nonlinear, anisotropic, incompressible, and visco-elastic properties of the cardiac tissue. Numerous ones were proposed in the literature, see, e.g., [6, 19–22, 38, 49, 55] and references therein. The particularity of the models used here is that they were designed to have a complexity compatible with the clinical data used for the personalization. As apparent motion and left ventricular pressure are the main components of the observations, we rely on models with limited parameters representing the passive and active parts of the constitutive law.

We use two different electromechanical models for the muscle contraction, depending on the application. We first introduce a simplified model as a deformable model in order to extract the motion and contours from the dynamic images (Sect. 10.5.1). We then use this information with additional pressure data in order to personalize a more complex model of the myocardium mechanics, which allows to adjust contractility and estimate pressures (Sect. 10.5.2). The cardiac mechanical models that we use here were presented in detail in [51] and [50]. They rely on the following key ingredients.

- An electrically activated constitutive equation based on a multiscale approach accounting for the behavior of myosin molecular motors, as originally presented in [4].
- A 3D continuum mechanics formulation integrating this active behavior (acting along the muscle fibers) with 3D passive visco-elastic components (based on hyper-elastic potentials and viscous pseudo-potentials) using a rheological model of Hill–Maxwell type [17].

To carry out simulations, additional needs are Windkessel models and valve laws to represent the blood flows, and adequate finite element and energy-preserving time discretization strategies.

We present in the two following subsections how a simplified model is used to estimate the cardiac motion, and then how a more complex model is used to simulate the cardiac mechanics.

10.5.1 Personalized Kinematics

In this subsection, we show a deformable model approach to estimate the motion of the heart using Cine-MRI data and an electromechanical model. The model used here is a simplified electromechanical model designed for cardiac image analysis and simulation [51]. We want the complexity of the model to match the relatively sparse measurements. Thus, we use here a simplified electromechanical model derived from a multiscale modeling of the myocardium described in [4]. It is composed of two elements. The first one is a parallel element which is anisotropic linear visco-elastic and which represents the passive properties of the tissue. The second one is an active contractile element controlled by the electrophysiological command. Furthermore, we simulate the four cardiac phases (filling, isovolumetric contraction, ejection, and isovolumetric relaxation) as detailed in [51]. Finally, the arterial pressures were computed using a three-element Windkessel model described in [56].

We estimate the motion of the heart by coupling an electromechanical model and Cine-MRI data, based on the proactive deformable model described in [51]. We have shown in [5] that this method is related to the data assimilation approach described in [35]. Numerous works on the adjustment of a geometrical model of the heart to time series of medical images are based on the concept of deformable models [34, 36, 44]. In this framework, a surface is fitted to the apparent boundaries of the myocardium by minimizing the sum of two energies: a data attachment term and a regularization term. In our case, this regularization term consists in the energy of the dynamical system of the simplified electromechanical model of the heart.

We want to minimize the difference between the simulated motion of the myocardium and the apparent motion in the images. As Cine-MRI only provides the

apparent (radial) motion of the endocardium (we do not have information on the tangential motion), we use the distance from the contours detected in the images to the mesh. To compute it, we seek for each surface vertex the closest boundary voxel (based on criteria on the image gradient) along the normal direction of the mesh. We then apply a force in that direction, proportional to the distance to this boundary voxel.

Figure 10.6 shows the MR images at end-diastole and at end-systole of the cardiac cycle. The superimposed lines represent the endocardium and epicardium surfaces of the estimated mesh. Colors correspond to the intensity of the image forces.

We can observe that despite the limited quality of clinical routine images, the estimation of the myocardium contours is good, especially for the LV. Due to the lack of contrast on the epicardium and the small thickness of the RV, achieving a good dynamic segmentation of the RV is still very challenging. This approach allows estimating a complete motion, including the twisting of the heart, while only using the data where it is reliable, which is in the normal direction for Cine-MRI. This estimated motion is then used to guide the adjustment of a more complex model in order to simulate the pressure variation in the ventricles.

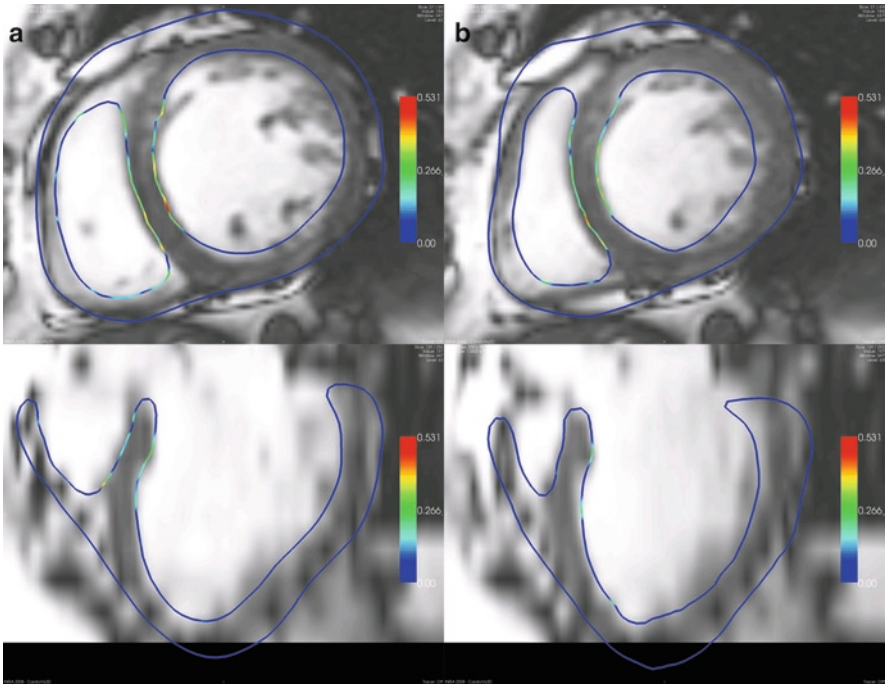

Fig. 10.6 Results of the motion tracking: delineation of the estimated mesh superimposed with Cine-MRI at (**a**) end-diastole and (**b**) end-systole. Color encodes the intensity of the image forces (*blue*: small, *red*: large) [54]

10.5.2 Personalized Mechanics

We now utilize the estimated motion to personalize the mechanical parameters, in a more complex model in order to ensure a realistic simulation of the stress. Most of the components of the mechanical model discussed in this section (detailed in [50]) are quite classically used in heart models. Nevertheless, the emphasis and originality of our approach lies in the careful choice of modeling ingredients that are relevant from a physiological point of view and consistent with essential thermo-mechanical requirements and in their global integration in ways that preserve these requirements at all steps, from the continuous dynamical equations to the discrete versions with which actual simulations are performed.

This active constitutive law was used within a rheological model of Hill–Maxwell type [7]. This rheological model is compatible with large displacements and strains and led to a continuum mechanics description of the cardiac tissue [50]. In the parallel branch of the Hill–Maxwell model we considered a visco-elastic behavior, with a hyper-elastic potential given by the Ciarlet–Geymonat volumic energy [29]. The pressure within the ventricles is then an output of the model simulation.

Adjusting the material parameters is made difficult by the fact that we are concerned with patients whose parameter values differ from nominal ones in pathological regions, e.g., decreased contractility and increased stiffness in infarcted parts. Some valuable information on the spatial distribution of these pathological regions may be obtained from clinical measurements such as late enhancement MRI, but the actual values of the perturbed parameters cannot be directly measured. Therefore, the objective of (automatically) estimating the parameter values – using some appropriate data assimilation procedures – is of utmost clinical interest. Such a complete automated estimation – still a major scientific challenge – is out of the scope of the present chapter, but we demonstrate that a proper calibration of the parameters based on global physiological indicators and using the personalization steps presented above can provide satisfactory predictability in the direct simulation of the cardiac function.

For this simulation where image information is no longer used, boundary conditions are especially important. As can be seen, e.g., in MRI sequences, there is an epicardium area near the apex on the inferior wall with small displacements, probably in relation with the attachment of the pericardium to the diaphragm. We modeled this physiological feature by prescribing some stiff visco-elastic support as boundary conditions in this area. Furthermore, we used similar visco-elastic support conditions on the base to model the truncated anatomy. The corresponding visco-elastic coefficients also require proper calibration with respect to the kinematics observed in image sequences.

The other anatomical and electrophysiological parameters have been set as in the previous sections. The mechanical parameters have been calibrated using the pressure–volume medical indicators, and also the MRI sequence as explained above for the boundary conditions. In order to take into account the infarct, the

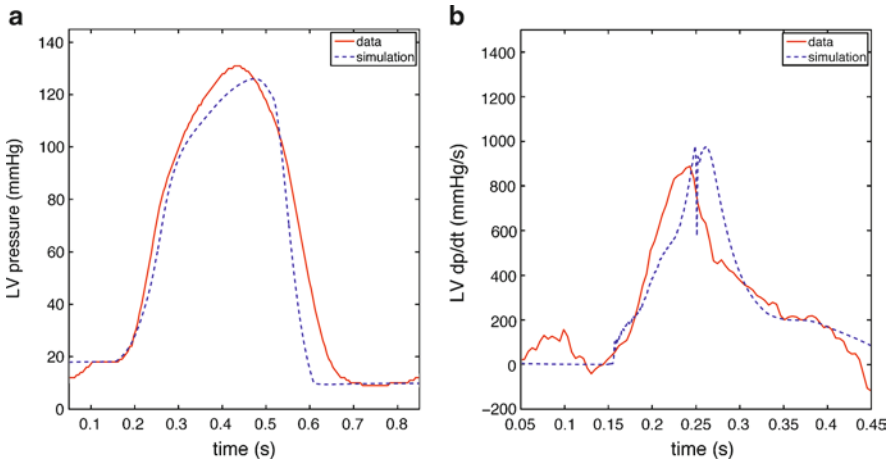

Fig. 10.7 (**a**) Measured (*solid*) and simulated (*dashed*) pressure curves in sinus rhythm. (**b**) Measured (*solid*) and simulated (*dashed*) d*P*/d*t* curves during systole in sinus rhythm

contractility parameters were decreased in the scar tissue. We then obtained a simulated motion relatively close to the one from the personalized kinematics. While there are still discrepancies, the general behavior is very similar. However, the automatic adjustment of local parameters is needed in order to be able to improve the fitting. The work in progress on this automatic identification is very promising [35, 53].

This personalized mechanical model produces simulated pressure in very good agreement with the catheter measurement (Fig. 10.7).

10.6 Prediction of the Acute Effects of Pacing on Left Ventricular Pressure

During the electrophysiology study, different pacing conditions are tested to evaluate the effect of different pacing lead locations and delays. This also gives the opportunity to estimate what could be the expected benefit from the pacemaker implantation. There is still a lot of research on what is the optimal number of electrodes, where are the optimal locations, and what are the optimal delays. This creates a large number of degrees of freedom that are difficult to optimize during the intervention itself. Being able to perform this optimization a priori and using an in silico model would be very useful.

In this section, we test the ability of our personalized electromechanical model of the myocardium to predict the changes in the heart due to a new pacing condition. The pacing protocol tested is biventricular pacing with simultaneous endocardial left ventricular pacing (we will call here this pacing sequence P1TRIV).

For the mechanical simulation, we use here the model personalized in Sect. 10.5.2 on baseline in sinus rhythm without changing any parameter. We then input the new

Table 10.1 Measured and simulated values for (dP/dt_{max}) in mmHg/s for five different conditions

	Sinus rhythm	Atrial	Right ventricle	LV endocardium	P1TRIV
Measurement	890	960	1,020	1,410	1,450
Simulation	910	970	1,000	1,480	1,440

electrical command corresponding to the pacing. The volumetric isochrones were derived as described in Sect. 10.4. We then observe the resulting simulated pressure curve allowing to test in particular predictions on the slope of this pressure during isovolumetric contraction. As this is the major cardiac phase that is sought to be optimized by CRT, we mainly focus on the model predictive power during this phase, and early ejection.

When simulating this P1TRIV pacing with the model personalized from baseline measurements, we observe a very good agreement of the pressure curve with the recorded data from the pressure catheter, and the dP/dt curve is also very similar. From the data, we can see that dP/dt_{max} goes from 890 mmHg/s at baseline to 1,450 mmHg/s for P1TRIV pacing. In the simulations we obtain 910 mmHg/s at baseline and 1,440 mmHg/s with pacing. So we can see that the improvement of the cardiac function brought by the pacing is well predicted by the in silico simulations. We used this methodology on four different pacing modes, with very promising results on the model predictions (Table 10.1).

10.7 Conclusion

We presented the personalization of a complete electromechanical model of the myocardium using XMR interventional data and how this personalized model could be used to predict therapy effects. The behavior of the model in sinus rhythm as well as the predictions of the model under pacing compare well with the measured data, which make such an approach very promising. This is the first case study demonstrating how models of the heart can be adjusted to be patient-specific and a first proof of concept of how this approach can be useful for therapy planning. While several steps still require interactive adjustment, the methodology for automatic parameter estimation is becoming available [8, 35, 53]. By integrating information about the anatomy, the electrophysiology, the kinematics, and the mechanics, we can explore the correlation between these different aspects for a given patient in order to provide an integrated view of the patient cardiac function and simulate and evaluate different therapies before their actual application. In the case of CRT, such predictions could help optimize in silico the pacemaker settings, which include the pacing lead locations and the delays between the electrodes. This will be the purpose of a future work.

Acknowledgments The authors would like to thank their co-workers in this project: R. Chabiniok, P. Chinchapatnam, T. Mansi, F. Billet, P. Moireau, J.M. Peyrat, K. Rhode, M. Ginks, P. Lambiase, S. Arridge, H. Delingette, M. Sorine, C.A. Rinaldi, D. Chapelle, and N. Ayache.

References

1. Aliev, R., Panfilov, A.: A simple two-variable model of cardiac excitation. Chaos, Solitons and Fractals 7(3), 293–301 (1996).
2. Beeler, G.W., Reuter, H.: Reconstruction of the action potential of ventricular myocardial fibers. Journal of Physiology 268, 177–210 (1977).
3. Beshai, J.F., Grimm, R.A., Nagueh, S.F., Baker, J.H., Beau, S.L., Greenberg, S.M., Pires, L.A., Tchou, P.J.: Cardiac-resynchronization therapy in heart failure with narrow QRS complexes. The New England Journal of Medicine 357(24), 2461–2471 (2007).
4. Bestel, J., Clément, F., Sorine, M.: A biomechanical model of muscle contraction. In: W. Niessen, M. Viergever (eds.) Medical Image Computing and Computer-Assisted intervention (MICCAI'01), *Lecture Notes in Computer Science (LNCS)*, vol. 2208, pp. 1159–1161. Springer-Verlag, Berlin, Germany (2001).
5. Billet, F., Sermesant, M., Delingette, H., Ayache, N.: Cardiac Motion Recovery and Boundary Conditions Estimation by Coupling an Electromechanical Model and Cine-MRI Data. In: Proceedings of Functional Imaging and Modeling of the Heart 2009 (FIMH'09), Lecture Notes in Computer Science (LNCS), vol. 5528, pp. 376–385, Nice, France, 3–5 June 2009.
6. Caillerie, D., Mourad, A., Raoult, A.: Cell-to-muscle homogenization. Application to a constitutive law for the myocardium. Mathematical Modeling and Numerical Analysis 37(4), 681–698 (2003).
7. Chapelle, D., Clément, F., Génot, F., Tallec, P.L., Sorine, M., Urquiza, J.: A physiologically-based model for the active cardiac muscle contraction. In: T. Katila, I. Magnin, P. Clarysse, J. Montagnat, J. Nenonen (eds.) Functional Imaging and Modeling of the Heart (FIMH'01), no. 2230 in *Lecture Notes in Computer Science (LNCS)*, pp. 128–133. Springer, Berlin (2001).
8. Chinchapatnam, P., Rhode, K., Ginks, M., Rinaldi, C., Lambiase, P., Razavi, R., Arridge, S., Sermesant, M.: Model-based imaging of cardiac apparent conductivity and local conduction velocity for diagnosis and planning of therapy. IEEE Transactions on Medical Imaging 27(11), 1631–1642 (2008).
9. Chinchapatnam, P.P., Rhode, K.S., King, A., Gao, G., Ma, Y., Schaeffter, T., Hawkes, D., Razavi, R.S., Hill, D.L., Arridge, S., Sermesant, M.: Anisotropic wave propagation and apparent conductivity estimation in a fast electrophysiological model: application to XMR interventional imaging. Medical Image Computing and Computer-Assisted Intervention: International Conference on Medical Image Computing and Computer-Assisted Intervention, 10, 575–583 (2007).
10. Chung, E.S., Leon, A.R., Tavazzi, L., Sun, J.P., Nihoyannopoulos, P., Merlino, J., Abraham, W.T., Ghio, S., Leclercq, C., Bax, J.J., Yu, C.M., Gorcsan, J., St John Sutton, M., De Sutter, J., Murillo, J.: Results of the predictors of response to crt (PROSPECT) trial. Circulation 117(20), 2608–2616 (2008).
11. Colli Franzone, P., Guerri, L., Rovida, S.: Wavefront propagation in activation model of the anisotropic cardiac tissue: Asymptotic analysis and numerical simulations. Journal of Mathematical Biology 28(2), 121–176 (1990).
12. Crampin, E.J., Halstead, M., Hunter, P., Nielsen, P., Noble, D., Smith, N., Tawhai, M.: Computational physiology and the physiome project. Experimental Physiology 89(1), 1–26 (2004).
13. Dou, J., Reese, T.G., Tseng, W.Y.I., Wedeen, V.J.: Cardiac Diffusion MRI without motion effects. Magnetic Resonance in Medicine 48(1), 105–114 (2002).
14. Ecabert, O., Peters, J., Schramm, H., Lorenz, C., von Berg, J., Walker, M.J., Vembar, M., Olszewski, M.E., Subramanyan, K., Lavi, G., Weese, J.: Automatic model-based segmentation of the heart in ct images. IEEE Transactions on Medical Imaging 27(9), 1189–1201 (2008).

15. Faris, O., Evans, F., Ennis, D., Helm, P., Taylor, J., Chesnick, A., Guttman, M., Ozturk, C., McVeigh, E.: Novel technique for cardiac electromechanical mapping with magnetic resonance imaging tagging and an epicardial electrode sock. Annals of Biomedical Engineering 31(4), 430–440 (2003).
16. FitzHugh, R.: Impulses and physiological states in theoretical models of nerve membrane. Biophysical Journal 1, 445–466 (1961).
17. Hill, A.: The heat of shortening and the dynamic constants in muscle. Proceedings of the Royal Society of London, Series B 126, 136–195 (1938).
18. Hodgkin, A., Huxley, A.: A quantitative description of membrane current and its application to conduction and excitation in nerve. Journal of Physiology 177, 500–544 (1952).
19. Humphrey, J.: Cardiovascular Solid Mechanics. Springer, Berlin (2002).
20. Humphrey, J., Strumpf, R., Yin, F.: Determination of a constitutive relation for passive myocardium: I. A new functional form. ASME Journal of Biomechanical Engineering 112, 333–339 (1990).
21. Hunter, P., McCulloch, A., Keurs, H.: Modeling the mechanical properties of cardiac muscle. Progress in Biophysics and Molecular Biology 69, 289–331 (1998).
22. Hunter, P., Nash, M., Sands, G.: Computational Biology of the Heart, chap. 12: Computational Electromechanics of the Heart, pp. 345–407. John Wiley & Sons Ltd, West Sussex, UK (1997).
23. Hunter, P., Nielsen, P.: A strategy for integrative computational physiology. Physiology (Bethesda) 20, 316–325 (2005).
24. Hunter, P., Pullan, A., Smaill, B.: Modeling total heart function. Annual Review of Biomedical Engineering 5, 147–177 (2003).
25. Keener, J., Sneyd, J.: Mathematical Physiology. Springer, Berlin (1998).
26. Kerckhoffs, R.C., Lumens, J., Vernooy, K., Omens, J.H., Mulligan, L.J., Delhaas, T., Arts, T., McCulloch, A.D., Prinzen, F.W.: Cardiac resynchronization: Insight from experimental and computational models. Progress in Biophysics and Molecular Biology 97(2–3), 543–561 (2008).
27. Kerckhoffs, R.C., McCulloch, A.D., Omens, J.H., Mulligan, L.J.: Effects of biventricular pacing and scar size in a computational model of the failing heart with left bundle branch block. Medical Image Analysis 13(2), 362–369 (2009).
28. Kilner, P., Yang, G., Wilkes, A., Mohiaddin, R., Firmin, D., Yacoub, M.: Asymmetric redirection of flow through the heart. Nature 404, 759–761 (2000).
29. Le Tallec, P.: Numerical methods for nonlinear three-dimensional elasticity. In: P. Ciarlet, J.L. Lions (eds.) Handbook of Numerical Analysis, vol. 3. Elsevier, North-Holland (1994).
30. Luo, C., Rudy, Y.: A model of the ventricular cardiac action potential: depolarization, repolarization, and their interaction. Circulation Research 68, 1501–1526 (1991).
31. MacLeod, R., Yilmaz, B., Taccardi, B., Punske, B., Serinagaolu, Y., Brooks, D.: Direct and inverse methods for cardiac mapping using multielectrode catheter measurements. Journal of Biomedizinische Technik 46, 207–209 (2001).
32. Masood, S., Yang, G., Pennell, D., Firmin, D.: Investigating intrinsic myocardial mechanics: the role of MR tagging, velocity phase mapping and diffusion imaging. Journal of Magnetic Resonance Imaging 12(6), 873–883 (2000).
33. McCulloch, A., Bassingthwaighte, J., Hunter, P., Noble, D., Blundell, T., Pawson, T.: Computational biology of the heart: From structure to function. Progress in Biophysics and Molecular Biology 69(2/3), 151–559 (1998).
34. McInerney, T., Terzopoulos, D.: Deformable models in medical images analysis: a survey. Medical Image Analysis 1(2), 91–108 (1996).
35. Moireau, P., Chapelle, D., Le Tallec, P.: Joint state and parameter estimation for distributed mechanical systems. Computer Methods in Applied Mechanics and Engineering 197, 659–677 (2008).
36. Montagnat, J., Delingette, H.: 4D deformable models with temporal constraints: application to 4D cardiac image segmentation. Medical Image Analysis 9(1), 87–100 (2005).

37. Moreau-Villéger, V., Delingette, H., Sermesant, M., Ashikaga, H., McVeigh, E., Ayache, N.: Building maps of local apparent conductivity of the epicardium with a 2D electrophysiological model of the heart. IEEE Transactions on Biomedical Engineering 53(8), 1457–1466 (2006).
38. Nash, M.: Mechanics and material properties of the heart using an anatomically accurate mathematical model. Ph.D. thesis, University of Auckland (1998).
39. Nickerson, D., Nash, M., Nielsen, P., Smith, N., Hunter, P.: Computational multiscale modeling in the IUPS physiome project: modeling cardiac electromechanics. Systems Biology 50(6), 617–630 (2006).
40. Nielsen, P., Grice, I.L., Smail, B., Hunter, P.: Mathematical Model of Geometry and Fibrous Structure of the Heart. American Journal of Physiology -Heart and Circulatory Physiology 260(29), H1365–H1378 (1991).
41. Noble, D.: A modification of the Hodgkin–Huxley equations applicable to purkinje fiber action and pace-maker potentials. Journal of Physiology 160, 317–352 (1962).
42. Noble, D.: Modeling the heart. Physiology 19, 191–197 (2004).
43. Noble, D., Varghese, A., Kohl, P., Noble, P.: Improved guinea-pig ventricular cell model incorporating a diadic space, *IKr* and *IKs*, and length and tension dependent processes. Canadian Journal of Cardiology 14, 123–134 (1998).
44. Park, J., Metaxas, D., Axel, L.: Analysis of left ventricular wall motion based on volumetric deformable models and MRI-SPAMM. Medical Image Analysis 1, 53–71 (1996).
45. Peyrat, J.M., Sermesant, M., Pennec, X., Delingette, H., Xu, C., McVeigh, E.R., Ayache, N.: A computational framework for the statistical analysis of cardiac diffusion tensors: Application to a small database of canine hearts. IEEE Transactions on Medical Imaging 26(11), 1500–1514 (2007). doi: 10.1109/TMI.2007.907286.
46. Peyrat, J.M., Sermesant, M., Pennec, X., Delingette, H., Xu, C., McVeigh, E.R., Ayache, N.: Statistical Comparison of Cardiac Fiber Architectures. In: Proceedings of the 4th International Conference on Functional Imaging and Modeling of the Heart (FIMH'07), vol. 4466 of LNCS, pp. 413–423 (2007).
47. Pollard, A., Hooke, N., Henriquez, C.: Cardiac propagation simulation. Critical Reviews in Biomedical Engineering 20(3,4), 171–210 (1992).
48. Rhode, K., Sermesant, M., Brogan, D., Hegde, S., Hipwell, J., Lambiase, P., Rosenthal, E., Bucknall, C., Qureshi, S., Gill, J., Razavi, R., Hill, D.: A system for real-time XMR guided cardiovascular intervention. IEEE Transactions on Medical Imaging 24(11), 1428–1440 (2005).
49. Sachse, F.B.: Computational Cardiology, Modeling of Anatomy, Electrophysiology, and Mechanics, *Lecture Notes in Computer Science*, vol. 2966. Springer, Berlin (2004).
50. Sainte-Marie, J., Chapelle, D., Cimrman, R., Sorine, M.: Modeling and estimation of the cardiac electromechanical activity. Computers and Structures 84, 1743–1759 (2006).
51. Sermesant, M., Delingette, H., Ayache, N.: An electromechanical model of the heart for image analysis and simulation. IEEE Transactions in Medical Imaging 25(5), 612–625 (2006).
52. Sermesant, M., Konukoglu, E., Delingette, H., Coudiere, Y., Chinchaptanam, P., Rhode, K., Razavi, R., Ayache, N.: An anisotropic multi-front fast marching method for real-time simulation of cardiac electrophysiology. In: Proceedings of Functional Imaging and Modeling of the Heart 2007 (FIMH'07), *LNCS*, vol. 4466, pp. 160–169 (2007).
53. Sermesant, M., Moireau, P., Camara, O., Sainte-Marie, J., Andriantsimiavona, R., Cimrman, R., Hill, D.L., Chapelle, D., Razavi, R.: Cardiac function estimation from MRI using a heart model and data assimilation: advances and difficulties. Medical Image Analysis 10(4), 642–656 (2006).
54. Sermesant M, Billet F, Chabiniok R, Mansi T, Chinchapatnam P, Moireau P, Peyrat JM, Rhode K, Ginks M, Lambiase P, Arridge S, Delingette H, Sorine M, Rinaldi A, Chapelle D, Razavi R, Ayache N. Personalised Electromechanical Model of the Heart for the Prediction of the Acute Effects of Cardiac Resynchronisation Therapy. In: Proceedings of Functional Imaging and Modeling of the Heart 2009 (FIMH'09), *LCNS,* vol. 5528, pp. 239–248 (2009).
55. Smith, N., Nickerson, D., Crampin, E., Hunter, P.: Computational mechanics of the heart from tissue structure to ventricular function. Journal of Elasticity 61(1), 113–141 (2000).

56. Stergiopulos, N., Westerhof, B., Westerhof, N.: Total arterial inertance as the fourth element of the windkessel model. American Journal of Physiology 276, H81–H88 (1999).
57. Streeter, D.: Gross Morphology and Fiber Geometry of the Heart. In: R. Berne (ed.) Handbook of Physiology, chap. The Cardiovascular System, Williams & Wilkins, Baltimore (1979).
58. Sutton, M.S., Keane, M.G.: Reverse remodeling in heart failure with cardiac resynchronization therapy. Heart 93(2), 167–171 (2007). doi: 10.1136/hrt.2005.067967.
59. Ten Tusscher, K., Noble, D., Noble, P., Panfilov, A.: A model of the human ventricular myocyte. American Journal of Physiology -Heart and Circulatory Physiology 286(4), 1573–1589 (2004).
60. Tomlinson, K.: Finite element solution of an eikonal equation for excitation wavefront propagation in ventricular myocardium. Ph.D. thesis, University of Auckland (2000).
61. Toussaint, N., Mansi, T., Delingette, H., Ayache, N., Sermesant, M.: An Integrated Platform for Dynamic Cardiac Simulation and Image Processing: Application to Personalized Tetralogy of Fallot Simulation. In: Proceedings of the Eurographics Workshop on Visual Computing for Biomedicine (VCBM). Delft, The Netherlands (2008).
62. Turk, G., O'Brien, J.: Variational implicit surfaces. Tech. rep., Georgia Institute of Technology (1999).
63. Xia, L., Huo, M.: Analysis of ventricular wall motion based on an electromechanical biventricular model. In: A. Murray (ed.) Computers in Cardiology, pp. 315–318. IEEE, New York NY, USA (2003).

Chapter 11
Patient-Specific Modeling of Hypoxic Response and Microvasculature Dynamics

Joanna Nathan and Amina Ann Qutub

11.1 Introduction

Human life evolved in the presence of oxygen, and even small alterations to this essential element can trigger a cascade of biological events. Conditions affecting how we metabolize oxygen and respond to hypoxia determine whether we thrive or succumb to disease. Physiological processes such as exercise, aging, hormonal cycle, and wound healing depend on genetic, epigenetic, and protein level changes in hypoxic response. Furthermore, all leading causes of death in the USA involve hypoxia and alter the microvasculature, through increases or decreases in the degree of angiogenesis (i.e., the growth capillaries from preexisting blood vessels). Patient variability – both in physiological and pathological conditions – determines how a given individual will respond to hypoxic exposure, and therapies targeting hypoxic pathways. The degree and breadth of patient variability is so wide regarding oxygen sensing and response, that computational modeling has become necessary to capture its complexity.

In this chapter, we focus on patient-specific computational modeling of hypoxic response through the hypoxia-inducible factor 1 pathway, and related changes in the microvasculature. In order to add context to the modeling, we first provide a brief overview of hypoxic response on multiple biological levels.

At the intracellular level, oxygen is required for aerobic respiration, production of reactive oxygen species (to some extent), and for the hydroxylation of a key transcription factor hypoxia-inducible 1 (HIF1). One protein subunit of HIF1, HIF1α, is ubiquitously expressed in cells with a nucleus. However, because of HIF1α's rapid degradation in the presence of oxygen, through a process that depends on HIF1α hydroxylation, it is rarely detected in cells. When oxygen is limited, HIF1α escapes hydroxylation and degradation, and instead enters the nucleus where it binds to its dimer, HIF1β. The pair can then activate genes at hypoxic response

A.A. Qutub (✉)
Department of Bioengineering, BioSciences Research Collaborative, Rice University, 6500 Main St., Rm 613, Houston, TX 77030, USA
e-mail: aminaq@rice.edu

R.C.P. Kerckhoffs (ed.), *Patient-Specific Modeling of the Cardiovascular System: Technology-Driven Personalized Medicine*, DOI 10.1007/978-1-4419-6691-9_11,

elements. While initially HIF1 was thought to activate hundreds of genes, the current estimate is HIF1 activates thousands of hypoxic-dependant genes, including those involved in cell cycle, metabolism, and angiogenesis [36, 77].

HIF1-induced angiogenesis leads to further changes in oxygen and hypoxic response. Angiogenesis is the growth of capillaries from preexisting microvessels. It is a process that in theory provides a new source of oxygen (from hemoglobin carrying red blood cells in the blood stream) to a hypoxic region. In practice, the degree to which angiogenesis alleviates hypoxia varies based on tissue type and local microenvironment. Some new vessels can be tortuous, narrow, or leaky; some are not capable of carrying blood.

To better understand how angiogenesis contributes to variability in hypoxic states, it is useful to break down the process into events (Fig. 11.1). Following transcriptional activation of genes, growth factors like vascular endothelial growth factor (VEGF) and fibroblast growth factor (FGF) are secreted by hypoxic cells and start to diffuse through the extracellular matrix. The growth factors are sensed by adjacent endothelial cells on quiescent vessels, and if enough growth factor is

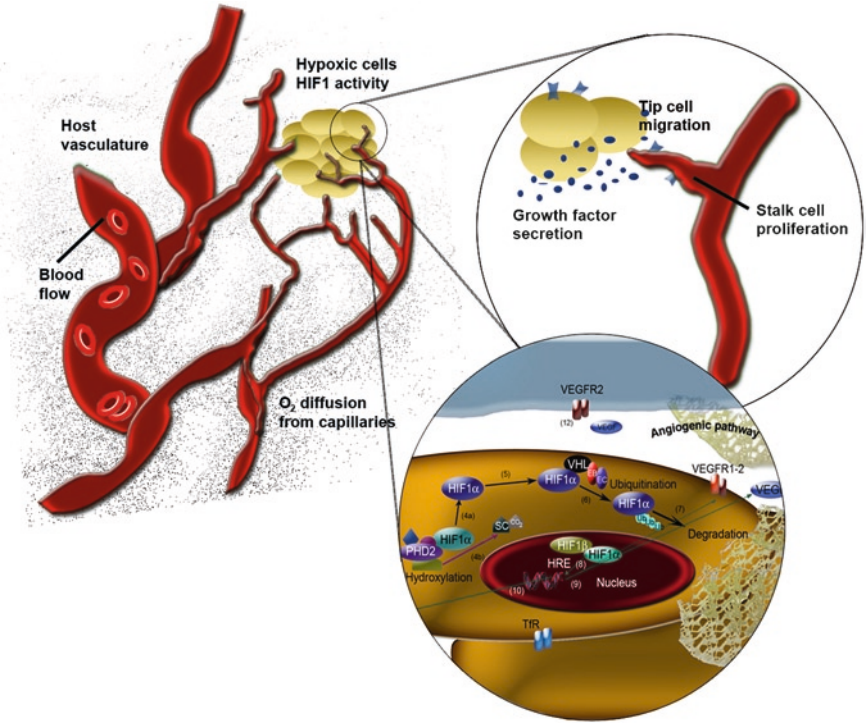

Fig. 11.1 Hypoxic response in capillaries involve intracellular signaling through the HIF pathway, and angiogenic sprouting from existing vessels. *HIF1* hypoxia-inducible factor 1, *VHL* von Hippel–Lindau protein, *HRE* hypoxic response element, *VEGF* vascular endothelial growth factor, *VEGFR* VEGF receptor, *Ub* ubiquitin, *PHD2* prolyl hydroxylase domain enzyme 2, *EB & EC* elongins B & C, *TfR* transferrin receptor

present, the cells can become activated. An activated endothelial cell, called a tip cell, starts to migrate through the local extracellular matrix toward the source of secreted growth factors, i.e., the hypoxic region. This migration involves proteins called MMPs, matrix metalloproteinases, which serve to degrade the matrix, and pave the way for the cell to move forward. As the tip cell crawls forward, it elongates the stalk cell attached behind it on the capillary sprout. The stalk cell in turn is stimulated to grow and divide, pushing the tip cell ahead. This process repeats, leading to a capillary sprout that can range in length from a few microns to over 400 μm. Capillaries anastomose or attach together; eventually a lumen may form within the sprout and blood can flow in the new vessel. Angiogenesis then can be thought of as a consequence of hypoxic response at the cell or tissue level.

New capillary growth is not the only means the body has to adapt to hypoxia at the cell or tissue level. Changes in cell metabolism can alter the demand for oxygen. Signaling through vasodilators like nitric oxide (NO) and vasoconstricting compounds like angiotensin II can change both the HIF1 response and the amount of blood that flows through large vessels. The production of red blood cells, through hypoxia- and HIF1-dependant increases in erythropoietin (EPO) can increase oxygen availability. At the organ and organ system level, the endocrine system may play a role in regulating hypoxic response through hormones like estrogen – known to influence HIF1 levels. The nervous system too can alter ventilation, heart rate, and brain metabolism, causing an increase or decrease in the lungs' demand for oxygen from air, and other organs' demand for oxygenated blood.

These changes can all occur in normal physiological responses to a decrease in oxygen. Examples could be a brisk walk, an intensive mental exercise, or exposure to high altitude. In disease, the mechanisms underlying hypoxic response and adaptation become even more complex, and yet all the more critical to understand.

11.2 Hypoxic Response in Disease

A disruption in oxygen and changes to the hypoxic response pathways are associated with multiple diseases and disorders, including heart disease, cerebrovascular disease, pulmonary hypertension, and cancer (Fig. 11.2).

Each of these diseases involves the HIF1 pathway and downstream angiogenic proteins. Atherosclerosis leads to the impaired perfusion of downstream tissues, resulting in myocardial ischemia. Ischemia deprives the myocardium of oxygen and glucose which in severe cases can lead to infarction. HIF1 signaling helps prevent cardiac cell death through promoting angiogenesis. Similarly, in cerebral ischemia, HIF1 activity is increased in the viable tissue around the occlusion, resulting in increased glycolytic metabolism and VEGF expression –offering a degree of neuroprotection. The extent of ischemia-induced VEGF expression is age-dependent. The impairment of VEGF production in aged patients is caused partly by decreased hypoxia-induced HIF1 activity. Therefore, the increased angiogenic activity is often inadequate to prevent infarction.

Fig. 11.2 Physiological and pathological conditions associated with hypoxia, at multiple biological levels

Hypoxia affects many other diseases independent of ischemia. In some patients with chronic obstructive lung disease, alveolar hypoxia induces vascular remodeling, resulting in pulmonary hypertension. This is characterized by increased pulmonary resistance and decreased vessel lumen diameter, leading to progressive right heart failure and potentially, death. Several HIF1 target genes are involved in this process, including endothelin-1, insulin-like growth factor, and VEGF. Here, unlike its preventive role in the case of ischemic cardiovascular diseases, HIF1 is involved in the pathogenesis of pulmonary hypertension. HIF1 plays a similar malignant role in cancer. HIF1 overexpression is associated with a worse tumor grade and tumor progression. HIF1α overexpression may propagate tumor growth by providing these cancerous cells with an adequate supply of oxygen through angiogenesis. Furthermore, hypoxic tumor cells are resistant to radiation and chemotherapy, and studies have correlated this resistance to higher HIF1 levels [76]. Complicating the picture even more, macrophage response, and specifically a protein called

macrophage migration inhibitory factor, has recently been shown to stabilize HIF1, and itself has been correlated to neovascularization in inflammatory and hypoxic conditions both in cancer and in atherosclerosis [59, 72, 81, 82].

11.3 Hypoxic Response and Oxygen Sensing Models

Given the power of hypoxic response to alter the course of disease, the pharmaceutical industry's interest in targeting related pathways, and the complexity of the interwoven mechanisms of oxygen sensing and response, the development of computational modeling in hypoxic research is been watched with growing fascination. Computational techniques that have been used to study hypoxia include gene networks, circuit analysis, ordinary differential equation-based chemical-kinetics, rule-based cell-level algorithms, compartmental modeling, and computational fluid dynamics (Fig. 11.3). Existing models can be divided broadly into five biological categories: blood flow and oxygen transport; NO and vasodilation; hypoxic response regulation through transcription factors; growth factor signaling; and angiogenesis.

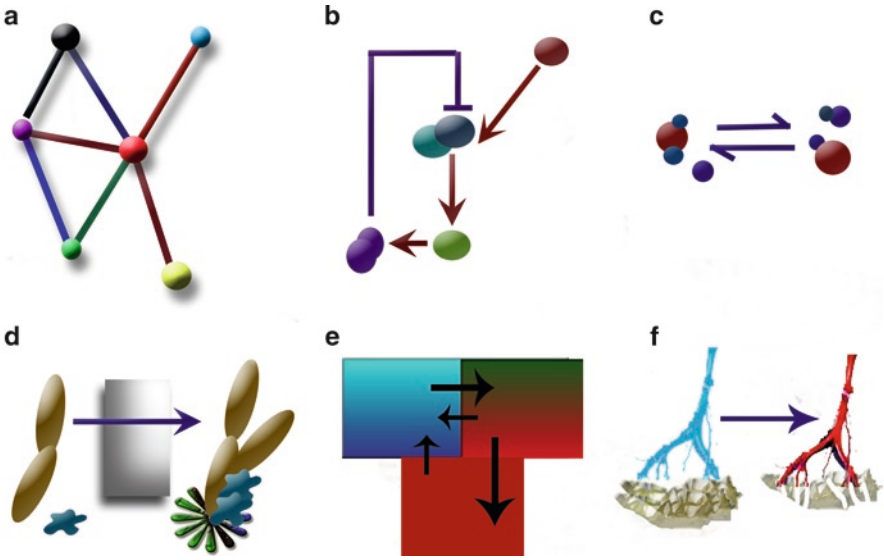

Fig. 11.3 Types of computational techniques used to model patient-specific hypoxic response and microvascular dynamics include the following: (**a**) probabilistic gene networks; (**b**) biocircuits; (**c**) chemical-kinetic models; (**d**) logic-based spatial models; (**e**) compartmental models; and (**f**) computational fluid dynamics

11.3.1 Blood Flow and Oxygen Transport

Insufficient blood flow to meet a tissue's metabolic demand for oxygen is a main cause of local hypoxia, and stimulation of angiogenesis. Blood flow and oxygen transport models in the microvasculature date back a century or more, with initial publications that included August Krogh's work on capillary circulation [40]. A review on the subject describes the field today [27].

Briefly, we offer an example of how these computational models of blood flow and oxygen transport work. A 3D geometrical model of a capillary network in a specified tissue volume can be constructed from estimated vessel dimensions and spacing published in the literature (e.g., [35]), or from coupling noninvasive MR imaging of the vasculature using contrast agents, with increasingly sophisticated image analysis algorithms (e.g., [61]). Given appropriate boundary conditions (pressure or flow), blood flow and hematocrit distribution can be calculated throughout the network. This is achieved through a set of nonlinear algebraic equations for pressure at the network nodes (bifurcations) and blood flow rate and hematocrit in the vascular segments [87]. Once blood flow and local hematocrit in the network is determined, convection–diffusion–reaction partial differential equations governing oxygen transport are solved numerically, resulting in 3D distribution of oxygen in the microvascular network and surrounding tissue [35]. Sophisticated experimental and computational advances in studying blood flow in capillaries, have led to research into flow effects in blind-ended capillary sprouts [29], as well as numerous studies looking at the effects of microvascular flow on blood cell shape and leukocyte rolling, and vice versa. Future work in this area will couple high-resolution imaging of capillary blood flow within hypoxic tissue regions with models of oxygen diffusion and detailed hematology. Imaging coupled with analysis of blood hematocrit will provide the models with patient-specific parameters of initial capillary network structure and blood oxygen content. Results from the oxygen diffusion models, in turn, can be coupled with models detailing molecular and cellular details, described below, to provide predictions that are tailored to individuals.

11.3.2 NO and Vasodilation

Nitrites, and specifically nitric oxide (NO), can alter the degree of local hypoxia through its vasodilatory effects on the microcirculation. It has been purposed that red blood cells sense local tissue requirements as they travel through capillaries, and may release NO to enhance local blood flow in hypoxic regions [33]. Endogenous nitrite has also been credited with modulating mitochondrial respiration and cellular protection from ischemic insult [88]. NO additionally has been shown to regulate HIF1 levels by signaling with ROS or through the HIF1 hydroxylation pathway – whether the observed regulation is up or down has depended on

the amount of NO present [1, 12, 14, 31, 90]. A number of computational models have been developed to help quantify the amount of NO present in the microvasculature in healthy and diseased conditions, and to represent NO's signaling pathways [16–18, 21, 55]. The calculated distribution of NO and oxygen, and the NO signaling cascade predicted from the above models provide a basis for modeling cellular response to hypoxia via transcription factors.

11.3.3 Hypoxia-Inducible Factor 1: The Hypoxia Transcription Factor

A number of transcription factors play a role in hypoxic response including the erythroblastosis virus E26 oncogene homolog (ETS) family transcription factors [73], the family of hypoxia-inducible factor proteins (HIF1, HIF2, HIF3) [83]; the PI3K-Akt-mTOR pathway molecules; NF-κB; and p53, among others. One of the most influential transcription factors during hypoxia is hypoxia-inducible factor HIF1. During hypoxia, HIF1α rapidly accumulates within a cell, enters into the cell nucleus, binds to its dimer HIF1β, and triggers gene expression [64, 77]. Thousands of genes can be activated by HIF1 on their hypoxic response elements. These hypoxic response genes are broad in scope and associated with numerous pathways – ranging from angiogenesis in cancer, exercise, and ischemia; energy metabolism; nutrient transport; cell cycle; and cell migration [77, 89]. In turn, the number of human diseases and physiological conditions affected by HIF1 is extensive, as discussed above. Because of the complexity of the HIF1 pathway, systems biology models have emerged to analyze its effects, with a particular focus on pathway changes in response to disease conditions, and on ways the pathway can be therapeutically modulated.

11.3.3.1 Therapeutic Modulation of Cofactors in the HIF1 Pathway

Targeting the HIF1 pathway presents an attractive way to regulate angiogenesis [2, 3, 10, 25, 78]. While targeting HIF1 in cancer has arguably been the focus of most HIF1 therapeutic studies, recent reviews have specifically looked at manipulating the HIF1 for potential treatments related to central nervous system ischemia [22] and cardiovascular disease [32].

There are many ways to alter HIF1 expression and transcriptional activity. Computational models can be used to help guide the appropriate targets in the pathway, and modify the therapy on an individual patient level. Cofactors in HIF1α hydroxylation and degradation are prime molecular level targets to regulate the protein's expression levels. These molecules include prolyl hydroxylases, iron, ascorbate, hydrogen peroxide, 2-oxoglutarate, succinate, and von Hippel–Lindau protein. Computational modeling tested two possible molecular therapies in conditions of transient cellular hypoxia – that of supplementing with ascorbate alone, and the

combination therapy of supplementing with iron and ascorbate [68]. The model predicted the degree to which HIF1α was hydroxylated, as a function of the relative initial concentrations of cofactors in the microenvironment (conditions that would change depending on the patient, tissue type, and cell type undergoing hypoxia). Both therapies decreased HIF1α expression during hypoxia. Where iron was in limited supply, the model showed ascorbate had a significant effect in modulating oxygen response and HIF1α expression. The utility of ascorbate supplementation, through its HIF1 hydroxylation role, has now been validated experimentally and shown to inhibit tumor growth in vivo [24] and inhibit physiological angiogenic growth in rat aortic ring and Matrigel plug mouse models [56]. Interestingly, iron supplementation has recently been shown to attenuate hypoxic pulmonary hypertension in humans, while the relationship to HIF1 in this situation is yet to be proven [84].

11.3.3.2 Effects of Chronic Hypoxia at the Molecular Level

In cancer, prolonged exercise, and some cases of ischemia, a patient could have tissue hypoxia that lasts for several hours, days, or months. During these chronic conditions, hypoxic response adapts. This adaptation can be seen by a cell's higher hypoxia tolerance threshold before increasing HIF1α, or by an attenuated increase in HIF1α levels in response to hypoxia, compared to the level found after exposure to the same low oxygen but in transient conditions [38]. Preexposure to hypoxia (called hypoxic preconditioning) also contributes to a limited hypoxic response in reoxygenated cells [19]. Preconditioning shows protective effects in mammals exposed to ischemia, as well [80]. HIF1α's hydroxylation enzymes contribute to this setpoint adjustment [19, 37, 38, 85]. Furthermore, a computational model showed how three feedback loops (HIF1α synthesis, prolyl hydroxylase synthesis, and succinate (SC) production inhibition) combine to tightly regulate the effects of chronic hypoxia via control of HIF1α degradation [69]. The model demonstrated that prolyl hydroxylase domains, succinate, and HIF1α feedback determine intracellular HIF1α levels over the course of hours to days. This chronic hypoxia model was then applied to specific cases of ischemia reperfusion and cancer, where another molecular species in the microenvironment greatly influences HIF1 levels – reactive oxygen species.

11.3.3.3 Reactive Oxygen Species Effect in the Hypoxic Response Signaling Pathway

Several hypotheses exist as to how reactive oxygen species (ROS) interact with HIF1 and its pathway (related reviews include [7, 23, 30, 63, 86]). Studies have suggested that one ROS, hydrogen peroxide, oxidizes ferrous iron (Fe^{2+}) to its ferric form (Fe^{3+}), preventing the necessary binding of ferrous iron to the HIF1α hydroxylation enzymes prolyl hydroxylases (PHDs) [60]. A complementary process could be that ascorbate is recruited as a free radical scavenger during hypoxia, limiting its

access to the HIF1 hydroxylation pathway. This would prevent ascorbate from reducing ferric iron, and/or prevent ascorbate from binding directly to the PHDs. In contrast, some studies have suggested that ROS increase rather than decrease free Fe^{2+}, and HIF1α hydroxylation instead increases in the presence of ROS [39]. 2-oxoglutarate (2OG) and succinate are compounds involved in HIF1α hydroxylation whose concentrations could also be altered by free radicals and mitochondrial dysfunction [28, 39, 60]. Furthermore, ROS could influence the HIF1 pathway by changing the location and availability of cellular oxygen, limiting its ability to bind directly to the PHDs, or ROS could be changing PHD phosphorylation [86]. A computational model, based initially on the chronic hypoxia model described above, was developed to characterize these alternate mechanisms of ROS [66, 69]. The model helped distinguish competing factors involved in pro- and antioxidant therapy in two diseases: cancer and ischemia (Fig. 11.4a). Model results justified

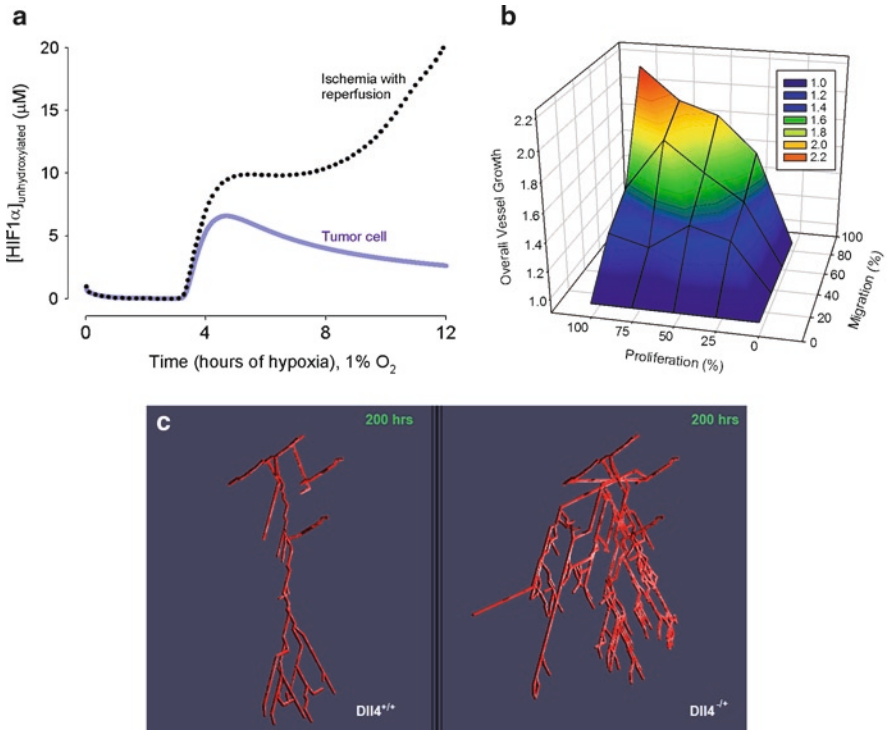

Fig. 11.4 Example of model predictions of hypoxic response, from the intracellular (**a**) to the tissue level (**b**, **c**), where patient-specific properties (e.g., initial vasculature network structure; ischemic duration; genetic mutations in Dll4) can be given as initial parameters. (**a**) Relative hydroxylated HIF1 as a function of hypoxic duration in conditions of endothelial cells undergoing ischemia reperfusion injury (dotted line) and in hypoxic glioma cells (solid line). (**b**) Predicted overall vessel growth depends on relative rates of endothelial cell migration and proliferation. (**c**) Model results showing vessel growth after 200 h for control conditions (*left panel*) and haploinsufficiency of the Notch ligand Dll4 (*right panel*)

the hypothesis that reactive oxygen species work by two opposite ways on the HIF1 system, both up- and downregulating HIF1, through modulation of PHD2 levels. The model also predicted the degree to which ROS intracellular levels differ in tumor cells compared to endothelial cells in ischemic conditions, leading to different apoptotic rates of the two cell types.

11.3.3.4 HIF1 Intracellular Signaling Leading to VEGF Expression Changes

Understanding the molecular interactions involved in hypoxic response is critical, but so too is understanding how transcriptional signaling affects hypoxia-induced angiogenesis. Some of the key genes induced by HIF1 are VEGF, VEGFR1, and GLUT1. VEGF is one of the most potent angiogenic growth factors, and studying its activity in hypoxia has been the focus of a number of computational models.

The interactions between HIF1 and VEGF during hypoxia involve several feed-forward and feedback mechanisms, and many different receptor–ligand interactions. There are five VEGF genes, multiple isoforms of each gene, and five VEGF cell-surface receptors – each with different responsiveness to hypoxia and different roles in angiogenesis [51]. A series of computational models have been dedicated to characterizing the binding of different VEGF isoforms with their respective receptors, and used to predict the effect of therapies that modulate the VEGF family, with applications in cancer and in peripheral artery disease [46–50, 52]. The molecular-based models of VEGF have been coupled with the blood flow and oxygen transport models described earlier to simulate VEGF distribution and signaling in hypoxic skeletal muscle, based on experimentally observed relationships between local oxygen levels, HIF1 and HIF1-induced VEGF [34, 45].

New observations add complexity to the regulation of VEGF in hypoxia. Independent of HIF1, hypoxia can upregulate VEGFR2, and other protein PGC1, recently has been shown to be key regulator of VEGF and angiogenesis in skeletal muscle during exercise in parallel or independent of HIF1 [5, 6, 26, 58]. Additionally, the ERK1/2 pathway has been shown to upregulate VEGF–VEGFR1 binding and signaling, which leads to a positive feedback, upregulating ERK1/2 and HIF1 [20]. Glucose metabolism and GLUT1, both regulated by HIF1, can alter the expression levels and signaling of VEGF and its receptors at least in some cell types [62]. To fully characterize the regulation of VEGF, both autocrine signaling (e.g., in a cancer cell, in specific skeletal muscle cells during exercise or even in endothelial cells during angiogenesis) and paracrine signaling (e.g., where VEGF levels secreted from an adjacent tissue upregulate the expression of HIF1 within endothelial cells) need to be considered.

As the HIF1-VEGF connectivity is being explored experimentally, in silico network modeling and biocircuit representations can help highlight which signaling pathways dominate under different physiological conditions and predict dynamics of the interactions during neovascularization. Beyond transcriptional regulation and

signaling pathways, the subsequent cellular and tissue response to hypoxia is an active, growing area for patient-specific modeling.

11.3.4 Cell-Level and Integrated, Multiscale Angiogenesis Models

Aside from VEGF, many other proangiogenic factors change during hypoxia, including fibroblast growth factor, angiopoietins, tumor necrosis factor, and transforming growth factor. Microvascular growth is determined by a balance of these proangiogenic factors with antiangiogenic factors, e.g., endostatin, thrombospondin-1, and angiostatin. The angiogenic events of endothelial cell activation, migration, and proliferation are a function of local growth factor concentrations and gradients. They also are a function of the local matrix, which cells respond to through a synergy of chemical and mechanical changes. Enzymes like matrix metalloproteinases, MMPs, allow an activated cell to proteolyze its surrounding basement membrane and extracellular matrix (ECM). The moving tip cell releases ECM-bound growth factors as it moves. The fate of a growing capillary sprout is determined by the surrounding microenvironment. It can attach to adjacent vessel, retract, split, or branch. As sprouts form and connect, a new capillary network arises, potentially capable of carrying blood and bringing oxygen to hypoxic regions.

This angiogenic process has been modeled computationally in many forms since the 1970s; for a review of the methods and characteristics of these models, see [65]. Cellular level and multiscale modeling has become increasingly popular as a means to tie intracellular signaling to phenotypical changes in the capillary network [15, 67]. A paradigm, which seems well-suited to expanding models modularly and developing them in a patient-specific manner, is agent-based or hybrid models of vascular growth. These models have varied in their applications – including a study assessing the effect of circulating monocytes on angiogenesis in mouse spinotrapezius muscle [8]; a experimentally-coupled model of the formation and inactivation of tip cells [9]; and a simulation studying the effect of regulating the coupled processes of endothelial migration, elongation, and proliferation [70]. The commonality of the models lies in their ability to model cellular and molecular events in angiogenesis through the use of logical rules. These rules are hypotheses based on published data in literature or experiments. They can be articulated as equations, statements, or values guiding the behavior of agents. Results from these agent-based or hybrid models are frequently emergent properties of a capillary network that would not have been easily predicted from behavior that is governed at the cell or molecular level (e.g., see Fig. 11.4b, c). The cell-based models are also increasingly coupled to experiments that can test out some of their predictions or offer an initial set of parameters specific to the in vitro or in vivo assay of interest. A recent modeling advance has been the integration of a cell-level agent-based model with detailed blood flow, oxygen transport, HIF1,

and VEGF molecular interactions models [65, 67]. This integrated, multiscale model allowed predictions of new vasculature formation in a skeletal muscle tissue from changes at the intracellular and molecular levels. While the described models have captured variability at multiple biological levels and in several different disease applications, so far these models have yet to be applied to humans.

11.4 Modeling Individual Variability

Patient-specific hypoxic response involves a phenomenal degree of complexity and sources for variability across biological levels (Fig. 11.5). Genetic variations – from deletions to mutations to epigenetic effects – can alter how hypoxic responsive genes respond. Key examples of this include mutations in p53 and VHL, both genes whose proteins interact with HIF1. VHL is known as a tumor suppressor gene, while p53 is involved in cell death. Mutations in either gene alter a patient's susceptibility to cancer, and have been tied to changes in HIF1 levels [42, 53, 54, 92].

Genetic variability in hypoxic response has been studied in a number of conditions affecting humans, outside of diseases. An effort to understand why some people succumb to mountain sickness and others do not, has led to conclusions about genetic variations in humans living in high altitude. Adaptation to altitude has been observed in inhabitants of the Andes and Himalayan mountain ranges, and high planes in Ethiopia. Himalayan and Ethiopian mountain inhabitants lack the strong hypoxic response, such as changes in ventilation and cerebral circulation, shown in Andeans and control (non-high altitude dwellers) when exposed to hypoxia. Concomitantly, genetic markers for hypoxia have been correlated to this response [91].

At the molecular level, individuals can vary based on the various degrees and durations of hypoxia they are exposed to, as well as their baselines values for hypoxia-responsive proteins. Different durations or levels of hypoxia yield different activity of HIF degradation enzymes, HIF synthesis and reactive oxygen species,

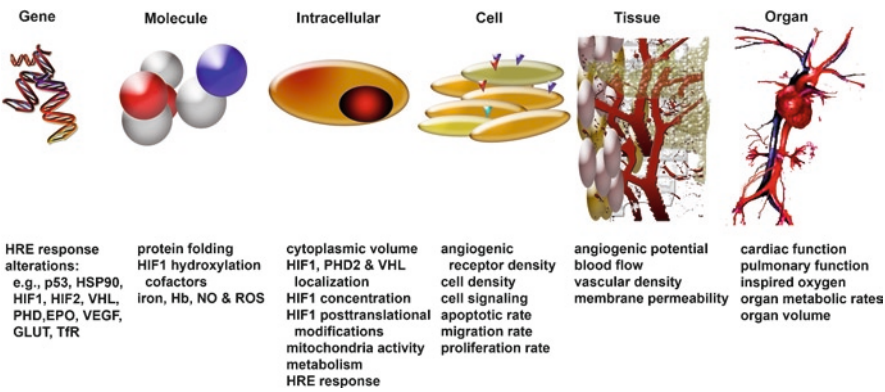

Fig. 11.5 Main sources of patient variability in hypoxic response spanning all biological levels

and hence oxygen sensitivity. There are three known isoforms of HIF, three main isoforms of HIF prolyl hydroxylases; seven isoforms of one VEGF gene, five VEGF genes, five VEGF cell-surface receptors; three isoforms of MMP2, 1 of the 26 MMPs [4], and hundreds of peptides endogenous to the local matrix capable of altering cell migration or proliferation. Furthermore, ROS can affect the HIF1 pathway through changes in at least five compounds (H_2O_2, Fe^{2+}, Asc, 2OG or SC levels), based on experiments [43, 60]; and the interactions between HIF1, VEGF, and MMPs expand to include dozens if not hundreds of other proteins and molecules through regulatory loops.

There is substantial experimental evidence suggesting that levels of these proteins and biochemicals can vary among healthy individuals, and certainly in disease. Interindividual variability in the ability to produce VEGF in response to hypoxia has been shown in a study on coronary artery collateral circulation [75]. A more recent study demonstrated that between normal, healthy individuals, there is a statistically significant variation in HIF1 regulated transcript expression in response to hypoxia [11].

Modeling has predicted that cell apoptosis and H_2O_2 steady-state levels are highly dependent on extracellular H_2O_2 levels, and largely independent of initial intracellular H_2O_2 levels, during hypoxia; in turn, intracellular H_2O_2 levels can be used to help predict HIF1α expression levels in time [66]. Should it hold true in humans that extracellular ROS determines intracellular HIF1α activity, this pinpoints another source of hypoxic response variability in healthy individuals – depending on age, diet, exercise, level of local inflammation, and potentially stress levels [44, 57].

A meta-analysis of published data on cancer patients and healthy individuals has helped to provide a quantitative value for the variability in VEGF levels found in human plasma [41]. Patient meta-analyses combined with techniques to locally measure HIF1, VEGF, and VEGFR expression levels in vitro and in vivo will provide essential cell- and tissue-specific input parameters for the hypoxia-induced angiogenesis models (recent measurement examples include RT-PCR measurements of VEGF164, VEGF188 and VEGF120 mRNA levels in embryonic and adult skeletal muscle [13]; and flow cytometry studies of VEGF121 and VEGF189 levels as well as VEGF receptors expression in brain-derived and retinal endothelial cells [71]). VEGF effects on 3-D microvascular density has also recently been quantified by microcomputed tomography [74]

At a more macroscopic level, variability is also an important factor. In healthy patients, interindividual variations in ventilatory response have been reported in a number of studies, as have variations with respect to erythropoietin levels in response to hypoxia. Variability in organ size (e.g., heart and lung) can alter the metabolic rate and transport of oxygen throughout the body.

Certain conditions that decrease oxygen can alter the hypoxic state of an entire organ or the whole body: these include altitude, sleep apnea, stroke, hemorrhage, or clot, obesity, inflammation, degree of exercise, pulmonary disease, aging, cardiovascular disease, and cancer. Aging, for instance, is associated with an increased incidence of hypoxia–ischemia-related diseases, such as stroke and myocardial

infarction. Reduced protein expression of HIF1α is correlated with aging, which may in part explain the increased incidence of hypoxia-related conditions in the elderly and their reduced ability to cope with it [79]. Increased incidence of inflammation and inflammatory diseases is also associated with age and variations in hypoxic response. For example, rheumatoid arthritis is characterized by an inflamed, thickened synovium, which results in an increasing gap between proliferating cells of the tissue and the nearest blood vessels, leading to hypoxia. Several forms of vasculitis (inflammatory destruction of blood vessels) can occur in rheumatoid arthritis; due to a decrease in the number of functioning blood vessels, vasculitis escalates the level of hypoxia.

All of these sources of variability – from the gene to the whole body level – should be taken into consideration when extrapolating hypoxic response models from their idealized applications in in vitro or in animal models to the human body.

11.5 Discussion and Conclusions: Integrating and Validating Inter- and Intra-patient Variation on Multiple Scales

As the models of hypoxic response at the microvasculature become increasingly patient specific, they will incorporate genetic, temporal, and spatial variation. Genetic variation will need to go beyond the presence or absence of a gene or chromosome, to look at gradients, haploinsufficiencies and epigenetic effects. Temporal variation – everything from variations attributed to circadian rhythms to cell cycle to duration of hypoxia – will become more tightly coupled to spatial variation. In turn, spatial variation in three dimensions, which current hypoxic response models address at the cell and tissue level, will reach down to intracellular levels and up to whole body differences. The current state-of-the-art in hypoxic response modeling is integration of models representing multiple levels of biology, from intracellular molecular interactions to cell-level behavior to capillary network formation to oxygen levels in the tissue to whole body distribution of growth factors. Coupling all of these models to patient-specific parameters through the use of experimental techniques such as functional MRI and flow cytometry to assess angiogenic growth and cell-specific protein expression in vivo will bring us a step closer to using hypoxic response and microvascular models in conjunction with, and as a precursor to, clinical trials.

References

1. Agani, F. H., Puchowicz, M., Chavez, J. C., Pichiule, P. & Lamanna, J. (2002) Role of nitric oxide in the regulation of HIF-1alpha expression during hypoxia. *Am J Physiol Cell Physiol,* 283, C178–86.
2. Airley, R. E. & Mobasheri, A. (2007) Hypoxic regulation of glucose transport, anaerobic metabolism and angiogenesis in cancer: novel pathways and targets for anticancer therapeutics. *Chemotherapy,* 53, 233–56.

3. Alqawi, O., Moghaddas, M. & Singh, G. (2006) Effects of geldanamycin on HIF-1alpha mediated angiogenesis and invasion in prostate cancer cells. *Prostate Cancer Prostatic Dis,* 9, 126–35.
4. Amalinei, C., Caruntu, I. D. & Balan, R. A. (2007) Biology of metalloproteinases. *Rom J Morphol Embryol,* 48, 323–34.
5. Arany, Z. (2008) PGC-1 coactivators and skeletal muscle adaptations in health and disease. *Curr Opin Genet Dev,* 18, 426–34.
6. Arany, Z., Foo, S. Y., Ma, Y., Ruas, J. L., Bommi-Reddy, A., Girnun, G., Cooper, M., Laznik, D., Chinsomboon, J., Rangwala, S. M., Baek, K. H., Rosenzweig, A. & Spiegelman, B. M. (2008) HIF-independent regulation of VEGF and angiogenesis by the transcriptional coactivator PGC-1alpha. *Nature,* 451, 1008–12.
7. Archer, S. L., Gomberg-Maitland, M., Maitland, M. L., Rich, S., Garcia, J. G. & Weir, E. K. (2008) Mitochondrial metabolism, redox signaling, and fusion: a mitochondria-ROS-HIF-1alpha-Kv1.5 O2-sensing pathway at the intersection of pulmonary hypertension and cancer. *Am J Physiol Heart Circ Physiol,* 294, H570–8.
8. Bailey, A. M., Thorne, B. C. & Peirce, S. M. (2007) Multi-cell agent-based simulation of the microvasculature to study the dynamics of circulating inflammatory cell trafficking. *Ann Biomed Eng,* 35, 916–36.
9. Bentley, K., Mariggi, G., Gerhardt, H. & Bates, P. A. (2009) Tipping the balance: robustness of tip cell selection, migration and fusion in angiogenesis. *PLoS Comput Biol,* 5, e1000549.
10. Brahimi-Horn, M. C. & Pouyssegur, J. (2007) Harnessing the hypoxia-inducible factor in cancer and ischemic disease. *Biochem Pharmacol,* 73, 450–7.
11. Brooks, J. T., Elvidge, G. P., Glenny, L., Gleadle, J. M., Liu, C., Ragoussis, J., Smith, T. G., Talbot, N. P., Winchester, L., Maxwell, P. H. & Robbins, P. A. (2009) Variations within oxygen-regulated gene expression in humans. *J Appl Physiol,* 106, 212–20.
12. Brune, B. & Zhou, J. (2003) The role of nitric oxide (NO) in stability regulation of hypoxia inducible factor-1alpha (HIF-1alpha). *Curr Med Chem,* 10, 845–55.
13. Bryan, B. A., Walshe, T. E., Mitchell, D. C., Havumaki, J. S., Saint-Geniez, M., Maharaj, A. S., Maldonado, A. E. & D'Amore, P. A. (2008) Coordinated vascular endothelial growth factor expression and signaling during skeletal myogenic differentiation. *Mol Biol Cell,* 19, 994–1006.
14. Callapina, M., Zhou, J., Schmid, T., Kohl, R. & Brune, B. (2005) NO restores HIF-1alpha hydroxylation during hypoxia: role of reactive oxygen species. *Free Radic Biol Med,* 39, 925–36.
15. Chaplain, M. A., McDougall, S. R. & Anderson, A. R. (2006) Mathematical modeling of tumor-induced angiogenesis. *Annu Rev Biomed Eng,* 8, 233–57.
16. Chen, K., Pittman, R. N. & Popel, A. S. (2007) Vascular smooth muscle NO exposure from intraerythrocytic SNOHb: a mathematical model. *Antioxid Redox Signal,* 9, 1097–110.
17. Chen, K. & Popel, A. S. (2006) Theoretical analysis of biochemical pathways of nitric oxide release from vascular endothelial cells. *Free Radic Biol Med,* 41, 668–80.
18. Chen, K. & Popel, A. S. (2007) Vascular and perivascular nitric oxide release and transport: Biochemical pathways of neuronal nitric oxide synthase (NOS1) and endothelial nitric oxide synthase (NOS3). *Free Radic Biol Med,* 42, 811–22.
19. D'Angelo, G., Duplan, E., Boyer, N., Vigne, P. & Frelin, C. (2003) Hypoxia up-regulates prolyl hydroxylase activity: a feedback mechanism that limits HIF-1 responses during reoxygenation. *J Biol Chem,* 278, 38183–7.
20. Das, B., Yeger, H., Tsuchida, R., Torkin, R., Gee, M. F., Thorner, P. S., Shibuya, M., Malkin, D. & Baruchel, S. (2005) A hypoxia-driven vascular endothelial growth factor/Flt1 autocrine loop interacts with hypoxia-inducible factor-1alpha through mitogen-activated protein kinase/extracellular signal-regulated kinase 1/2 pathway in neuroblastoma. *Cancer Res,* 65, 7267–75.
21. Deonikar, P. & Kavdia, M. (2009) An integrated computational and experimental model of nitric oxide-red blood cell interactions. *Ann Biomed Eng,* 38, 357–70.
22. Freeman, R. S. & Barone, M. C. (2005) Targeting hypoxia-inducible factor (HIF) as a therapeutic strategy for CNS disorders. *Curr Drug Targets CNS Neurol Disord,* 4, 85–92.
23. Galanis, A., Pappa, A., Giannakakis, A., Lanitis, E., Dangaj, D. & Sandaltzopoulos, R. (2008) Reactive oxygen species and HIF-1 signalling in cancer. *Cancer Lett,* 266, 12–20.

24. Gao, P., Zhang, H., Dinavahi, R., Li, F., Xiang, Y., Raman, V., Bhujwalla, Z. M., Felsher, D. W., Cheng, L., Pevsner, J., Lee, L. A., Semenza, G. L. & Dang, C. V. (2007) HIF-dependent antitumorigenic effect of antioxidants in vivo. *Cancer Cell,* 12, 230–8.
25. Garcia, J. A. (2006) HIFing the brakes: therapeutic opportunities for treatment of human malignancies. *Sci STKE,* 2006, pe25.
26. Geng, T., Li, P., Okutsu, M., Yin, X., Kwek, J., Zhang, M. & Yan, Z. (2010) PGC-1{alpha} plays a functional role in exercise-induced mitochondrial biogenesis and angiogenesis but not fiber-type transformation in mouse skeletal muscle. *Am J Physiol Cell Physiol,* 298, C572–9.
27. Goldman, D. (2008) Theoretical models of microvascular oxygen transport to tissue. *Microcirculation,* 15, 795–811.
28. Gottlieb, E. & Tomlinson, I. P. (2005) Mitochondrial tumour suppressors: a genetic and biochemical update. *Nat Rev Cancer,* 5, 857–66.
29. Guerreiro-Lucas, L. A., Pop, S. R., Machado, M. J., Ma, Y. L., Waters, S. L., Richardson, G., Saetzler, K., Jensen, O. E. & Mitchell, C. A. (2008) Experimental and theoretical modelling of blind-ended vessels within a developing angiogenic plexus. *Microvasc Res,* 76, 161–8.
30. Guzy, R. D. & Schumacker, P. T. (2006) Oxygen sensing by mitochondria at complex III: the paradox of increased reactive oxygen species during hypoxia. *Exp Physiol,* 91, 807–19.
31. Herr, B., Zhou, J., Drose, S. & Brune, B. (2007) The interaction of superoxide with nitric oxide destabilizes hypoxia-inducible factor-1alpha. *Cell Mol Life Sci*, 64, 3295–305.
32. Hoenig, M. R., Bianchi, C. & Sellke, F. W. (2008) Hypoxia inducible factor-1 alpha, endothelial progenitor cells, monocytes, cardiovascular risk, wound healing, cobalt and hydralazine: a unifying hypothesis. *Curr Drug Targets,* 9, 422–35.
33. Jensen, F. B. (2009) The dual roles of red blood cells in tissue oxygen delivery: oxygen carriers and regulators of local blood flow. *J Exp Biol,* 212, 3387–93.
34. Ji, J. W., Mac Gabhann, F. & Popel, A. S. (2007) Skeletal muscle VEGF gradients in peripheral arterial disease: simulations of rest and exercise. *Am J Physiol Heart Circ Physiol,* 293, H3740–9.
35. Ji, J. W., Tsoukias, N. M., Goldman, D. & Popel, A. S. (2006) A computational model of oxygen transport in skeletal muscle for sprouting and splitting modes of angiogenesis. *J Theor Biol,* 241, 94–108.
36. Jiang, B. H., Semenza, G. L., Bauer, C. & Marti, H. H. (1996) Hypoxia-inducible factor 1 levels vary exponentially over a physiologically relevant range of O2 tension. *Am J Physiol,* 271, C1172–80.
37. Jones, N. M., Lee, E. M., Brown, T. G., Jarrott, B. & Beart, P. M. (2006) Hypoxic preconditioning produces differential expression of hypoxia-inducible factor-1alpha (HIF-1alpha) and its regulatory enzyme HIF prolyl hydroxylase 2 in neonatal rat brain. *Neurosci Lett,* 404, 72–7.
38. Khanna, S., Roy, S., Maurer, M., Ratan, R. R. & Sen, C. K. (2006) Oxygen-sensitive reset of hypoxia-inducible factor transactivation response: prolyl hydroxylases tune the biological normoxic set point. *Free Radic Biol Med,* 40, 2147–54.
39. Kozhukhar, A. V., Yasinska, I. M. & Sumbayev, V. V. (2006) Nitric oxide inhibits HIF-1alpha protein accumulation under hypoxic conditions: implication of 2-oxoglutarate and iron. *Biochimie,* 88, 411–8.
40. Krogh, A. (1919) The supply of oxygen to the tissues and the regulation of the capillary circulation. *J Physiol,* 52, 457–74.
41. Kut, C., Mac Gabhann, F. & Popel, A. S. (2007) Where is VEGF in the body? A meta-analysis of VEGF distribution in cancer. *Br J Cancer,* 97, 978–85.
42. Li, Z., Wang, D., Messing, E. M. & Wu, G. (2005) VHL protein-interacting deubiquitinating enzyme 2 deubiquitinates and stabilizes HIF-1alpha. *EMBO Rep*, 6, 373–8.
43. Lopez-Lazaro, M. (2007) Dual role of hydrogen peroxide in cancer: possible relevance to cancer chemoprevention and therapy. *Cancer Lett,* 252, 1–8.
44. Lopez-Torres, M. & Barja, G. (2008) Lowered methionine ingestion as responsible for the decrease in rodent mitochondrial oxidative stress in protein and dietary restriction possible implications for humans. *Biochim Biophys Acta,* 1780, 1337–47.

45. Mac Gabhann, F., Ji, J. W. & Popel, A. S. (2007) Multi-scale computational models of pro-angiogenic treatments in peripheral arterial disease. *Ann Biomed Eng,* 35, 982–94.
46. Mac Gabhann, F. & Popel, A. S. (2004) Model of competitive binding of vascular endothelial growth factor and placental growth factor to VEGF receptors on endothelial cells. *Am J Physiol Heart Circ Physiol,* 286, H153–64.
47. Mac Gabhann, F. & Popel, A. S. (2005) Differential binding of VEGF isoforms to VEGF Receptor 2 in the presence of Neuropilin-1: a computational model. *Am J Physiol Heart Circ Physiol*, 288, H2851–60.
48. Mac Gabhann, F. & Popel, A. S. (2006) Targeting neuropilin-1 to inhibit VEGF signaling in cancer: comparison of therapeutic approaches. *PLoS Comput Biol,* 2, e180.
49. Mac Gabhann, F. & Popel, A. S. (2007) Dimerization of VEGF receptors and implications for signal transduction: a computational study. *Biophys Chem,* 128, 125–39.
50. Mac Gabhann, F. & Popel, A. S. (2007) Interactions of VEGF isoforms with VEGFR-1, VEGFR-2, and neuropilin in vivo: a computational model of human skeletal muscle. *Am J Physiol Heart Circ Physiol,* 292, H459–74.
51. Mac Gabhann, F. & Popel, A. S. (2008) Systems biology of vascular endothelial growth factors. *Microcirculation,* 15, 715–38.
52. Mac Gabhann, F., Yang, M. T. & Popel, A. S. (2005) Monte Carlo simulations of VEGF binding to cell surface receptors in vitro. *Biochim Biophys Acta,* 1746, 95–107.
53. Matouk, I. J., Mezan, S., Mizrahi, A., Ohana, P., Abu-Lail, R., Fellig, Y., Degroot, N., Galun, E. & Hochberg, A. (2010) The oncofetal H19 RNA connection: Hypoxia, p53 and cancer. *Biochim Biophys Acta*, 1803, 443–51.
54. Maxwell, P. H., Wiesener, M. S., Chang, G. W., Clifford, S. C., Vaux, E. C., Cockman, M. E., Wykoff, C. C., Pugh, C. W., Maher, E. R. & Ratcliffe, P. J. (1999) The tumour suppressor protein VHL targets hypoxia-inducible factors for oxygen-dependent proteolysis. *Nature,* 399, 271–5.
55. Menyhard, D. K. (2009) Comparative computational analysis of active and inactive cofactors of nitric oxide synthase. *J Phys Chem B,* 113, 3151–9.
56. Mikirova, N. A., Casciari, J. J. & Riordan, N. H. (2010) Ascorbate inhibition of angiogenesis in aortic rings ex vivo and subcutaneous Matrigel plugs in vivo. *J Angiogenes Res,* 2, 2.
57. Miquel, J. (2002) Can antioxidant diet supplementation protect against age-related mitochondrial damage? *Ann N Y Acad Sci,* 959, 508–16.
58. O'Hagan, K. A., Cocchiglia, S., Zhdanov, A. V., Tambuwala, M. M., Cummins, E. P., Monfared, M., Agbor, T. A., Garvey, J. F., Papkovsky, D. B., Taylor, C. T. & Allan, B. B. (2009) PGC-1alpha is coupled to HIF-1alpha-dependent gene expression by increasing mitochondrial oxygen consumption in skeletal muscle cells. *Proc Natl Acad Sci U S A,* 106, 2188–93.
59. Oda, S., Oda, T., Nishi, K., Takabuchi, S., Wakamatsu, T., Tanaka, T., Adachi, T., Fukuda, K., Semenza, G. L. & Hirota, K. (2008) Macrophage migration inhibitory factor activates hypoxia-inducible factor in a p53-dependent manner. *PLoS One,* 3, e2215.
60. Pan, Y., Mansfield, K. D., Bertozzi, C. C., Rudenko, V., Chan, D. A., Giaccia, A. J. & Simon, M. C. (2007) Multiple factors affecting cellular redox status and energy metabolism modulate hypoxia-inducible factor prolyl hydroxylase activity in vivo and in vitro. *Mol Cell Biol,* 27, 912–25.
61. Pathak, A. P., Ward, B. D. & Schmainda, K. M. (2008) A novel technique for modeling susceptibility-based contrast mechanisms for arbitrary microvascular geometries: the finite perturber method. *Neuroimage,* 40, 1130–43.
62. Pfafflin, A., Brodbeck, K., Heilig, C. W., Haring, H. U., Schleicher, E. D. & Weigert, C. (2006) Increased glucose uptake and metabolism in mesangial cells overexpressing glucose transporter 1 increases interleukin-6 and vascular endothelial growth factor production: role of AP-1 and HIF-1alpha. *Cell Physiol Biochem,* 18, 199–210.
63. Pouyssegur, J. & Mechta-Grigoriou, F. (2006) Redox regulation of the hypoxia-inducible factor. *Biol Chem,* 387, 1337–46.
64. Powell, F. L. (2003) Functional genomics and the comparative physiology of hypoxia. *Annu Rev Physiol,* 65, 203–30.

65. Qutub, A., Gabhann, F., Karagiannis, E., Vempati, P. & Popel, A. (2009) Multiscale models of angiogenesis. *IEEE Eng Med Biol Mag,* 28, 14–31.
66. Qutub, A. & Popel, A. (2008) Reactive oxygen species regulate hypoxia-inducible factor HIF1alpha differentially in cancer and ischemia. *Mol Cell Biol,* 28, 5106–19.
67. Qutub, A. A., Liu, G., Vempati, P. & Popel, A. S. (2009) Integration of angiogenesis modules at multiple scales: from molecular to tissue. *Pac Symp Biocomput*, 316–27.
68. Qutub, A. A. & Popel, A. S. (2006) A computational model of intracellular oxygen sensing by hypoxia-inducible factor HIF1 alpha. *J Cell Sci,* 119, 3467–80.
69. Qutub, A. A. & Popel, A. S. (2007) Three autocrine feedback loops determine HIF1 alpha expression in chronic hypoxia. *Biochim Biophys Acta,* 1773, 1511–25.
70. Qutub, A. A. & Popel, A. S. (2009) Elongation, proliferation & migration differentiate endothelial cell phenotypes and determine capillary sprouting. *BMC Syst Biol,* 3, 13.
71. Rajah, T. T. & Grammas, P. (2002) VEGF and VEGF receptor levels in retinal and brain-derived endothelial cells. *Biochem Biophys Res Commun,* 293, 710–3.
72. Rendon, B. E., Willer, S. S., Zundel, W. & Mitchell, R. A. (2009) Mechanisms of macrophage migration inhibitory factor (MIF)-dependent tumor microenvironmental adaptation. *Exp Mol Pathol,* 86, 180–5.
73. Salnikow, K., Aprelikova, O., Ivanov, S., Tackett, S., Kaczmarek, M., Karaczyn, A., Yee, H., Kasprzak, K. S. & Niederhuber, J. (2008) Regulation of hypoxia-inducible genes by ETS1 transcription factor. *Carcinogenesis,* 29, 1493–9.
74. Schmidt, C., Bezuidenhout, D., Beck, M., Van der Merwe, E., Zilla, P. & Davies, N. (2009) Rapid three-dimensional quantification of VEGF-induced scaffold neovascularisation by microcomputed tomography. *Biomaterials,* 30, 5959–68.
75. Schultz, A., Lavie, L., Hochberg, I., Beyar, R., Stone, T., Skorecki, K., Lavie, P., Roguin, A. & Levy, A. P. (1999) Interindividual heterogeneity in the hypoxic regulation of VEGF: significance for the development of the coronary artery collateral circulation. *Circulation,* 100, 547–52.
76. Semenza, G. L. (2002) HIF-1 and tumor progression: pathophysiology and therapeutics. *Trends Mol Med,* 8, S62–7.
77. Semenza, G. L. (2004) Hydroxylation of HIF-1: oxygen sensing at the molecular level. *Physiology (Bethesda),* 19, 176–82.
78. Semenza, G. L. (2006) Development of novel therapeutic strategies that target HIF-1. *Expert Opin Ther Targets,* 10, 267–80.
79. Semenza, G. L. (2009) Regulation of vascularization by hypoxia-inducible factor 1. *Ann N Y Acad Sci,* 1177, 2–8.
80. Sharp, F. R., Ran, R., Lu, A., Tang, Y., Strauss, K. I., Glass, T., Ardizzone, T. & Bernaudin, M. (2004) Hypoxic preconditioning protects against ischemic brain injury. *Neurorx,* 1, 26–35.
81. Sluimer, J. C. & Daemen, M. J. (2009) Novel concepts in atherogenesis: angiogenesis and hypoxia in atherosclerosis. *J Pathol,* 218, 7–29.
82. Sluimer, J. C., Gasc, J. M., Van Wanroij, J. L., Kisters, N., Groeneweg, M., Sollewijn Gelpke, M. D., Cleutjens, J. P., Van den Akker, L. H., Corvol, P., Wouters, B. G., Daemen, M. J. & Bijnens, A. P. (2008) Hypoxia, hypoxia-inducible transcription factor, and macrophages in human atherosclerotic plaques are correlated with intraplaque angiogenesis. *J Am Coll Cardiol,* 51, 1258–65.
83. Smith, T. G., Robbins, P. A. & Ratcliffe, P. J. (2008) The human side of hypoxia-inducible factor. *Br J Haematol,* 141, 325–34.
84. Smith, T. G., Talbot, N. P., Privat, C., Rivera-Ch, M., Nickol, A. H., Ratcliffe, P. J., Dorrington, K. L., Leon-Velarde, F. & Robbins, P. A. (2009) Effects of iron supplementation and depletion on hypoxic pulmonary hypertension: two randomized controlled trials. *JAMA,* 302, 1444–50.
85. Stiehl, D. P., Wirthner, R., Koditz, J., Spielmann, P., Camenisch, G. & Wenger, R. H. (2006) Increased prolyl 4-hydroxylase domain proteins compensate for decreased oxygen levels. Evidence for an autoregulatory oxygen-sensing system. *J Biol Chem,* 281, 23482–91.
86. Taylor, C. T. (2008) Mitochondria and cellular oxygen sensing in the HIF pathway. *Biochem J,* 409, 19–26.

87. Tsoukias, N. M., Goldman, D., Vadapalli, A., Pittman, R. N. & Popel, A. S. (2007) A computational model of oxygen delivery by hemoglobin-based oxygen carriers in three-dimensional microvascular networks. *J Theor Biol,* 248, 657–74.
88. Van Faassen, E. E., Bahrami, S., Feelisch, M., Hogg, N., Kelm, M., Kim-Shapiro, D. B., Kozlov, A. V., Li, H., Lundberg, J. O., Mason, R., Nohl, H., Rassaf, T., Samouilov, A., Slama-Schwok, A., Shiva, S., Vanin, A. F., Weitzberg, E., Zweier, J. & Gladwin, M. T. (2009) Nitrite as regulator of hypoxic signaling in mammalian physiology. *Med Res Rev,* 29, 683–741.
89. Wang, G. L., Jiang, B. H., Rue, E. A. & Semenza, G. L. (1995) Hypoxia-inducible factor 1 is a basic-helix-loop-helix-PAS heterodimer regulated by cellular O2 tension. *Proc Natl Acad Sci U S A,* 92, 5510–4.
90. Wellman, T. L., Jenkins, J., Penar, P. L., Tranmer, B., Zahr, R. & Lounsbury, K. M. (2004) Nitric oxide and reactive oxygen species exert opposing effects on the stability of hypoxia-inducible factor-1alpha (HIF-1alpha) in explants of human pial arteries. *FASEB J,* 18, 379–81.
91. Xing, G., Qualls, C., Huicho, L., Rivera-Ch, M., Stobdan, T., Slessarev, M., Prisman, E., Ito, S., Wu, H., Norboo, A., Dolma, D., Kunzang, M., Norboo, T., Gamboa, J. L., Claydon, V. E., Fisher, J., Zenebe, G., Gebremedhin, A., Hainsworth, R., Verma, A. & Appenzeller, O. (2008) Adaptation and mal-adaptation to ambient hypoxia; Andean, Ethiopian and Himalayan patterns. *PLoS One,* 3, e2342.
92. Zhang, H., Gao, P., Fukuda, R., Kumar, G., Krishnamachary, B., Zeller, K. I., Dang, C. V. & Semenza, G. L. (2007) HIF-1 inhibits mitochondrial biogenesis and cellular respiration in VHL-deficient renal cell carcinoma by repression of C-MYC activity. *Cancer Cell,* 11, 407–20.

Chapter 12
A Computational Framework for Patient-Specific Multi-Scale Cardiac Modeling

Jazmin Aguado-Sierra, Roy C.P. Kerckhoffs, Fred Lionetti, Darlene Hunt, Chris Villongco, Matt Gonzales, Stuart G. Campbell, and Andrew D. McCulloch

12.1 Introduction

Systems biology has introduced new paradigms in science by switching from a reductionist point of view to a more integrative approach toward the study of systems. As researchers over the past years have produced an extraordinary wealth of knowledge on human physiology, we now aim at integrating this knowledge to decipher the intimate relationships between the different components and scales that form the delicate balance in physiological systems. Our aim is to study the heart.

The heart has always produced great interest to scientists since ancient times. Aristotle was one of the first philosophers to acknowledge that "the heart is the beginning and origin of life, and without it, no part can live" [29]. Ever since, anatomists, physiologist, mathematicians, physicists, biologists, biochemists, and geneticists have studied the cardiovascular system, reducing it to its smallest components. Integrative physiology aims to put all these parts together, and the tool employed is computational modeling. The aim of Cardiac Computational Modeling is to create a multi-scale framework to understand the heart physiology, from genes to the whole cardiovascular function. The task is not an easy one. The heart physiology is widely complex, and different tools and algorithms have to be created to intertwine the different systems acting at different levels.

Mathematics is the quantitative tool to represent reality and analyze the physical and biological world around us. One of the best examples of a mathematical model is the one created by Hodgkin and Huxley, which earned them the Nobel Prize in Medicine in 1963, in which they describe the action potential generation quantitatively using voltage–current–capacitance relationships and voltage-dependent conductances of distinct ions. This pivotal work that implements mathematical models to describe ionic flow across excitable membranes is still integrated conceptually in various cellular models of electrophysiology (Chap. 3). By the estimation of the

J. Aguado-Sierra (✉)
Department of Bioengineering, University of California, 9500 Gilman Dr, La Jolla, Mailcode #0412, San Diego, CA 92093-0412, USA
e-mail: jaguadosierra@ucsd.edu

R.C.P. Kerckhoffs (ed.), *Patient-Specific Modeling of the Cardiovascular System: Technology-Driven Personalized Medicine*, DOI 10.1007/978-1-4419-6691-9_12,

conductance and the capacitance, this model is able to capture the kinetics of sodium and potassium ion channels of neurons [10]. Mathematical descriptions of the myocytes have followed so that generic models of propagation have been modified and used to simulate the electrical propagation in the heart [26]. Highly detailed models have now been used successfully, like the one published by Greenstein [13] and modified by Flaim [11] to include myocyte heterogeneities. High-performance computing is a major determinant for the implementation of computational costly models, Graphic Processing Units (GPUs) can be used to accelerate processing times of parallel problems [17], while existing software and technologies can serve as plug-in applications to a flexible architecture that can integrate these tools to solve multi-scale problems.

Data richness drives biomedicine. Data sharing and collaborations are of utmost importance in our globalized world. Improvements in technology on biology, engineering, physics, biochemistry, mathematics, and computing impact the production and accessibility of data. Particularly, developments in imaging and their extended use in the clinical setting provide large amounts of data at fine resolution. Computed Tomography (CT) and Magnetic Resonance Imaging (MRI) are now common tools used to improve the diagnoses in patients; however, their full potential has not yet been exploited.

We have approached a new era in which medicine can be personalized, and the existent knowledge on mathematical models of physiology can be put into use for the benefit of patients using flexible, easy-to-use, fast, modular computational tools for bedside predictions in the cardiology units.

12.2 Multi-Scale Framework of Cardiac Modeling

Various tools for authoring computational models have been created; namely, Continuity (http://www.continuity.ucsd.edu), OpenCell (http://www.opencellproject.org), Open CMISS and CMGUI (http://www.cmiss.org), GIMIAS (http://www.gimias.org/), OpenSIM (http://www.simtk.org/home/opensim), JSim (http://www.nsr.bioeng.washington.edu/jsim), SOFA (http://www.sofa-framework.org/home), SBML (http://www.sbml.org/Main_Page), etc. These tools use different structures, languages, and architectures to create multi-scale models. We will base herein on the general experience gathered by developing the tool named Continuity. The basic structure for a software program to create patient-specific multi-scale models requires ease of use; it needs to be computationally efficient, reliable, and mathematically correct, so that modelers and nonmodelers can use it to its full extent in the clinical setting. Environments for problem-solving multi-scale physics need to be modular, user-friendly and with an architecture that enables data and model sharing, so that databases are publicly accessible and models are reused and collaboration for further scientific advancement is ensured. Accessibility, compatibility to various operating systems (OSs), and ease of model generation are a must. Various of the multi-scale

modeling tools use Extensible Markup Language (XML) for standardizing the ways of encoding the mathematical models; however, this makes it complicated for non-programmers to easily generate their own authored models and integrate them into their multi-scale simulations because the markup specification language can become lengthy, and it is not easily readable to nonexperts. Therefore, the use of simple, straightforward, symbolic, mathematical, authorable model editors is preferred, so that the generation of the procedural code is automatic, optimal, and efficient.

Multi-scale modeling tools require an ease of data handling throughout the whole work pipeline to create a model. Imaging technologies in the clinic and multi-scale physics environments require flexible and compatible data handling tools for pre-and post-processing information.

12.3 Input Data Pipeline for Patient-Specific Multi-Scale Cardiac Modeling

In order to generate a patient-specific model of the heart, a series of measurements should be performed by the physicians [16, 21] (Fig. 12.1), see also Chaps. 2, 8–10. One of the first main steps toward a patient-specific model is to acquire a detailed, patient-specific geometrical description of the anatomy using CT or MRI imaging. Boundary conditions to a cardiac model relate to all of the adjacent structures or systems interacting with the organ of study. Therefore, measures of hemodynamics and electrophysiology are also important to set up a personalized model, but they require to be selected appropriately according to the nature of the simulation.

12.3.1 Ventricular Anatomy and Fiber Architecture

The anatomy can be obtained using CT and contrast MRI. The images require processing for segmentation and registration to generate a mesh (see Sect. 12.9). Data such as fiber architecture cannot generally be obtained in a patient-specific manner; however, studies have shown that fiber architecture is highly conserved among individuals and species after accounting for the geometric variations between the anatomies [14].

It is also possible to locate scarred or ischemic tissue using measures from gadolinium-enhanced MRI, to determine as detailed as possible the patient's physiology, as part of the mesh generation and parameter estimation for baseline simulations.

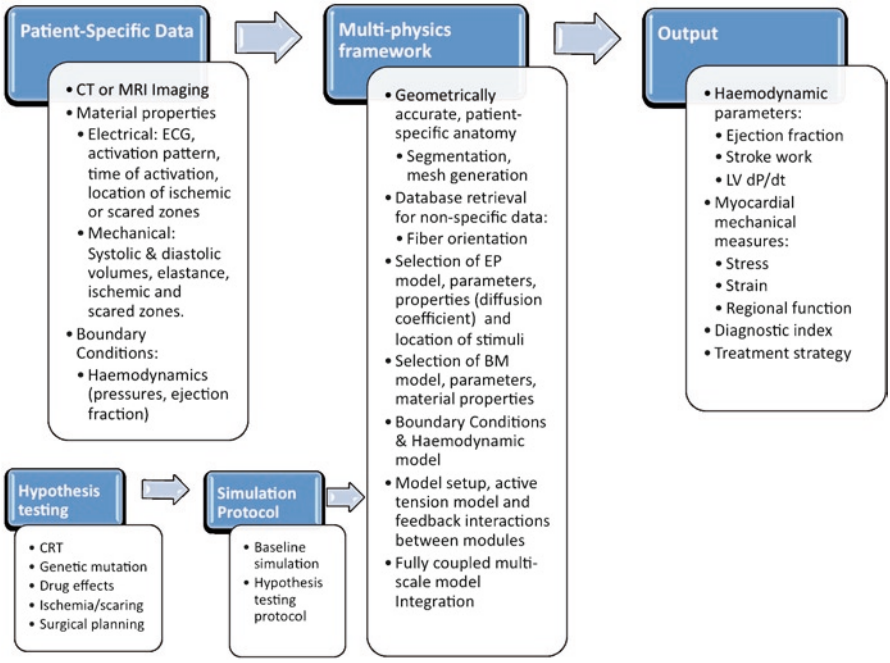

Fig. 12.1 Data pipeline for patient-specific, multi-scale computational cardiac models

12.3.2 Hemodynamics

The use of hemodynamic data allows the estimation of patient-specific material properties of the myocardium and parameters for the circulatory system model. Cardiac ultrasound techniques provide approximations to volumes and pressures [19]. Measures of aortic pressure, left and right ventricular pressure and volumes during both systole and diastole, stroke volume, and ejection fraction help the user to define the appropriate circulatory boundary conditions. Pericardial pressure, for example, can be selected and included in the model from existing data and would not require to be measured since it is not easily obtained in a patient-specific manner. Ventricular pressure and volume can be used to obtain an elastance model for the myocardium using the end-diastolic pressure–volume relationship (EDPVR) and end-systolic pressure–volume relationship (ESPVR) if measures of a couple of beats are obtained at different preload conditions. This is generally achieved clinically by inducing a premature ventricular contraction in patients with a pacemaker. With both EDPVR and ESPVR, the passive and active material properties of the myocardium can be estimated (Chap. 8) [32, 33]. The 3D geometrical reconstruction of the ventricles is then inflated to its passive (EDPVR) and active (ESPVR) levels. This will yield the model properties, by estimating the passive stress-scaling factor, passive exponential shape coefficient,

and the active stress-scaling factor through minimizing the difference between the model and the measured patient-specific pressure–volume relations.

12.3.3 Electrophysiology

Electrophysiological data are also necessary to replicate as closely as possible the patient's heart electrical activity for the baseline simulation. The acquisition of the ECG is simple, and it is used to obtain the total ventricular activation time using the QRS complex, and it can be used to roughly estimate the myocardial conductivity. However, the best measure of electrical endocardial activity is obtained with electroanatomic mapping tools, to set up the stimulation pattern endocardially and estimate the electrical properties of the tissue [34] (Chap. 10). The conductivity and the stimuli can be adjusted in the model to approximate the measurements taken from the patient. The earliest activated regions will provide the stimuli information, while matching the activation patterns will provide the conductivity. Unfortunately, this measurement is quite invasive, and sometimes, it is not convenient to perform.

It is also possible to solve the inverse problem by measuring the epicardial activation from body surface potentials [24], but a model of the torso is necessary to solve the inverse problem.

12.4 Software Architecture

The structure suggested for a multi-scale physics environment is shown in Fig. 12.2. An adequate architecture can comprise three major components: a Database Server, a Solver Client, and a Solver Server and any number of Plug-in applications. The Client serves as a graphical user interface (GUI), and the Server carries out all the numerical calculations for solving the problem. This architecture allows the user to launch the program as a client or a server or both. In this way, the user can locally run a client session, while a remote server or host does all the calculations; otherwise, it can also be used as a whole application together on the local machine. There should be no need for client and server to run in the same OS.

12.5 Database Server

The aim for technology development and collaborative research in cardiac modeling is to have access to services, web services, training, and dissemination to enable, catalyze, and conduct medical research by combining technologies and focusing them on targeted translational and multi-scale challenges in the biomedical arena.

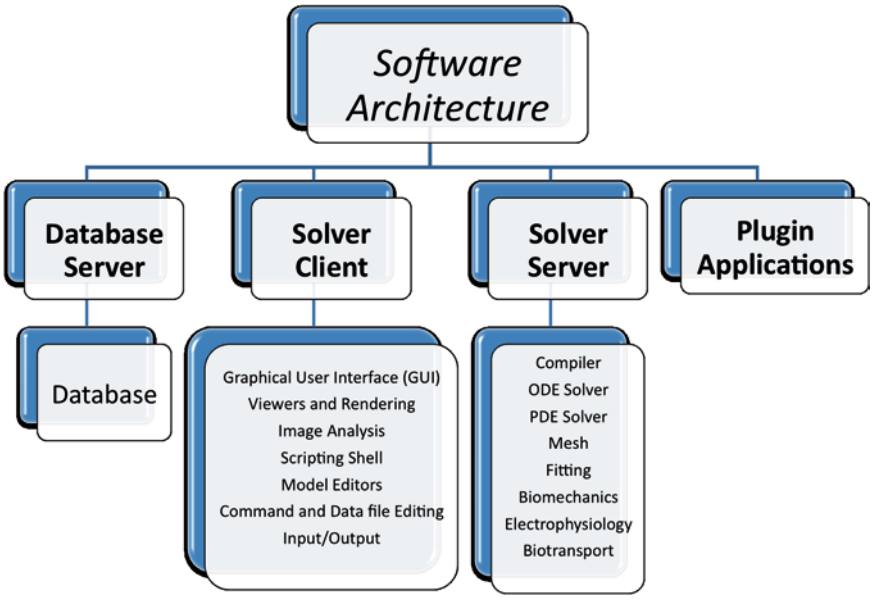

Fig. 12.2 Software architecture for computational multi-scale cardiac modeling

The National Biomedical Computation Resource (NBCR) (http://www.nbcr.net) provides the support and infrastructure to the developers of Continuity to achieve that goal. The objective for the development of computational cardiac modeling is to improve treatment planning for heart disease through individual patient modeling, by providing the framework to incorporate personalized data into new or existing models to aid in an accurate, personalized diagnosis and predict outcomes of existent therapies (i.e., cardiac resynchronization therapy). In order to achieve this aim, a multi-scale framework requires access to a database or library.

The Database is designed to facilitate model sharing, reusing, and classification, by making the models fully annotatable (Fig. 12.3). The owner of the model can choose to share a model with the public or the public can own the model or the owner can lock its contents for personal use only. The database models should be anonymized appropriately and backed up frequently for security. The database is configured to maximize its functionality, rather than just becoming a storage space. The library can be used to store only the small changes on an already existing model. For example, if the user changes a small part of a model, like the initial conditions, then the library will only store and organize the objects changed instead of duplicating the rest of the model content. It also contains all the information related to the model like date of production, description, basis functions, node labels, electrophysiology model, circulatory model, etc. Therefore, all the objects in the library are easily accessible since the user can search on the database by title, a description of the model, the metadata, or any biological attributes defined

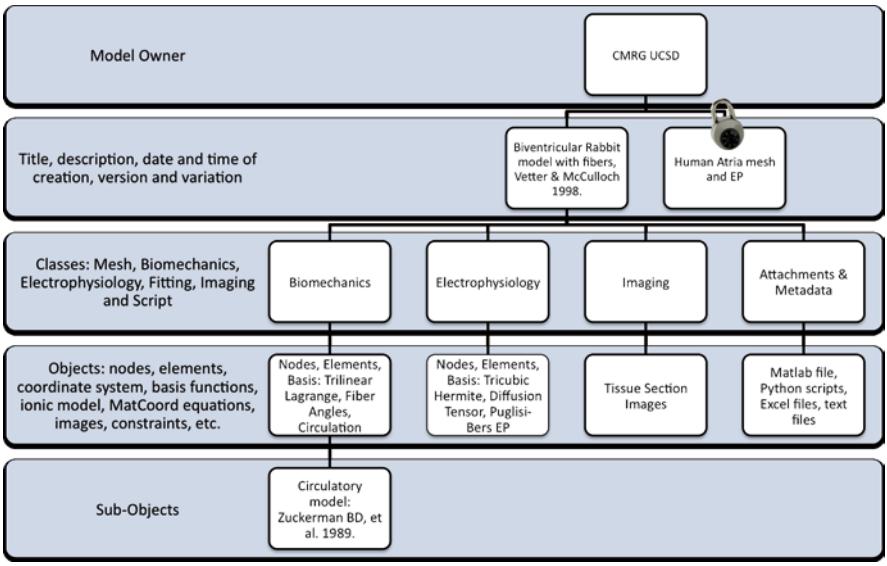

Fig. 12.3 Database structure

(i.e., species, organ-related labels). The user can also retrieve whole models or only specific objects from different models. Attributes can be added to any model, class, object, or subobject, as well as any other file or script necessary to pre- or postprocess data.

The database is a place where users can share complete models, for example, a full model that has been published, so that the scientific audience can reproduce the author's results. The users should be registered to use the Database for a better control over its contents.

The design of the database described mimics the structure of a Continuity file (*.cont6). The hierarchic structure of the database is shown in Fig. 12.3. At the top end, there are owners, who can have any number of models that are publicly available, or private. Each model has a title, description, date and time of creation, version, variation, and any number of classes. The classes are any loadable modules from the Solver Server. Below the classes are Objects, which contain the data from the Editors' forms including coordinate system, basis function, elements, material coordinate equations, ionic model, fitting constraints, images, scripts, etc. (Fig. 12.4). Objects like the nodes, initial conditions in biomechanics, and fitting constraints have subobjects. These subobjects provide a different attribute to their parent object (i.e., nodes of a human model with fitted fibers from a different species). Every model, class, object, and subobject can have either the same or different attributes (i.e., species, organ system, organ, tissues, reference author, reference title, reference date, reference publication). Every hierarchy of the classification is useful for retrieving data in the whole database structure.

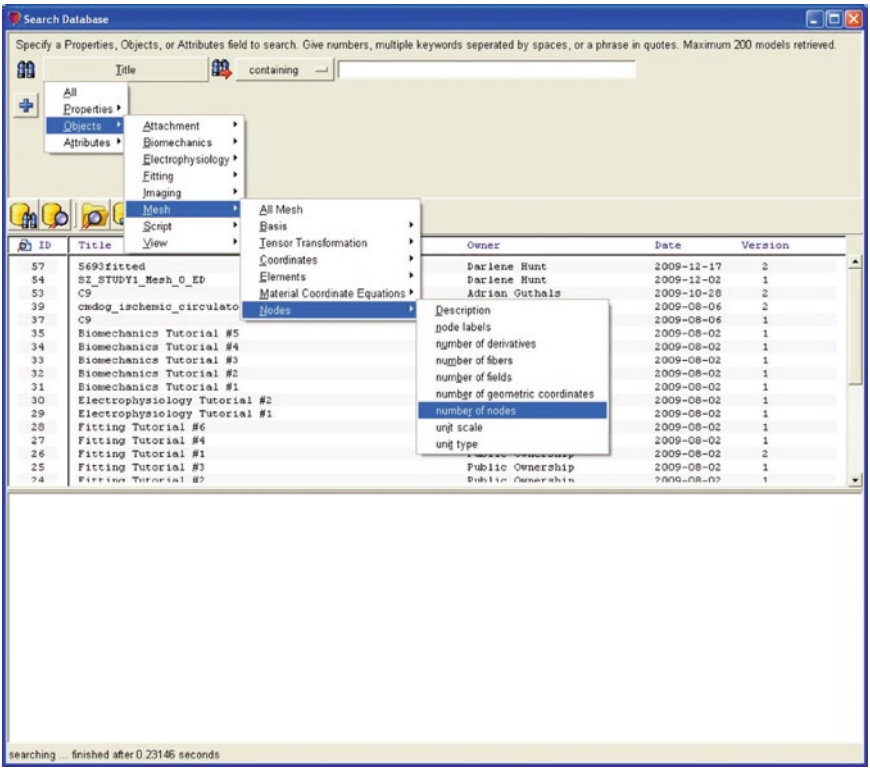

Fig. 12.4 Database search using a GUI interface

A user can deposit a model and different versions of it. As a rule, a new version of the model saves only the changes to the model and references back to the original model for the unchanged information. To create a new model, a new unique title has to be used. Only the owner of a confidential model can delete its files and all its contents, while the public cannot erase public models for safety.

12.6 Solver Client

The client serves as a graphic user interface and includes a viewer framework with dynamically loadable menus, commands and data file editing for Input and Output files, viewers, including 3D visualization and animation, rendering controls, graphical plotting and image analysis, a scripting shell, and message area. It also provides the interface to web services, compiling, and registration of users to access the software and the database. Toolbars are commonly used and create an easy, straightforward interaction to the solver. Menus should also contain commands for setting and adjusting visualization parameters and for saving images,

animations, or simulations. Important components of the Solver Client are the model editors that form part of each module. The graphic user interface also provides the framework to support external plug-in applications or libraries. For example, the imaging module in Continuity includes a heart-wall marker, some tracking methods, image registration, and segmentation methods; it can also access a library from an Imaging ToolKit (ITK Snap library) for image registration, segmentation, and automatic mesh-building (http://www.itksnap.org/pmwiki/pmwiki.php). A framework that provides access to plug-in applications makes it compatible with other solution methods or pre-/postprocessing applications.

12.7 Model Editors

Any software platform that uses symbolic, mathematical, authorable model editors makes the generation of procedural code automatic and efficient. They are built to facilitate modelers and nonprogrammers the implementation of new mathematical models, or reuse existing ones. One language used for the implementation of the mathematical models is a symbolic mathematics library for python called "SymPy" (http://www.docs.sympy.org/index.html). This python library works as a computer algebra system to make coding as simple as possible and comprehensible. The use of symbolic mathematics makes it easier for the users to directly read and understand the model, and they are not required to learn a programming language to create new models. Online tutorials make it easy to understand and use SymPy. Therefore, each model editor provides the framework to compile the mathematical model using a web service, or if compilers are available in the host computer, then the user can compile his own models. Therefore, the output generated can actually be obtained in any format necessary, that is, C, Python, Fortran, CUDA, or even XML. An XML input can also be translated into readable python, C, or SymPy code.

12.8 Solver Server

The server carries out the numerical calculations for simulation and problem solving. It has dynamically compilable and loadable numerical analysis functions for finite element modeling, nonlinear elasticity and biomechanics, reaction–diffusion systems and electrophysiology, and transport processes and biophysics for cell systems modeling.

The common methods used for cardiac multi-scale modeling are finite element methods (FEMs) for nonlinear mechanics. FEMs are numerical analysis tools to solve partial differential equations (PDEs) in a complex domain (see "Preface" to the book). It is convenient to employ a modular software that includes the

anatomy for fitting and creating a mesh; the biomechanics where material properties and circulatory boundaries can be set; the electrophysiology where membrane kinetics are modeled; biotransport to model reaction–diffusion problems; and finally, but most importantly, a method for specifying the interaction and feedback between modules.

More specifically, we can set a system of ordinary differential equations (ODEs) at a particular point in a physical domain called node, defined in a nodes form (Fig. 12.5a). The mathematical model introduced at this level is the smallest scale to be used in our simulation, and it represents a network of biochemical or biophysical interactions at the subcellular and cellular scale. To spatially couple this pointwise network, we include constitutive laws that represent the physical properties of the system. The solution in the mesh is approximated by linear or higher order functions defined element-wise (Fig. 12.5b). By doing so, we construct the substrate with all the properties of the next scale; this is a detailed arrangement at the tissue level that includes the tissue anisotropy/orthotropy, result of the fibrous and laminar construct of the myocardium. The tissue structure is a major determinant of both the contraction and propagation of the action potential. PDEs are used

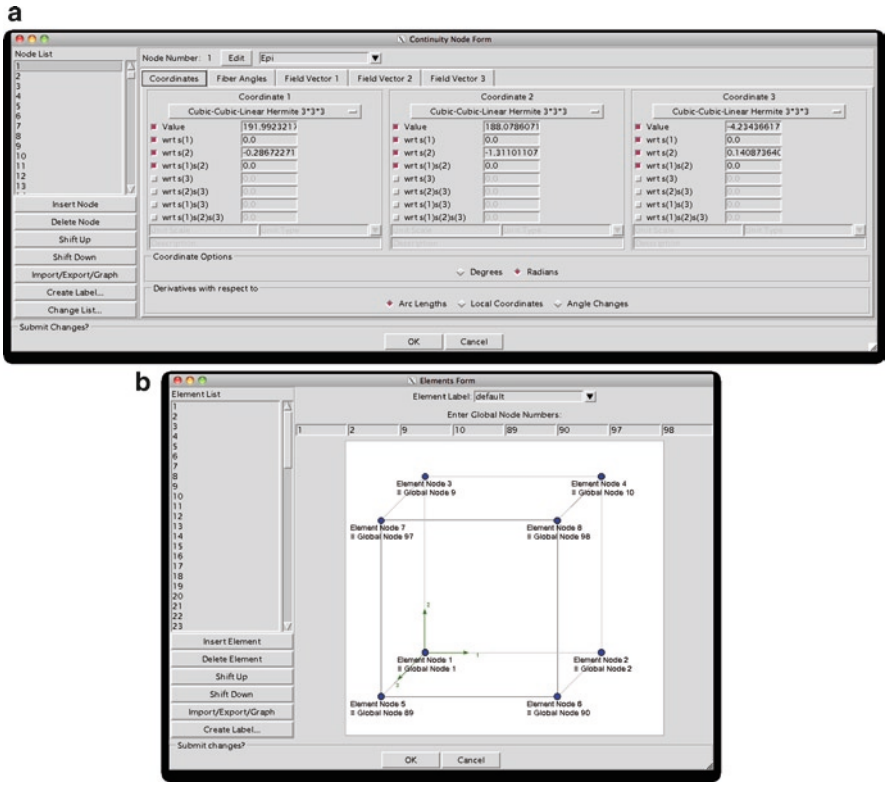

Fig. 12.5 Nodes (**a**) and elements (**b**) forms

to establish the space and time overall behavior and the conservation laws governing the physics over the whole geometry or anatomy of the system. It is also important to establish the adequate boundary conditions that represent the interactions of the heart with neighboring structures. Hemodynamic models are necessary to establish an adequate arterioventricular coupling. Lumped parameter models of the circulation are generally used for this purpose. The modeler can also author the tight relationships between the mathematical models for excitation–contraction coupling (ECC) and their interactions. Information between modules can be passed in a coordinated and efficient manner by scripting the different time steps at which each system requires feedback.

In this way, we can create highly detailed, fully-coupled, patient-specific anatomic models of electromechanics of the heart, setting up boundary conditions in a patient-specific manner.

12.9 Imaging and Fitting Modules

The imaging and fitting modules allow the user to create patient-specific finite element meshes of the heart. The imaging module includes segmentation (ITK Snap library) and automatic mesh-building tools. The user can import a stack of MR, CT, or other types of volumetric imaging data, apply scaling, rotation, or translation to position the stack in the model space, and manually or automatically segment different contours of interest. The pixels that define the segmented contours are sampled as the data to which the initial mesh will be fit. A rough initial mesh is first built in the imaging module using segmented images as a guide. The data points for each contour can be identified with a label to easily distinguish each contour. Once contours have been differentiated, an initial mesh can be conveniently built.

Each contour of the heart (typically left ventricular cavity, right ventricular cavity, epicardium, septum, etc.) is represented by hollow volumes with nodes as vertices. The volumes together form the entire mesh. The user can place these nodes directly on to the segmented image data at the desired slices to create 2D surfaces of each contour. This allows the user to build an initial mesh that already closely approximates the real geometry.

Another rough geometrically approximated mesh created in parallel is built using the fitting module. The rough mesh is fitted next to the segmented data for a more accurate representation of the geometry. The fitting process minimizes the difference between the coordinates of the segmented data and their corresponding interpolated coordinates on the mesh. The corresponding interpolated coordinate data on the mesh are defined by projecting each data point onto the closest surface of the segmented mesh. The maximum projection and angle with the surface can be controlled to filter out noisy data. The user can define fitting constraints on the coordinates and derivatives of the nodes to have control of the fit. Smoothing weights can also be applied to penalize for large changes in stretching and bending of the mesh surface in the process of fitting; they allow the user to

fine-tune the smoothness of the fit if data is sparse or noisy. Finally, data points from all contours can be fitted to their corresponding mesh surfaces simultaneously; this can be done using appropriate labels that distinguish between data points of different contours and their matching surface elements. The fitting module can also fit fields such as fiber angles to the geometry. Fiber direction is generally defined nodewise in the nodes form.

The myofiber architecture is an important component of multi-scale models of the heart. The heart has a characteristic arrangement of fibers that is roughly conserved among individuals [14]. It is possible to obtain accurate measurements of the myofiber orientation using diffusion tensor MRI (DTMRI), or histologically in postmortem hearts; however, there exist some databases (like the Johns Hopkins University public database, http://www.ccbm.jhu.edu/research/dSets.php) where cardiac fiber angles can be obtained and morphed into a new ventricular geometry for patient-specific applications [3] (Chap. 9). In the human and the dog left ventricle, the muscle fiber angle typically varies continuously from about −60° at the epicardium to about +70° at the endocardium, with a higher rate of change at the epicardium [30].

12.10 Mesh Module

The mesh is the geometrical representation of the anatomy to be modeled. It is the frame that holds together the models of different scales. The mesh is obtained from image segmentation from CT or MRI scans and fitted adequately to create a structure that will be discretized into a collection of a finite number of points (nodes), which conform the vertices to the various subdomains (elements). The definition of nodes and elements is a requirement for creating the mesh. The nodes are discrete points in the surfaces of the desired anatomy that are specified on a coordinate system (Fig. 12.5a). The elements establish the connection pattern between the nodes, to dictate the ordered location and connectivity of the elements (Fig. 12.5b). The mesh locates the anatomy into a coordinate system. It is advantageous to have the ability to use various coordinate systems: rectangular cartesian, cylindrical polar, spherical polar, prolate spheroidal, or oblate spheroidal. This variety of coordinate systems allows the user to easily construct a mesh by making use of its geometrical features and using the appropriate coordinate references (for use in Fitting). The left ventricular geometry can be initially approximated by nested ellipses of revolution, that is, two fitted truncated ellipses revolving on the major axis, that is, a prolate spheroidal coordinate system [9]. Cylindrical coordinates facilitate the description of tubular objects, while the spherical polar is useful to describe sphere-shaped geometries [8].

One characteristic of FEMs is the approximation of the continuum using a finite number of functions (finite element interpolation), so the construction of the elements is approximated by basis functions, and their parameters are defined at the nodes. Continuity supports a variety of basis functions for isoparametric finite

element interpolation, generally 1D, 2D, and 3D hexahedral Lagrangian and Hermite piecewise polynomial functions as well as Gauss quadrature integration. In a Mesh module, the user can define numerical and graphical functions associated with nodes; use finite element operations and mathematical functions associated with the mesh; use dependent variables including interpolation, global-element mapping, coordinate transformations, and computations of metric tensors and related quantities such as arc lengths and areas. The Mesh module interfaces problem definitions and numerical solutions. It includes algorithms for solution of nonlinear equations, element and global equation assembly, residual calculations, least squares, eigenvalue and time-stepping algorithms, general utility operations, basic numerical algorithms. The simplest type of elements are piecewise linear Lagrange elements. Basis functions are defined in terms of independent variables, that is, spatial coordinates, so that various combinations of interpolation can be used to create the desired geometry, that is, by taking tensor products to create 1D, 2D, or 3D geometries. Both kinds of interpolation can be estimated with two or three collocation points. Collocation points are distinct points in the element trajectory for which the solution satisfies the initial condition. These points are then used to estimate the solution using their derivatives.

The common structure for a complete mesh for a FEM would include four coordinate systems: a rectangular Cartesian global reference coordinate system, an orthogonal curvilinear coordinate system to describe the geometry and deformation, a general curvilinear finite element coordinates (at each element), and a local orthonormal body coordinates, defining the material structure or fiber and sheet angles.

Every component in the software requires a user-friendly interface editor. The nodes and element forms are the mostly used ones to set up a computational model (Fig. 12.5). In the nodes form, we can define the coordinates for the nodes, the interpolation required for each coordinate, and the fiber angle information; it also contains Fields that can be used to define any other parameters required for the simulation. These Fields can be assigned and used inside any model editor.

12.11 Biomechanics

The structural organization of the myocardium is an important determinant of the cardiac mechanics and its material properties. The passive mechanical properties of tissue have mostly been studied on isolated, arrested whole hearts, or on tissue preparations; however, the total stress in the heart is generally considered as the sum of passive stress, when the tissue is at rest, and active stress generated by the contraction of the myocytes.

Governing equations that relate material properties to continuum tissue behavior must be set in the biomechanics module. The myocardial stress and strain distributions are needed to characterize the regional ventricular function, particularly in pathological conditions like ischemia or scarring. The stress is related to the forces

exerted at a specific location in the myocardium and is normally calculated with respect to an orthogonal system to the fiber orientations. The strain refers to the deformation, or local shape change, as a result of the applied forces. The passive ventricle can be defined by an exponential strain–energy function, which treats the myocardium as nonlinear, anisotropic, and nearly incompressible material. Various parameters in the models can be used to describe the scaling factors for the stress magnitude, incompressibility, and anisotropy of the tissue. The active stress can be described using a time-varying elastic model and can be dependent on time, sarcomere length, and intracellular calcium concentration [20]; with Hill-type models, where the active fiber stress development is modified by shortening or lengthening according to the force–velocity relation, so that fiber tension is reduced by increased shortening velocity or fully history-dependent models that are more complex, based on cross-bridge theory [6].

In the biomechanics module, the Circulatory model is set as a boundary condition to the mechanics. Various types of circulatory models are available in the literature to set the conditions necessary for the simulation [1].

12.12 Electrophysiology Module

The cell electrophysiology is a complex biological system, determined by ion movement across membranes, changing ionic concentrations in different cellular compartments in a nonlinear fashion. The modification of the function of ion channels by genetic mutation, infarcts, scars, or remodeling can create blocks, cardiac arrhythmias, or even sudden cardiac death. The main aim of computational models of electrophysiology is to integrate the vast knowledge on ion channel properties, generally studied in a single-channel fashion, into full cellular models with feedback interactions to relate the molecular-level dynamics to the whole cell function and their clinical phenotype. ECC occurs at the molecular level, particularly involving Ca^{2+} ion movement in various cellular compartments to create a transient rise of intracellular Ca^{2+}, which activates contractile proteins of the cell. Consequently, the heart mechanics also have feedback effects on ion dynamics [25, 26].

Various models of electrophysiology for various species (human, mouse, rabbit, dog, guinea pig, etc.) with different complexity have been published. Various reviews have been published on the subject [7, 28]. The biggest source of mathematical models of electrophysiology available online is the one provided in the CellML repository (http://www.models.cellml.org/electrophysiology). Most of the models contained in this repository use the XML and have various levels of curation. Models of electrophysiology range from a simple two-equation model that describes the propagation wave in the tissue [26] to models with much higher number of ODEs to be solved and that account for cellular heterogeneities in the myocardium, like the model by Flaim et al. [11].

The electrophysiology module in Continuity was created to solve Monodomain problems, that is, a unitary reaction–diffusion equation, a single compartment,

instead of two that represent the intracellular and extracellular spaces, called Bidomain. Comparisons between both methods have been fully studied, and results are highly correlated (0.9971 for an orthotropic conduction), with the advantage that the monodomain solution is less computationally demanding [12]. In the electrophysiology model editor, all of the parameters can be set in a nodewise fashion in a field in the nodes form, so that a stimuli current can be applied at defined regions in the mesh. A set of initial values can be assigned to distinct elements using labels, so that regions of heterogeneous cell kinetics can be simulated. The purpose is to approximate normal or pathological tissue as close as possible to its natural physiology. For example, by labeling elements containing endocardial, midmyocardial, and epicardial cells, we can simulate their heterogeneous behavior [5]. Furthermore, every model can access a set of Parameters defined in the nodes form as fields. These parameters can be used in the model to set up gradients and nodewise variations in the tissue (i.e., apex-to-base cell heterogeneity, ischemic regions).

Direction of propagation in the myocardium depends on fiber rotation and the electrical properties of the tissue determined by its conductivity and capacitance to simulate the myocardium as an orthotropic substrate [4]. These myocardium propagation properties are determined by a diffusion tensor. All the matrix transformations and rotations should be conveniently set in the software, so that the user can easily create the required diffusion tensor in the electrophysiology module by just adding a diffusion coefficient for each orthogonal direction to the fiber orientation.

In general, the electrophysiology model used for each simulation is dependent on the objectives and requirements of the study. Simple models have proven to provide good approximations for excitation propagation in the myocardium, like the model of Beeler and Reuter with only eight ODEs [2], with the advantage of requiring little computational power. Larger models with a greater number of ODEs describe various ion channels and Ca^{2+} kinetics using Markov chain models or including gene mutations [7]. These models are well suited for more detailed analysis using meshes with larger number of elements, which increases computer-processing time, but it is up to the users to choose the electrophysiology model that would provide the best information for their simulations.

12.13 Fully Coupled Electromechanics Models

ECC is a complex mechanism that occurs at the subcellular level, where local changes of membrane potential lead to the release of Ca^{2+} and hence production of force by the myofilaments. Cells are tightly coupled and have a well-structured arrangement in the myocardium. The ionic currents propagate through gap junctions allowing the activation of the whole myocardium. The mechanical coupling of the myocytes is directly linked to cytoskeletal structures, the extracellular matrix,

and the contiguous myocytes. The ventricular wall deforms during the cardiac cycle; this deformation is influenced by the myocardium architecture, which in turn, influences the excitation propagation of the wave.

A fully-coupled, electromechanic model is able to set the interaction between the action potential propagation, the contractile force generation, and the myocardial deformation under realistic hemodynamic boundary conditions in an anatomically accurate finite element mesh of the left ventricle [5]. The degree of coupling can be set up through scripting. This means that the algorithms for coupling various models are fully authorable by the user [23]. This form of coupling is useful for investigating questions related to mechanoelectric feedback [22] at physiological and pathological conditions.

Electrophysiology models with various degrees of complexity can be used to simulate the action potential, ionic channels, and Ca^{2+} ion dynamics. The active tension model is generally the intermediate model between the biomechanics and electrophysiology. The active tension model is able to reproduce the dynamic response of cardiac muscle to time-varying inputs of sarcomere length and cytosolic Ca^{2+} [25].

Different schemes for fully coupled electromechanics can be implemented; however, the challenge is to create stable numerical algorithms that are able to interchange information between the different modules at various time steps. In general, electrophysiology contains the smaller scale in the simulations (subcellular and cellular), so the time steps to solve the electrophysiology are small. After a few small time steps, the larger scales, like mechanics can be updated using the Ca^{2+} transient generated by the cell model. This will update the change of shape of the geometry due to the contraction, using the sarcomere length as a parameter, for example.

12.14 Plug-in Applications

The software architecture allows for the implementation and data communication with useful plug-in applications for pre- or postprocessing implementations. One of the most notable plug-in applications is the implementation of Non-Uniform Rational B-Splines (NURBS) methods. NURBS is a convenient tool that is frequently used for commercial purposes by industry and entertainment. NURBS is a method for parameterizing curved surfaces and volumes through tensor products of polynomials (Fig. 12.6a). Finite element modeling, utilizing NURBS, is convenient because these surfaces can be bended and deformed in a user-friendly "point-and-click" manner. Existent methods are able to convert imaging data to NURBS surfaces [35] in a quick, efficient manner and to reparameterize them to finite element meshes with a different set of polynomial basis functions. The resulting NURBS surface or volumetric object can be used in finite element analysis directly (Fig. 12.6b). This implementation makes the process of geometrical reconstruction less time consuming.

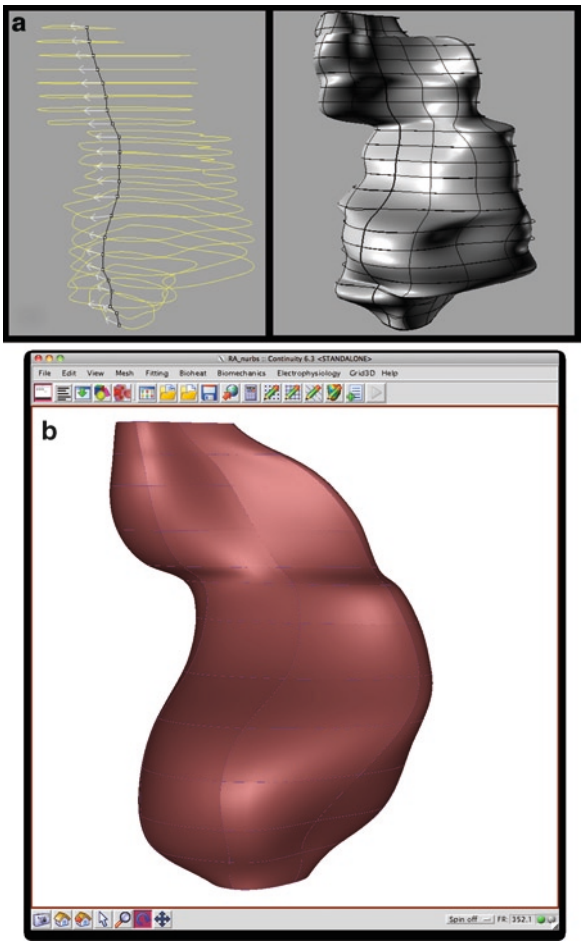

Fig. 12.6 Right atrium mesh generation for a patient-specific application from (**a**) NURBS surfaces to (**b**) tricubic finite element mesh for electrophysiology simulations

12.15 Computational Requirements

As the complexity of the subcellular and cellular models is increasing, the computational frameworks used become challenged. Particularly, systems like the cell pose a great number of ODEs and states to the numerical calculations, which need to be manipulated by processors. Computational power and tools keep increasing exponentially, so a patient-specific computational framework should be able to follow and apply the latest improvements on data processing. In 2002, a coupled model of 3D cardiac electromechanics in an anatomically detailed canine heart with 19,200 degrees of freedom [31] had a total computation time of 78 h and

20 min on a single processor, of which the mechanics problem with 1,960 degrees of freedom took about 6½ h. Soon after, most of the computationally challenging problems were parallelized, so that a similar mechanics problem in 2008 [15] took 40 min per cardiac cycle on 12 nodes of a cluster. These processing times were still long to be used for patient-specific modeling, given that a cluster was available for dedicated modeling in the clinic, and the patient-specific mesh was already fitted and set to solve the problem. The recent extended usage of GPUs for numerical processing purposes is setting new trends for computationally expensive applications. Nowadays, the use of GPUs has been extended to computational models of electromechanics [18], so that using an nVidia GTX-295 GPU (of about US$ 500) for a desktop computer can improve the performance and can speed up calculations over a cluster by 91 times, and 134 times over standard communication interfaces. This work opens up the possibility for real-time simulations for diagnostic purposes in the clinical setting. Furthermore, this kind of application was designed to be used by nonexpert programmers and is easily implemented as part of the computational framework.

The GPU usage in Continuity is invisible to the user. The workflow for the simulations begins with a python program that specifies the mathematical model using the model editor with the SymPy Python library code input. This input is translated into a naïve CUDA C, which is later optimized using source-to-source transformations [17]. The resultant code is compiled with CUDA C, which manages the registers and handles the memory in the GPU to introduce all the thread parallelism to solve the ODEs. PDE calculation is still handled by the CPU, but the computational time required is not as big as the ODEs (before the GPU optimization). However, PDE computations in the GPUs are still part of future work to further speed up computation times. In general, the use of a GPU significantly reduces the computational bottleneck in an 87 ODEs electrophysiology model [11], to simulate a single heartbeat from 4.5 h on a 48 core Opteron cluster to 12.7 min on a desktop workstation without the knowledge of the GPU or CUDA programming.

12.16 Limitations

A mathematical model is an approximation to reality; therefore, all models are inherently wrong. However, mathematical models are still extremely useful to understand the knowledge acquired through experimentation and the components missing to explain the differences between the theoretical knowledge and the actual physiological function. Multi-scale computational models have been thoroughly validated in animal models [15] and may prove useful for prediction and understanding of CRT responder and nonresponder cases (Chaps. 1 and 10). There is a great number of mathematical models for cardiac models of animal physiology, mainly mouse, rat, dog, rabbit, etc. However, human physiology is somewhat different from animal physiology. Accessibility to human heart tissue is limited due to ethical constraints, so new methods and approaches to obtain human cardiac

tissue are being implemented to enlarge our knowledge on human cardiac subcellular, cellular, and organ physiology in health and various stages of disease [27]. However, all the gaps on our knowledge on human physiology can be complemented with animal models. Studies on cardiac electrophysiology and arrhythmogenesis have been extensive in animal tissues and have provided a wealth of knowledge, particularly regarding genetic manipulation, mutations, and physiopathologies. For patient-specific applications in the clinical setting, it is important to take into account the objectives of the simulation, so that reduced or minimal models with validated accuracy can be used to minimize the computation times, so that real-time simulations are feasible.

An important limitation to real-time simulations is the reconstruction of the geometrical data from measurements of patient-specific geometries in the clinic. Better tools for automatic segmentation of CT and MRI imaging, and generation of geometrical representations of the anatomy (the finite element mesh) are required. In general, this process is still lengthy and time consuming and may still pose a challenge for the use of computational modeling in the clinical setting.

Acknowledgements The authors acknowledge the support of NIH grants P41 RR08605, 1R01 HL96544, 1R01 HL086400, 1R01 HL091036, 1R01 HL083359, NSF grant BES-0506252, and UC Discovery grant it106-10159. ADM is a cofounder of Insilicomed, a licensee of UCSD software developed in this research. Insilicomed was not involved and did not support this research.

References

1. Arts, T, T Delhaas, P Bovendeerd, X Verbeek, and F W Prinzen. “Adaptation to mechanical load determines shape and properties of heart and circulation: the CircAdapt model.” *American Journal of Physiology, Heart Circulation Physiology* 288 (2005): 1943–1954.
2. Beeler, G W, and H Reuter. “Reconstruction of the action potential of ventricular myocardial fibres.” *The Journal of Physiology* 268 (June 1977): 177–210.
3. Beg, Mirza Faisal, Patrick A Helm, Elliot McVeigh, Michael I Miller, and Raimond L Winslow. “Computational cardiac anatomy using MRI.” *Magnetic Resonance in Medicine* 52, no. 5 (November 2004): 1167–1174.
4. Caldwell, Bryan J, Mark L Trew, Gregory B Sands, Darren A Hooks, Ian J LeGrice, and Bruce H Smaill. “Three distinct directions of intramural activation reveal nonuniform side-to-side electrical coupling of ventricular myocytes.” *Circulation: Arrhythmia and Electrophysiology* 2 (2009): 433–440.
5. Campbell, Stuart G, et al. “Effect of transmurally heterogenous myocyte excitation–contraction coupling on canine left ventricular electromechanics.” *Experimental Physiology* 94, no. 5 (May 2009): 541–552.
6. Campbell, Stuart G, Sarah N Flaim, Chae H Leem, and Andrew D McCulloch. “Mechanisms of transmurally-varying myocyte electromechanics in an integrated computational model.” *Philosophical Transactions of the Royal Society A* 366, no. 1879 (September 2008): 3361–3380.
7. Clancy, C E, Z I Zhu, and Y Rudy. “Pharmacogenetics and anti-arrhythmic drug therapy: a theoretical investigation.” *American Journal of Physiology, Heart and Circulatory Physiology* 292, no. 1 (January 2007): 66–75.

8. Costa, K D, P J Hunter, J M Rogers, J M Guccione, L K Waldman, and A C McCulloch. "A three-dimensional finite element method for large elastic deformations of ventricular myocaridum: I – cylindrical and spherical polar coordinates." *Transactions of the ASME, Journal of Biomechanical Engineering (ASME)* 118 (November 1996): 452–463.
9. Costa, K D, P J Hunter, J S Wayne, L K Waldman, J M Guccione, and A D McCulloch. "A three-dimensional finite element method for large elastic deformations of ventricular myocardium: II – prolate spheroidal coordinates." *Transactions of the ASME, Journal of Biomechanical Engineering (ASME)* 118 (November 1996): 464–472.
10. FitzHugh, R. "Impulses and physiological states in theoretical models of nerve membrane." *Biophysical Journal* 1, no. 6 (July 1961): 445–466.
11. Flaim, Sarah N, Giles R Wayne, and Andrew D McCulloch. "Contributions of sustained INA and IKv43 to transmural heterogeneity of early repolarization and arrhythmogenesis in canine left ventricular myocytes." *American Journal of Physiology Heart Circulatory Physiology* 291 (2006): 2617–2629.
12. Franzone, Colli P, L F Pavarino, and B Taccardi. "Simulating patterns of excitationm, repolarization and action potential duration with cardiac bidomain and monodomain models." *Mathematical Biosciences* 197, no. 1 (September 2005): 35–66.
13. Greenstein, Joseph L, Robert Hinch, and Raimond L Winslow. "Mechanisms of excitation–contraction coupling in an integrative model of the cardiac ventricular myocyte." *Biophysical Journal* 90 (January 2006): 77–91.
14. Helm, Patrick A, et al. "Evidence of structural remodeling in the dyssynchronous failing heart." *Circulation Research* 98 (2006): 125–132.
15. Kerckhoffs, Roy CP, Andrew D McCulloch, Jeffrey H Omens, and Lawrence J Mulligan. "Effects of biventricular pacing and scar size in a computational model of the failing heart with left bundle branch block." *Medical Image Analysis* 13, no. 2 (April 2009): 362–369.
16. Kerckhoffs, Roy CP, Sanjiv M Narayan, Jeffrey H Omens, Lawrence J Mulligan, and Andrew D McCulloch. "Computational modeling for bedside application." *Heart Failure Clinics* 4 (2008): 371–378.
17. Lionetti, F, Andrew D McCulloch, and Scott B Baden. "GPU accelerated solvers for ODEs describing cardiac membrane equations." *nVidia GPU Technology Conference*. San Jose, CA: nVidia, 2009. 34.
18. Lionetti, Fred. *GPU accelerated cardiac electrophysiology*. La Jolla, CA: UCSD, Master's thesis, 2010.
19. Malm, S, S Frigstad, E Sagberg, H Larsson, and T Skjaerpe. "Accurate and reproducible measurement of left ventricular volume and ejection fraction by contrast echocardiography: a comparison with magnetic resonance imaging." *Journal of the American College of Cardiology* 44 (2004): 1030–1035.
20. McCulloch, Andrew D. Cardiac biomechanics, vol. I, in *The Biomedical Engineering Handbook*, by Joseph D Bronzino, 28:1–26. Boca Raton, FL: CRC Press, 2000.
21. Neal, Maxwell Lewis, and Roy CP Kerckhoffs. "Current progress in patient-specific modeling." *Briefings in Bioinformatics* 11, no. 1 (January 2010): 111–126.
22. Niederer, S A, and N P Smith. "A mathematical model of the slow force response to stretch in rat ventricular myocytes." *Biophysical Journal* 92, no. 11 (June 2007): 4030–4044.
23. Niederer, Steven A, and Nicolas P Smith. "An improved numerical method for strong coupling of excitation and contraction models in the heart." *Progress in Biophysics and Molecular Biology* 96, no. 1–3 (January–April 2008): 90–111.
24. Ramanathan, Jia P, R N Ghanem, P Jia, K Ryu, and Y Rudy. "Noninvasive electrocardiographic imaging for cardiac electrophysiology and arrhythmia." *Nature Medicine* 10 (2004): 422–428.
25. Rice, J J, F Wang, D M Bers, and P P de Tombe. "Approximate model of cooperative activation and crossbridge cycling in cardiac muscle using ordinary differential equations." *Biophysical Journal* 95, no. 5 (September 2008): 2368–2390.

26. Rogers, J M, and A D McCulloch. "A collocation-Galerkin finite element model of cardiac action potential propagation." *IEEE Transactions on Biomedical Engineering (IEEE EMBS)* 41, no. 8 (August 1994): 743–757.
27. Rudy, Yoram, et al. "Systems approach to understanding electromechanical activity in the human heart." *Circulation* (A National Heart, Lung, and Blood Institute Workshop Summary) 118 (2008): 1202–1211.
28. Rudy, Yoram, and Jonathan R Silva. "Computational biology in the study of cardiac ion channels and cell electrophysiology." *Quarterly Reviews of Biophysics* 39, 1, (2006): 57–116.
29. Shaw, James Rochester. "Models for cardiac structure and function in Aristotle." *Journal of the History of Biology* 5, no. 2 (September 1972): 355–388.
30. Streeter, D D Jr. "Gross morphology and fiber geometry of the heart." In *Handbook of physiology, section 2: the cardiovascular system, chapter 4*, by M. B. R., 61–112. Bethesda, MD: American Physiological Society, 1979.
31. Usyk, Taras P, Ian J LeGrice, and Andrew D McCulloch. "Computational model of three-dimensional cardiac electromechanics." *Computing and Visualization in Science* 4 (2002): 249–257.
32. Walker, J C, et al. "MRI-based finite-element analysis of left ventricular aneurysm." *American Journal of Physiology, Heart and Circulation Physiology* 289 (2005): 692–700.
33. Watanabe, H, S Sugiura, H Kafuky, and T Hisada. "Multiphysics simulation of left ventricular filling dynamics using fluid–structure interaction finite element method." *Biophysical Journal* 87 (2004): 2074–2085.
34. Yue, A M, M R Franz, P R Roberts, and J M Morgan. "Global endocardial electrical restitution in human right and left ventricles determined by noncontact mapping." *Journal of the American College of Cardiology* 46 (2005): 1067–1075.
35. Zhang, Yongjie, Yuri Balzilevs, Samrat Goswami, Chandrajit L Bajaj, and Thomas JR Hughes. "Patient-specific vascular NURBS modeling for isogeometric analysis of blood flow." *Computer Methods in Applied Mechanics and Engineering* 196, no. 29–30 (May 2007): 2943–2959.

Appendix: Mathematical Modeling Language Code for the Hemodynamic Model in Fig. 5.1b

```
JSim v1.1
        import nsrunit;
        unit conversion on;
        math MyModel {

realDomain t sec; t.min=0; t.max=60; t.delta=0.01;

// double slash indicates a comment


// PARAMETERS (CONSTANTS):

real PRint = 0.12 sec;
real HR = 77 1/min;

// Varying elastance model for ventricles
real EmaxLV = 5.91908558 mmHg/ml;   // Maximum elastance of left ventricle
real EminLV = 0.0922898032 mmHg/ml; // Minimum elastance of left ventricle
real EmaxRV = 0.45938612 mmHg/ml;   // Maximum elastance of right ventricle
real EminRV = 0.0342539388 mmHg/ml; // Minimum elastance of right ventricle

real VrestLVs = 23.6993603412 ml;  // Peak-systolic rest volume of left ventricle
real VrestLVd = 71.816243458 ml;   // Diastolic rest volume of left ventricle
real VrestRVs = 53.4983766234 ml;  // Peak-systolic rest volume of right ventricle
real VrestRVd = 102.8814935065 ml; // Diastolic rest volume of right ventricle

// Varying elastance model for atria
real EmaxLA = 0.5056326299 mmHg/ml;  // Maximum elastance of left atrium
real EminLA = 0.404506104 mmHg/ml;   // Minimum elastance of left atrium
real EmaxRA = 0.3218841186 mmHg/ml;  // Maximum elastance of right atrium
real EminRA = 0.2575072949 mmHg/ml;  // Minimum elastance of right atrium

real VrestLAs = 73.9735665827 ml;  // Peak-systolic rest volume of left atrium
real VrestLAd = 73.9735665827 ml;  // Diastolic rest volume of left atrium
real VrestRAs = 75.9202393875 ml;  // Peak-systolic rest volume of right atrium
real VrestRAd = 75.9202393875 ml;  // Diastolic rest volume of right atrium

// Systemic circulation parameters
real Rartcap =
        0.6923076923 mmHg*sec/ml; // Resistance of systemic arteries & capillaries
real RSysVeins = 0.1384615385 mmHg*sec/ml;    // Resistance of systemic veins
real RAorticValve = 0.0046153846 mmHg*sec/ml; // Resistance of aortic valve
real RMitralValve = 0.0046153846 mmHg*sec/ml; // Resistance of mitral valve
real CSysArtCaps =
        8.6167741935 ml/mmHg; // Compliance of systemic arteries & capillaries
real CSysVeins = 70.00951584 ml/mmHg; // Compliance of systemic veins
real VrestSysArtCaps = 311.64 ml;     // Rest-volume of systemic arteries & capillaries
real VrestSysVeins = 1829.03 ml;      // Rest-volume of systemic veins

// Pulmonary circulation parameters
real RPulArtCaps =
        0.0775384615 mmHg*sec/ml; // Resistance of pulmonary arteries & capillaries
real RPulVeins = 0.0092307692 mmHg*sec/ml;   // Resistance of pulmonary veins
real RPulValve = 0.0046153846 mmHg*sec/ml;   // Resistance of pulmonary valve
real RTricuspidValve = 0.0046153846 mmHg*sec/ml; // Resistance of tricuspid valve
real CPulArtCaps = 13.25 ml/mmHg;  // Compliance of pulmonary arteries & capillaries
real CPulVeins = 20.405 ml/mmHg;   // Compliance of pulmonary veins
real VrestPulArtCaps = 74.2 ml;   // Rest-volume of pulmonary arteries & capillaries
real VrestPulVeins = 169.07 ml;   // Rest-volume of pulmonary veins
// VARIABLES
```

```
// Varying elastance heart variables
real ActFuncVentricles(t) dimensionless; // Activation fxn for ventricular elastance
real ActFuncAtria(t) dimensionless;      // Activation fxn for atrial elastance
real ELV(t) mmHg/ml;        // Elastance of left ventricle
real VrestLV(t) ml;         // Rest volume of left ventricle
real VLV(t) ml;             // Volume of left ventricle
realState EDVLV(t) ml;      // End-diastolic volume of left ventricle
real ERV(t) mmHg/ml;        // Elastance of right ventricle
real VrestRV(t) ml;         // Rest volume of right ventricle
real VRV(t) ml;             // Volume of right ventricle
realState EDVRV(t) ml;      // End-diastolic volume of right ventricle
real VrestLA(t) ml;         // Rest volume of left atrium
real VLA(t) ml;             // Volume of left atrium
real ELA(t) mmHg/ml;        // Elastance of left atrium
real PLV(t)  mmHg;          // Pressure in left ventricle
real PLA(t)  mmHg;          // Pressure in left atrium
real PRV(t) mmHg;           // Transmural pressure in right ventricle
real PRA(t) mmHg;           // Transmural pressure in right atrium
real VrestRA(t) ml;         // Rest volume of right atium
real VRA(t) ml;             // Volume of right atrium
real ERA(t) mmHg/ml;        // Elastance of right atrium
real FTricuspidValve(t) ml/sec;  // Flow through tricuspid valve
real FAorticValve(t) ml/sec;     // Flow through aortic valve
real FMitralValve(t) ml/sec;     // Flow through mitral valve
real FPulValve(t) ml/sec;        // Flow through pulmonary valve
real CardiacOutput(t) L/min;     // Cardiac output

// Systemic circulation varibles
real Paorta(t)  mmHg;       // Pressure in aorta
real PSysVeins(t)  mmHg;    // Pressure in systemic veins
real VSysArtCaps(t) ml;     // Volume of systemic arteries & capillaries
real VSysVeins(t) ml;       // Volume of systemic veins
real FSysArtCaps(t) ml/sec; // Flow through systemic arteries & capillaries
real FSysVeins(t) ml/sec;   // Flow through systemic veins

// Pulmonary circulation variables
real PPulArtCaps(t) mmHg;   // Pressure in pulmonary arteries & capillaries
real PPulVeins(t) mmHg;     // Pressure in pulmonary veins
real VPulArtCaps(t) ml;     // Volume of pulmonary arteries & capillaries
real VPulVeins(t) ml;       // Volume of pulmonary veins
real FPulVeins(t) ml/sec;   // Flow through pulmonary veins
real FPulArtCaps(t) ml/sec; // Flow through pulmonary arteries & capillaries

real Vtotal(t) ml;          // Total blood volume


// ALGEBRAIC EQUATIONS:

// Custom activation functions
ActFuncAtria = if (sin(2*PI*t*HR) >= 0 ) sin(2*PI*t*HR) else 0;
ActFuncVentricles = if (sin(2*PI*(t-PRint)*HR) >= 0) sin(2*PI*(t-PRint)*HR) else 0;

event(sin(2*PI*(t-PRint)*HR) >= 0 and sin(2*PI*(t-PRint-t.delta)*HR) < 0) {
 EDVRV = VRV;
 EDVLV = VLV;
}

// Left ventricle equations
ELV = (EmaxLV-EminLV)*ActFuncVentricles + EminLV;  // Custom fxn
VrestLV = (1-ActFuncVentricles)*(VrestLVd-VrestLVs) + VrestLVs; // Custom fxn
PLV = ELV*(VLV-VrestLV);    // Law of elastance
CardiacOutput:t = (FAorticValve-CardiacOutput)/(15sec);  // Low-pass filter

// Right ventricle equations
ERV = (EmaxRV-EminRV)*ActFuncVentricles + EminRV;  // Custom fxn
VrestRV = (1-ActFuncVentricles)*(VrestRVd-VrestRVs) + VrestRVs;  // Custom fxn
PRV = ERV*(VRV-VrestRV);    // Law of elastance
```

```
// Left atrium equations
ELA = ActFuncAtria*(EmaxLA-EminLA) + EminLA;  // Custom fxn
VrestLA = (1-ActFuncAtria)*(VrestLAd-VrestLAs) + VrestLAs;  // Custom fxn
PLA = ELA*(VLA-VrestLA);  // Law of elastance

// Right atrium equations
ERA = ActFuncAtria*(EmaxRA-EminRA) + EminRA;  // Custom fxn
VrestRA = (1-ActFuncAtria)*(VrestRAd-VrestRAs) + VrestRAs;  // Custom fxn
PRA = ERA*(VRA-VrestRA);  // Law of elastance


//Systemic circulation equations
Paorta = ((VSysArtCaps-VrestSysArtCaps)/CSysArtCaps); // Law of elastance
PSysVeins = ((VSysVeins-VrestSysVeins)/CSysVeins);    // Law of elastance
FAorticValve = if (PLV>Paorta) (PLV-Paorta)/RAortic Valve
            else 0; // Ohm's Law (valve)
FMitralValve = if (PLA>PLV) (PLA-PLV)/RMitralValve
            else 0;  // Ohm's Law (valve)
FSysVeins = (PSysVeins-PRA)/RSysVeins;     // Ohm's Law
FSysArtCaps = (Paorta-PSysVeins)/Rartcap;  // Ohm's Law

// Pulmonary equations
PPulArtCaps = ((VPulArtCaps-VrestPulArtCaps)/CPulArtCaps);  // Law of elastance
PPulVeins = ((VPulVeins-VrestPulVeins)/CPulVeins);  // Law of elastance
FPulValve = if (PRV>PPulArtCaps) (PRV-PPulArtCaps)/RPulValve
            else 0; // Ohm's Law (valve)
FTricuspidValve = if (PRA>PRV) (PRA-PRV)/RTricuspid Valve
            else 0; // Ohm's Law (valve)
FPulVeins = (PPulVeins-PLA)/RPulVeins;              // Ohm's Law
FPulArtCaps = (PPulArtCaps-PPulVeins)/RPulArtCaps;   // Ohm's Law

// Summation of volumes
Vtotal = VLV+VSysArtCaps+VSysVeins+VRA+VRV+VPulArtCaps+VPulVeins+VLA;


// ORDINARY DIFFERENTIAL EQUATIONS

// All based on Kirchoff Current Law analog for fluids
VLV:t = FMitralValve-FAorticValve;
VSysArtCaps:t = FAorticValve-FSysArtCaps;
VSysVeins:t = FSysArtCaps-FSysVeins;
VRV:t = FTricuspidValve-FPulValve;
VPulArtCaps:t = FPulValve-FPulArtCaps;
VPulVeins:t = FPulArtCaps-FPulVeins;
VLA:t = FPulVeins-FMitralValve;
VRA:t = FSysVeins-FTricuspidValve;


// INITIAL CONDITIONS

when (t=t.min) {
    VSysArtCaps = 1113;
    VSysVeins = 3153.5;
    VLV = 125.9934095755;
    VPulArtCaps = 265;
    VPulVeins = 291.5;
    VRV = 175.8658008658;
    VLA = 87.5703947794;
    VRA = 87.5703947794;
    CardiacOutput = 6.5;
    EDVLV = VLV(t.min);
    EDVRV = VRV(t.min);
    }
}
```

Biography

Roy Kerckhoffs earned his Ph.D. degree in biomedical engineering in 2003 at Eindhoven University of Technology in the Netherlands. He is working as a NBCR researcher (National Biomedical Computation Resource) at the Cardiac Mechanics Research Group at the University of California San Diego. His research interests include multiscale modeling of cardiovascular mechanics and electrophysiology. Currently, his main focus lies on the development of multiscale (animal- and patient-specific) computational models of cardiac electromechanics.

Index

N